

OSTD

**Calibration of the Flow in the  
Extended Test Section of the  
Low-Speed Wind Tunnel  
at DSTO**

Lincoln P. Erm

DSTO-TR-1384

**DISTRIBUTION STATEMENT**  
Approved for Public Release  
Distribution Unlimited

20031001 127



# Calibration of the Flow in the Extended Test Section of the Low-Speed Wind Tunnel at DSTO

*Lincoln P. Erm*

**Air Vehicles Division  
Platforms Sciences Laboratory**

DSTO-TR-1384

## **ABSTRACT**

In 1996, the circuit of the low-speed wind tunnel was modified by extending the length of the test section and installing a redesigned contraction. This was done to enable longer models to be tested in the tunnel and also to possibly obtain some improvement in the quality of the flow in the test section. In this report, the results are given of a detailed calibration of the flow in the extended test section of the tunnel. The calibration was performed to: (1) provide a data base of the flow quality, to be used when analysing tests carried out in the tunnel since 1996, and (2) provide a data base for assessing the changes in the flow quality resulting from installing the extended test section and new contraction in 1996. Longitudinal mean-flow velocities, flow angles, turbulence intensities and spectra, were measured at up to 155 grid points across the flow for longitudinal positions of  $x_T = -2.0, -1.0, 0.0$  and  $+1.0$  m from the centre of the turntables in the test section for nominal free-stream velocities of 30, 45, 60 and 75 m/s. The most important area of the test section, where models are usually located, is the region comprising approximately the central 50% of the cross sectional area of the test section. In this region, over the longitudinal measurement range ( $x_T = -2.0$  to  $+1.0$  m), the following flow non-uniformities were observed. For the four velocities, longitudinal mean-flow velocities deviated within the range  $-1.2\%$  to  $+1.6\%$  from their values at the centre of the tunnel test section ( $x_T = 0.0$  m). For velocities of 30 and 60 m/s, horizontal flow angles deviated within the range  $-0.8^\circ$  to  $+0.8^\circ$  and vertical flow angles deviated within the range  $-1.2^\circ$  to  $+0.4^\circ$ . For velocities of 30 and 60 m/s, the u-component turbulence intensities were generally below 0.4%, and the v- and w-component intensities were generally below 0.7%. Corresponding spectra for the u- v- and w-components of the turbulence were relatively smooth over the frequency range 0.3 Hz to 10 kHz, with no significant spikes associated with irregularities in the flow. There was a slight improvement in the quality of the flow in the test section resulting from the modifications to the tunnel in 1996.

## **RELEASE LIMITATION**

*Approved for public release*

AQ F03-12-2550

*Published by*

*DSTO Platforms Sciences Laboratory  
PO Box 4331  
Melbourne Victoria 3001*

*Telephone: (03) 9626 7000  
Fax: (03) 9626 7999*

*© Commonwealth of Australia 2003  
AR-012-551  
January 2003*

**APPROVED FOR PUBLIC RELEASE**

# Calibration of the Flow in the Extended Test Section of the Low-Speed Wind Tunnel at DSTO

## Executive Summary

The low-speed wind tunnel at the Platforms Sciences Laboratory (PSL) in the Defence Science and Technology Organisation (DSTO) was commissioned in 1941. It has a closed return circuit with an octagonal test section 2.74 m wide and 2.13 m high, and the maximum velocity in the test section is about 100 m/s. The tunnel circuit remained essentially unchanged from 1941 until 1996, when the test section length was increased from 4.12 m to 6.56 m and a new contraction was installed upstream of the original contraction. This was done to enable longer models to be tested and also to possibly obtain some improvement in the quality of the flow.

The flow in a tunnel test section is never completely uniform. Detailed measurements need to be taken in the empty test section to see how the flow deviates from location to location. Tunnels are calibrated to: (1) establish if corrections have to be made to test results, (2) indicate if adjustments are needed to the orientation of a model when testing and (3) assess the suitability of the tunnel for a given test. Although some early calibration data was taken for specific purposes, it was not comprehensive.

In this report, the results are given of a detailed and comprehensive calibration of the flow in the extended test section of the tunnel. The calibration was performed to: (1) provide a data base to facilitate detailed analysis of tests conducted since 1996, and (2) provide a data base for assessing the flow quality resulting from installing an extended test section and a new contraction in 1996. A range of longitudinal mean-flow velocities, flow angles, turbulence intensities and spectra were measured in the test section. Data were taken at up to 155 grid points across the flow at each of four longitudinal distances of  $x_T = -2.0, -1.0, 0.0$  and  $+1.0$  m from the centres of the upper and lower turntables and for nominal free-stream velocities of 30, 45, 60 and 75 m/s.

The most important area of the test section, where models are usually located, is approximately the central 0.7 of the width and 0.7 of the height, i.e. the central 50% of the cross sectional area of the test section. In this region, over the longitudinal measurement range  $x_T = -2.0$  to  $+1.0$  m, the following flow non-uniformities were observed. For velocities of 30, 45, 60 and 75 m/s, longitudinal mean-flow velocities deviated within the range  $-1.2\%$  to  $+1.6\%$  from their values at the centre of the tunnel test section ( $x_T = 0.0$  m). For velocities of 30 and 60 m/s, horizontal flow angles deviated within the range  $-0.8^\circ$  to  $+0.8^\circ$  and vertical flow angles deviated within the range  $-1.2^\circ$  to  $+0.4^\circ$ . These are the maximum limits of variation over the complete velocity range, but for any given velocity the deviations in mean velocities and flow angles were generally substantially less than these values. For velocities of 30 and 60 m/s, the u-component turbulence intensities were below 0.4%, and the v- and w-component intensities were below 0.7%. Spectra for the u- v- and w-components of the turbulence were relatively smooth over the frequency range 0.3 Hz to 10 kHz, with no significant spikes associated with irregularities in the flow. The quality of the flow in the extended test section was found to be slightly better than that in the original test section.

The literature indicates that, for a low-speed tunnel, longitudinal velocities should not deviate from the mean value by more than  $\pm 0.75\%$ , and horizontal and vertical flow angles should not deviate from the longitudinal direction by more than  $\pm 0.25^\circ$ . The u-component turbulence intensities should be less than about 0.1% for research, but intensities as high as 0.5% are acceptable for developmental testing. The variations in mean velocities and flow angles for the DSTO tunnel are a little higher than some other tunnels. In the future, additional modifications could be made, such as replacing the honeycomb or installing screens, to improve the quality of the flow in the test section.

## Author



**Lincoln P. Erm**  
Air Vehicles Division

*Lincoln Erm obtained a Bachelor of Engineering (Mechanical) degree in 1967 and a Master of Engineering Science degree in 1969, both from the University of Melbourne. His Master's degree was concerned with the yielding of aluminium alloy when subjected to both tensile and torsional loading. He joined the Aeronautical Research Laboratories (now called the Platforms Sciences Laboratory) in 1970 and has worked on a wide range of research projects, including the prediction of the performance of gas turbine engines under conditions of pulsating flow, parametric studies of ramrocket performance, flow instability in aircraft intakes and problems associated with the landing of a helicopter on the flight deck of a ship. Concurrently with some of the above work, he studied at the University of Melbourne and in 1988 obtained his Doctor of Philosophy degree for work on low-Reynolds-number turbulent boundary layers. Lincoln is currently undertaking research investigations in the low-speed wind tunnel, the transonic wind tunnel and the water tunnel.*

---

# Contents

<b>1. INTRODUCTION.....</b>	<b>1</b>
<b>2. MEAN-VELOCITY MEASUREMENTS.....</b>	<b>3</b>
2.1 Test Schedule .....	3
2.2 Procedure Used to Measure Reference Free-Stream Velocities.....	3
2.3 Cross-Tunnel Rake.....	5
2.4 Procedure Used to Measure Mean Velocities .....	5
2.5 Analysis of Mean Velocities .....	9
2.5.1 Analysis With Respect to Each Cross Section .....	9
2.5.2 Analysis With Respect to the Central Cross Section .....	9
2.5.3 Longitudinal Velocity Variation .....	26
2.5.4 Effect of Change in Nominal Free-Stream Velocity .....	26
2.5.5 Effect of Probe Misalignment With Respect to the Flow .....	26
2.6 Errors in Measured Mean Velocities.....	27
<b>3. FLOW-ANGLE MEASUREMENTS.....</b>	<b>27</b>
3.1 Test Schedule .....	27
3.2 Six-Hole Probe .....	27
3.3 Transformation of Coordinates .....	33
3.4 Traversing Mechanism .....	34
3.5 Procedure Used to Measure Flow Angles.....	40
3.6 Corrections to Flow Angles to Allow for Probe Support Interference.....	41
3.7 Analysis of Flow Angles .....	44
3.8 Errors in Measured Flow Angles.....	44
3.8.1 Instrumentation Errors.....	45
3.8.2 Probe Setup Errors.....	45
3.8.3 Accumulation of Errors .....	45
<b>4. TURBULENCE-INTENSITY MEASUREMENTS.....</b>	<b>56</b>
4.1 Test Schedule .....	56
4.2 Modified Cross-Tunnel Rake.....	56
4.3 Procedure Used to Measure Turbulence Intensities .....	56
4.4 Analysis of Turbulence Intensities.....	58
4.5 Errors in Measured Turbulence Intensities.....	59
<b>5. SPECTRAL MEASUREMENTS .....</b>	<b>59</b>
5.1 Test Schedule .....	59
5.2 Procedure Used to Measure Spectra .....	59
5.3 Analysis of Spectra .....	72
<b>6. COMPARISON OF FLOW QUALITY IN THE ORIGINAL AND THE EXTENDED TEST SECTIONS OF THE LSWT .....</b>	<b>73</b>
6.1 Mean Velocities.....	73
6.2 Flow Angles .....	91
6.3 Turbulence Intensities.....	91
6.4 Spectra.....	91
6.5 Overall Effect of Modifying the Contraction and the Length of the Test Section of the LSWT in 1996.....	91

<b>7. ASSESSMENT OF FLOW QUALITY IN THE LSWT.....</b>	<b>104</b>
<b>7.1 Mean Velocities.....</b>	<b>104</b>
<b>7.2 Flow Angles.....</b>	<b>104</b>
<b>7.3 Turbulence Intensities and Spectra.....</b>	<b>105</b>
<b>7.4 Adequacy of Flow Quality in the LSWT.....</b>	<b>105</b>
 <b>8. POSSIBLE CAUSES OF FLOW NON UNIFORMITIES AND POSSIBLE METHODS FOR IMPROVING THE FLOW.....</b>	 <b>106</b>
 <b>9. CONCLUDING REMARKS.....</b>	 <b>109</b>
 <b>10. ACKNOWLEDGEMENTS.....</b>	 <b>110</b>
 <b>11. REFERENCES.....</b>	 <b>111</b>
 <b>APPENDIX A: MODIFICATIONS TO THE LSWT IN 1996.....</b>	 <b>113</b>

**Reproduced From  
Best Available Copy \_**

---

**Copies Furnished to DTIC  
Reproduced From  
Bound Original**

---

## Notation

$C_{p_n}$	Pressure coefficients associated with the six-hole probe, $C_{p_n} = (p_n - p_{ref}) / (0.5 \rho V_\infty^2)$ , ( $n = 1$ to $6$ ).
$f$	Frequency, (Hz).
$H$	Height of the test section of the low-speed wind tunnel, ( $H = 2134$ mm).
$M$	Molecular weight of air ( $M = 28.9644$ ), (dimensionless).
$p_{cu}, p_{cd}$	Static pressures at the upstream and downstream ends respectively of the tunnel contraction, (Pa).
$p_{ref}$	Reference pressure (Pa).
$p_1, p_2, p_3, \dots$	Pressures associated with the six-hole probe or the cross-tunnel rake (pressures are not necessarily total or static), (Pa).
$R^*$	Universal gas constant ( $R^* = 8314.32$ J/[K.kg Mol]).
$S_u, S_v, S_w$	Normalized power spectral densities for the $u$ , $v$ and $w$ components of the turbulence respectively, (dimensionless).
$t$	Static temperature of the air in the test section, (K).
$u$	Fluctuating component of velocity in the $x_T$ direction, (m/s).
$U$	Velocity in the $x_T$ direction ( $U = \bar{U} + u$ ), (m/s).
$\bar{U}$	Mean velocity in the $x_T$ direction, (m/s).
$\bar{U}_B$	Mean velocity in the $x_B$ direction in the probe body coordinate system, (m/s)
$\bar{U}_{NOM}$	Nominal free-stream velocity in the $x_T$ direction, (m/s).
$\bar{U}_{REF}$	Reference free-stream velocity at the "centre" of the test section, (m/s).
$\bar{U}_T$	Mean velocity in the $x_T$ direction in the tunnel coordinate system, (m/s).
$\bar{U}_{-2.0}$	Mean velocity in the $x_T$ direction at the location where $x_T = -2.0$ m, $y_T = 0.0$ m and $z_T = 0.0$ m, (m/s).
$\bar{U}_{-1.0}$	Mean velocity in the $x_T$ direction at the location where $x_T = -1.0$ m, $y_T = 0.0$ m and $z_T = 0.0$ m, (m/s).
$\bar{U}_{0.0}$	Mean velocity in the $x_T$ direction at the location where $x_T = 0.0$ m, $y_T = 0.0$ m and $z_T = 0.0$ m, (m/s).
$\bar{U}_{1.0}$	Mean velocity in the $x_T$ direction at the location where $x_T = 1.0$ m, $y_T = 0.0$ m and $z_T = 0.0$ m, (m/s).
$v$	Fluctuating component of velocity in the $y_T$ direction, (m/s).
$\bar{V}_B$	Mean velocity in the $y_B$ direction in the probe body coordinate system, (m/s)
$\bar{V}_T$	Mean velocity in the $y_T$ direction in the tunnel coordinate system, (m/s).



$V_Y$	Velocity vector as measured with the six-hole probe (yawmeter) (Figure 14), (m/s).
$w$	Fluctuating component of velocity in the $z_T$ direction, (m/s).
$W$	Width of the test section of the low-speed wind tunnel, ( $W = 2743$ mm).
$\overline{W}_B$	Mean velocity in the $z_B$ direction in the probe body coordinate system, (m/s)
$\overline{W}_T$	Mean velocity in the $z_T$ direction in the tunnel coordinate system, (m/s).
$x_B, y_B, z_B$	Body coordinate system (right-handed) for the six-hole probe (Figure 14). The origin is located at centre of the hemisphere which forms the tip of the probe. The $x_B$ axis is along the probe longitudinal axis, the $y_B$ axis is in the plane passing through holes 2, 4 and 5 and the $z_B$ axis is in the plane passing through holes 1, 3 and 5. The axes remain fixed with respect to the probe.
$x_B, y_B, z_B$	Directions or distances in the probe body coordinate system (Figure 14), (m)
$x_T, y_T, z_T$	Tunnel coordinate system (right-handed) (Figure 2). The origin is located at the midpoint of the line joining the centres of the lower and upper turntables in the test section. The $x_T$ axis is on the test section longitudinal centreline and is positive in the downstream direction, the $y_T$ axis is horizontal and is positive to port and the $z_T$ axis is positive vertically downwards. The axes remain fixed with respect to the tunnel.
$x_T, y_T, z_T$	Directions or distances in the tunnel coordinate system (Figure 2), (m).
$\epsilon_H$	Horizontal flow angle in the tunnel coordinate system (Figure 19), (deg).
$\epsilon_V$	Vertical flow angle in the tunnel coordinate system (Figure 19), (deg).
$\theta$	Pitch angle for the six-hole probe, relative to the tunnel coordinate system, $x_T, y_T, z_T$ (Figure 14), (deg).
$\theta_Y$	Flow angle as measured with the six-hole probe (yawmeter) (Figure 14), (deg).
$[\lambda]_{BT}$	Matrix of direction cosines used to transform velocities from the tunnel coordinate system to the probe body coordinate system.
$[\lambda]_{TB}$	Matrix of direction cosines used to transform velocities from the probe body coordinate system to the tunnel coordinate system.
$\rho$	Density of the air in the test section, ( $\text{kg/m}^3$ ).
$\phi$	Roll angle for the six-hole probe, relative to the tunnel coordinate system, $x_T, y_T, z_T$ (Figure 14), (deg).
$\phi_Y$	Flow angle as measured with the six-hole probe (yawmeter) (Figure 14), (deg).
$\psi$	Yaw angle for the six-hole probe, relative to the tunnel coordinate system, $x_T, y_T, z_T$ (Figure 14), (deg).

## 1. Introduction

The low-speed wind tunnel (LSWT) at the Platforms Sciences Laboratory (PSL) in the Defence Science and Technology Organisation (DSTO) was designed in 1939 and commissioned in 1941 (Reference 1). It has a closed return circuit with an octagonal test section 2.74 m wide and 2.13 m high, and the maximum velocity obtainable in the test section is about 100 m/s. At the downstream end of the test section there is a pressure equalizing slot which maintains the test section at near atmospheric pressure. The flow circuit remained essentially unchanged from 1941 until 1996, when the length of the test section was increased, enabling longer models to be tested, and a redesigned contraction was installed. Within the constraints imposed by the space available in the existing settling chamber and the new contraction design, the length of the test section was increased from 4.12 m to 6.56 m. The modifications to the tunnel in 1996 followed the design recommendations given by Watmuff (Reference 2). The modified tunnel is shown diagrammatically in Figure 1 (Reference 1), which also shows an outline of the original contraction. Details of the new contraction design are given in Appendix A.

Ideally, the flow in the test section of a wind tunnel is uniform throughout, is parallel to the tunnel walls (for parallel-walled tunnels) and has zero turbulence. However, the flow is never perfect and it is necessary to calibrate the flow to determine the extent of the irregularities. To calibrate the flow in a tunnel, detailed flow measurements are taken throughout the empty test section to see how the flow deviates from location to location. The calibration establishes the corrections to be made to test results, e.g. corrections may have to be made to measurements if the angle of the flow incident on one wing of an aircraft is slightly different from that on the other wing. The calibration also indicates what adjustments have to be made to the orientation of a model when testing, e.g. the flow may have some angularity so that a strain-gauge balance in a model may need to be aligned with the flow rather than the axes of the tunnel. A calibration enables an assessment to be made of the suitability of a tunnel for a given project, e.g. a tunnel having a high free-stream turbulence intensity may be unsuitable for fundamental experiments in which boundary-layer transition is important, since high turbulence levels can significantly affect the characteristics of the flow being studied. A calibration establishes the limitations of the tunnel.

A comprehensive calibration of the flow in the test section of the tunnel with the extended test section and new contraction has been carried out and details of the calibration are given in this report. It is important that the tunnel is calibrated to ensure that the quality of the data produced is suitable for its intended purpose. An extensive range of longitudinal mean-flow velocities, flow angles, turbulence intensities and turbulence spectra were measured. Data were taken at up to 155 grid points across the flow at each of four longitudinal distances of -2.0, -1.0, 0.0 and +1.0 m from the datum of the tunnel coordinate system (see Section 2.1) and for nominal free-stream velocities of 30, 45, 60 and 75 m/s. The calibration data are presented and analysed and explanations of flow behaviour are given.



Figure 1. Diagrammatic representation of the LSWT at PSL, showing the new contraction and extended test section (based on a diagram given in Reference 1)

An earlier calibration was carried out not long before the extended test section and new contraction were installed in 1996. The calibration measurements taken were similar to those listed above. Details of this earlier calibration are given in Reference 3. Selected data from the earlier calibration are given in the current report to assess the effectiveness of the extended test section and the new contraction. All comparisons will be made for the flow cross section at the datum of the tunnel coordinate system (see Section 2.1).

## 2. Mean-Velocity Measurements

### 2.1 Test Schedule

Longitudinal mean velocities,  $\bar{U}$ , were measured in the test section of the tunnel at the 155 grid points shown in Figure 2 for each of four longitudinal positions,  $x_T$  (see below), of -2.0, -1.0, 0.0 and +1.0 m and for nominal free-stream velocities,  $\bar{U}_{NOM}$ , of 30, 45, 60 and 75 m/s.

The origin of the tunnel coordinate system,  $x_T y_T z_T$ , shown in Figure 2, is located at the midpoint of the line joining the centres of the concentric lower and upper turntables in the test section. The  $x_T$  axis is on the test section longitudinal centreline and is positive in the downstream direction, the  $y_T$  axis is horizontal and is positive to the port side of the tunnel and the  $z_T$  axis is positive vertically downwards. The axes form a right-handed coordinate system and remain fixed with respect to the tunnel.

In Figure 2, the grid points are spaced at intervals of 137.0 mm in the  $y_T$  direction, corresponding to the spacing of the pressure probes on the cross-tunnel rake (Section 2.3), and at intervals of 213.4 mm in the  $z_T$  direction. The  $y_T$  spacing corresponds to 1/20th of the width of the octagonal test section and the  $z_T$  spacing corresponds to 1/10th of the height of the test section ( $W = 2743$  mm and  $H = 2134$  mm).

### 2.2 Procedure Used to Measure Reference Free-Stream Velocities

Reference free-stream velocities at the "centre" of the test section of the tunnel were set using the static pressures,  $p_{CU}$  and  $p_{CD}$ , at the upstream and downstream ends respectively of the new contraction. The new contraction was calibrated shortly after being installed and it was determined that

$$\bar{U}_{REF} = \left[ \frac{1.079 \times 2(p_{CU} - p_{CD})}{\rho} \right]^{0.5} \quad (1)$$

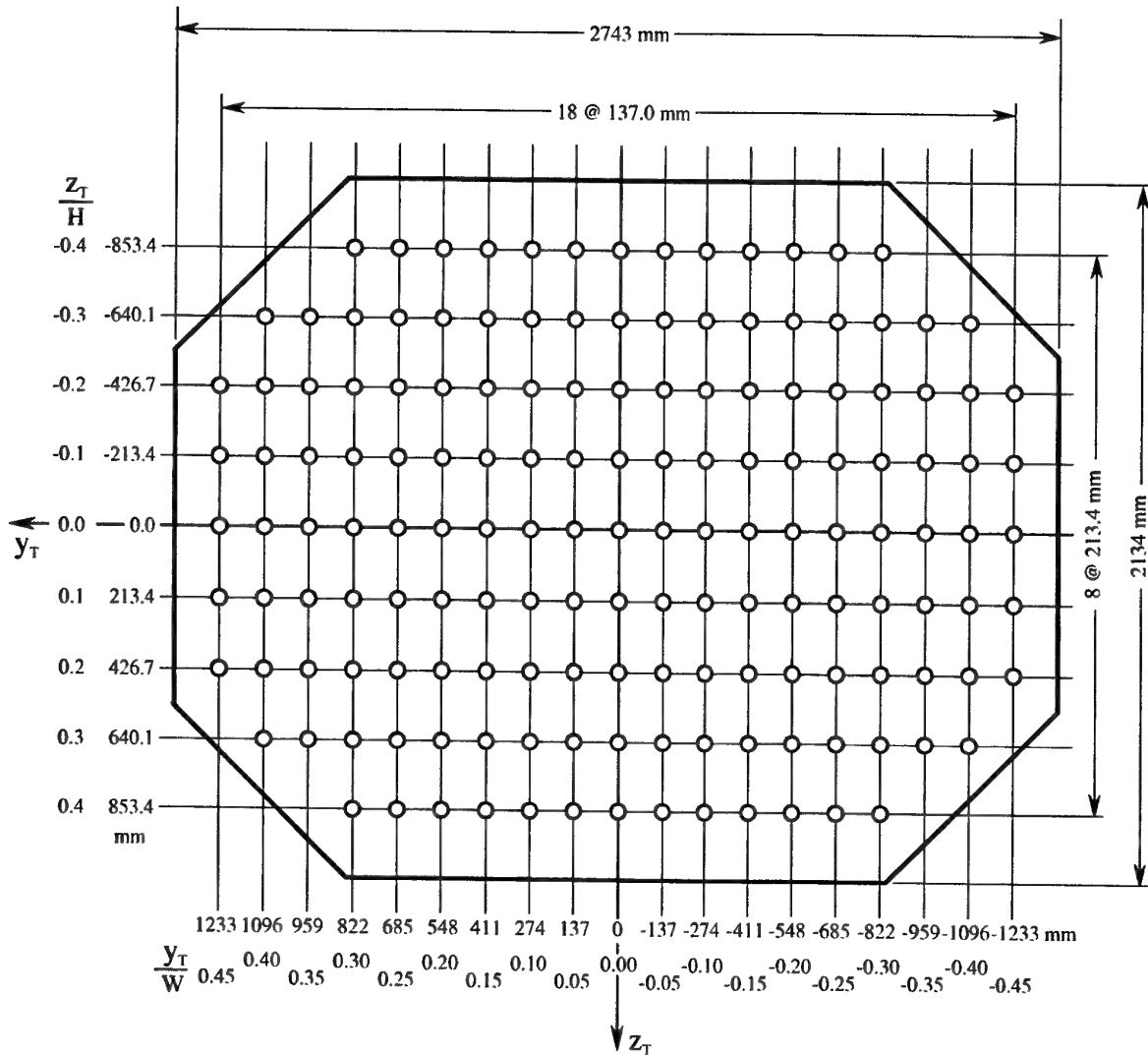


Figure 2. Grid points, shown circled, at which mean velocities and flow angles were measured.

The 1.079 factor is an empirical calibration factor that applies specifically to the LSWT. The density of the air in the test section,  $\rho$ , is given by (Reference 4)

$$\rho = \frac{M p_{cd}}{R^* t} \quad (2)$$

$M$  is the molecular weight of air ( $M = 28.9644$  [dimensionless]),  $R^*$  is the universal gas constant ( $R^* = 8314.32$  J/[K.kg Mol]) and  $t$  is the static temperature of the air in the test section. Equation 1 was used to set the reference free-stream velocity in the test section when the detailed calibration measurements were taken.

## 2.3 Cross-Tunnel Rake

The cross-tunnel rake shown in Figure 3 was used to measure pressures at the different grid points shown in Figure 2. The rake is made up of a number of sections bolted together and contains 15 total-pressure probes and 4 static-pressure probes, arranged as shown in Figure 3. For  $z_r/H$  locations of 0.0,  $\pm 0.1$  and  $\pm 0.2$  (Figure 2), the rake contained probes 1 to 19 and was bolted to the side walls of the test section using mounting brackets. To allow for the corner fillets in the octagonal test section, the length of the rake could be altered by using different end sections. For  $z_r/H = \pm 0.3$ , the rake contained probes 2 to 18 and for  $z_r/H = \pm 0.4$ , the rake contained probes 4 to 16. When the rake was shortened, supporting stands were attached to the rake so that it could be bolted to the floor or the roof of the test section.

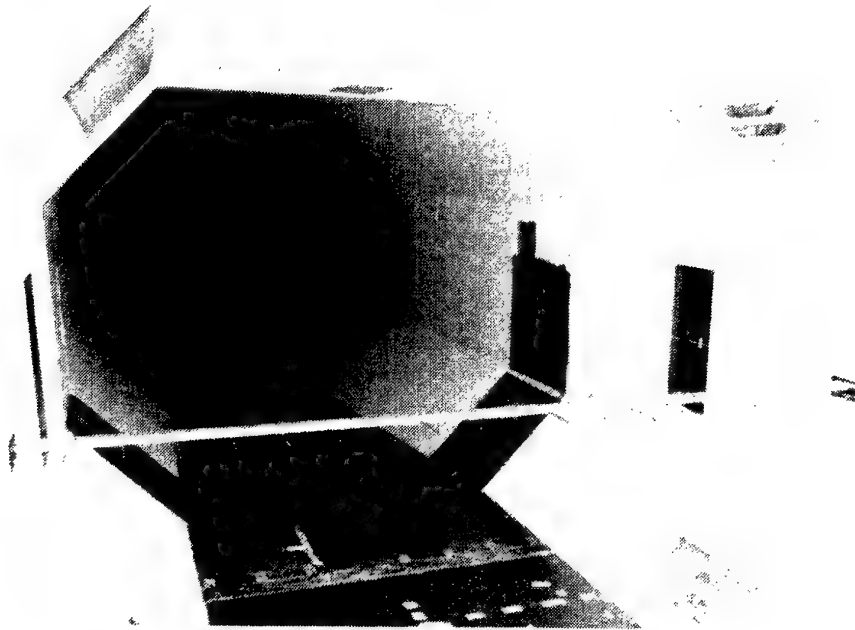
## 2.4 Procedure Used to Measure Mean Velocities

Longitudinal mean velocities at different grid points were measured using the pressure probes on the cross-tunnel rake. Pressures were measured using a Pressure Systems Incorporated (PSI)<sup>1</sup> 8400 Electronic Measurement System, configured with a 32 port Electronic Pressure Scanner capable of measuring 32 differential pressures. The scanner had a range of  $\pm 2490$  Pa ( $\pm 10.0$  inches of water) for  $\bar{U}_{\text{NOM}} = 30$  m/s and a range of  $\pm 6895$  Pa ( $\pm 1.0$  psi) for  $\bar{U}_{\text{NOM}} = 45, 60$  and  $75$  m/s. Software used to control and operate the system is located on a PC. The features of the system are described in References 5 and 6.

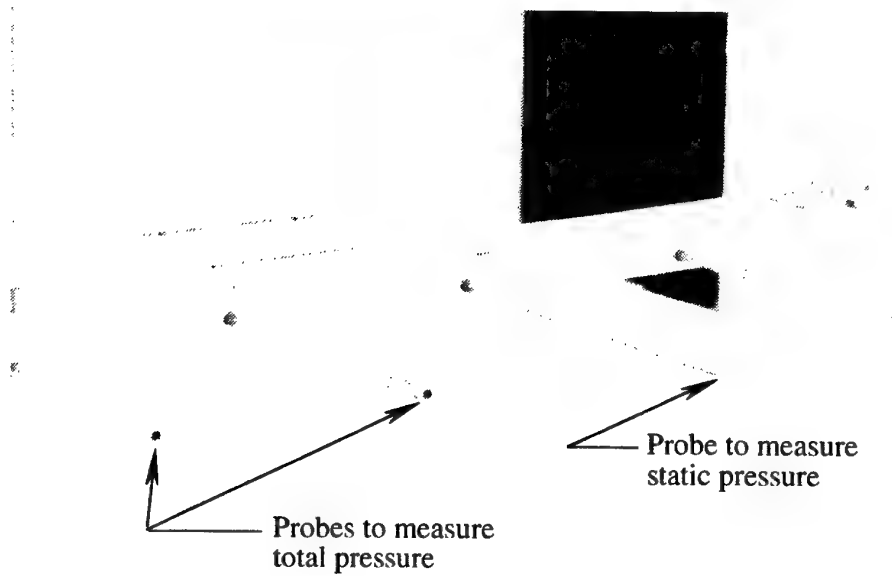
The total and static pressure ports on the probes on the rake, as well as the static pressure ports in the upstream and downstream ends of the contraction, used when measuring  $p_{\text{cu}}$  and  $p_{\text{cd}}$  (static pressure in the test section) respectively, were connected to ports on the scanner, and all ports were referenced to  $p_{\text{cd}}$ . Prior to any given run, the pressure transducers in the scanner were calibrated over the range of pressures likely to be encountered during subsequent measurements. Four different ranges of pressures were used, corresponding to nominal free-stream velocities of 30, 45, 60 and 75 m/s. The accuracy of the calibration was verified by checking that all measured differential pressures were close to zero, as observed graphically on a monitor, when there was no flow in the tunnel.

The software allowed the user to specify sampling controls when acquiring data. The differential pressures corresponding to each of the ports were sampled 50 times at intervals of  $65\,000\ \mu\text{s}$  and then average pressures for each port were calculated and recorded. The  $65\,000\ \mu\text{s}$  interval was the maximum allowable with the system and corresponds to a sampling frequency of 15.4 Hz. The total sampling time for the 50 samples was about 3.2 s. By setting the sampling frequency at the lowest possible value allowed by the equipment, any large scale, slowly varying, pressure oscillations in the tunnel were more likely to be averaged. The above sampling was repeated 10 times

<sup>1</sup> Pressure Systems Incorporated, 34 Research Drive, Hampton, VA, 23666, USA.



Rake mounted in the test section



Details of the pressure probes and the enclosure containing the pressure scanner

Figure 3a. Cross-tunnel rake used to measure mean-flow velocities.

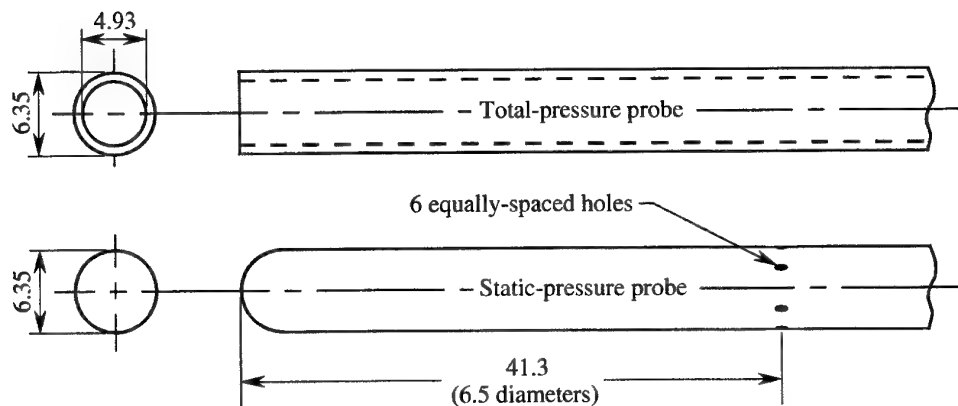
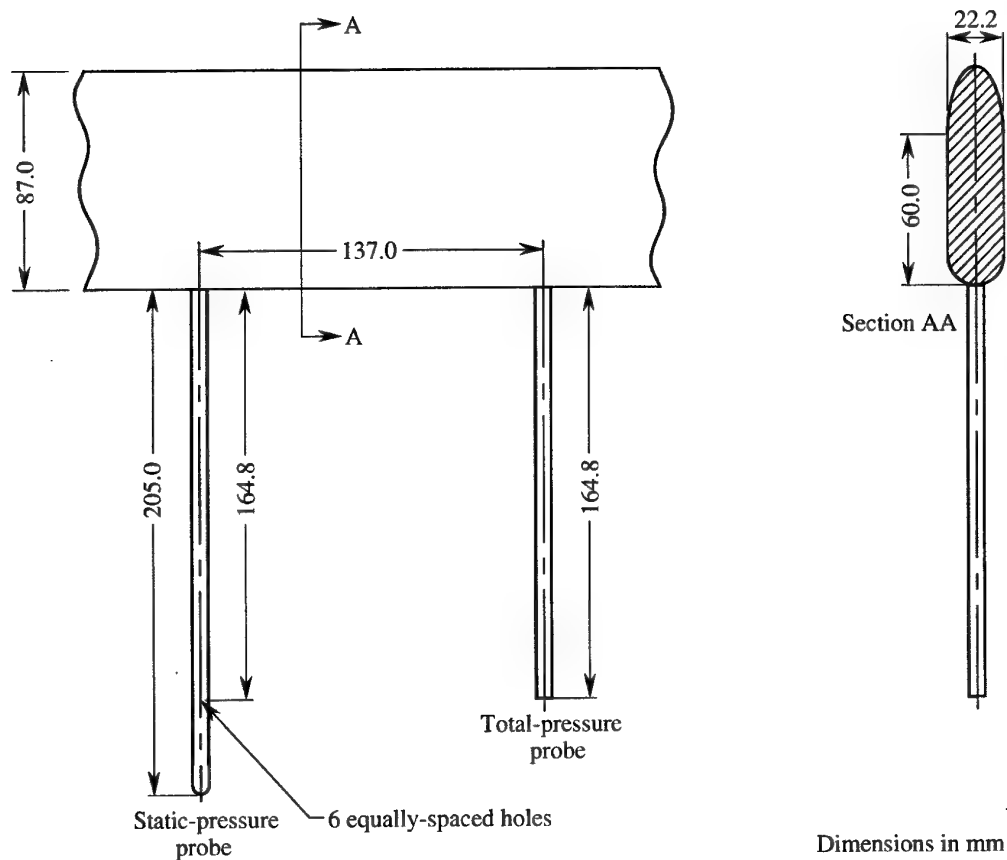
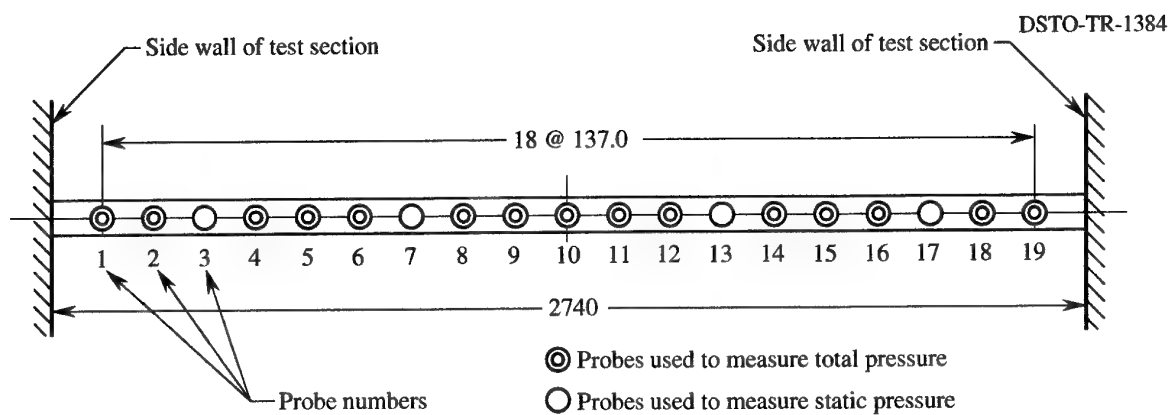


Figure 3b. Cross-tunnel rake used to measure mean-flow velocities showing diagrammatic representation of rake (top), cross section of rake (middle) and details of probes (bottom). 7



with a 5 s time delay between sampling each data set. The differential pressures corresponding to each of the ports were then averaged for the 10 sets of data to obtain overall averages, each of which corresponds to  $50 \times 10 = 500$  individual samples.

As can be seen from Figure 3, the arrangement of the probes on the rake meant that either the total pressure or the static pressure was measured at each grid point. Since it was necessary to know both the static and the total pressure at a given point to calculate the velocity at that point, approximations had to be made when calculating velocities. When calculating velocities at grid points where total pressures were known, nearby static pressures were used. For example, the velocity at point 4 was based upon  $p_4$  (total pressure),  $p_3$  (static pressure) and  $p_7$  (static pressure). A mean velocity denoted by  $\bar{U}_{4A}$  was computed using

$$\bar{U}_{4A} = \left[ \frac{2(p_4 - p_3)}{\rho} \right]^{0.5} \quad (3)$$

and a mean velocity denoted by  $\bar{U}_{4B}$  was computed using

$$\bar{U}_{4B} = \left[ \frac{2(p_4 - p_7)}{\rho} \right]^{0.5} \quad (4)$$

The mean velocity  $\bar{U}_4$  at position 4 was then determined from  $\bar{U}_{4A}$  and  $\bar{U}_{4B}$  using linear interpolation as follows

$$\bar{U}_4 = 0.75 [\bar{U}_{4A}] + 0.25 [\bar{U}_{4B}] \quad (5)$$

At grid points where static pressures were known, mean velocities were determined using linear interpolation of the calculated adjoining velocities. For example, the mean velocity at point 3 was determined from  $\bar{U}_2$  and  $\bar{U}_4$  using linear interpolation as follows

$$\bar{U}_3 = 0.5 [\bar{U}_2 + \bar{U}_4] \quad (6)$$

The reference free-stream velocity,  $\bar{U}_{REF}$ , determined using equation 1, varied slightly for the different positions of the cross-tunnel rake, due to the practical difficulties of a tunnel operator setting the free-stream velocity at precisely the same value for the different rake positions. To obtain a consistent set of values of  $\bar{U}$  measured with the rake, the values of  $\bar{U}$  were non-dimensionalised with respect to the appropriate value of  $\bar{U}_{REF}$ . To obtain a consistent set of results with respect to a given cross section in the tunnel, for example at the centre of the cross section where  $x_T = 1.0$ , the results were then normalized with respect to the  $\bar{U}_{1.0} / \bar{U}_{REF}$  ratio at this point.

## 2.5 Analysis of Mean Velocities

Longitudinal mean velocities are presented as contours of  $(\bar{U} - \bar{U}_{-2.0})/\bar{U}_{-2.0}$ ,  $(\bar{U} - \bar{U}_{-1.0})/\bar{U}_{-1.0}$ ,  $(\bar{U} - \bar{U}_{0.0})/\bar{U}_{0.0}$  and  $(\bar{U} - \bar{U}_{1.0})/\bar{U}_{1.0}$  (expressed as a percentage) for different values of  $x_T$  and  $\bar{U}_{NOM}$ .  $\bar{U}_{-2.0}$ ,  $\bar{U}_{-1.0}$ ,  $\bar{U}_{0.0}$  and  $\bar{U}_{1.0}$  are the mean velocities in the  $x_T$  direction on the tunnel longitudinal centreline ( $y_T = 0.0$  m and  $z_T = 0.0$  m) at the locations where  $x_T = -2.0, -1.0, 0.0$  and  $+1.0$  m respectively. Contour plots of mean velocities, as well as contour plots of flow angles and turbulence intensities, are presented with the direction of the flow out of the page.

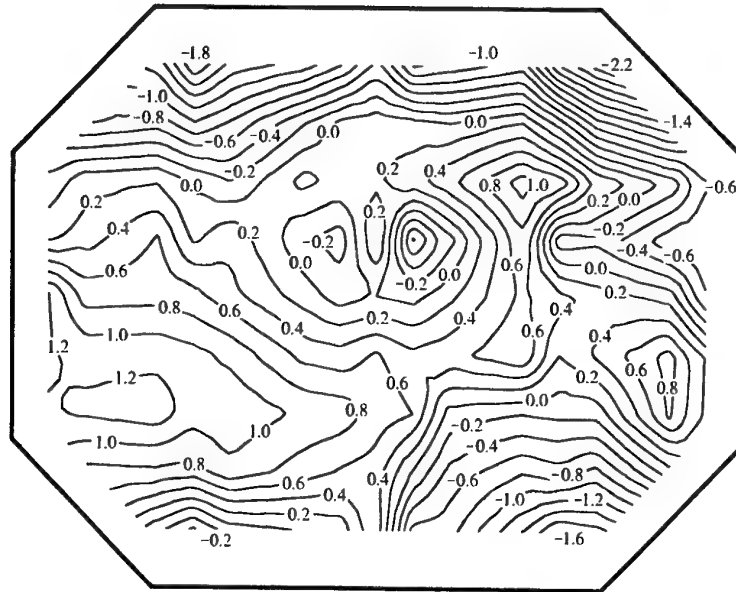
The most important area of the test section, where models are usually located, is the region comprising approximately the central 0.7 of the width and 0.7 of the height, i.e. approximately the central 50% of the cross-sectional area of the test section. Discussion on the variation of mean velocities, as well as on flow angles and turbulence intensities, will mainly apply to these central regions of flow cross sections.

### 2.5.1 Analysis With Respect to Each Cross Section

Contours of  $(\bar{U} - \bar{U}_{-2.0})/\bar{U}_{-2.0}$  for  $x_T = -2.0$  m,  $(\bar{U} - \bar{U}_{-1.0})/\bar{U}_{-1.0}$  for  $x_T = -1.0$  m,  $(\bar{U} - \bar{U}_{0.0})/\bar{U}_{0.0}$  for  $x_T = 0.0$  m and  $(\bar{U} - \bar{U}_{1.0})/\bar{U}_{1.0}$  for  $x_T = +1.0$  m, all for  $\bar{U}_{NOM} = 30$  m/s, are shown in Figure 4. Corresponding plots for  $\bar{U}_{NOM} = 45, 60$  and  $75$  m/s are shown in Figures 5, 6 and 7 respectively. For each of the 16 sets of contours shown in Figures 4 to 7, the normalizing velocity, i.e.  $\bar{U}_{-2.0}$ ,  $\bar{U}_{-1.0}$ ,  $\bar{U}_{0.0}$  or  $\bar{U}_{1.0}$ , is associated with the  $x_T$  location of the contours, i.e.  $\bar{U}_{-2.0}$  is used for contours at  $x_T = -2.0$  m, and likewise for  $\bar{U}_{-1.0}$ ,  $\bar{U}_{0.0}$  and  $\bar{U}_{1.0}$ . For each of the four values of  $\bar{U}_{NOM}$ , the general pattern of the contours at the four  $x_T$  locations is similar, with little evidence of the flow becoming more uniform as it moves downstream. Regions of high or low mean velocity are simply convected downstream with little transverse movement, indicating that there are no large-scale swirls in the test section. For  $\bar{U}_{NOM} = 30$  m/s, for  $x_T = -2.0, -1.0, 0.0$  and  $+1.0$  m, longitudinal mean-flow velocities typically deviated between  $-0.8\%$  and  $+1.2\%$  from their values at the centre of each tunnel cross section (Figure 4). Corresponding deviations for  $\bar{U}_{NOM} = 45, 60$  and  $75$  m/s were from  $-0.6\%$  to  $+1.2\%$  (Figure 5), from  $-0.4\%$  to  $+1.2\%$  (Figure 6) and from  $-0.4\%$  to  $+1.4\%$  (Figure 7) respectively.

### 2.5.2 Analysis With Respect to the Central Cross Section

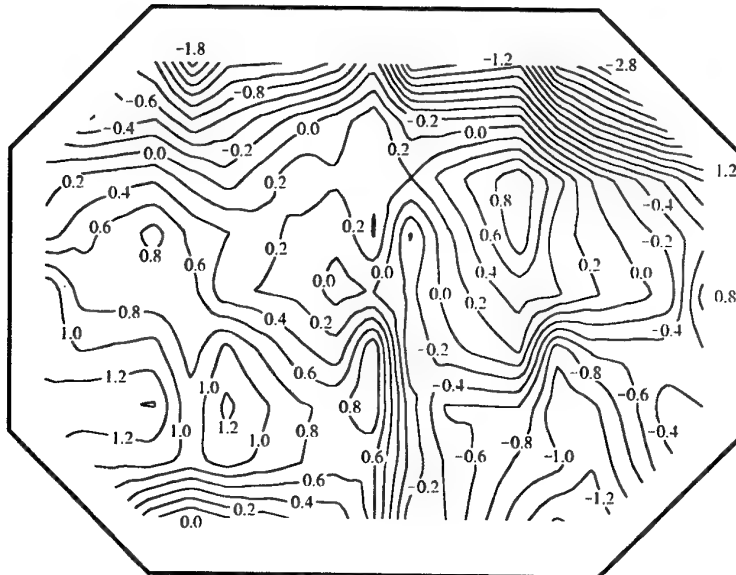
Contours of  $(\bar{U} - \bar{U}_{0.0})/\bar{U}_{0.0}$  for  $\bar{U}_{NOM} = 30$  m/s and  $x_T = -2.0, -1.0, 0.0$  and  $+1.0$  m are shown in Figure 8. Corresponding plots for  $\bar{U}_{NOM} = 45, 60$  and  $75$  m/s are shown in Figures 9, 10 and 11 respectively. For the 16 sets of contours shown in Figures 8 to 11, a single normalizing velocity at the centre of the test section, i.e.  $\bar{U}_{0.0}$ , is used for each value of  $\bar{U}_{NOM}$ , which means that the normalizing velocity is not always associated with the  $x_T$  location of the contours, e.g.  $\bar{U}_{0.0}$  is used for contours at  $x_T = -2.0, -1.0$  and  $+1.0$  m. The contours in each of Figures 8 to 11 therefore show how mean velocities vary in the longitudinal or  $x_T$  direction. Mean velocities at given values of  $y_T$  and  $z_T$  increase as the flow moves downstream, which is consistent with the fact that the test



$$\frac{\bar{U} - \bar{U}_{-2.0}}{\bar{U}_{-2.0}} \%$$

$$\bar{U}_{\text{NOM}} = 30 \text{ m/s}$$

$$x_T = -2.0 \text{ m}$$



$$\frac{\bar{U} - \bar{U}_{-1.0}}{\bar{U}_{-1.0}} \%$$

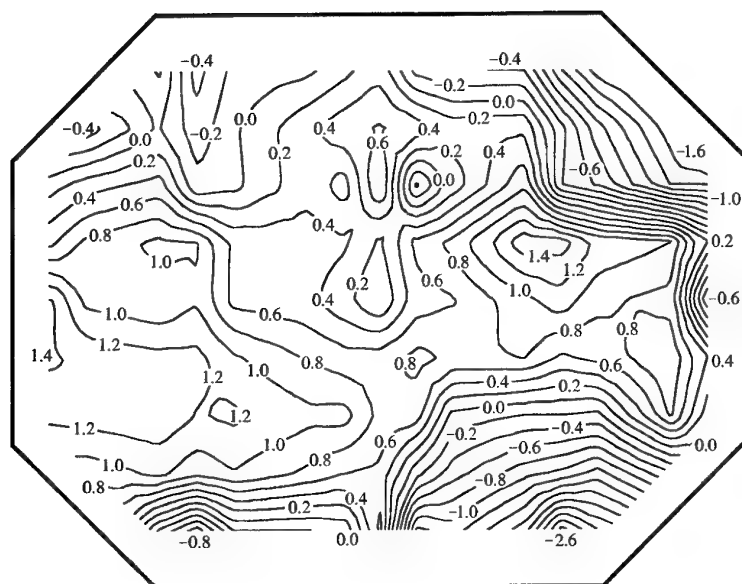
$$\bar{U}_{\text{NOM}} = 30 \text{ m/s}$$

$$x_T = -1.0 \text{ m}$$

Figure 4. Contours of velocity deviation for  $\bar{U}_{\text{NOM}} = 30 \text{ m/s}$  for  $x_T = -2.0, -1.0, 0.0$  and  $1.0 \text{ m}$ .

(a)  $x_T = -2.0$  and  $-1.0 \text{ m}$ .

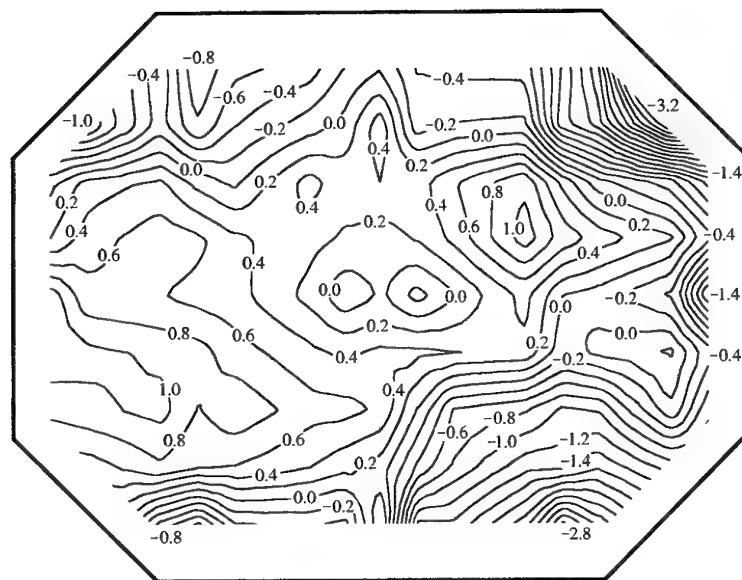
The flow is out of the page.



$$\frac{\bar{U} - \bar{U}_{0.0}}{\bar{U}_{0.0}} \%$$

$$\bar{U}_{\text{NOM}} = 30 \text{ m/s}$$

$$x_T = 0.0 \text{ m}$$



$$\frac{\bar{U} - \bar{U}_{1.0}}{\bar{U}_{1.0}} \%$$

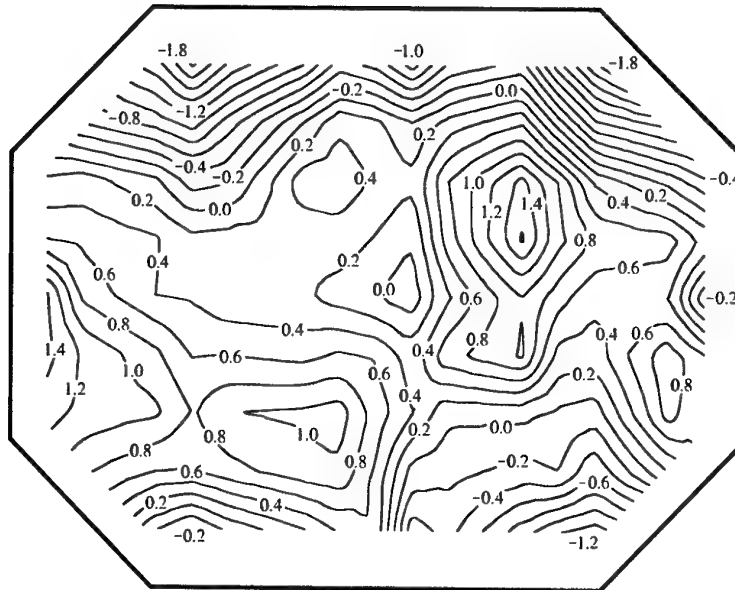
$$\bar{U}_{\text{NOM}} = 30 \text{ m/s}$$

$$x_T = 1.0 \text{ m}$$

Figure 4 cont'd. Contours of velocity deviation for  $\bar{U}_{\text{NOM}} = 30 \text{ m/s}$  for  $x_T = -2.0, -1.0, 0.0$  and  $1.0 \text{ m}$ .

(b)  $x_T = 0.0$  and  $1.0 \text{ m}$ .

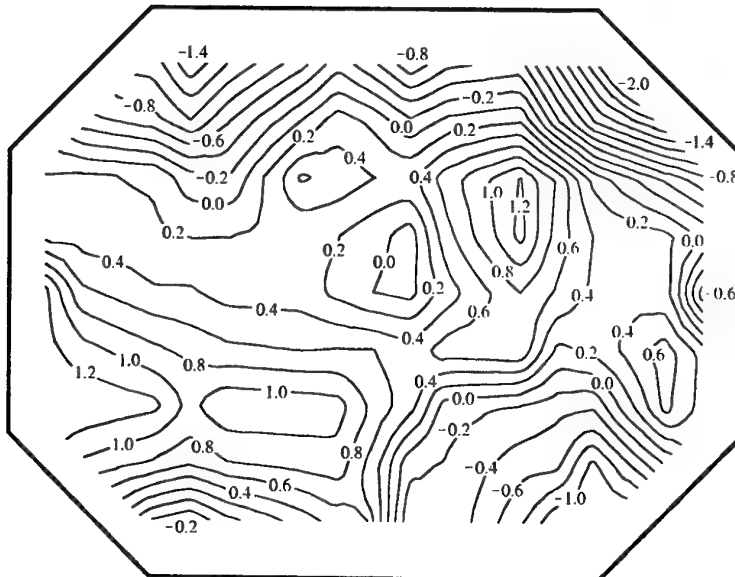
The flow is out of the page.



$$\frac{\bar{U} - \bar{U}_{-2.0}}{\bar{U}_{-2.0}} \%$$

$$\bar{U}_{\text{NOM}} = 45 \text{ m/s}$$

$$x_T = -2.0 \text{ m}$$



$$\frac{\bar{U} - \bar{U}_{-1.0}}{\bar{U}_{-1.0}} \%$$

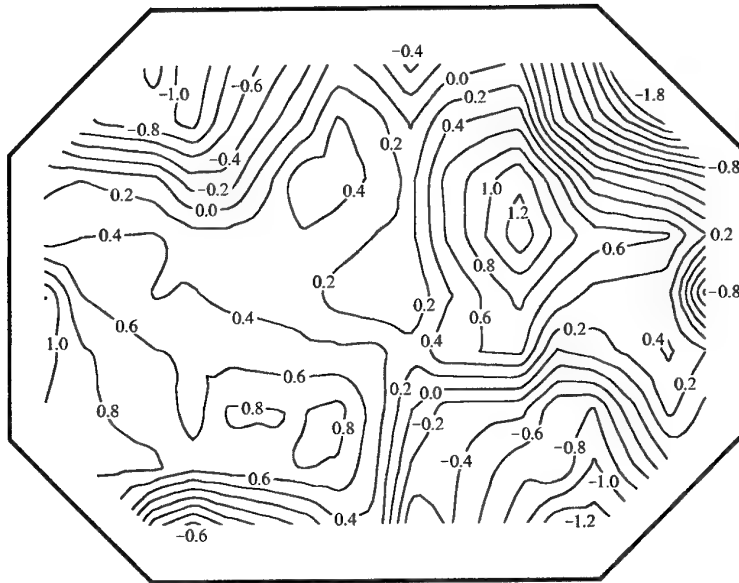
$$\bar{U}_{\text{NOM}} = 45 \text{ m/s}$$

$$x_T = -1.0 \text{ m}$$

Figure 5. Contours of velocity deviation for  $\bar{U}_{\text{NOM}} = 45 \text{ m/s}$  for  $x_T = -2.0, -1.0, 0.0$  and  $1.0 \text{ m}$ .

(a)  $x_T = -2.0$  and  $-1.0 \text{ m}$ .

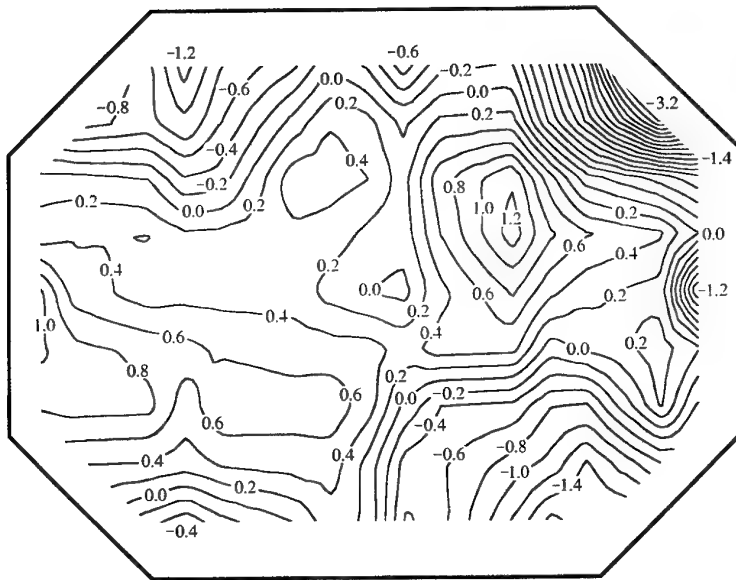
The flow is out of the page.



$$\frac{\bar{U} - \bar{U}_{0.0}}{\bar{U}_{0.0}} \%$$

$$\bar{U}_{\text{NOM}} = 45 \text{ m/s}$$

$$x_T = 0.0 \text{ m}$$



$$\frac{\bar{U} - \bar{U}_{1.0}}{\bar{U}_{1.0}} \%$$

$$\bar{U}_{\text{NOM}} = 45 \text{ m/s}$$

$$x_T = 1.0 \text{ m}$$

Figure 5 cont'd. Contours of velocity deviation for  $\bar{U}_{\text{NOM}} = 45 \text{ m/s}$  for  $x_T = -2.0, -1.0, 0.0$  and  $1.0 \text{ m}$ .

(b)  $x_T = 0.0$  and  $1.0 \text{ m}$ .

The flow is out of the page.

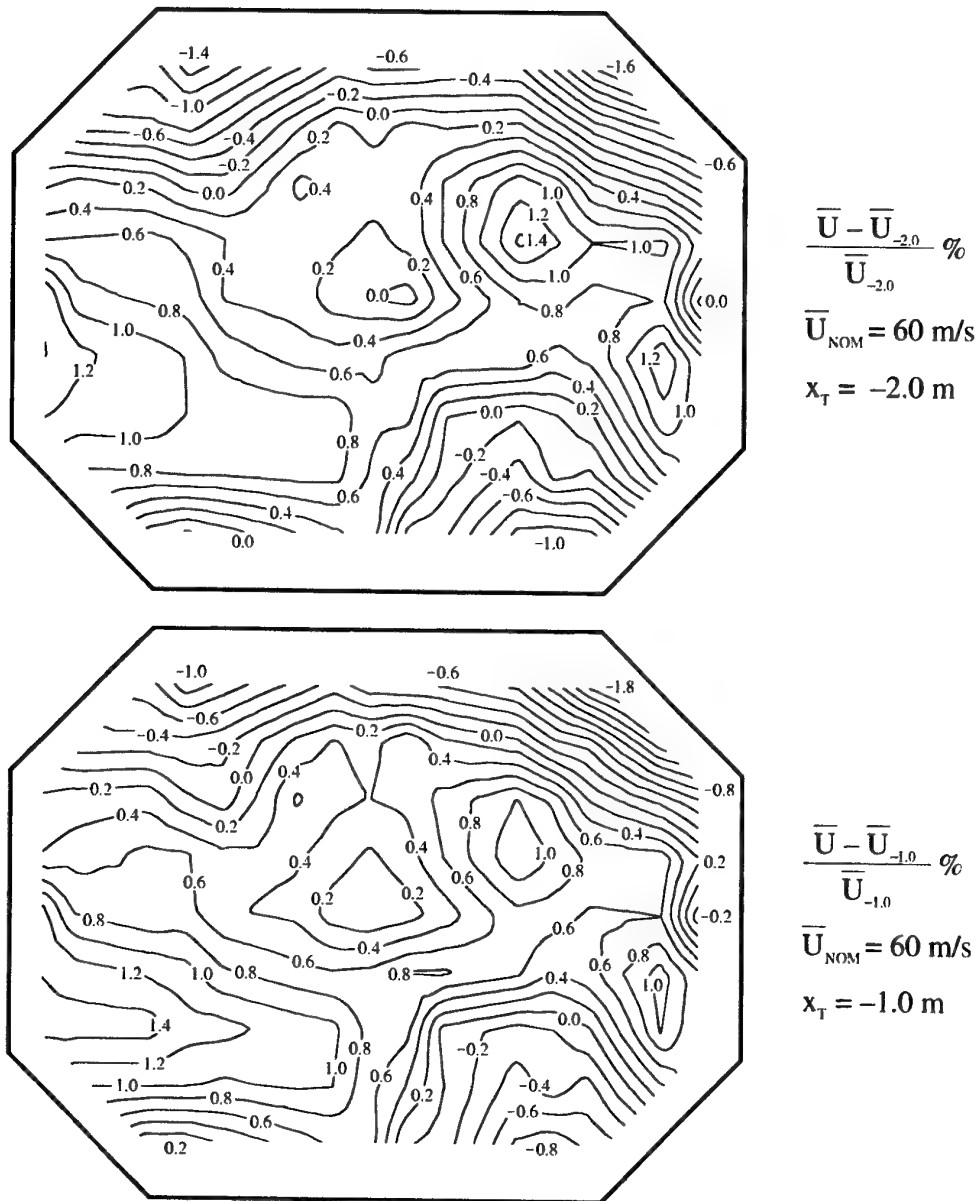
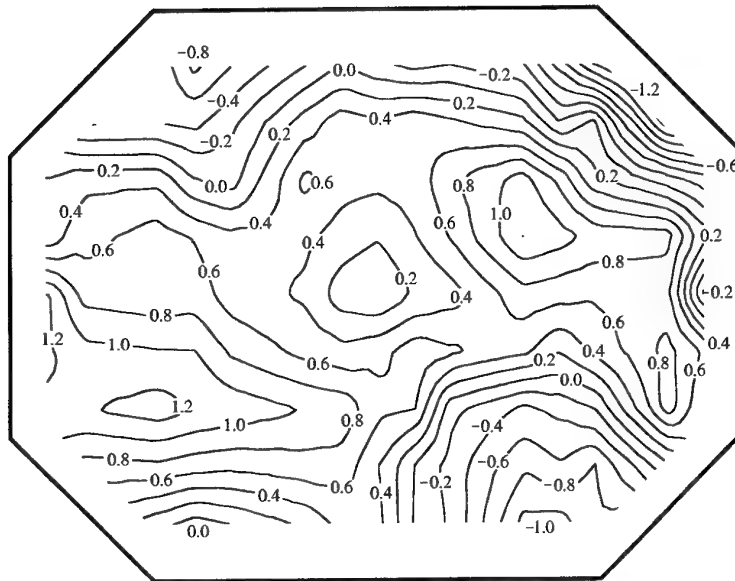


Figure 6. Contours of velocity deviation for  $\bar{U}_{\text{NOM}} = 60 \text{ m/s}$  for  $x_T = -2.0, -1.0, 0.0$  and  $1.0 \text{ m}$ .

(a)  $x_T = -2.0$  and  $-1.0 \text{ m}$ .

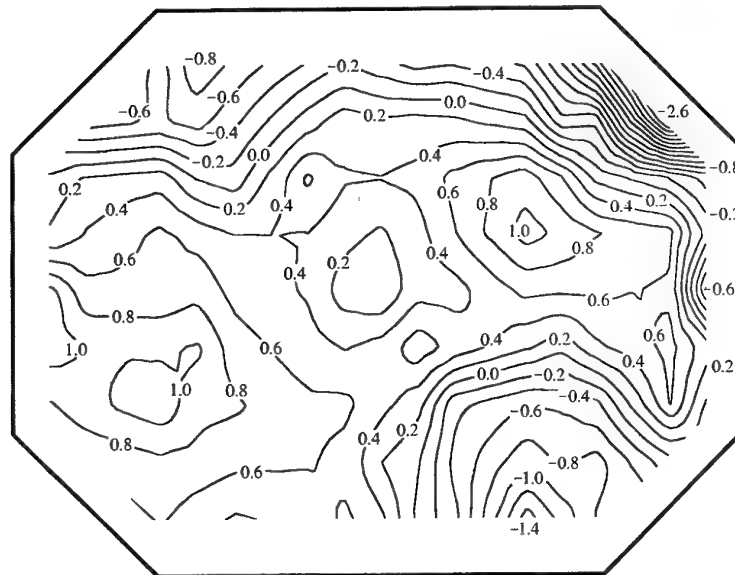
The flow is out of the page.



$$\frac{\bar{U} - \bar{U}_{0.0}}{\bar{U}_{0.0}} \%$$

$$\bar{U}_{\text{NOM}} = 60 \text{ m/s}$$

$$x_T = 0.0 \text{ m}$$



$$\frac{\bar{U} - \bar{U}_{1.0}}{\bar{U}_{1.0}} \%$$

$$\bar{U}_{\text{NOM}} = 60 \text{ m/s}$$

$$x_T = 1.0 \text{ m}$$

Figure 6 cont'd. Contours of velocity deviation for  $\bar{U}_{\text{NOM}} = 60 \text{ m/s}$  for  $x_T = -2.0, -1.0, 0.0$  and  $1.0 \text{ m}$ .

(b)  $x_T = 0.0$  and  $1.0 \text{ m}$ .

The flow is out of the page.



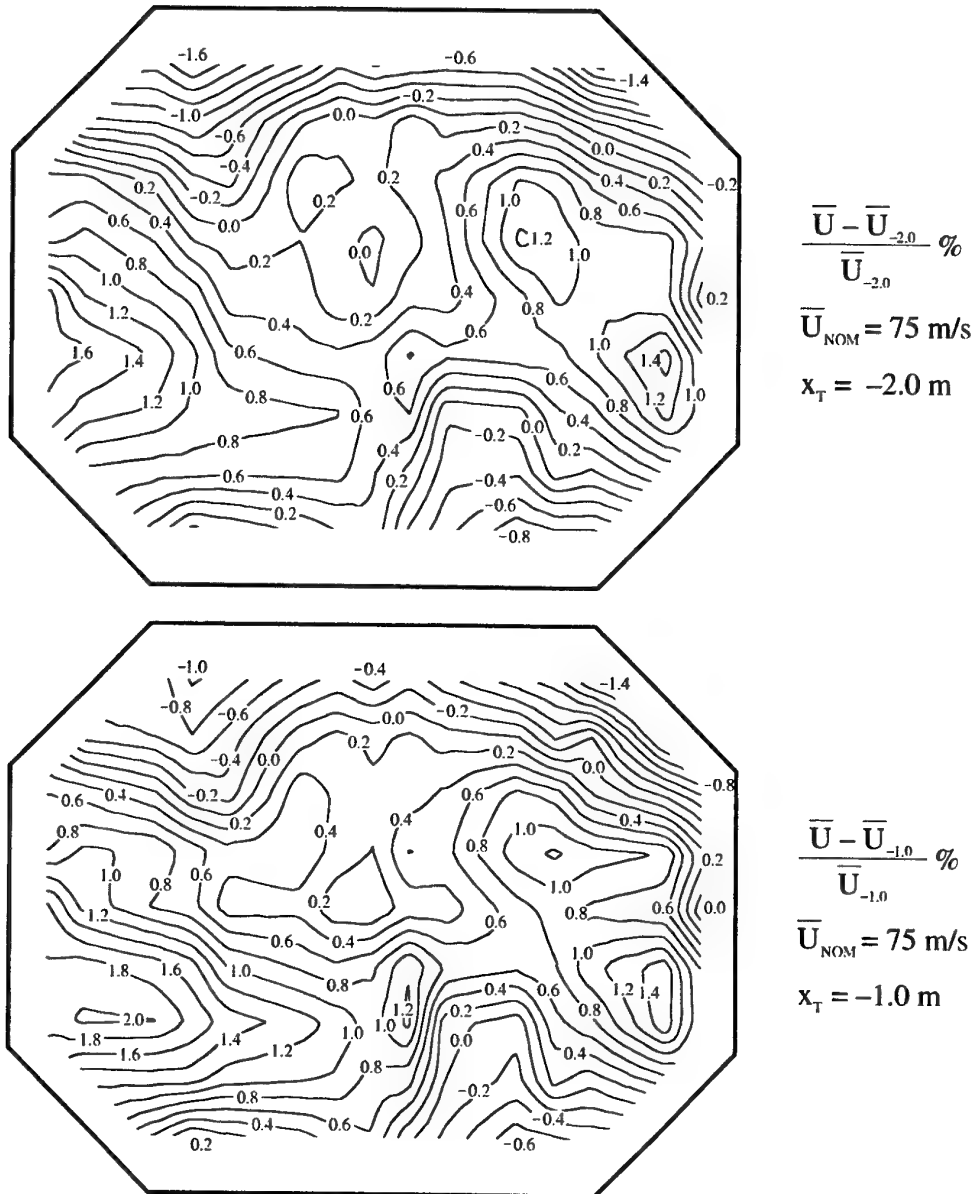
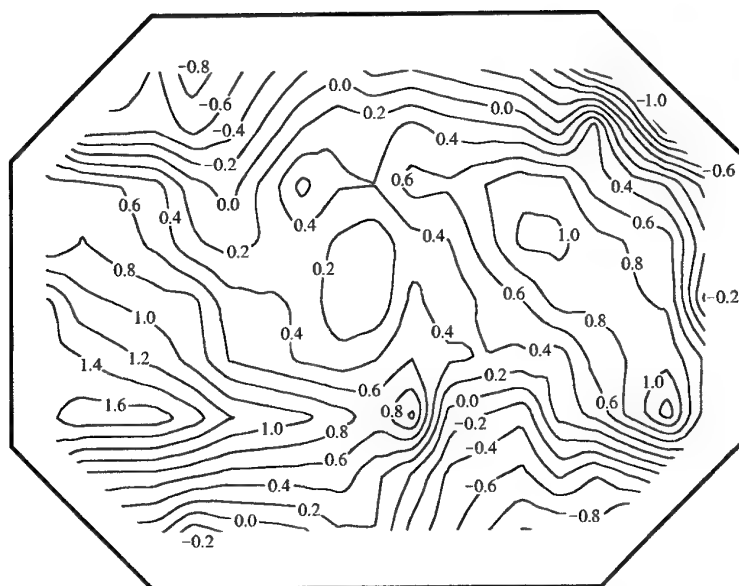


Figure 7. Contours of velocity deviation for  $\bar{U}_{\text{NOM}} = 75 \text{ m/s}$  for  $x_T = -2.0, -1.0, 0.0$  and  $1.0 \text{ m}$ .

(a)  $x_T = -2.0$  and  $-1.0 \text{ m}$ .

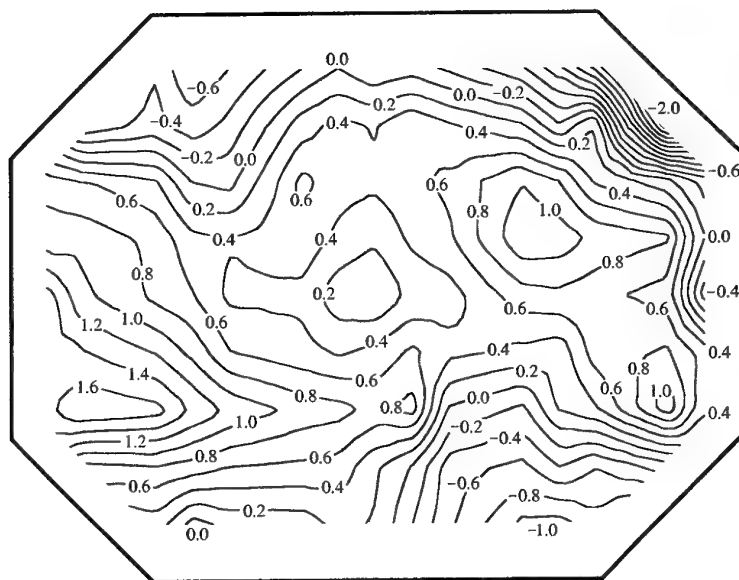
The flow is out of the page.



$$\frac{\bar{U} - \bar{U}_{0.0}}{\bar{U}_{0.0}} \%$$

$$\bar{U}_{\text{NOM}} = 75 \text{ m/s}$$

$$x_T = 0.0 \text{ m}$$



$$\frac{\bar{U} - \bar{U}_{1.0}}{\bar{U}_{1.0}} \%$$

$$\bar{U}_{\text{NOM}} = 75 \text{ m/s}$$

$$x_T = 1.0 \text{ m}$$

Figure 7 cont'd. Contours of velocity deviation for  $\bar{U}_{\text{NOM}} = 75 \text{ m/s}$  for  $x_T = -2.0, -1.0, 0.0$  and  $1.0 \text{ m}$ .

(b)  $x_T = 0.0$  and  $1.0 \text{ m}$ .

The flow is out of the page.

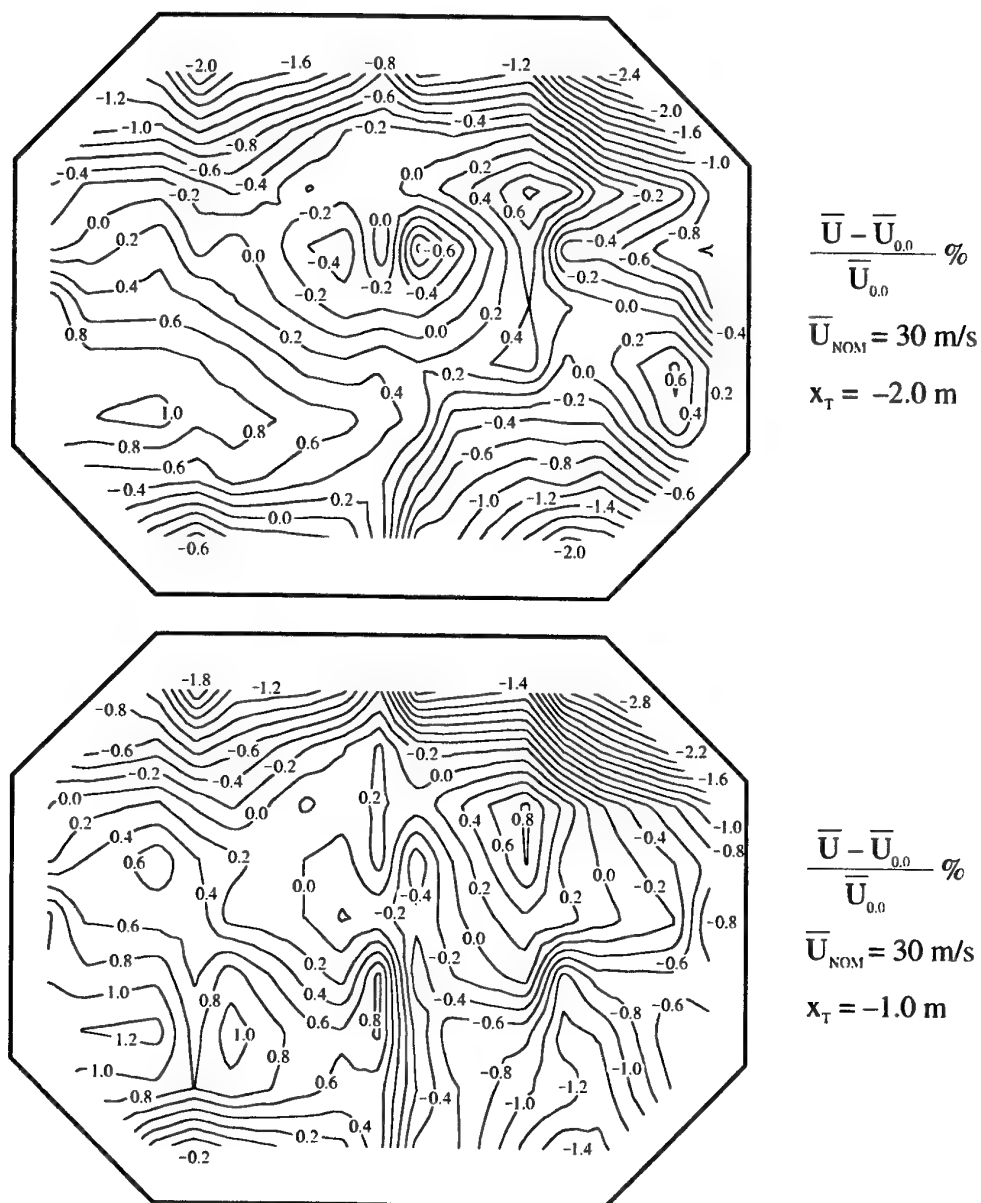
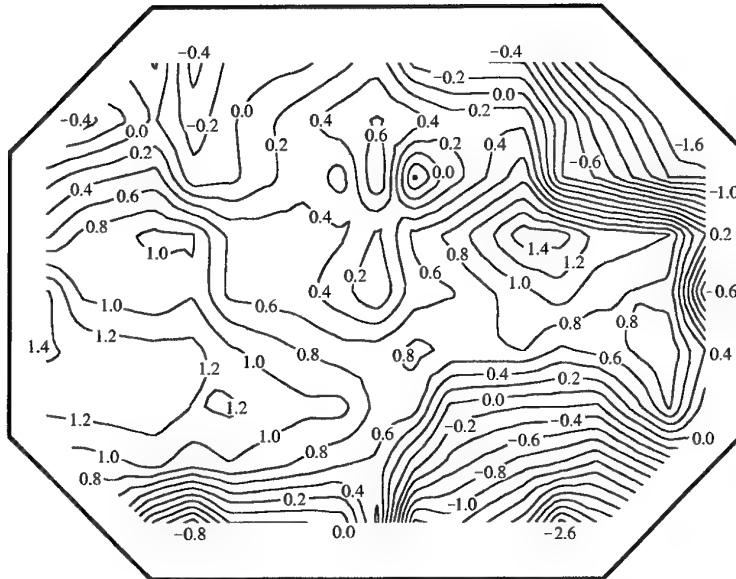


Figure 8. Contours of velocity deviation for  $\bar{U}_{\text{NOM}} = 30 \text{ m/s}$  for  $x_T = -2.0, -1.0, 0.0$  and  $1.0 \text{ m}$ .

(a)  $x_T = -2.0$  and  $-1.0 \text{ m}$ .

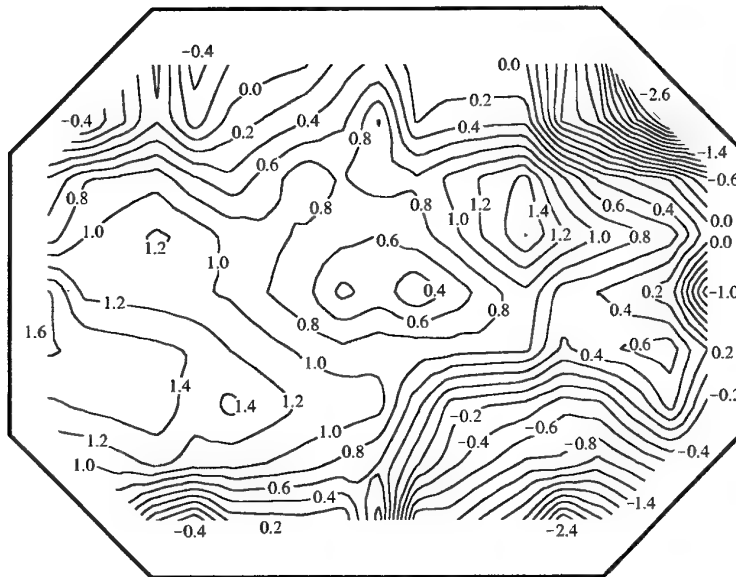
The flow is out of the page.



$$\frac{\bar{U} - \bar{U}_{0.0}}{\bar{U}_{0.0}} \%$$

$$\bar{U}_{\text{NOM}} = 30 \text{ m/s}$$

$$x_T = 0.0 \text{ m}$$



$$\frac{\bar{U} - \bar{U}_{0.0}}{\bar{U}_{0.0}} \%$$

$$\bar{U}_{\text{NOM}} = 30 \text{ m/s}$$

$$x_T = 1.0 \text{ m}$$

Figure 8 cont'd. Contours of velocity deviation for  $\bar{U}_{\text{NOM}} = 30 \text{ m/s}$  for  $x_T = -2.0, -1.0, 0.0$  and  $1.0 \text{ m}$ .

(b)  $x_T = 0.0$  and  $1.0 \text{ m}$ .

The flow is out of the page.

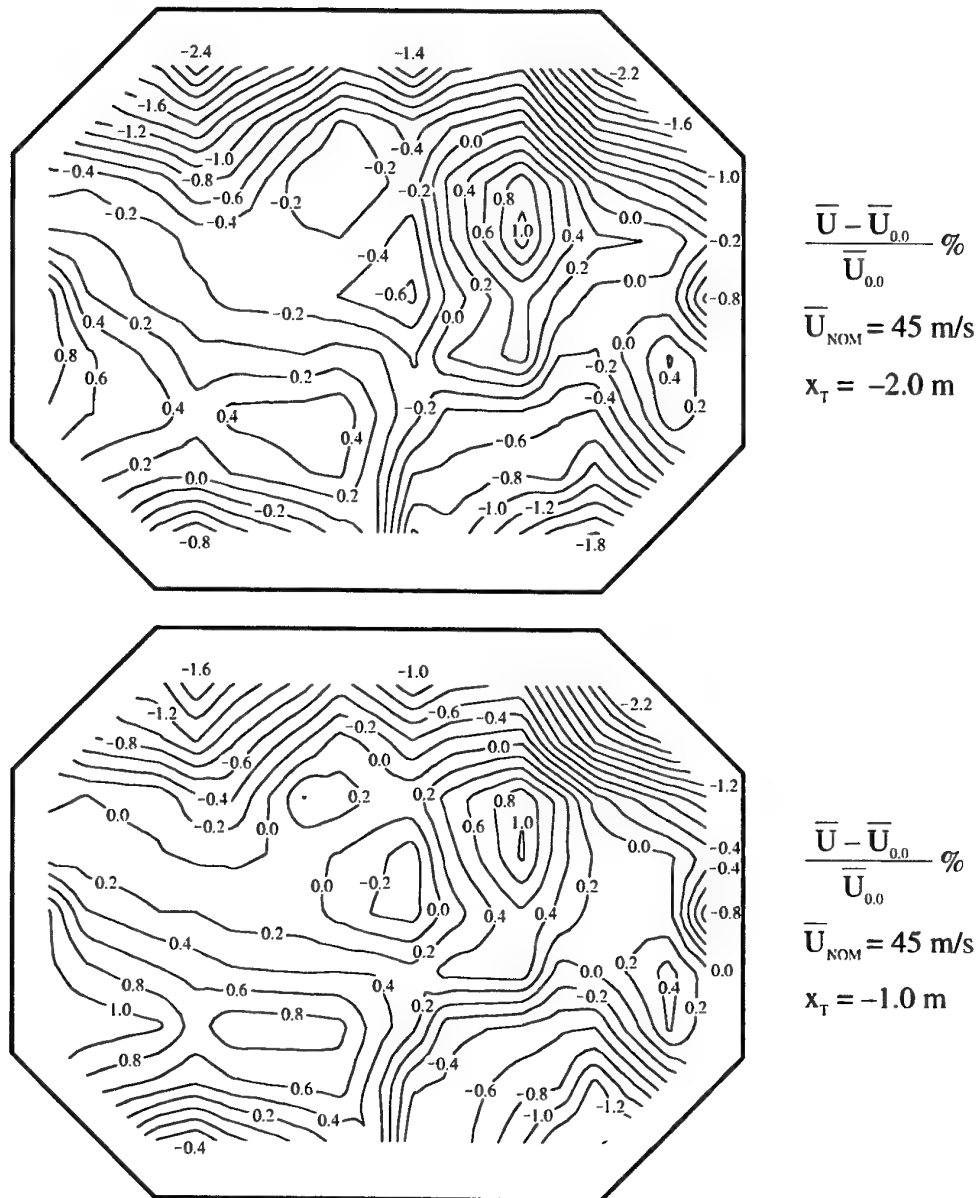
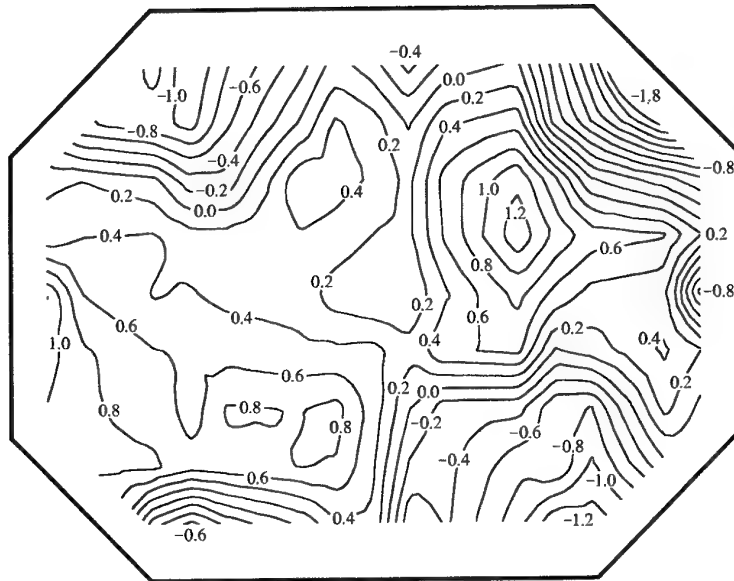


Figure 9. Contours of velocity deviation for  $\bar{U}_{NOM} = 45$  m/s for  $x_T = -2.0, -1.0, 0.0$  and  $1.0$  m.

(a)  $x_T = -2.0$  and  $-1.0$  m.

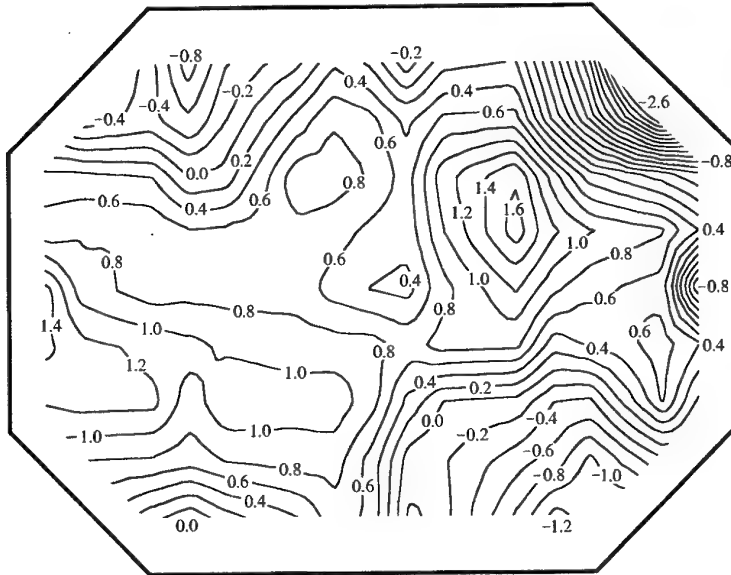
The flow is out of the page.



$$\frac{\bar{U} - \bar{U}_{0.0}}{\bar{U}_{0.0}} \%$$

$$\bar{U}_{\text{NOM}} = 45 \text{ m/s}$$

$$x_T = 0.0 \text{ m}$$



$$\frac{\bar{U} - \bar{U}_{0.0}}{\bar{U}_{0.0}} \%$$

$$\bar{U}_{\text{NOM}} = 45 \text{ m/s}$$

$$x_T = 1.0 \text{ m}$$

Figure 9 cont'd. Contours of velocity deviation for  $\bar{U}_{\text{NOM}} = 45 \text{ m/s}$  for  $x_T = -2.0, -1.0, 0.0$  and  $1.0 \text{ m}$ .

(b)  $x_T = 0.0$  and  $1.0 \text{ m}$ .

The flow is out of the page.

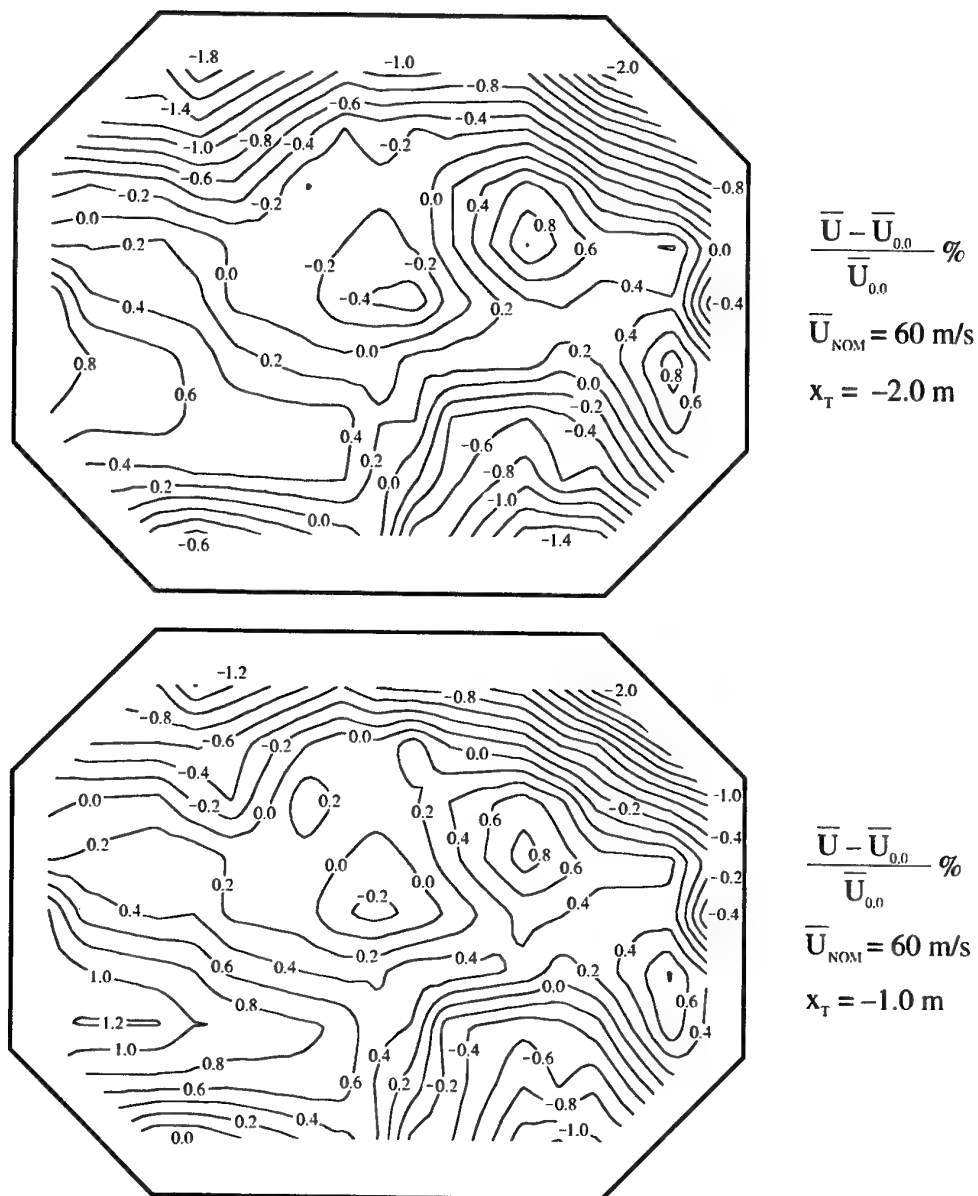


Figure 10. Contours of velocity deviation for  $\bar{U}_{\text{NOM}} = 60 \text{ m/s}$  for  $x_T = -2.0, -1.0, 0.0$  and  $1.0 \text{ m}$ .

(a)  $x_T = -2.0$  and  $-1.0 \text{ m}$ .

The flow is out of the page.

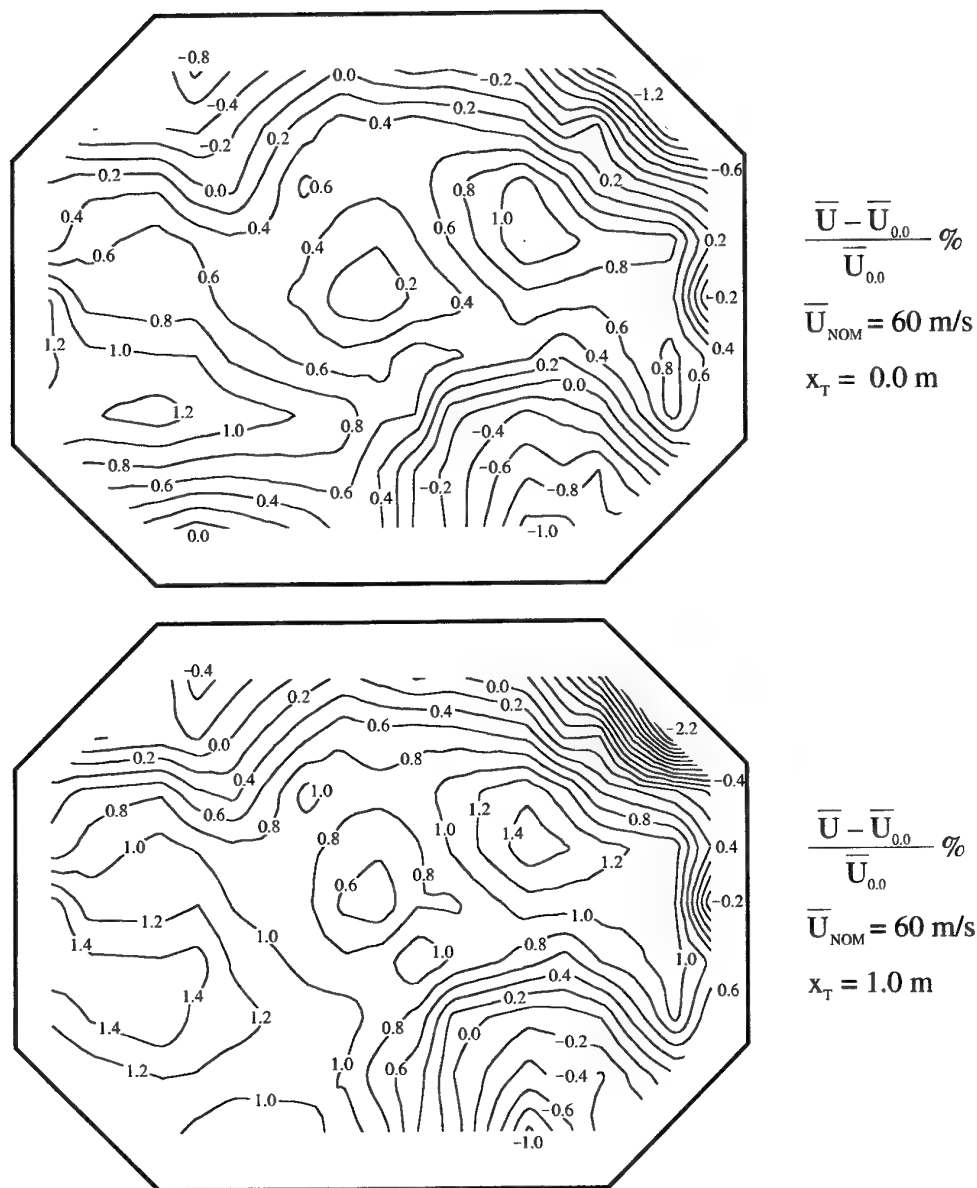


Figure 10 cont'd. Contours of velocity deviation for  $\bar{U}_{\text{NOM}} = 60 \text{ m/s}$  for  $x_T = -2.0, -1.0, 0.0$  and  $1.0 \text{ m}$ .

(b)  $x_T = 0.0$  and  $1.0 \text{ m}$ .

The flow is out of the page.



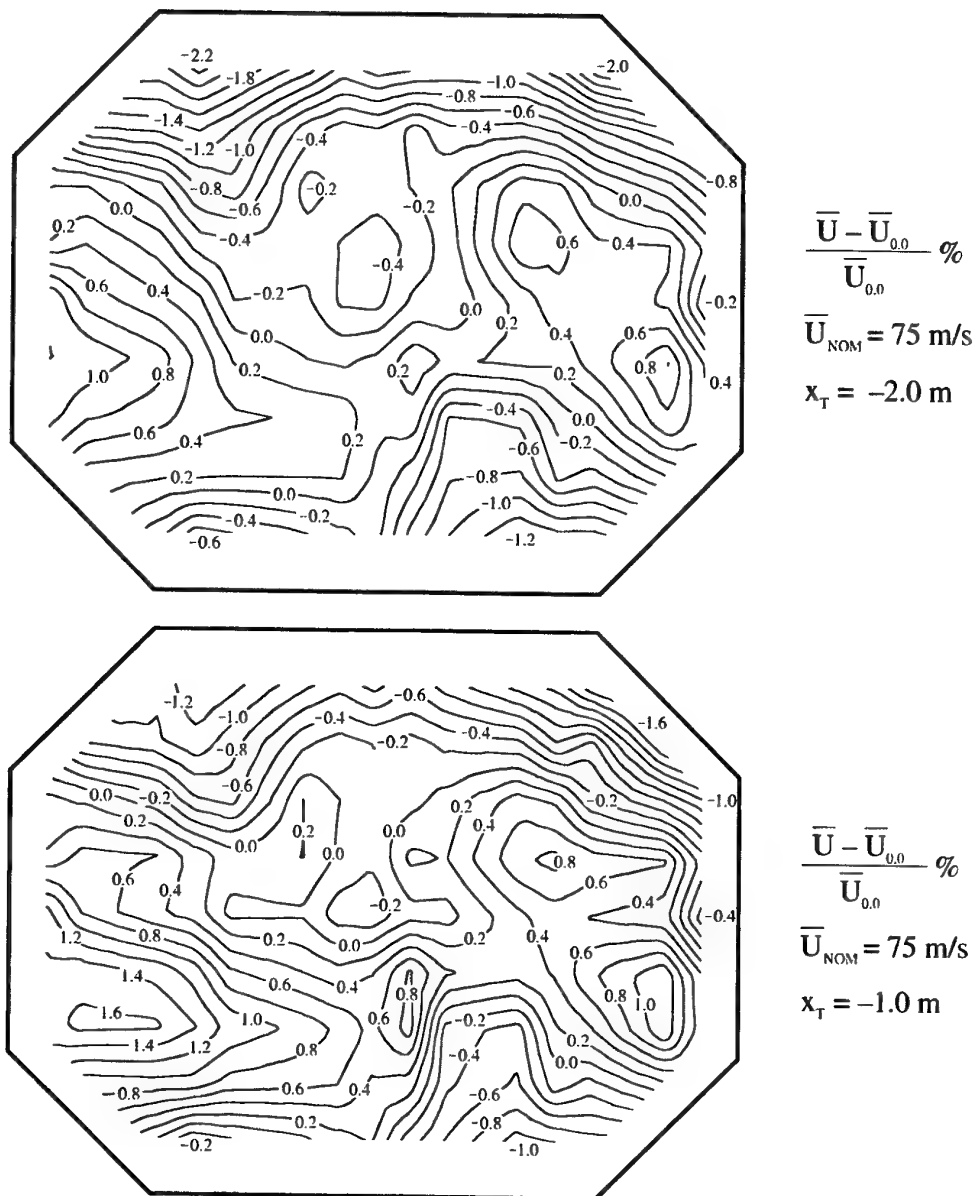
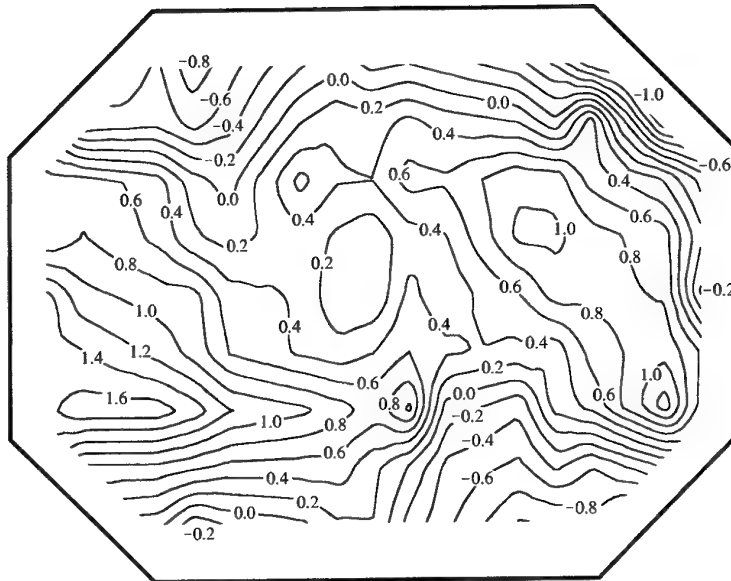


Figure 11. Contours of velocity deviation for  $\bar{U}_{\text{NOM}} = 75 \text{ m/s}$  for  $x_T = -2.0, -1.0, 0.0$  and  $1.0 \text{ m}$ .

(a)  $x_T = -2.0$  and  $-1.0 \text{ m}$ .

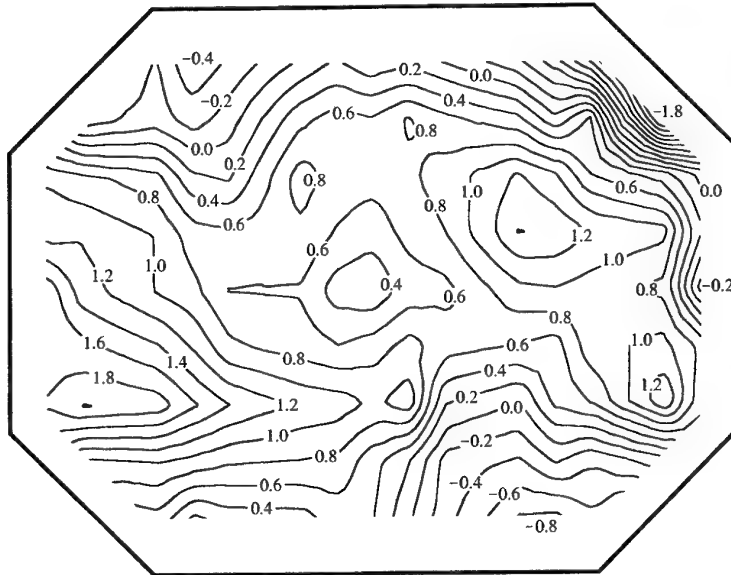
The flow is out of the page.



$$\frac{\bar{U} - \bar{U}_{0.0}}{\bar{U}_{0.0}} \%$$

$$\bar{U}_{\text{NOM}} = 75 \text{ m/s}$$

$$x_T = 0.0 \text{ m}$$



$$\frac{\bar{U} - \bar{U}_{0.0}}{\bar{U}_{0.0}} \%$$

$$\bar{U}_{\text{NOM}} = 75 \text{ m/s}$$

$$x_T = 1.0 \text{ m}$$

Figure 11 cont'd. Contours of velocity deviation for  $\bar{U}_{\text{NOM}} = 75 \text{ m/s}$  for  $x_T = -2.0, -1.0, 0.0$  and  $1.0 \text{ m}$ .

(b)  $x_T = 0.0$  and  $1.0 \text{ m}$ .

The flow is out of the page.

section has a fixed cross-sectional area in the direction of the flow so that the effective flow area reduces with increasing  $x_T$  as the wall boundary layer thickens after the end of the contraction. For  $\bar{U}_{NOM} = 30$  m/s, between  $x_T = -2.0$  and  $+1.0$  m, longitudinal mean velocities deviated between  $-1.0\%$  and  $+1.4\%$  from the value at the centre of the test section ( $x_T = 0.0$ ,  $y_T = 0.0$  and  $z_T = 0.0$  m) (Figure 8). Corresponding deviations for other values of  $\bar{U}_{NOM}$  were from  $-1.2\%$  to  $+1.6\%$  for  $\bar{U}_{NOM} = 45$  m/s (Figure 9), from  $-1.0\%$  to  $+1.4\%$  for  $\bar{U}_{NOM} = 60$  m/s (Figure 10) and from  $-1.2\%$  to  $+1.4\%$  for  $\bar{U}_{NOM} = 75$  m/s (Figure 11). However, between  $x_T = -1.0$  and  $+1.0$  m, the deviations were significantly smaller and they ranged from  $-1.0\%$  to  $+1.4\%$  for  $\bar{U}_{NOM} = 30$  m/s, from  $-0.6\%$  to  $+1.6\%$  for  $\bar{U}_{NOM} = 45$  m/s, from  $-0.6\%$  to  $+1.4\%$  for  $\bar{U}_{NOM} = 60$  m/s and from  $-0.8\%$  to  $+1.4\%$  for  $\bar{U}_{NOM} = 75$  m/s.

### 2.5.3 Longitudinal Velocity Variation

Selected data associated with the contours shown in Figures 8 to 11 have been replotted in Figure 12 to indicate how the mean velocities in the vertical and horizontal longitudinal centreplanes vary in the longitudinal or  $x_T$  direction. Data corresponding to the  $x_T$ - $z_T$  plane that passes through  $y_T = 0.0$  m (i.e. the vertical plane that is aligned with and passes through the tunnel longitudinal axis) are shown for  $z_T/H = 0.0, \pm 0.2$  and  $\pm 0.4$ . Similarly, data corresponding to the  $x_T$ - $y_T$  plane that passes through  $z_T = 0.0$  m (i.e. the horizontal plane that is aligned with and passes through the tunnel longitudinal axis) are shown for  $y_T/W = 0.0, \pm 0.15, \pm 0.30$  and  $\pm 0.45$ . In Figure 12, data corresponding to the longitudinal centreline of the tunnel are represented by thick lines. The longitudinal mean velocities increase slightly in the  $x_T$  direction, for reasons given above. Plots of mean velocity for the  $x_T$ - $y_T$  plane show that velocities on the inner side of the tunnel flow circuit, i.e. at  $y_T/W = -0.45$ , are the smallest and velocities on the outer side of the circuit, i.e. at  $y_T/W = 0.45$ , are the largest, for all four values of  $\bar{U}_{NOM}$ , as would be expected. As expected, mean velocities in the  $x_T$ - $z_T$  plane do not exhibit any asymmetry for  $z_T/H = -0.4$  to  $0.4$ , for all four values of  $\bar{U}_{NOM}$ .

### 2.5.4 Effect of Change in Nominal Free-Stream Velocity

The effect of change in nominal free-stream velocity are shown in Figures 8 to 11. For example, contours of  $(\bar{U} - \bar{U}_{0.0})/\bar{U}_{0.0}$  for  $x_T = 0.0$  m and  $\bar{U}_{NOM} = 30, 45, 60$  and  $75$  m/s are shown by the third contour plot in each of Figures 8 to 11. Such a set of contour plots indicates how the flow at a fixed  $x_T$  location changes as  $\bar{U}_{NOM}$  increases. The pattern of the contours and the magnitudes of the velocity deviations are approximately the same in each case, indicating that the distribution of the flow variations does not change significantly with  $\bar{U}_{NOM}$ .

### 2.5.5 Effect of Probe Misalignment With Respect to the Flow

The probability that the flow in the tunnel may be at a slight angle to the longitudinal axes of the probes on the cross-tunnel rake (Section 2.3) will not affect the test results significantly. In Reference 7 it is shown that, for total-pressure and static-pressure

probes similar to those used on the cross-tunnel rake (see Figure 3), errors in measured total pressures and static pressures due to misalignment of the probes with the flow are negligible for flows whose angle of incidence is within  $\pm 5^\circ$  of the longitudinal axis of a total-pressure probe and within  $\pm 1^\circ$  of the longitudinal axis of a static-pressure probe. The angularity of the flow in the test section is generally less than  $1^\circ$  (see Section 3.7), so that errors in the dynamic pressure and hence the velocity will be small, and although strictly speaking the contours shown in Figures 4 to 11 depict slightly inclined velocities, they can be considered to represent longitudinal velocities.

General discussion on the possible causes of the flow non-uniformities in the test section of the LSWT and suggested ways of improving the flow are given in Section 8.

## 2.6 Errors in Measured Mean Velocities

There are small errors in the velocity deviations, such as  $(\bar{U} - \bar{U}_{0.0})/\bar{U}_{0.0}$ , due to instrumentation errors. It was necessary to measure air temperatures and differential air pressures when determining mean velocities. Errors in the measured temperatures did not affect the velocity deviations as they are expressed as non-dimensional velocity ratios. The indicated readings of the scanners used to measure the differential pressures were accurate to within  $\pm 0.05\%$  of their full-scale reading. Three different types of scanners were used when measuring pressures and their ranges were  $\pm 2490$  Pa ( $\pm 10.0$  inches of water),  $\pm 6895$  Pa ( $\pm 1.0$  psi) and  $159$  kPa ( $23.0$  psi). For  $\bar{U}_{\text{NOM}} = 30, 45, 60$  and  $75$  m/s, errors in velocity deviations (e.g.  $(\bar{U} - \bar{U}_{0.0})/\bar{U}_{0.0}$ ) were about  $\pm 0.2, \pm 0.3, \pm 0.2$  and  $\pm 0.1$  percentage points respectively.

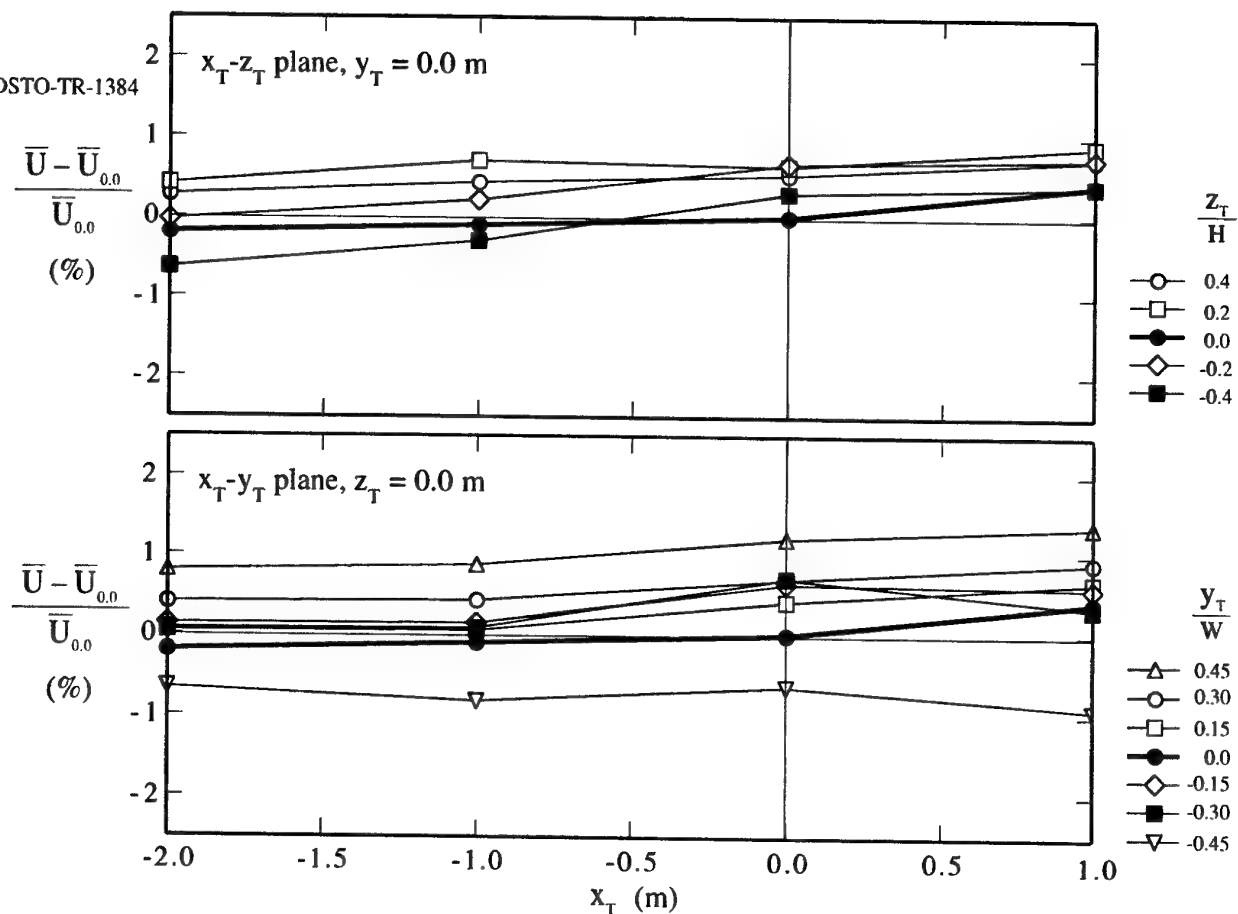
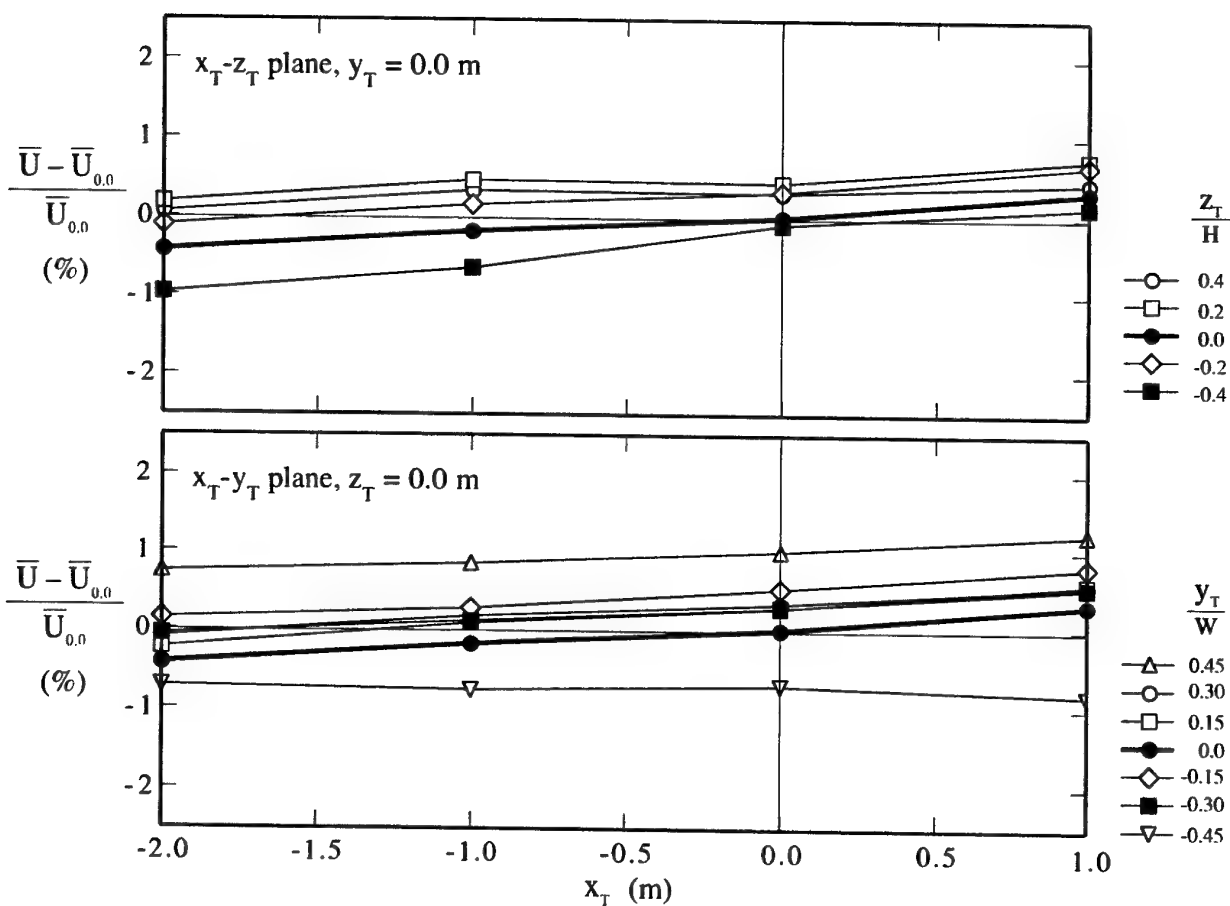
# 3. Flow-Angle Measurements

## 3.1 Test Schedule

Flow angles were measured in the test section at the 155 grid points shown in Figure 2 for  $x_T = -2.0, -1.0, 0.0$  and  $+1.0$  m and for  $\bar{U}_{\text{NOM}} = 30$  and  $60$  m/s.

## 3.2 Six-Hole Probe

A six-hole hemispherical head yawmeter, designed and calibrated by Melbourne & Griss (Reference 8), was used to measure magnitudes of mean velocities and corresponding flow angles at the different grid points. The probe is depicted diagrammatically in Figure 13. Holes 1 to 5 are located in the hemispherical head of the probe as shown and the series of 20 interconnected holes, designated hole 6, are equally spaced around the circumference of the probe and are located  $22.2$  mm ( $3.5$  probe

(a)  $\bar{U}_{\text{NOM}} = 30$  m/s.(b)  $\bar{U}_{\text{NOM}} = 45$  m/s.Figure 12. Velocity deviations in the  $x_T$  direction for  $\bar{U}_{\text{NOM}} = 30, 45, 60$  and  $75$  m/s.

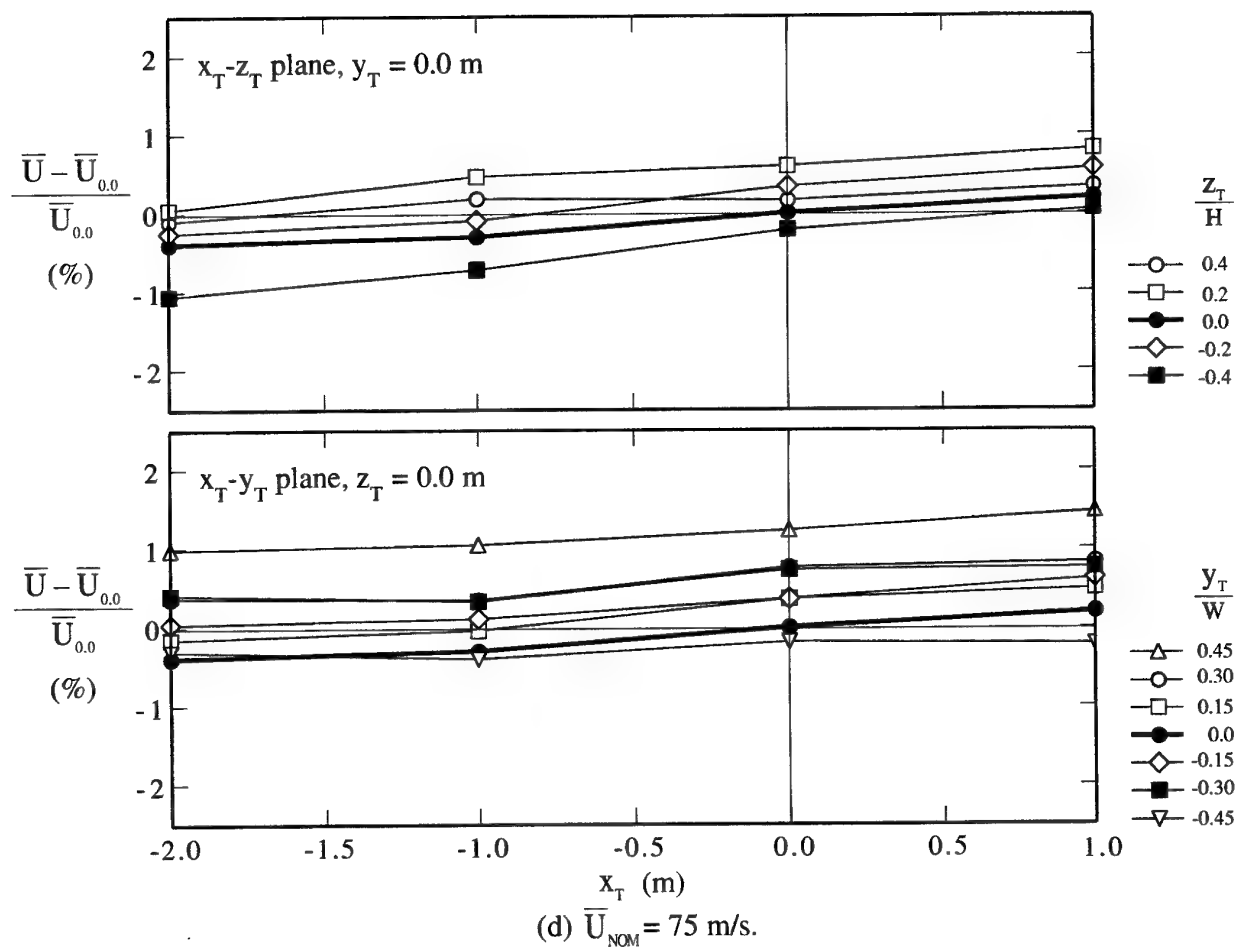
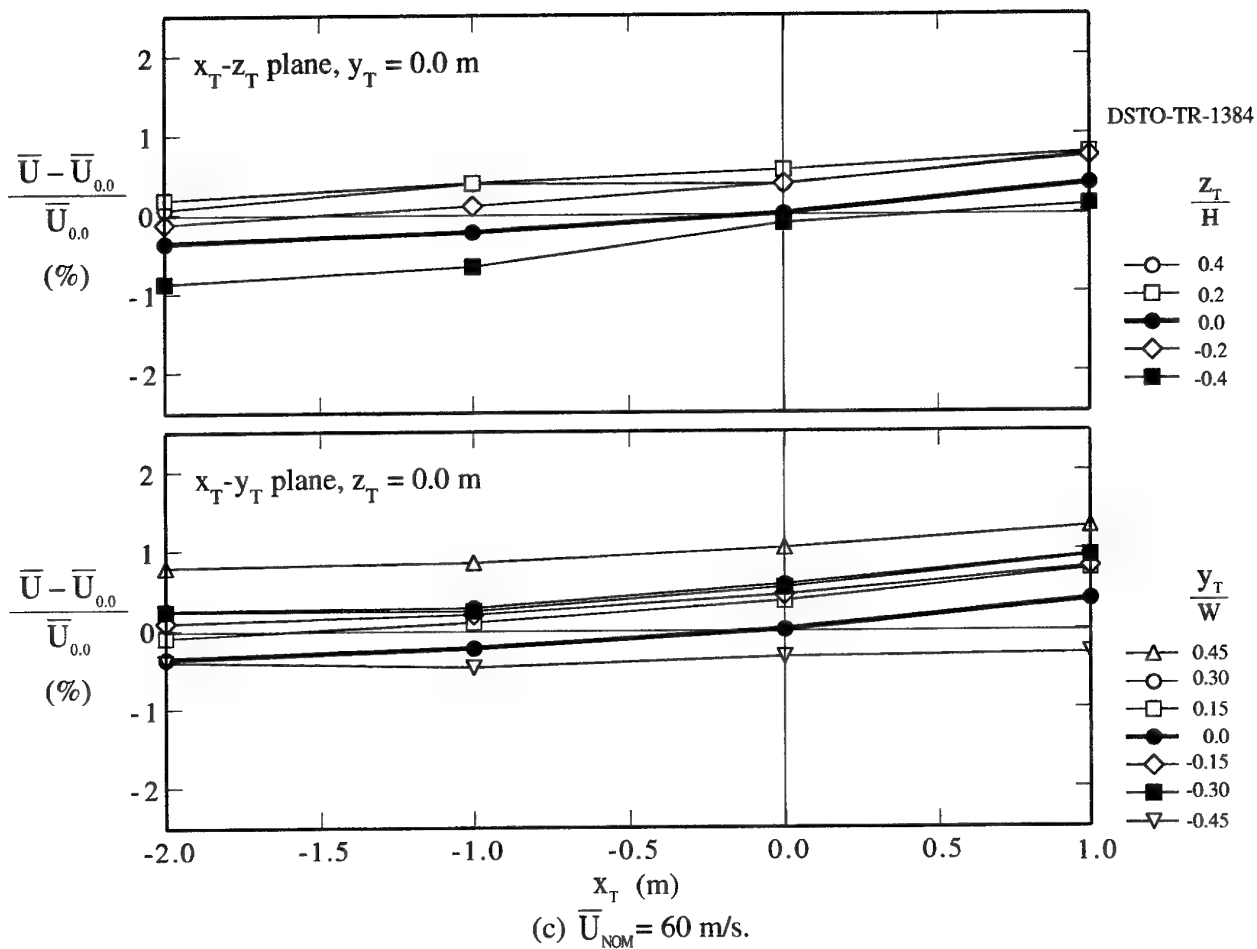


Figure 12 cont'd. Velocity deviations in the  $x_T$  direction for  $\bar{U}_{\text{NOM}} = 30, 45, 60$  and  $75$  m/s. 29

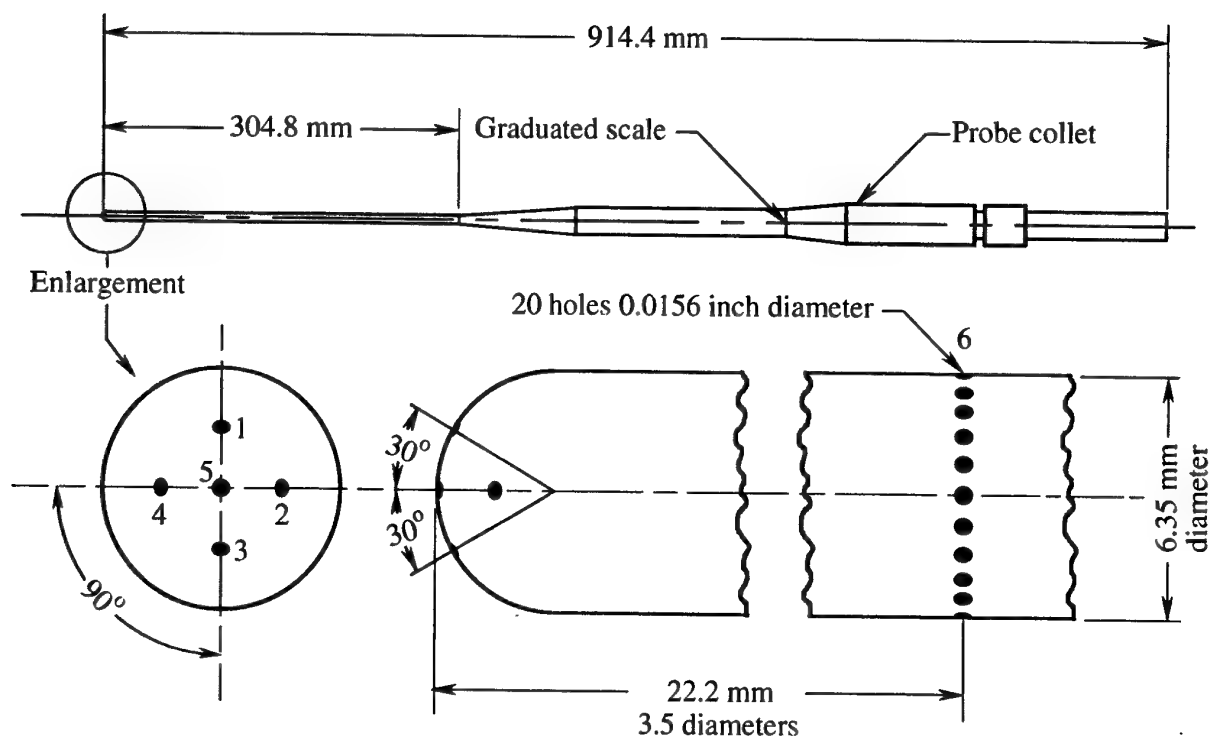


Figure 13. Six-hole probe (based on a diagram given in Reference 8).

diameters) from the probe tip. Each of holes 1 to 6 is connected internally to ports at the rear of the probe to enable the individual pressures to be measured. A datum line scribed on the probe body near hole 1 and contained in the plane passing through holes 1, 3 and 5, was used to differentiate the holes and to set the probe roll angle in the tunnel (Section 3.4).

The direction of the velocity vector,  $V_v$ , relative to the probe body coordinate system,  $x_b y_b z_b$ , is defined in terms of flow angles  $\theta_v$  and  $\phi_v$ , as shown in Figure 14. The coordinate system remains fixed with respect to the probe and its origin is located at the centre of the hemisphere which forms the tip of the probe. The  $x_b$  axis is along the probe longitudinal axis, the  $y_b$  axis is in the plane passing through holes 2, 4 and 5 and the  $z_b$  axis is in the plane passing through holes 1, 3 and 5. The positive directions of the axes are as shown and the axes form a right-handed orthogonal system. The axes convention is the same as that used by Fairlie (Reference 9). The tunnel coordinate system,  $x_t y_t z_t$ , introduced in Section 2.1, is also shown in Figure 14. The relationship between the two coordinate systems is given in Section 3.3.

The probe can be used in either the stationary or the null-sensing mode. In the stationary mode, the probe is given a known orientation with respect to the wind tunnel and by measuring the pressures in the six holes the velocity  $V_v$  and the flow angles  $\theta_v$  and  $\phi_v$  can be determined using calibration relationships. Velocities and flow angles

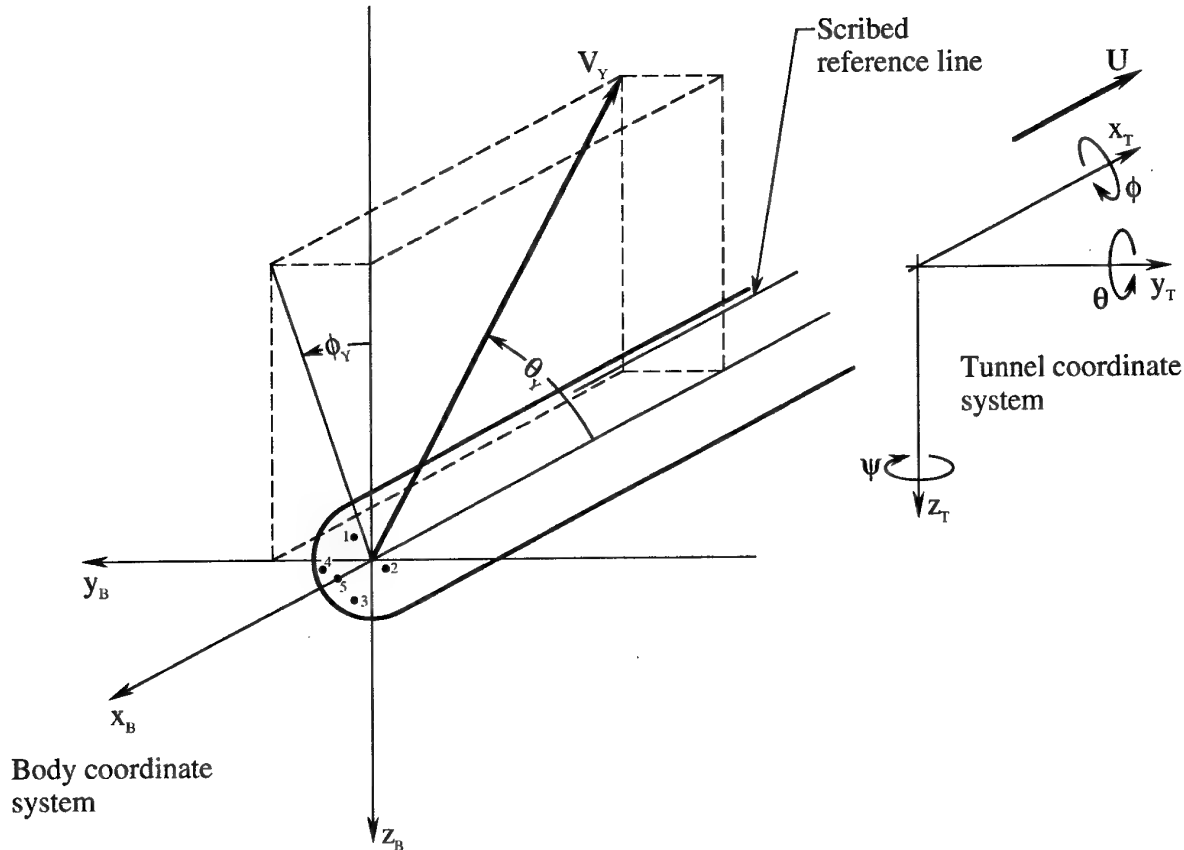


Figure 14. Six-hole probe showing velocity vector, flow angles and coordinate systems (based on a diagram given in Reference 8).

relative to the tunnel coordinate system can then be determined (Section 3.5). In the null-sensing mode, the probe is oriented so that the pressures in holes 1 to 4 are equal, which signifies that the velocity vector is parallel to the probe longitudinal axis. The magnitude of the velocity vector can then be determined in the conventional manner using the total and static pressures measured in holes 5 and 6 respectively, i.e.  $V_y = [2(p_s - p_t)/\rho]^{0.5}$ , and the direction of the velocity vector can be determined by measuring the orientation of the probe relative to the tunnel coordinate system. The null-sensing mode of operation is cumbersome and time consuming, whereas the stationary mode is straightforward and it was the method used for the current measurements.

Melbourne & Griss (Reference 8) calibrated the probe in the LSWT for free-stream velocities of 100 and 200 ft/s (30.5 and 61.0 m/s respectively) and obtained expressions relating  $V_y$ ,  $\theta_y$  and  $\phi_y$  to measured pressures,  $p_1$  to  $p_6$ . From their calibration measurements, they found that



$$\theta_Y = 1.983 R^3 - 2.105 R^2 + 16.917 R \quad (7)$$

for a free-stream velocity of 100 ft/s (30.5 m/s) and

$$\theta_Y = -0.050 R^3 + 2.686 R^2 + 14.013 R \quad (8)$$

for a free-stream velocity of 200 ft/s (61.0 m/s). In these two expressions,  $R$  is given by

$$R = \left\{ (C_{p_3} - C_{p_1})^2 + (C_{p_2} - C_{p_4})^2 \right\}^{0.5} \quad (9)$$

where the pressure coefficients,  $C_{p_n}$ , ( $n = 1$  to  $4$ ) are given by

$$C_{p_n} = \frac{(p_n - p_{ref})}{0.5 \rho V_Y^2} \quad (10)$$

Melbourne & Griss also found that

$$C_{p_5} - C_{p_6} = \frac{(p_5 - p_6)}{0.5 \rho V_Y^2} = -0.000493 \theta_Y^2 + 0.004472 \theta_Y + 1.003 \quad (11)$$

for a free-stream velocity of 100 ft/s (30.5 m/s) and

$$C_{p_5} - C_{p_6} = \frac{(p_5 - p_6)}{0.5 \rho V_Y^2} = -0.000535 \theta_Y^2 + 0.005854 \theta_Y + 1.014 \quad (12)$$

for a free-stream velocity of 200 ft/s (61.0 m/s). Equations 7, 8, 11 and 12 were determined using the method of least squares to fit data.

The flow angle,  $\phi_Y$ , is related to pressure coefficients by the following relationship:

$$\phi_Y = \tan^{-1} \left( \frac{C_{p_2} - C_{p_4}}{C_{p_3} - C_{p_1}} \right) \quad (13)$$

If  $\theta_Y$  is very small, the values of  $C_{p_1}$ ,  $C_{p_2}$ ,  $C_{p_3}$  and  $C_{p_4}$  will be approximately the same so that equation 13 will be ill-conditioned and may break down.

In the above calibration relationships (equations 7 to 13),  $V_y$ ,  $\theta_y$  and  $\phi_y$  are not given explicitly in terms of measured pressures,  $p_1$  to  $p_6$ , and it was necessary to determine the three variables iteratively. The procedure used is discussed in Section 3.5.

In the current investigation, the probe calibration applicable to a free-stream velocity of 100 ft/s (30.5 m/s) was only used for flow-angle measurements at  $\bar{U}_{\text{NOM}} = 30$  m/s and similarly the calibration applicable to a velocity of 200 ft/s (61.0 m/s) was only used for measurements at  $\bar{U}_{\text{NOM}} = 60$  m/s.

### 3.3 Transformation of Coordinates

The orientation of one set of axes relative to any other set can be given by three angles, which are the consecutive rotations about the (right-handed) axes  $z$ ,  $y$  and  $x$  in that order that carry one set of axes into coincidence with the other (Reference 9). In Figure 14, the angles that rotate the tunnel axes,  $x_T$ ,  $y_T$  and  $z_T$ , into coincidence with the body axes,  $x_B$ ,  $y_B$  and  $z_B$ , are referred to as the probe yaw angle,  $\psi$ , the pitch angle,  $\theta$ , and the roll angle,  $\phi$ . The positive directions of  $\psi$ ,  $\theta$  and  $\phi$  conform to the conventional right-hand screw rule about the relevant axes, as shown in Figure 14. For the orientation of the tunnel and body axes shown in Figure 14,  $\psi$  is  $180.0^\circ$ ,  $\theta$  is  $0.0^\circ$  and  $\phi$  is  $0.0^\circ$ .

The velocity vector,  $V_y$ , shown in Figure 14, can be resolved into three components of velocity in the body coordinate system to give  $\bar{U}_B$ ,  $\bar{V}_B$  and  $\bar{W}_B$ , corresponding to the  $x_B$ ,  $y_B$  and  $z_B$  directions respectively. For arbitrary values of  $\psi$ ,  $\theta$  and  $\phi$ , components of velocity in the tunnel coordinate system,  $\bar{U}_T$ ,  $\bar{V}_T$  and  $\bar{W}_T$ , can be determined from components of velocity in the body coordinate system,  $\bar{U}_B$ ,  $\bar{V}_B$  and  $\bar{W}_B$ , using

$$\begin{bmatrix} \bar{U}_T \\ \bar{V}_T \\ \bar{W}_T \end{bmatrix} = [\lambda]_{TB} \begin{bmatrix} \bar{U}_B \\ \bar{V}_B \\ \bar{W}_B \end{bmatrix} \quad (14)$$

where  $[\lambda]_{TB}$  is a matrix of direction cosines that is used to transform velocities from the body coordinate system to the tunnel coordinate system. The matrix  $[\lambda]_{TB}$  is given by

$$[\lambda]_{TB} = \begin{bmatrix} \cos \theta \cos \psi & \sin \phi \sin \theta \cos \psi & \cos \phi \sin \theta \cos \psi \\ & -\cos \phi \sin \psi & +\sin \phi \sin \psi \\ \cos \theta \sin \psi & \sin \phi \sin \theta \sin \psi & \cos \phi \sin \theta \sin \psi \\ & +\cos \phi \cos \psi & -\sin \phi \cos \psi \\ -\sin \theta & \sin \phi \cos \theta & \cos \phi \cos \theta \end{bmatrix} \quad (15)$$

which is the transpose of  $[\lambda]_{BT}$ , given for example in Reference 9.

### 3.4 Traversing Mechanism

A specially designed traversing mechanism was used to support the six-hole probe and to position it at different vertical locations in the tunnel when measuring velocities and flow angles. A photograph of the mechanism mounted in the tunnel is given in Figure 15 and a plan cross section assembly drawing of the mechanism showing the main features is given in Figure 16. Photographs of components of the mechanism are given in Figure 17. The probe is mounted on a carriage which can move up or down (into and out of the paper in Figure 16) between two linear-motion rails, and the carriage is connected to the linear-motion rails using three low-friction linear-motion bearings –see Figure 17 (b). A stepping motor is connected to a lead screw which passes through the carriage and instructions can be sent to the motor from a computer to rotate the lead screw and move the probe to a specified  $z_T$  location –see Figure 17 (c). Limit switches are installed near the top and near the bottom of the downstream linear-motion rail to prevent the carriage moving beyond acceptable lower and upper limits of travel –see Figure 17. An electric brake, which is activated when the switch to the stepping motor is off or when the power to the motor fails, was installed on the lead screw to prevent it from rotating under these conditions –see Figure 17 (a). Without the brake, the weight of the carriage and the components attached would cause the lead screw to rotate and the carriage would move down when there was no power to the motor. A dummy probe is attached to the traversing mechanism to counteract possible twisting of the mechanism that would arise from aerodynamic loads on a single probe. The active and dummy probes can be swapped as required by simply transferring the probes from one collet to the other (Figure 16), without changing the yaw, pitch and roll angles of the probes. The horizontal arm holding the probes is interchangeable with arms of different lengths, thereby enabling measurements to be taken at different  $y_T$  locations without changing the lateral position of the rig.

The traversing mechanism was bolted to two rectangular plates, one of which was bolted to the floor and the other to the roof of the test section. The plates were 0.4 m long and 1.6 m wide and occupied most of the width of the floor (or roof) not counting the fillets (the lower plate is shown in Figure 15). The lower plate was installed first and it was fixed to the floor of the test section so that its trailing edge was parallel to the  $y_T$  direction and so that the tip of the six-hole probe would be located at the required  $x_T$  position when the mechanism was bolted between the plates. The lower plate was aligned accurately by first ensuring that the midpoint of its trailing edge was positioned on the longitudinal centreline of the floor of the tunnel. If necessary, the yaw angle of the plate was then adjusted slightly so that the distances from each of the two extremities of the trailing edge to an upstream or downstream reference mark (at least 2.0 m from the trailing edge) on the longitudinal centreline of the floor of the tunnel were the same. Using this technique, the error in the setting of the yaw angle of the plate could be kept to less than about  $\pm 0.1^\circ$ . The alignment of the trailing edge of the plate with the  $y_T$  direction was critical since probe yaw angles were referenced to the plate trailing edge. The fore/aft location of the lower plate did not have to be precise, since the probe could be adjusted axially (by up to about 45 cm) through the probe

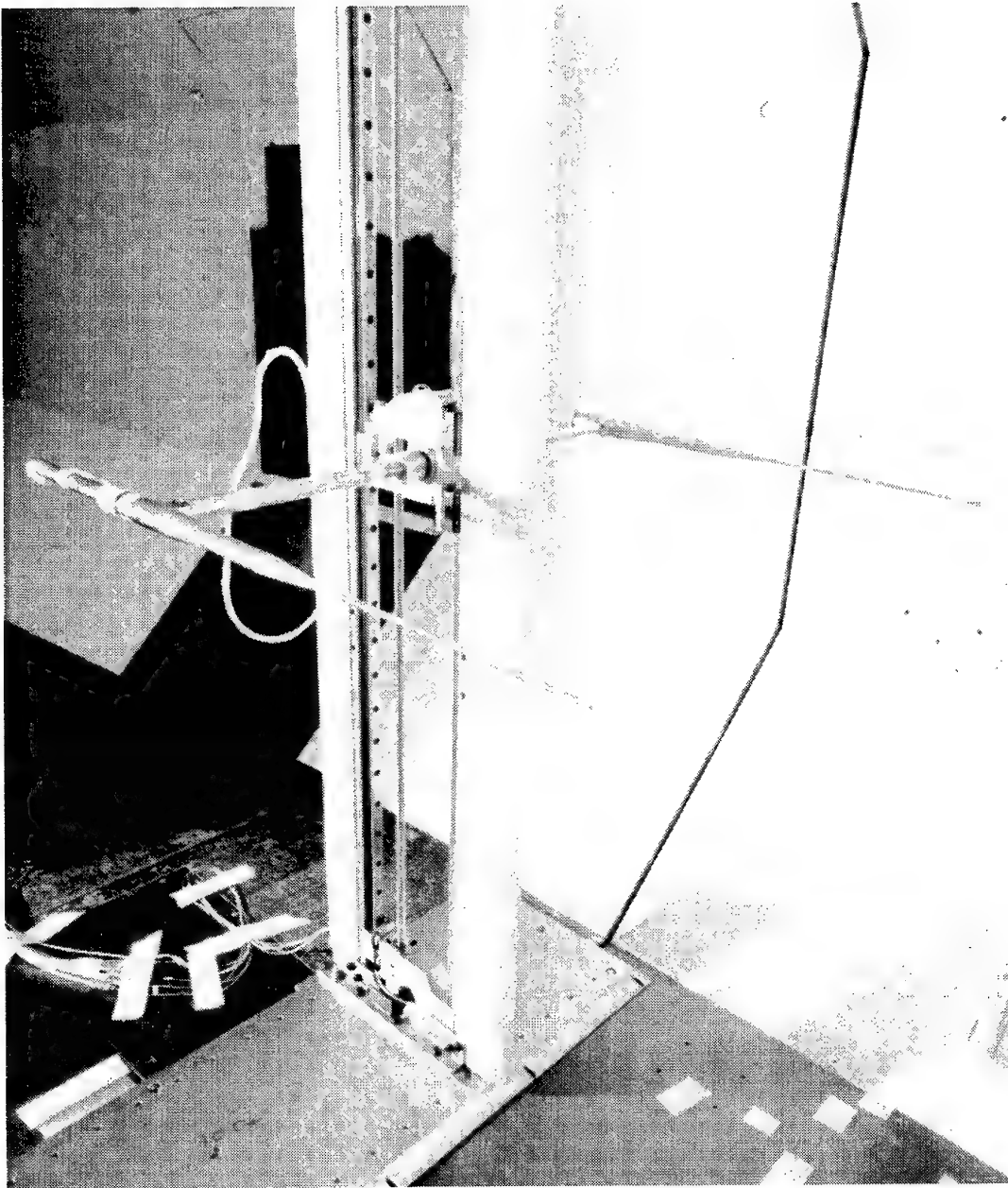


Figure 15. Traversing mechanism, with probes attached, mounted in the low-speed wind tunnel.

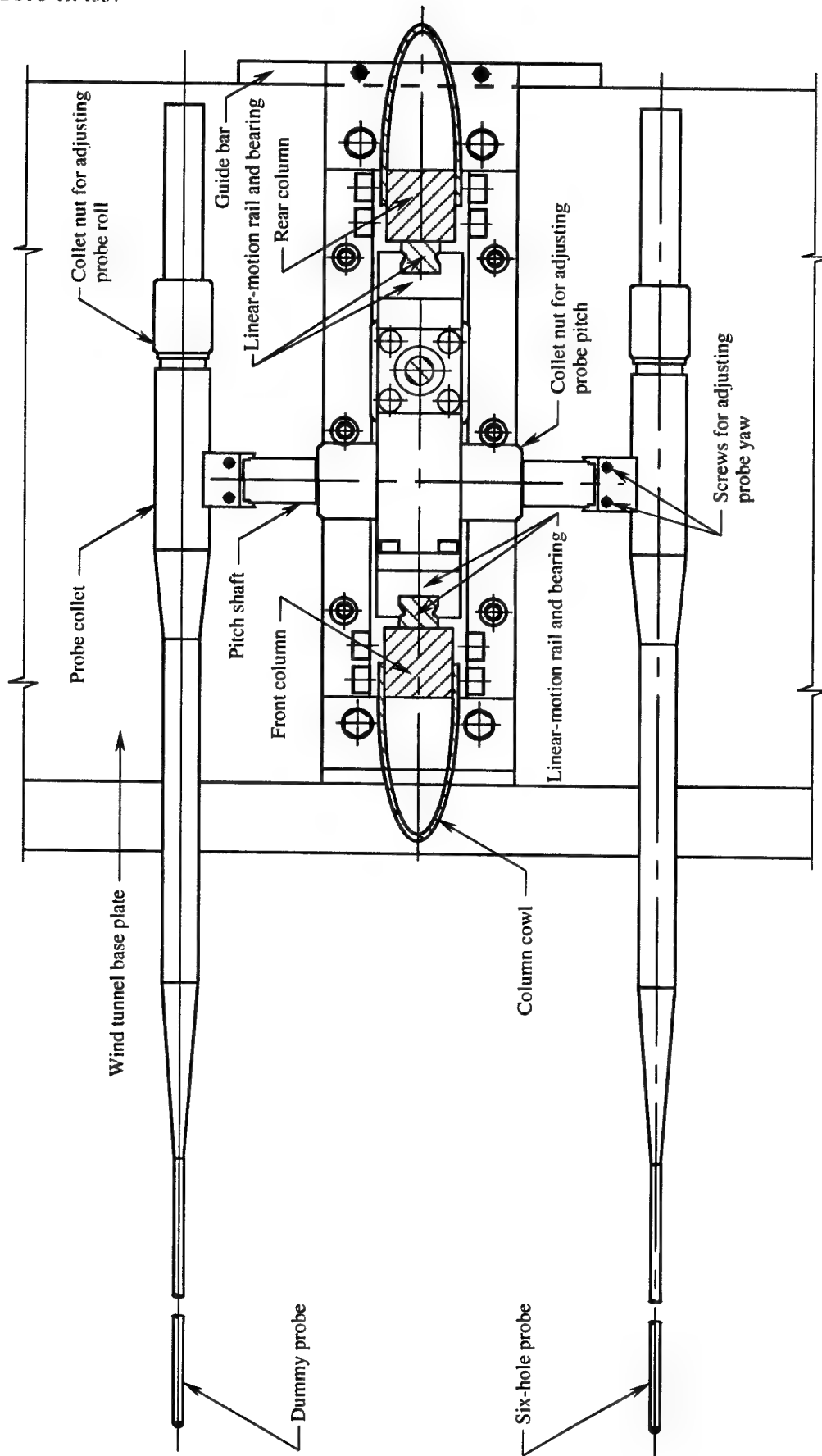
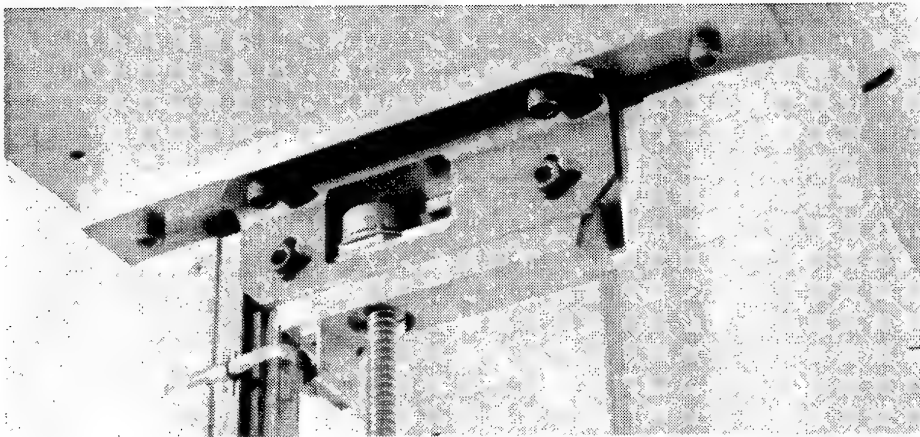
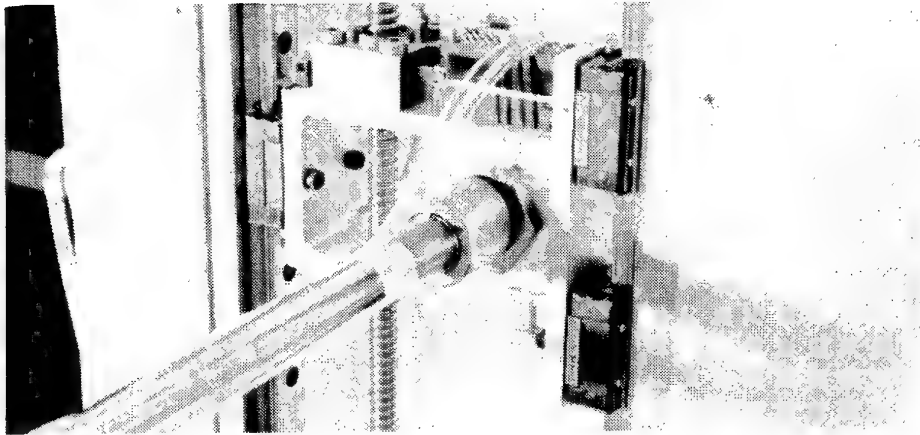


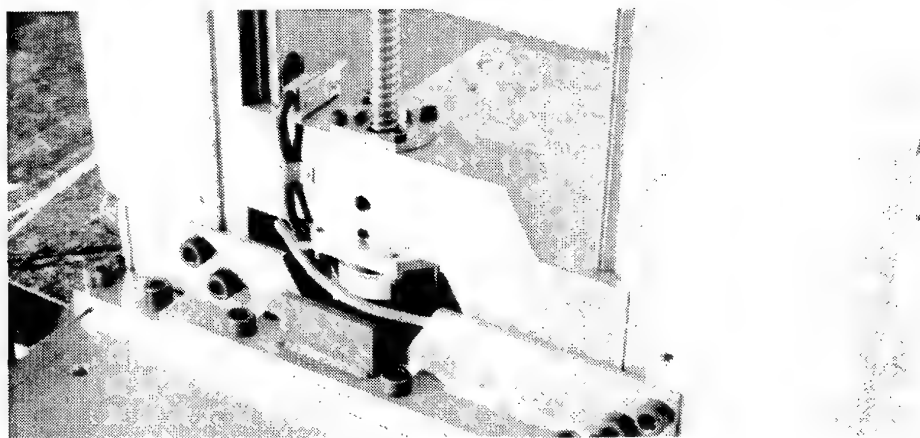
Figure 16. Assembly drawing of the traversing mechanism and probes.



(a) top part showing electric brake



(b) carriage



(c) bottom part showing stepping motor

Figure 17. Components of the traversing mechanism.

collet (Figure 16). A special alignment frame, shown in Figure 18, was used to ensure that the upper plate was located directly above the lower plate. The frame was bolted firmly to the lower plate, using dowel pins for alignment. The top plate was then mounted on four blocks attached to the frame, using dowel pins for alignment. Four set screws on the frame were used to lift the blocks and the top plate until the plate came into contact with the roof of the test section. Guide pins minimized lateral movement of the top plate while it was being raised. The top plate was then bolted to the roof of the test section and the frame was removed from the tunnel. The traversing mechanism was then positioned on the lower plate, using a guide bar at the foot of the mechanism (Figure 16) to ensure that the base of the mechanism was not twisted relative to the trailing edge of the lower plate. The traversing mechanism was then bolted to the lower plate so that the probe tip was located at the required  $y_T$  position. The two vertical linear-motion rails on the mechanism (Figure 16) were positioned so that they were less than  $0.05^\circ$  from the vertical, as measured with an inclinometer on two adjacent sides of each rail, and the mechanism was then bolted to the upper plate.

There is provision on the mechanism to change the orientation of the six-hole probe (and the dummy probe). The yaw angle,  $\psi$ , pitch angle,  $\theta$ , and roll angle,  $\phi$ , can all be altered independently (see Figure 16 for adjustment mechanisms). On the mechanism,  $\psi$  could be varied by about  $\pm 15^\circ$ ,  $\theta$  by  $360^\circ$  and  $\phi$  by  $360^\circ$ . It would have been relatively difficult to set values of  $\psi$  to the accuracy needed when the probe longitudinal axis was horizontal (i.e.  $\theta = 0^\circ$ ), but by rotating the pitch shaft (Figure 16) so that the probe longitudinal axis was temporarily approximately vertical, and then adjusting the yaw screws to set the probe vertical in the  $y_T$ - $z_T$  plane, using an inclinometer on the probe body, and then returning the probe to the horizontal position, values of  $\psi$  could be set to  $0.0^\circ$  to an accuracy of about  $\pm 0.02^\circ$ . An inclinometer was also used to set values of  $\theta$  to an accuracy of about  $\pm 0.02^\circ$ . Values of  $\phi$  were set by rolling the probe until the scribed reference line on the body of the probe (Figure 14) matched the appropriate scribed line on the graduated scale on the collet (Figure 13). A microscope was used when matching the scribed lines and values of  $\phi$  were set to an accuracy of about  $\pm 0.2^\circ$ .

The traversing mechanism is a precision device and was manufactured to high accuracy. However, as with any practical device, the individual components on the mechanism all had manufacturing tolerances. Checks were done and it was found that the possible error in the setting of the yaw angle of the six-hole probe due to these effects could be up to  $\pm 0.1^\circ$ . This would occur if components had been manufactured to the limits of their tolerances (either maximum or minimum limits) and then assembled so that the effects of the inbuilt imperfections were maximized, i.e. the worst possible case.

It was found that the engraved scales on both of the probe collets (Figure 13) had been rolled slightly from the true zero position and these offsets have to be allowed for when setting probe roll angles. The engraved scale on the port collet has a zero error of  $+2.10^\circ$  and the scale on the starboard collet has a zero error of  $+1.35^\circ$ , i.e. the engraved scales are both rolled clockwise when looking in the direction from the rear of the probe to the hemispherical tip of the probe (Figure 13).

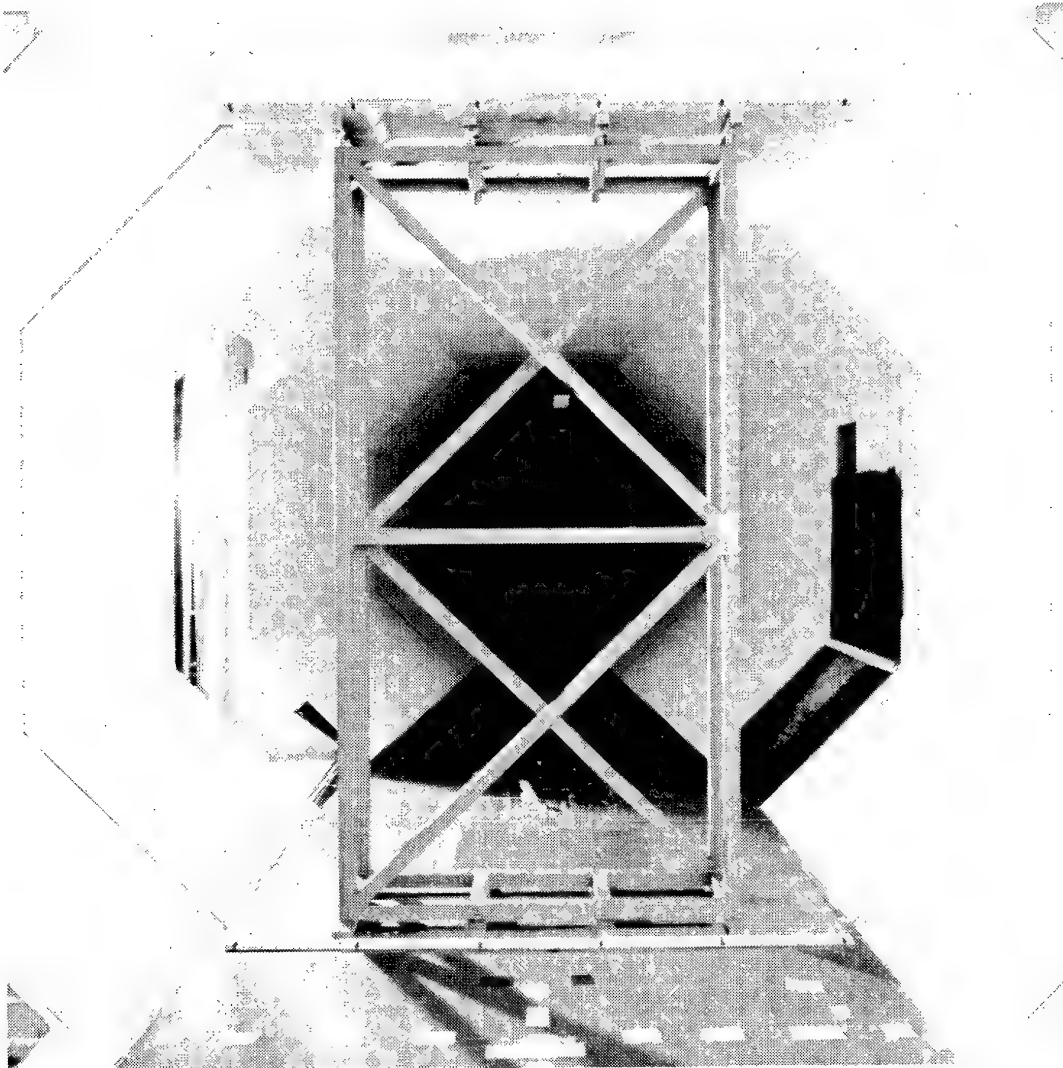


Figure 18. Alignment frame used when locating the upper plate of the traversing mechanism on the test section roof with respect to the lower plate on the floor.

The movement of the probe was controlled using program WINDRIG located on a PC. Initially the user must enter the current  $z_T$  position of the probe relative to the floor of the test section. This initial setting is used as a reference for subsequent positioning of the probe. The user must then enter the lower and upper  $z_T$  limits corresponding to the permissible probe movement. These limits are independent of the limits set by the limit switches (see above) and would be used, for example, if the probe was being traversed between the corner fillets in the octagonal test section. To minimize the possibility of damaging the probe and the traversing mechanism, the program has been written so that it is not possible to move the probe using the program unless these limits have been



entered. Finally, the user must enter the destination value of  $z_T$  and the mechanism then moves the probe as required. The smallest permissible probe movement from a given location is 0.1 mm and the probe can be positioned to an accuracy of 0.1 mm relative to its initial setting.

### 3.5 Procedure Used to Measure Flow Angles

When measuring velocities and flow angles, the probe was positioned in the tunnel so that the origin of the body coordinate system,  $x_B, y_B, z_B$  (Figure 14), was located at the grid point at which measurements were to be taken. For all of the current measurements, the probe orientation angles,  $\psi$ ,  $\theta$  and  $\phi$ , were set at  $180.0^\circ$ ,  $-1.0^\circ$  and  $0.0^\circ$  respectively (Figure 14). The probe vertical movement was restricted by the brake (at the top of the mechanism) and by the stepping motor (at the bottom of the mechanism) and it was necessary to set  $\theta$  at  $-1.0^\circ$  to enable measurements to be taken at both the upper and lower grid points at given  $y_T$  locations.

To determine the direction of the flow (Figure 14), it was first necessary to measure probe pressures,  $p_1$  to  $p_6$ . These pressures were measured using the same electronic manometer system and data sampling format that were used to measure the pressures for the mean velocities, as described in Section 2.4. For the flow angle measurements, a PSI Electronic Pressure Scanner having a full-scale range of  $\pm 2490$  Pa ( $\pm 10.0$  inches of water) was used.

Once  $p_1$  to  $p_6$  had been measured,  $V_y$ ,  $\theta_y$  and  $\phi_y$  were determined using the probe calibration (equations 7 to 13). As indicated in Section 3.2, the calibration relationships do not give  $V_y$ ,  $\theta_y$  and  $\phi_y$  explicitly in terms of measured pressures,  $p_1$  to  $p_6$ , and it was necessary to determine the three variables iteratively. The following procedure was used.

1. As a first approximation, the value of  $V_y$  was set below its known value (e.g.  $V_y$  was initially set at 27 m/s when the free-stream velocity at which the measurements were taken was known to be about 30 m/s).
2. Using this first approximation of  $V_y$ , first approximations of  $C_{p_n}$  ( $n = 1$  to 4),  $R$  and  $\theta_y$  were made using equations 10, 9 and 7 (or 8) respectively.
3. Using the first approximation of  $\theta_y$ , a second approximation of  $V_y$  was made using equation 11 (or 12).
4. Successive approximations of  $V_y$  were made and steps 1 to 3 were repeated until the velocities converged to within 0.001 m/s. At this stage,  $V_y$ ,  $\theta_y$ ,  $C_{p_1}$ ,  $C_{p_2}$ ,  $C_{p_3}$  and  $C_{p_4}$  were determined to an acceptable accuracy.
5. Once values of  $C_p$  were known,  $\phi_y$  was calculated using equation 13.

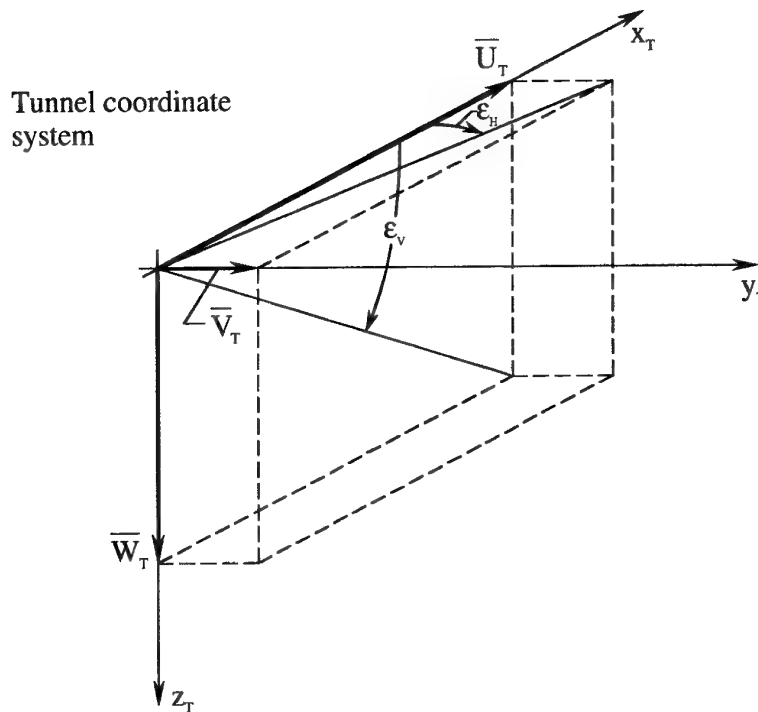


Figure 19. Velocities and flow angles in the tunnel coordinate system.

$V_y$  was resolved into  $\bar{U}_B$ ,  $\bar{V}_B$  and  $\bar{W}_B$ , the components of velocity in the  $x_B$ ,  $y_B$  and  $z_B$  directions respectively in the body coordinate system, and these velocities were transposed, using equation 14, into  $\bar{U}_T$ ,  $\bar{V}_T$  and  $\bar{W}_T$ , the components of velocity in the  $x_T$ ,  $y_T$  and  $z_T$  directions respectively in the tunnel coordinate system. Horizontal and vertical flow angles,  $\epsilon_H$  and  $\epsilon_v$  respectively, relative to the  $x_T$  axis as shown in Figure 19, were then calculated. All iterative calculations and data reduction were carried out using the program ANGLE located on a PC.

### 3.6 Corrections to Flow Angles to Allow for Probe Support Interference

The traversing mechanism used to position the six-hole probe in the tunnel when measuring flow angles was made to be reasonably rigid (Figures 15 and 16). The vertical column on the mechanism is 46 mm wide and extends from the floor to the roof of the test section, so that the ratio of the cross-sectional area of the column to the total transverse cross-sectional area of the test section is 0.019:1, i.e. 1.9%. Although such a value of blockage is significantly less than the value 7.5%, quoted in Reference 10 as being the upper limit of blockage acceptable for wind-tunnel testing, interference caused by the column nevertheless had a noticeable effect on measured flow angles. When the six-hole probe was supported on the port side of the vertical column, flow angles measured at given  $z_T$  locations on the vertical centreplane in the test section were

found to be noticeably different (see below) from those measured at the same locations when the probe was supported on the starboard side of the vertical column. Note that the vertical column on the traversing mechanism had to be moved from one side of the test section to the other side to obtain the two sets of measurements.

Experiments were undertaken to determine the corrections to be applied to measured flow angles to allow for the effects of the interference caused by the traversing mechanism. To determine a typical interference correction, the six-hole probe was mounted in a specially-designed thin supporting column (width of thin column is 16 mm), so that the tip of the probe was directly upstream of the column and the probe yaw, pitch and roll angles were set close to their values for normal operation. Flow angles were then measured for  $\bar{U}_{\text{NOM}} = 30$  and 60 m/s. The traversing mechanism was not in the test section for these measurements. The traversing mechanism was then positioned in the test section on either the port side of the probe or on the starboard side of the probe, but not actually attached to the probe, and flow angles were measured again. The vertical column on the traversing mechanism was located at the same lateral distance from the probe as it would be during normal operation, when the probe was attached to the mechanism. A typical experimental setup is shown in Figure 20 for the case when the thin column and the traversing mechanism are both in the test section. The interference corrections were then determined as the differences in corresponding flow angles measured both with the traversing mechanism in the tunnel and with the mechanism out of the tunnel.

When the six-hole probe was mounted on the thin column to assess probe support interference, it did not have to be set precisely at the yaw, pitch and roll angles used when the probe was attached to the traversing mechanism during normal operation. When determining interference corrections, the important measurements were the differences in flow angles measured when the traversing mechanism was in the tunnel and when it was not in the tunnel, rather than the absolute values of flow angles.

Interference corrections were determined in the  $x_T = 0.0$  m transverse plane of the test section for  $y_T/W = 0.0, \pm 0.15$  and  $\pm 0.3$ , and  $z_T/H = 0.0$  and  $\pm 0.3$ , where  $W = 2743$  mm and  $H = 2134$  mm are the width and height respectively of the test section of the LSWT (Figure 2). It was necessary to use three different thin supporting columns to support the six-hole probe at the three different  $z_T$  locations in the test section. The three columns were essentially the same, but had the probe attachment sleeve located at a different height ( $z_T$  location). Altogether, interference corrections were obtained for 15 locations, and corrections at other locations at which flow angles were measured were obtained by linear interpolation. The interference corrections varied depending on the location in the test section. For  $\bar{U}_{\text{NOM}} = 30$  and 60 m/s, average values of corrections for  $\epsilon_H$  were about  $0.4^\circ$  and those for  $\epsilon_V$  were about  $0.0^\circ$ . The corrections determined for the  $x_T = 0.0$  m transverse plane were applied to flow angles measured in this plane as well as in the  $x_T = -2.0, -1.0$  and  $1.0$  m transverse planes. The overlapping results at the vertical centreplane were effectively the same after the corrections had been applied.

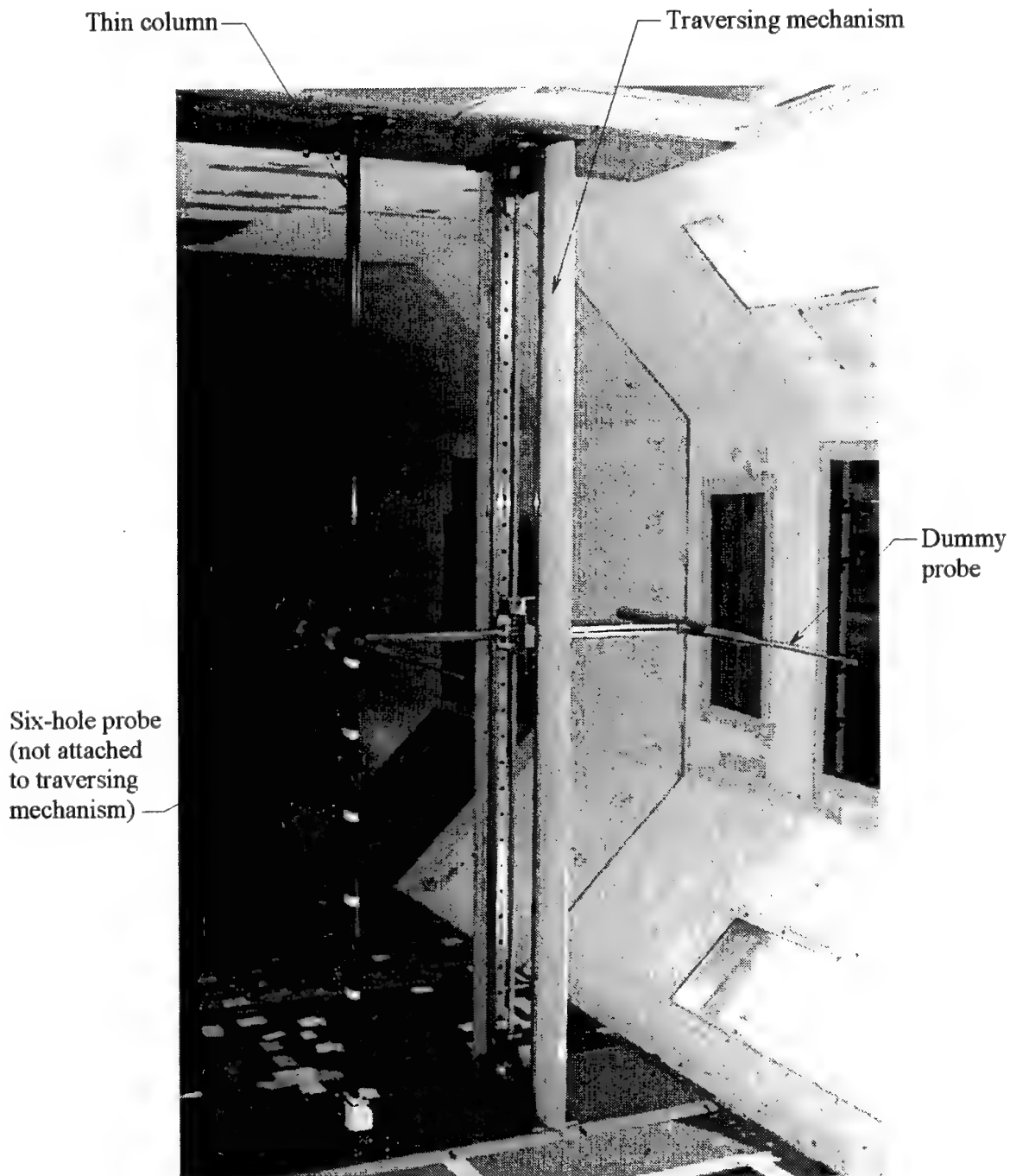


Figure 20. Traversing mechanism and thin column (supporting the six-hole probe) mounted in the test section of the low-speed wind tunnel.

### 3.7 Analysis of Flow Angles

Contours of  $\epsilon_H$  for  $\bar{U}_{\text{NOM}} = 30$  m/s for  $x_T = -2.0, -1.0, 0.0$  and  $+1.0$  m are shown in Figure 21. Corresponding plots for  $\epsilon_V$  are shown in Figure 22. Figures 23 and 24 show contours for  $\bar{U}_{\text{NOM}} = 60$  m/s. As for the mean velocities, Figures 21 to 24 each indicate how the flow angles change as the flow moves downstream. For the two values of  $\bar{U}_{\text{NOM}}$ , the general pattern of the  $\epsilon_H$  contours at the four  $x_T$  locations is similar (Figures 21 and 23), with little evidence of the flow becoming more uniform as it moves downstream, and likewise for the corresponding  $\epsilon_V$  contours (Figures 22 and 24). In the central 50% of the cross-sectional area of the test section, between  $x_T = -2.0$  and  $+1.0$  m, for  $\bar{U}_{\text{NOM}} = 30$  m/s, horizontal flow angles varied from  $-0.8^\circ$  to  $+0.4^\circ$  (Figure 21) and vertical flow angles varied from  $-1.0^\circ$  to  $+0.4^\circ$  (Figure 22). For  $\bar{U}_{\text{NOM}} = 60$  m/s, horizontal flow angles varied from  $-0.6^\circ$  to  $+0.8^\circ$  (Figure 23) and vertical flow angles varied from  $-1.2^\circ$  to  $+0.4^\circ$  (Figure 24). However, between  $x_T = -1.0$  and  $+1.0$  m, for  $\bar{U}_{\text{NOM}} = 30$  m/s, horizontal flow angles varied from  $-0.8^\circ$  to  $+0.4^\circ$  and vertical flow angles varied from  $-0.8^\circ$  to  $+0.4^\circ$ . For  $\bar{U}_{\text{NOM}} = 60$  m/s, horizontal flow angles varied from  $-0.4^\circ$  to  $+0.8^\circ$  and vertical flow angles varied from  $-1.0^\circ$  to  $+0.4^\circ$ . There is a pocket of flow in the lower starboard corner of the test section which has significantly larger values of vertical flow angles which range up to  $-1.4^\circ$  (Figure 24). Figures 21 and 22, for  $\bar{U}_{\text{NOM}} = 30$  m/s, and Figures 23 and 24, for  $\bar{U}_{\text{NOM}} = 60$  m/s, indicate that regions of high or low horizontal flow angles are not necessarily associated with corresponding regions of high or low vertical flow angles.

Selected data associated with the contours shown in Figures 21 to 24 have been replotted in Figure 25 to indicate how horizontal and vertical flow angles in the horizontal and vertical centreplanes vary in the longitudinal or  $x_T$  direction. The method of plotting the data is similar to that used in Section 2.5 for the mean velocities. Data corresponding to the  $x_T$ - $z_T$  plane that passes through  $y_T = 0.0$  m (i.e. the vertical plane that is aligned with and passes through the tunnel longitudinal axis) are shown for  $z_T/H = 0.0, \pm 0.2$  and  $\pm 0.4$ . Similarly, data corresponding to the  $x_T$ - $y_T$  plane that passes through  $z_T = 0.0$  m (i.e. the horizontal plane that is aligned with and passes through the tunnel longitudinal axis) are shown for  $y_T/W = 0.0, \pm 0.15, \pm 0.30$  and  $\pm 0.45$ . In Figure 25, data corresponding to the longitudinal centreline of the tunnel are represented by thick lines. Horizontal and vertical flow angles for the chosen locations remain approximately constant over the  $x_T$  range.

### 3.8 Errors in Measured Flow Angles

There are small errors in the measured horizontal and vertical flow angles,  $\epsilon_H$  and  $\epsilon_V$  respectively, due to (1) instrumentation errors and (2) probe setup errors. The probe setup errors occur because the six-hole probe is not set at precisely the required yaw, pitch and roll angles, relative to the tunnel coordinate system, when measuring flow angles.

### 3.8.1 Instrumentation Errors

Considering instrumentation errors, it was necessary to measure air temperatures and air pressures when determining flow angles. The sensing devices used to measure temperatures were only accurate to within  $\pm 0.5^\circ \text{C}$  and the indicated readings of the scanners used to measure pressures were only accurate to within  $\pm 0.05\%$  of their full-scale reading. Two different types of scanners were used when measuring pressures and their ranges were 159 kPa (23.0 psi) (used to measure reference velocities) and  $\pm 2490 \text{ Pa}$  ( $\pm 10.0$  inches of water). The possible errors in measured values of  $\epsilon_h$  and  $\epsilon_v$  corresponding to these instrumentation errors were determined. For  $\bar{U}_{\text{NOM}} = 30 \text{ m/s}$ , errors in  $\epsilon_h$  were about  $\pm 0.08^\circ$  and errors in  $\epsilon_v$  were about  $\pm 0.08^\circ$ . Corresponding errors for  $\bar{U}_{\text{NOM}} = 60 \text{ m/s}$  were about  $\pm 0.02^\circ$  for  $\epsilon_h$  and about  $\pm 0.02^\circ$  for  $\epsilon_v$ .

### 3.8.2 Probe Setup Errors

Considering probe setup errors, it is indicated in Section 3.4 that the possible errors in setting the yaw, pitch and roll angles of the six-hole probe are  $\pm 0.02^\circ$ ,  $\pm 0.02^\circ$  and  $\pm 0.2^\circ$  respectively. The  $\pm 0.02^\circ$  probe setup error given for the yaw angle corresponds to the possible misalignment of the probe relative to the traversing mechanism, and not the misalignment of the probe relative to the tunnel. It is also indicated in Section 3.4 that an additional error of  $\pm 0.1^\circ$  in probe yaw angle may exist since the traversing mechanism itself can only be set to an accuracy of  $0.1^\circ$  in yaw angle, due to difficulties in accurately positioning the lower plate which is used to align the mechanism. It is further indicated that an additional error of  $\pm 0.1^\circ$  in probe yaw angle may exist due to possible twisting of the mechanism relative to the lower plate, resulting from imperfect manufacture and assembly of the mechanism. Possible errors in measured values of  $\epsilon_h$  and  $\epsilon_v$  corresponding to the probe setup errors given above were determined. It was found that errors in  $\epsilon_h$  were about  $\pm 0.02^\circ$  and errors in  $\epsilon_v$  were about  $\pm 0.05^\circ$ . The setup error of  $\pm 0.1^\circ$  in probe yaw angle, due to the positioning the lower plate, results in an  $0.1^\circ$  increase or decrease in the possible error in  $\epsilon_h$ , and similarly for the setup error of  $0.1^\circ$  in probe yaw angle due to the twisting of the mechanism. These latter two setup errors in yaw angle have negligible effect on errors in measured values of  $\epsilon_v$ .

### 3.8.3 Accumulation of Errors

All possible errors in  $\epsilon_h$  and  $\epsilon_v$  given above are additive, i.e. the errors in  $\epsilon_h$  and  $\epsilon_v$  can be as large as  $\pm 0.22^\circ$  and  $\pm 0.05^\circ$  respectively. However, since the lower plate was not moved during any set of measurements at a given  $x_T$  location, any errors due to the positioning of the lower plate will affect all measured values of  $\epsilon_h$  equally at that  $x_T$  location, i. e. all measured values of  $\epsilon_h$  for a particular cross section of the flow may be high or low by up to  $0.1^\circ$  due to this effect. Similarly, since the traversing mechanism was not dismantled after initial assembly, any errors due to the twisting of the mechanism will affect all measured values of  $\epsilon_h$  equally for the entire set of angle measurements, i. e. all measured values of  $\epsilon_h$  for the entire experimental program may be high or low by up to an additional  $0.1^\circ$ .

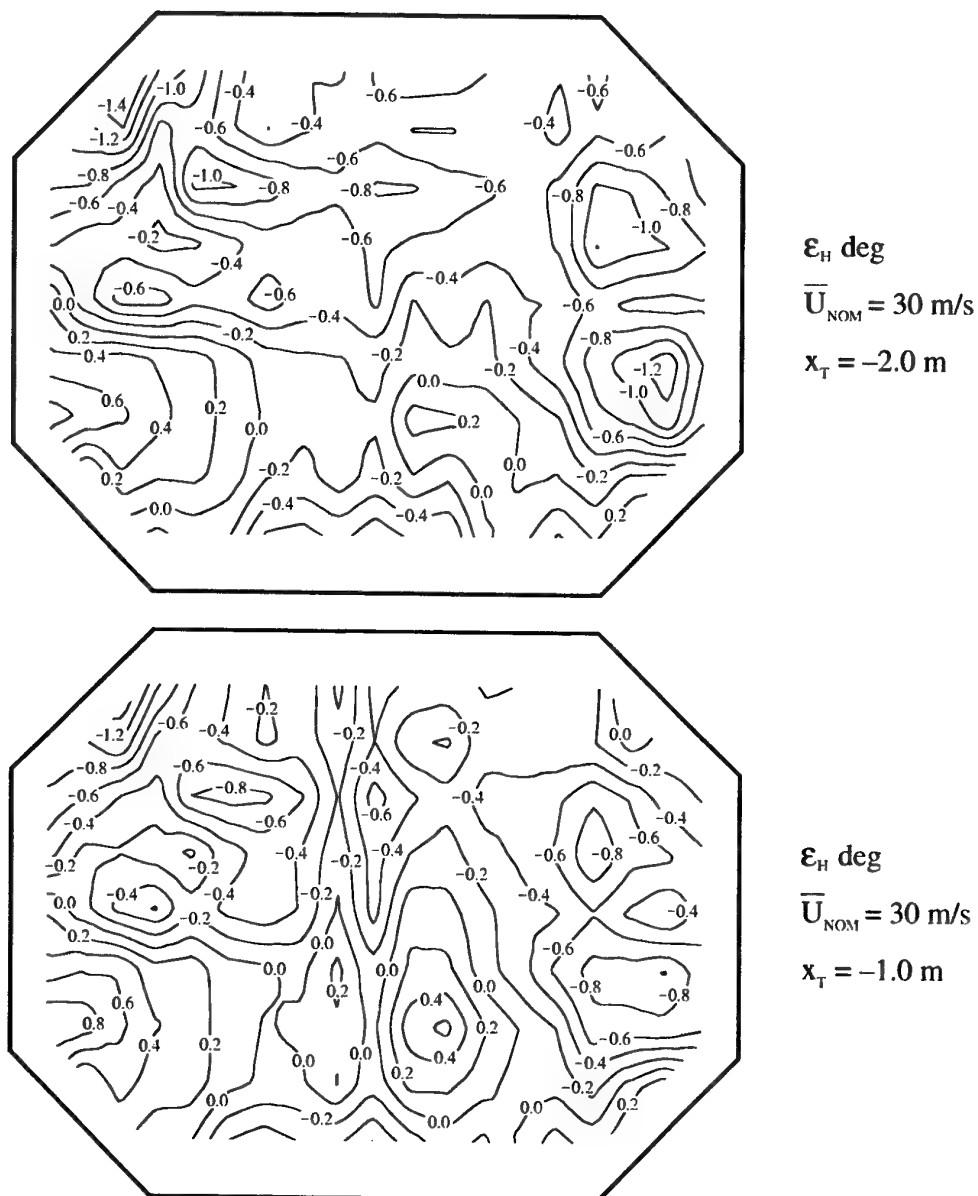


Figure 21. Contours of horizontal flow angle for  $\bar{U}_{\text{NOM}} = 30 \text{ m/s}$  for  $x_T = -2.0, -1.0, 0.0$  and  $1.0 \text{ m}$ .

(a)  $x_T = -2.0$  and  $-1.0 \text{ m}$ .

The flow is out of the page.

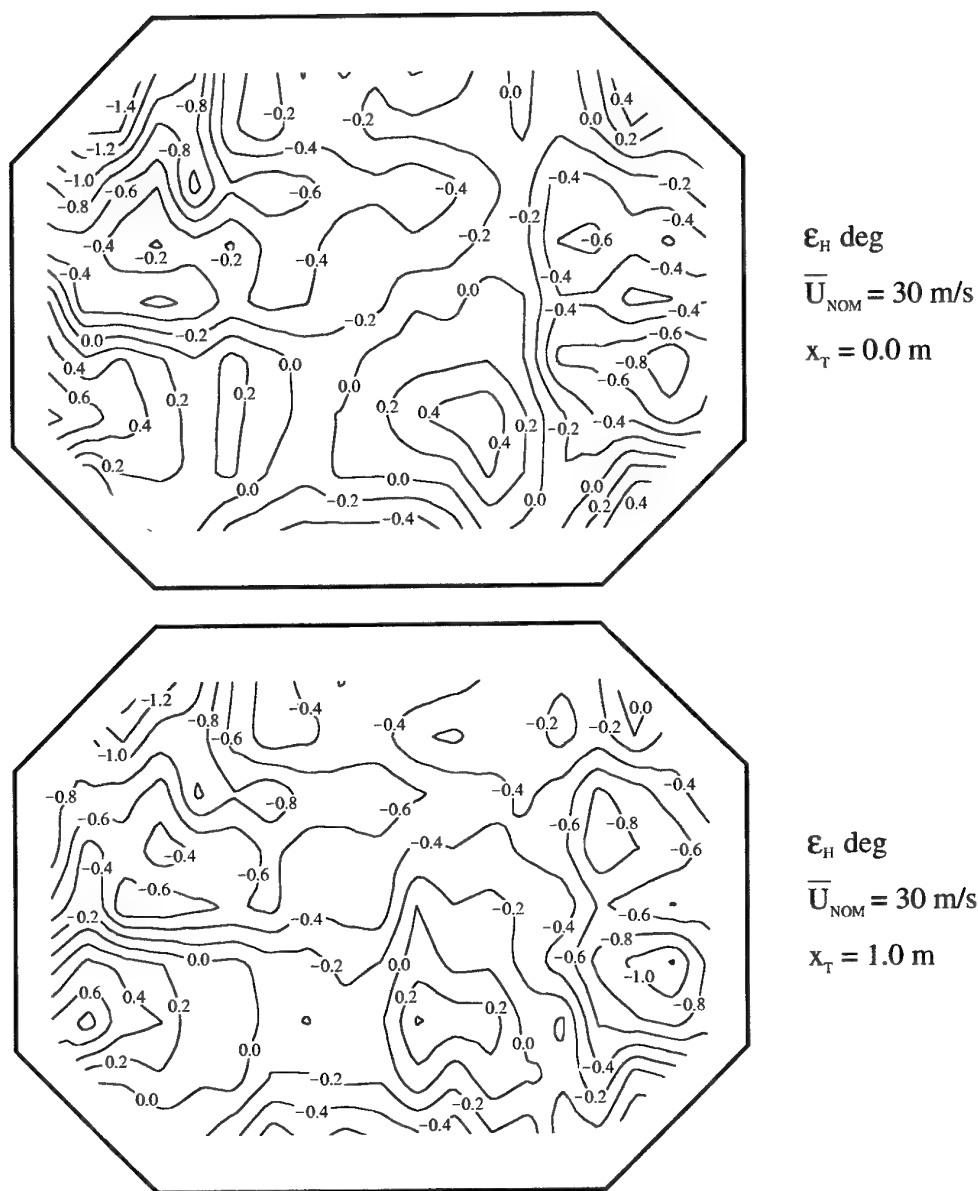


Figure 21 cont'd. Contours of horizontal flow angle for  $\bar{U}_{\text{NOM}} = 30 \text{ m/s}$  for  $x_T = -2.0, -1.0, 0.0$  and  $1.0 \text{ m}$ .

(b)  $x_T = 0.0$  and  $1.0 \text{ m}$ .

The flow is out of the page.



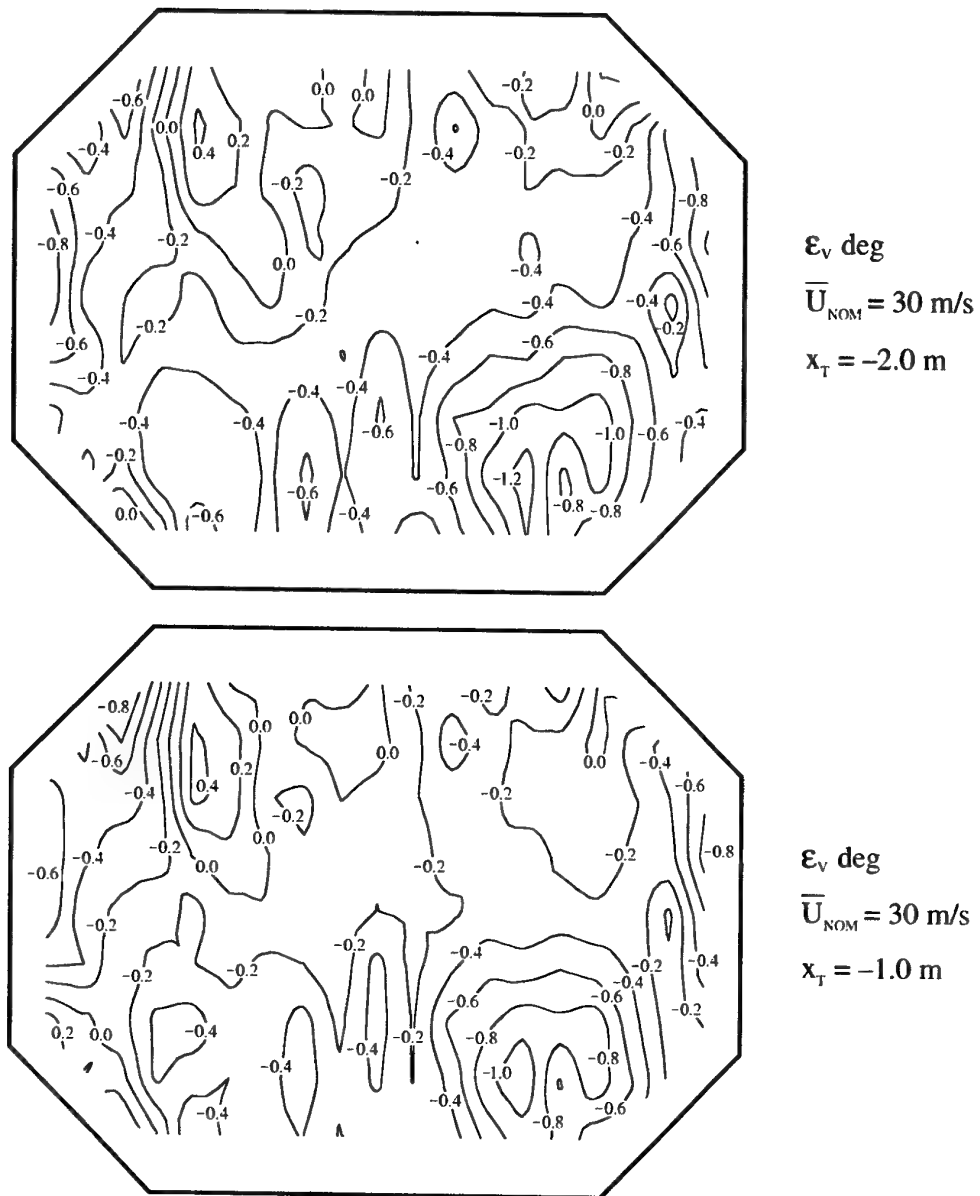


Figure 22. Contours of vertical flow angle for  $\bar{U}_{\text{NOM}} = 30 \text{ m/s}$  for  $x_T = -2.0, -1.0, 0.0$  and  $1.0 \text{ m}$ .

(a)  $x_T = -2.0$  and  $-1.0 \text{ m}$ .

The flow is out of the page.

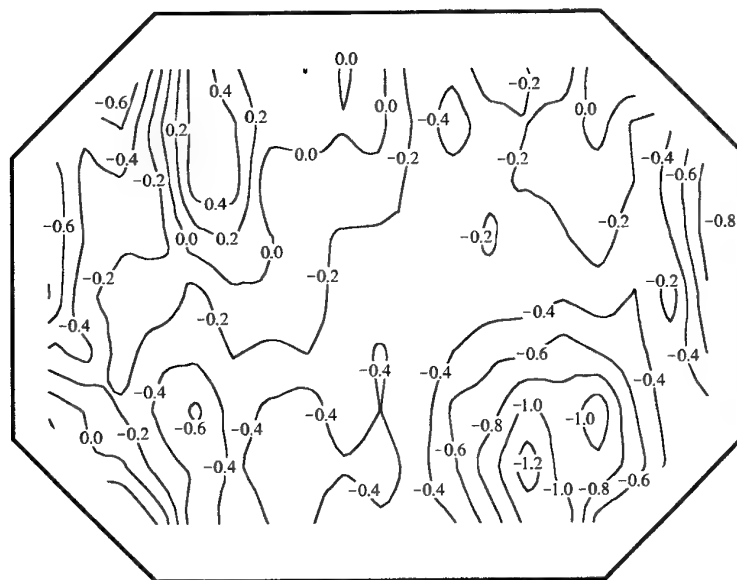
 $\epsilon_v$  deg $\bar{U}_{\text{NOM}} = 30$  m/s $x_T = 0.0$  m $\epsilon_v$  deg $\bar{U}_{\text{NOM}} = 30$  m/s $x_T = 1.0$  m

Figure 22 cont'd. Contours of vertical flow angle for  $\bar{U}_{\text{NOM}} = 30$  m/s for  $x_T = -2.0, -1.0, 0.0$  and  $1.0$  m.

(b)  $x_T = 0.0$  and  $1.0$  m.

The flow is out of the page.

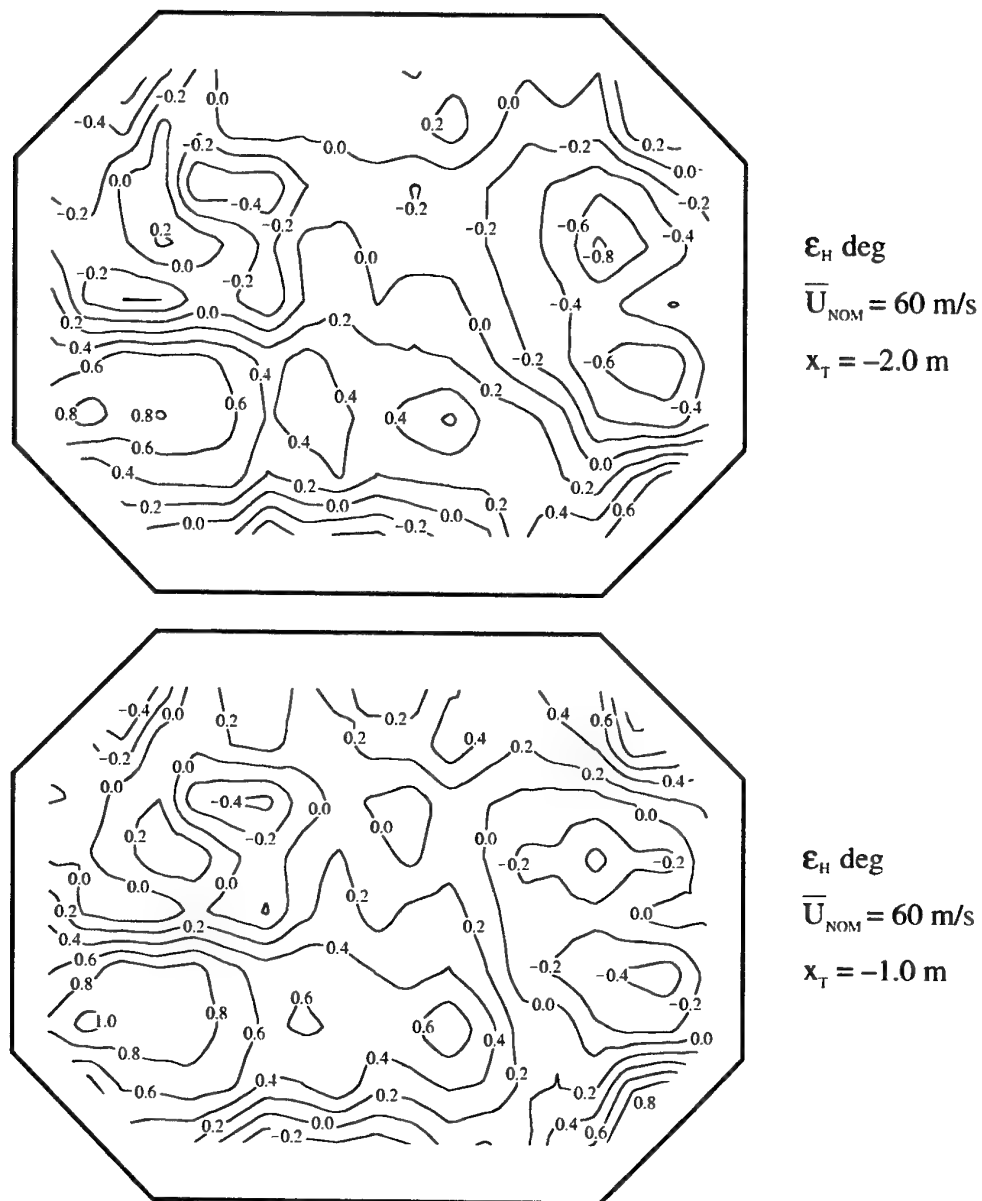


Figure 23. Contours of horizontal flow angle for  $\bar{U}_{NOM} = 60$  m/s for  $x_T = -2.0, -1.0, 0.0$  and  $1.0$  m.

(a)  $x_T = -2.0$  and  $-1.0$  m.

The flow is out of the page.

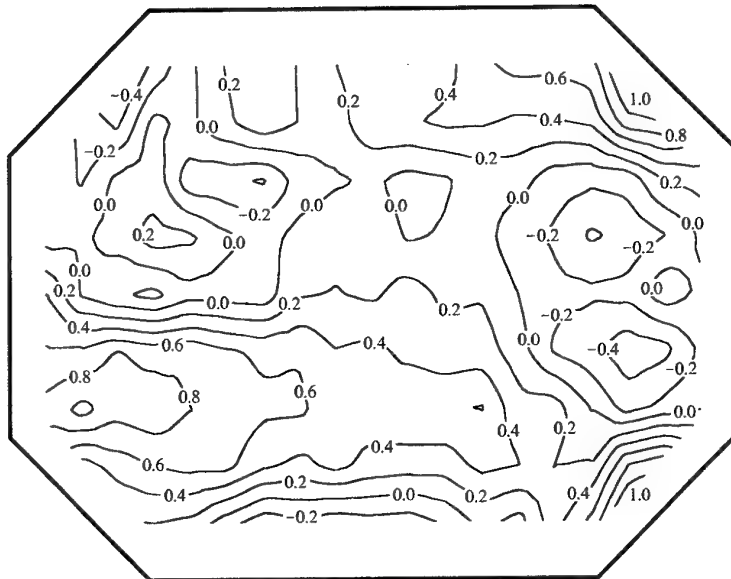
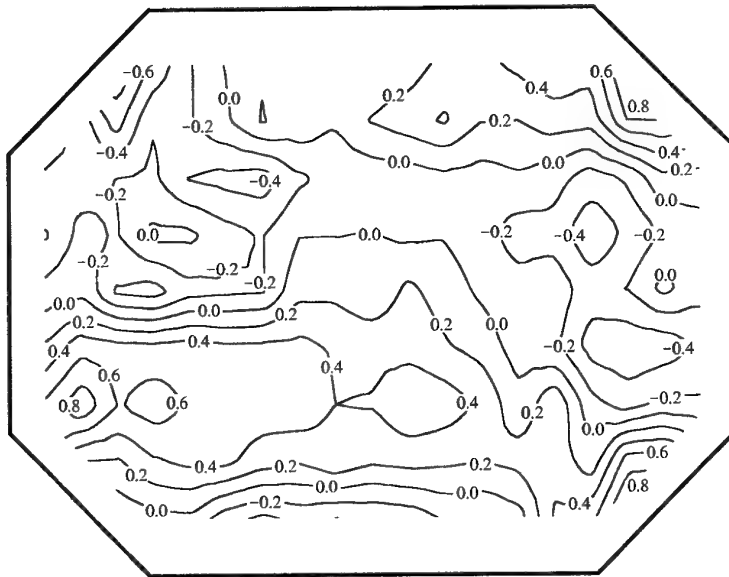
 $\epsilon_H$  deg $\bar{U}_{\text{NOM}} = 60 \text{ m/s}$  $x_T = 0.0 \text{ m}$  $\epsilon_H$  deg $\bar{U}_{\text{NOM}} = 60 \text{ m/s}$  $x_T = 1.0 \text{ m}$ 

Figure 23 cont'd. Contours of horizontal flow angle for  $\bar{U}_{\text{NOM}} = 60 \text{ m/s}$  for  $x_T = -2.0, -1.0, 0.0$  and  $1.0 \text{ m}$ .

(b)  $x_T = 0.0$  and  $1.0 \text{ m}$ .

The flow is out of the page.

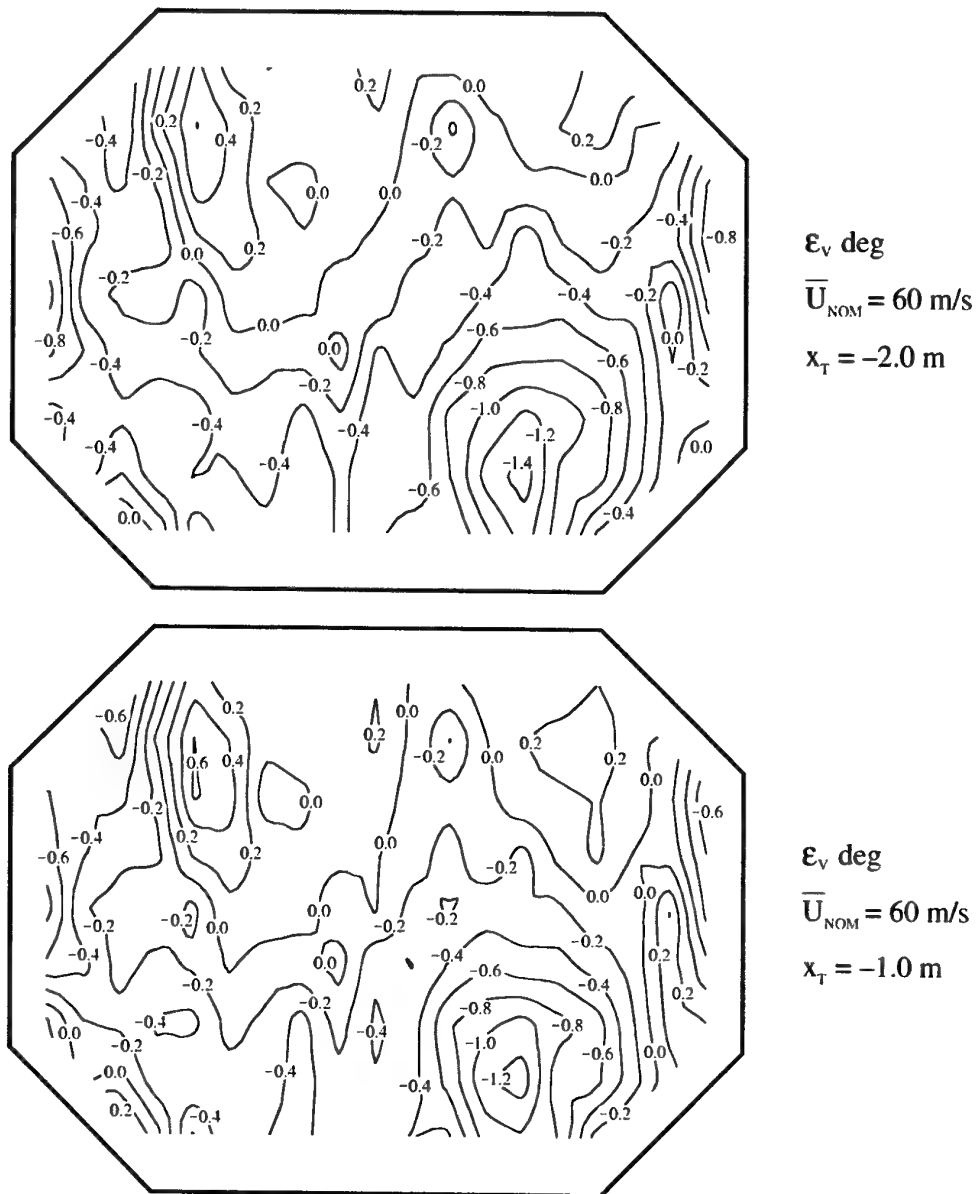


Figure 24. Contours of vertical flow angle for  $\bar{U}_{\text{NOM}} = 60$  m/s for  $x_T = -2.0, -1.0, 0.0$  and  $1.0$  m.

(a)  $x_T = -2.0$  and  $-1.0$  m.

The flow is out of the page.

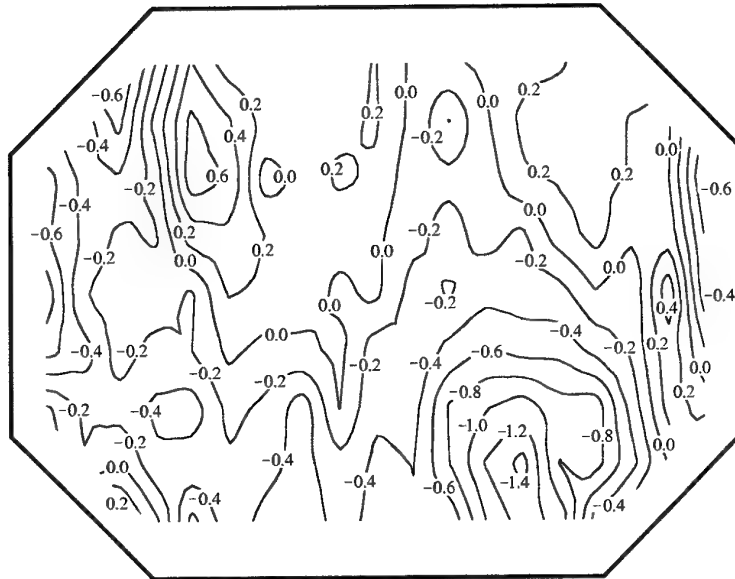
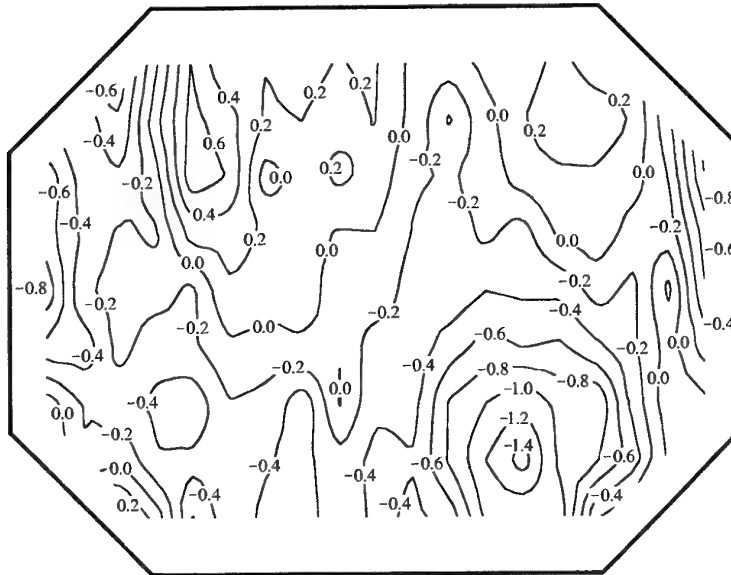
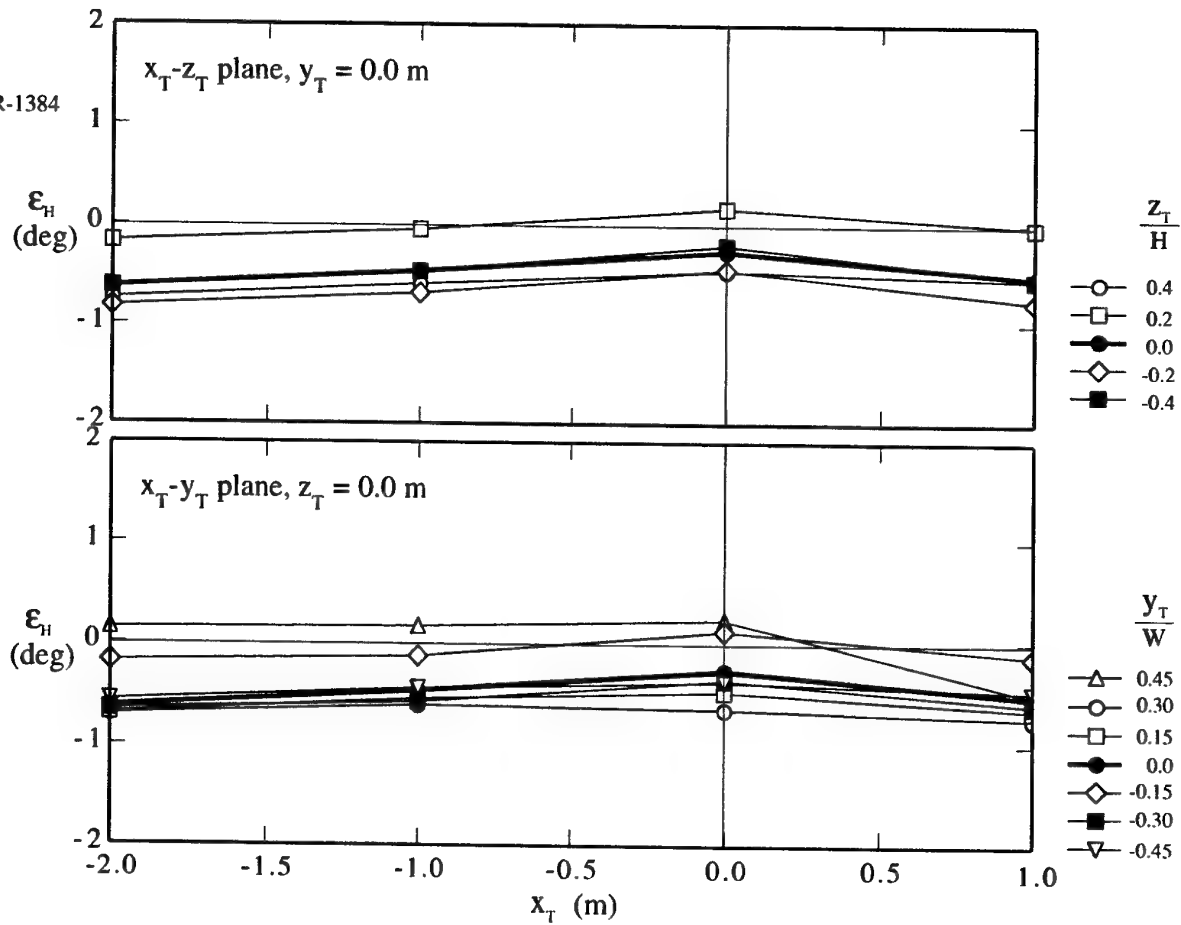
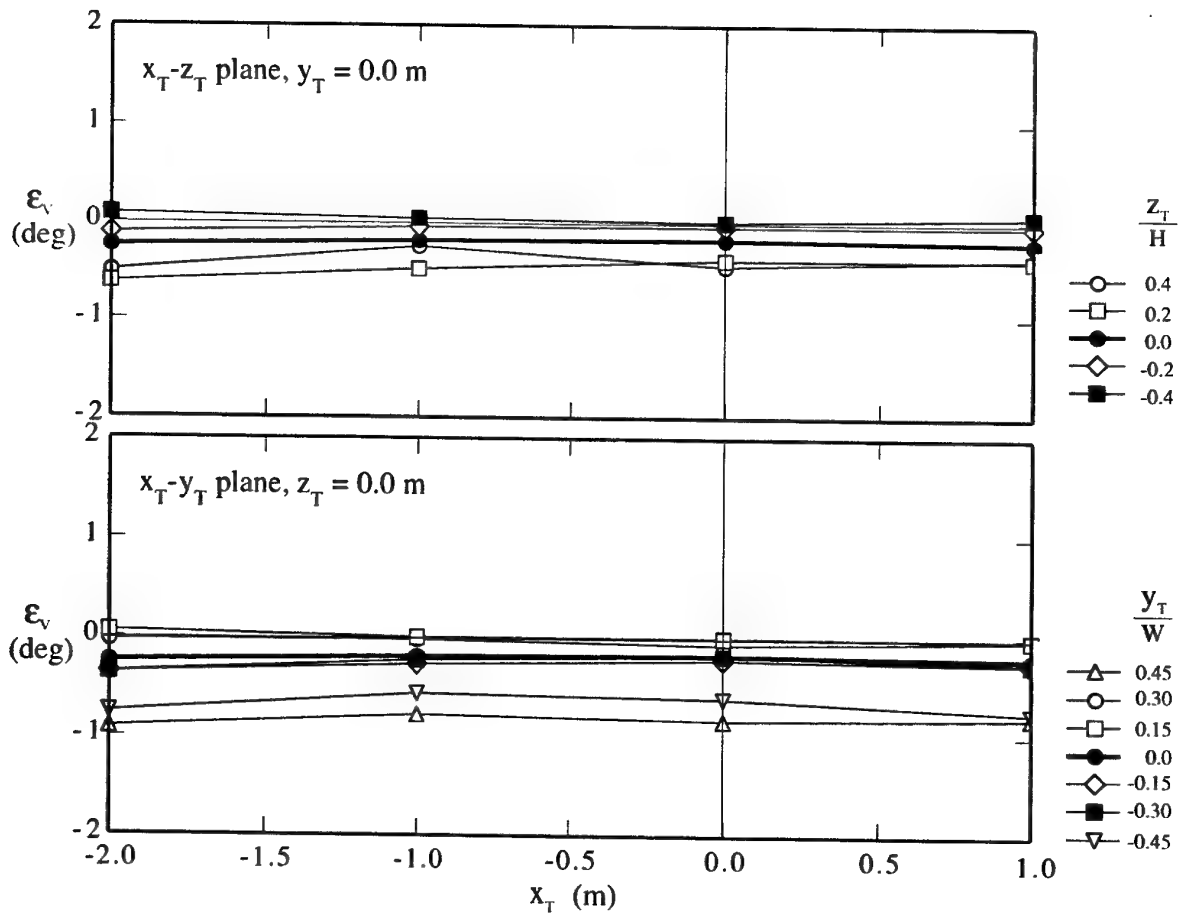
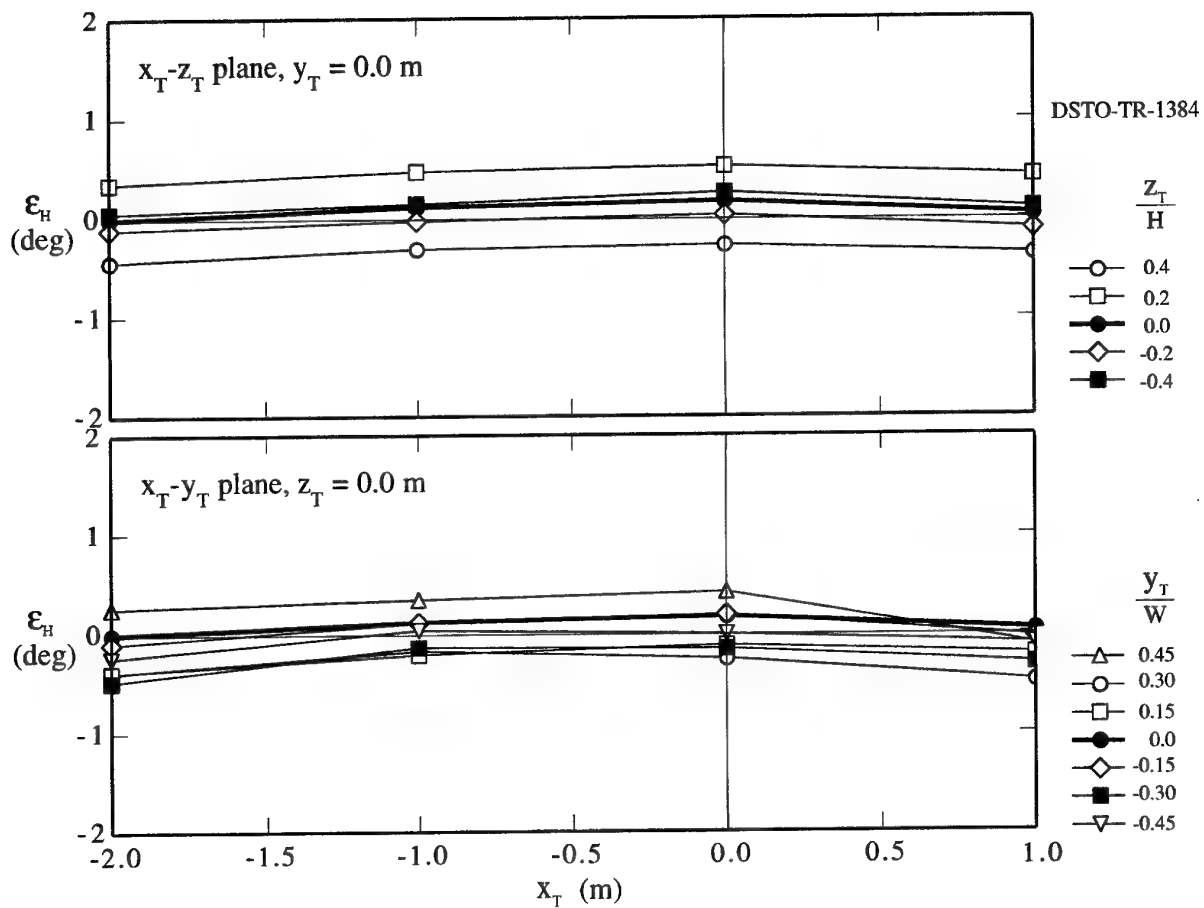
 $\epsilon_v$  deg $\bar{U}_{\text{NOM}} = 60 \text{ m/s}$  $x_T = 0.0 \text{ m}$  $\epsilon_v$  deg $\bar{U}_{\text{NOM}} = 60 \text{ m/s}$  $x_T = 1.0 \text{ m}$ 

Figure 24 cont'd. Contours of vertical flow angle for  $\bar{U}_{\text{NOM}} = 60 \text{ m/s}$  for  $x_T = -2.0, -1.0, 0.0$  and  $1.0 \text{ m}$ .

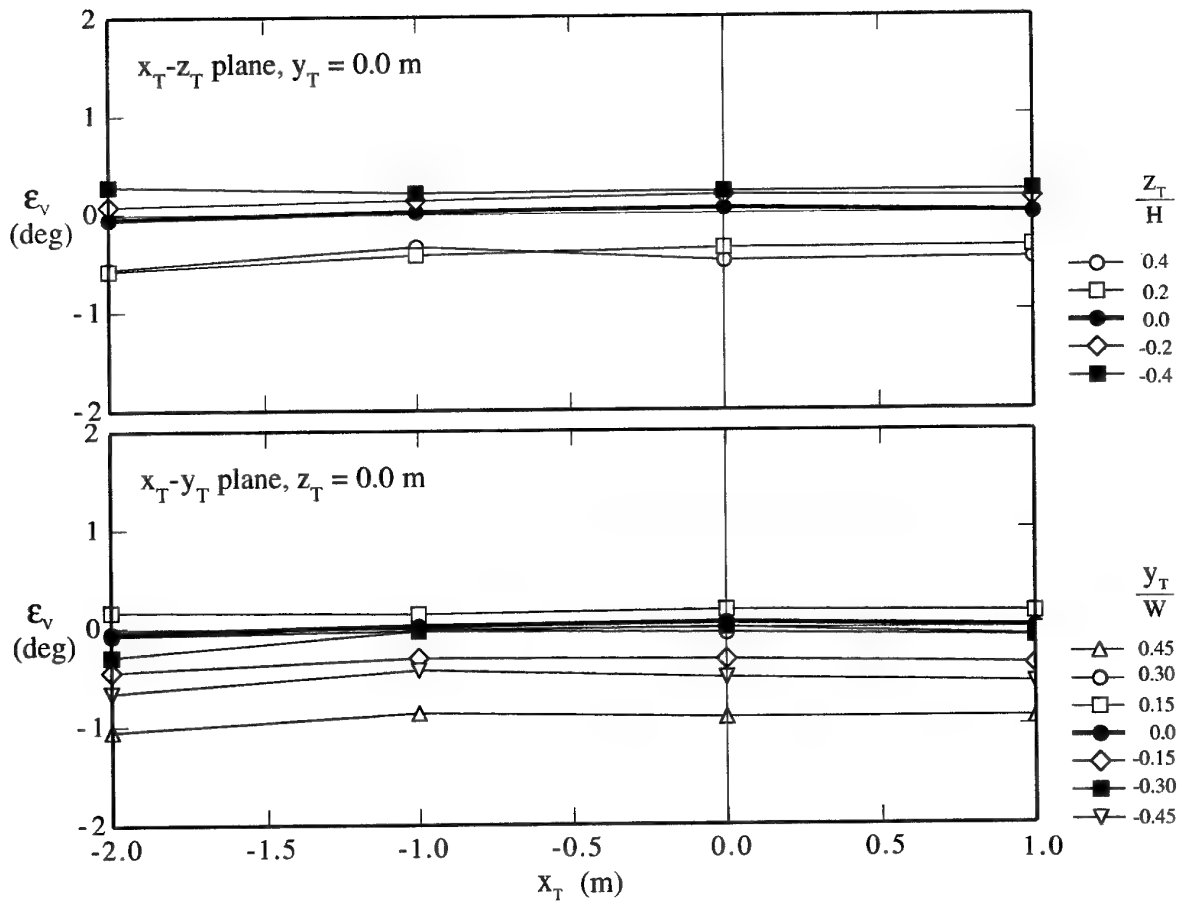
(b)  $x_T = 0.0$  and  $1.0 \text{ m}$ .

The flow is out of the page.

(a) Horizontal flow angles,  $\bar{U}_{NOM} = 30$  m/s.(b) Vertical flow angles,  $\bar{U}_{NOM} = 30$  m/s.



(c) Horizontal flow angles,  $\bar{U}_{NOM} = 60$  m/s.



(d) Vertical flow angles,  $\bar{U}_{NOM} = 60$  m/s.



## 4. Turbulence-Intensity Measurements

### 4.1 Test Schedule

Turbulence intensities,  $(\overline{u^2})^{0.5}/\overline{U}_{0.0}$ ,  $(\overline{v^2})^{0.5}/\overline{U}_{0.0}$  and  $(\overline{w^2})^{0.5}/\overline{U}_{0.0}$ , were measured in the test section at the 31 grid points shown in Figure 26 (a) for  $x_T = 0.0$  m as well as at the 15 grid points shown in Figure 26 (b) for  $x_T = -2.0, -1.0$  and  $+1.0$  m. Intensities were measured for  $\overline{U}_{\text{NOM}} = 30$  and  $60$  m/s. The symbols  $u$ ,  $v$  and  $w$  denote the fluctuating components of velocity in the  $x_T$ ,  $y_T$  and  $z_T$  directions respectively. (Note that in a fluctuating flow,  $U$ , the instantaneous velocity in the  $x_T$  direction, is related to the mean and fluctuating components of velocity in that direction by  $U = \overline{U} + u$ , and likewise for the  $y_T$  and  $z_T$  directions).

### 4.2 Modified Cross-Tunnel Rake

For the intensity measurements, the cross-tunnel rake (Section 2.3) was modified by removing some of the pressure probes and replacing them with posts, which were used to attach a hot-wire probe.

### 4.3 Procedure Used to Measure Turbulence Intensities

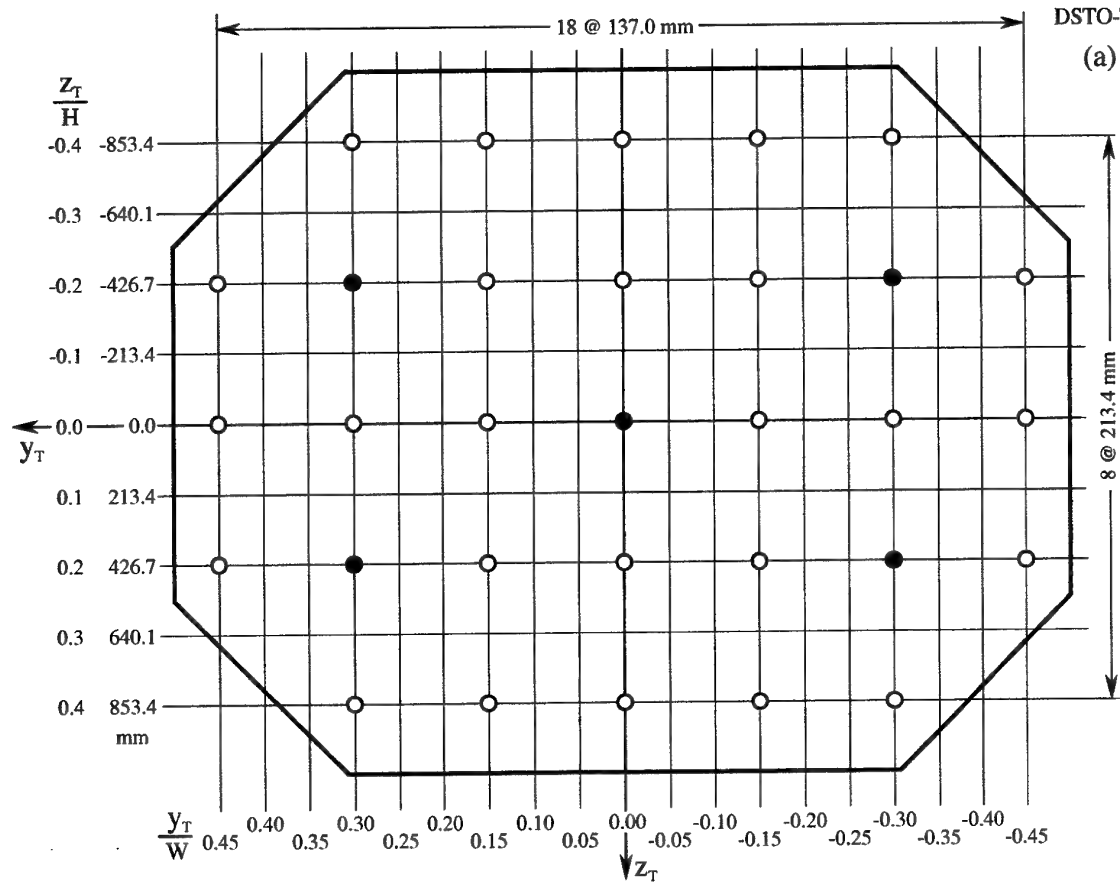
The turbulence intensities were measured using the PSL constant-temperature hot-wire anemometer system described in Reference 11. The system includes four anemometers, a matching box, a dynamic calibrator, four low-pass filters, a data-acquisition system (based on a PC) and software for calibrating the hot wires and for acquiring and reducing the data. For the current measurements, a DANTEC<sup>2</sup> 55P51 crossed-wire probe and corresponding leads were used, but the platinum-plated tungsten wires on the probe were removed and replaced with Wollaston wires. Although platinum-plated tungsten wires are stronger, Wollaston wires were used because the existing hot-wire anemometers had been optimized for use with this type of wire. Wollaston wires also have a more stable temperature calibration than platinum-plated tungsten wires (see Reference 11).

The procedures used to replace the hot wires, set the operating resistances of the wires, set the frequency responses of the anemometers, electronically match the wires, calibrate the wires using the dynamic calibrator, sample the wire voltages using the data-acquisition system and reduce the data to obtain the required turbulence terms, are described in Reference 11.

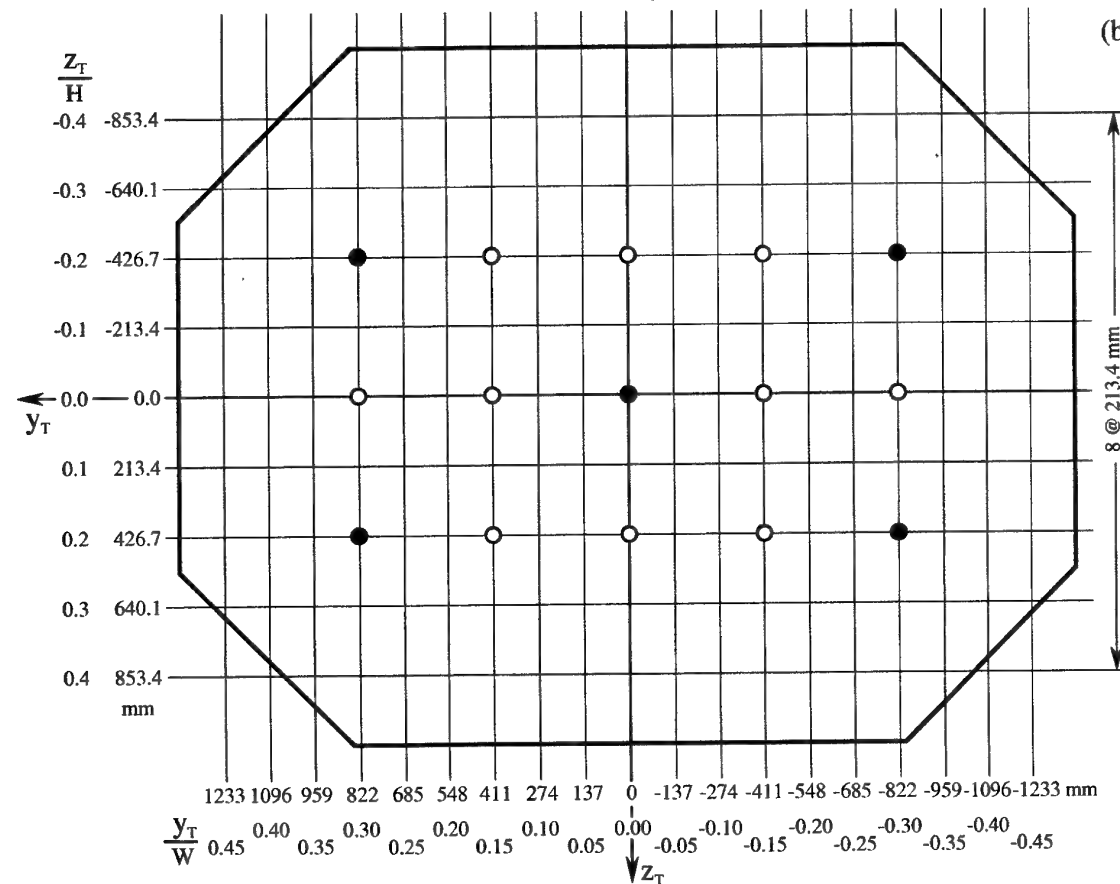
On the modified cross-tunnel rake (Section 4.2), only one hot-wire probe was used for the intensity measurements and it was necessary to roll the probe on its post or move the probe from post to post to enable the complete set of measurements to be taken. After

<sup>2</sup> DANTEC Elektronik, Tonsbakken 16-18, DK-2740, Skovlunde, Denmark.

(a)



(b)



The flow and the  $x_T$  axis are out of the page

Figure 26. Grid points at which turbulence intensities (unfilled plus filled circles) and spectra (filled circles) were measured. (a)  $x_T = 0.0$  m, (b)  $x_T = -2.0, -1.0$  and  $1.0$  m.

measuring intensities for the  $u$  and  $v$  components of the turbulence, the probe was rolled  $90^\circ$  to measure intensities for the  $u$  and  $w$  components of the turbulence. At each probe location, the  $u$ -component intensities were determined by averaging the two measured intensities corresponding to the two roll angles of the probe. The difference between the results for the two roll angles was small for  $\bar{U}_{\text{NOM}} = 30$  and  $60$  m/s, being typically of the order of  $0.02$  and  $0.06$  percentage points respectively. The tunnel had to be stopped each time the probe was rolled or relocated.

When measuring intensities, each hot-wire voltage was sampled  $30\,000$  times at a sampling frequency of  $200$  Hz and the low-pass filters were set at  $10$  kHz. These sampling parameters have been shown to be satisfactory for the measurement of intensities in the free-stream of the LSWT (Reference 11). Since the root-mean-square intensities were known to be much less than  $10\%$  at all locations in the flow, hot-wire non-linearity was neglected and intensities were evaluated by processing measured hot-wire voltages rather than by processing velocities determined from voltages (Reference 12). The hot wires were calibrated at both  $\bar{U}_{\text{NOM}} = 30$  and  $60$  m/s and hot-wire sensitivities were evaluated at these two velocities. The turbulence intensities were then determined using these sensitivities. Since sensitivities were only required at either  $\bar{U}_{\text{NOM}} = 30$  or  $60$  m/s, it was not necessary to carry out a complete dynamic calibration to obtain calibration equations covering a range of free-stream velocities.

For each position of the hot-wire probe, values of  $(\bar{u}^2)^{0.5}$ ,  $(\bar{v}^2)^{0.5}$  and  $(\bar{w}^2)^{0.5}$  were measured and at the same time corresponding values of  $\bar{U}_{\text{REF}}$  were recorded. Using these values of  $\bar{U}_{\text{REF}}$ , longitudinal mean velocities,  $\bar{U}$ , at each probe location were then determined from the mean-velocity measurements (Section 2). In general, the values of  $\bar{U}$  varied slightly across the cross section. Turbulence intensities,  $(\bar{u}^2)^{0.5}/\bar{U}$ ,  $(\bar{v}^2)^{0.5}/\bar{U}$  and  $(\bar{w}^2)^{0.5}/\bar{U}$ , were then computed at each point in the grid, using the appropriate value of  $\bar{U}$  for that location as the normalizing velocity. The calculated intensities were then corrected very slightly so that they were defined using  $\bar{U}_{0.0}$ , the mean velocity at the centre of the test section.

#### 4.4 Analysis of Turbulence Intensities

Contours of  $(\bar{u}^2)^{0.5}/\bar{U}_{0.0}$  for  $\bar{U}_{\text{NOM}} = 30$  m/s at  $x_T = -2.0, -1.0, 0.0$  and  $+1.0$  m are shown in Figure 27. Corresponding plots for  $(\bar{v}^2)^{0.5}/\bar{U}_{0.0}$  and  $(\bar{w}^2)^{0.5}/\bar{U}_{0.0}$  are shown in Figures 28 and 29 respectively. Figures 30, 31 and 32 show contours for  $\bar{U}_{\text{NOM}} = 60$  m/s. Each of Figures 27 to 32 have been plotted to indicate how the contours change as the flow moves downstream, i.e.  $x_T$  changes. For the two values of  $\bar{U}_{\text{NOM}}$ , the contours of  $(\bar{u}^2)^{0.5}/\bar{U}_{0.0}$  at the four  $x_T$  locations (Figures 27 and 30) have the same general features, as far as it is possible to tell from the limited data at  $x_T = -2.0, -1.0$  and  $+1.0$  m, and likewise for the corresponding contours of  $(\bar{v}^2)^{0.5}/\bar{U}_{0.0}$  (Figures 28 and 31 respectively) and  $(\bar{w}^2)^{0.5}/\bar{U}_{0.0}$  (Figures 29 and 32 respectively). This indicates that regions of a given turbulence intensity are convected downstream with little lateral spreading and there does not appear to be any significant decay of the turbulence as the flow moves

downstream. The most important result is the value of  $(\overline{u^2})^{0.5}/\overline{U}_{0.0}$ , which is a measure of the turbulence level in the tunnel. In the central 50% of the cross-sectional area of the test section, for  $\overline{U}_{\text{NOM}} = 30$  and 60 m/s,  $(\overline{u^2})^{0.5}/\overline{U}_{0.0}$  is generally below about 0.4%, at  $x_T = -2.0, -1.0, 0.0$  and  $+1.0$  m, whereas corresponding values of  $(\overline{v^2})^{0.5}/\overline{U}_{0.0}$  and  $(\overline{w^2})^{0.5}/\overline{U}_{0.0}$  are generally below about 0.7% (Figures 27 to 32). The intensity levels for the longitudinal (u) component of the turbulence are about two thirds those for the lateral (v and w) components. This non-isotropic behaviour is common in wind-tunnel flows since the longitudinal vorticity component is reduced by a greater amount than the lateral components by the contraction (Reference 13). The strongest gradients of intensity occur on the starboard side of the test section where the intensities attain their maximum values.

#### 4.5 Errors in Measured Turbulence Intensities

There are errors in the measured turbulence intensities due to instrumentation errors and also due to the fact that the calibration of the hot wires may have drifted slightly between the start and finish of a set of measurements. Instantaneous velocities measured by the hot wires were accurate to within about  $\pm 1.5\%$  due to the drifting of the calibration of the hot wires. It was found that, for  $\overline{U}_{\text{NOM}} = 30$  m/s, errors in  $(\overline{u^2})^{0.5}/\overline{U}_{0.0}$ ,  $(\overline{v^2})^{0.5}/\overline{U}_{0.0}$  and  $(\overline{w^2})^{0.5}/\overline{U}_{0.0}$  were about  $\pm 0.011$ ,  $\pm 0.018$  and  $\pm 0.018$  percentage points respectively. For example, if the measured value of  $(\overline{u^2})^{0.5}/\overline{U}_{0.0}$  at 30 m/s was 0.5% then its value could range from 0.511% to 0.489%. Corresponding errors for  $\overline{U}_{\text{NOM}} = 60$  m/s were about  $\pm 0.007$ ,  $\pm 0.013$  and  $\pm 0.013$  percentage points respectively.

## 5. Spectral Measurements

### 5.1 Test Schedule

Spectra for the u-, v- and w-components of the turbulence were measured in the test section at the 5 grid points shown in Figure 26 (a) for  $x_T = 0.0$  m as well as at the 5 grid points shown in Figure 26 (b) for  $x_T = -2.0, -1.0$  and  $+1.0$  m. Spectra were measured for  $\overline{U}_{\text{NOM}} = 30$  and 60 m/s.

### 5.2 Procedure Used to Measure Spectra

Spectra were measured using the hot-wire anemometer system and the modified cross-tunnel rake that were used for the intensity measurements. The spectral and intensity experimental programs were combined so that data for a given spectrum was generally measured immediately before or immediately after data for the corresponding intensity.

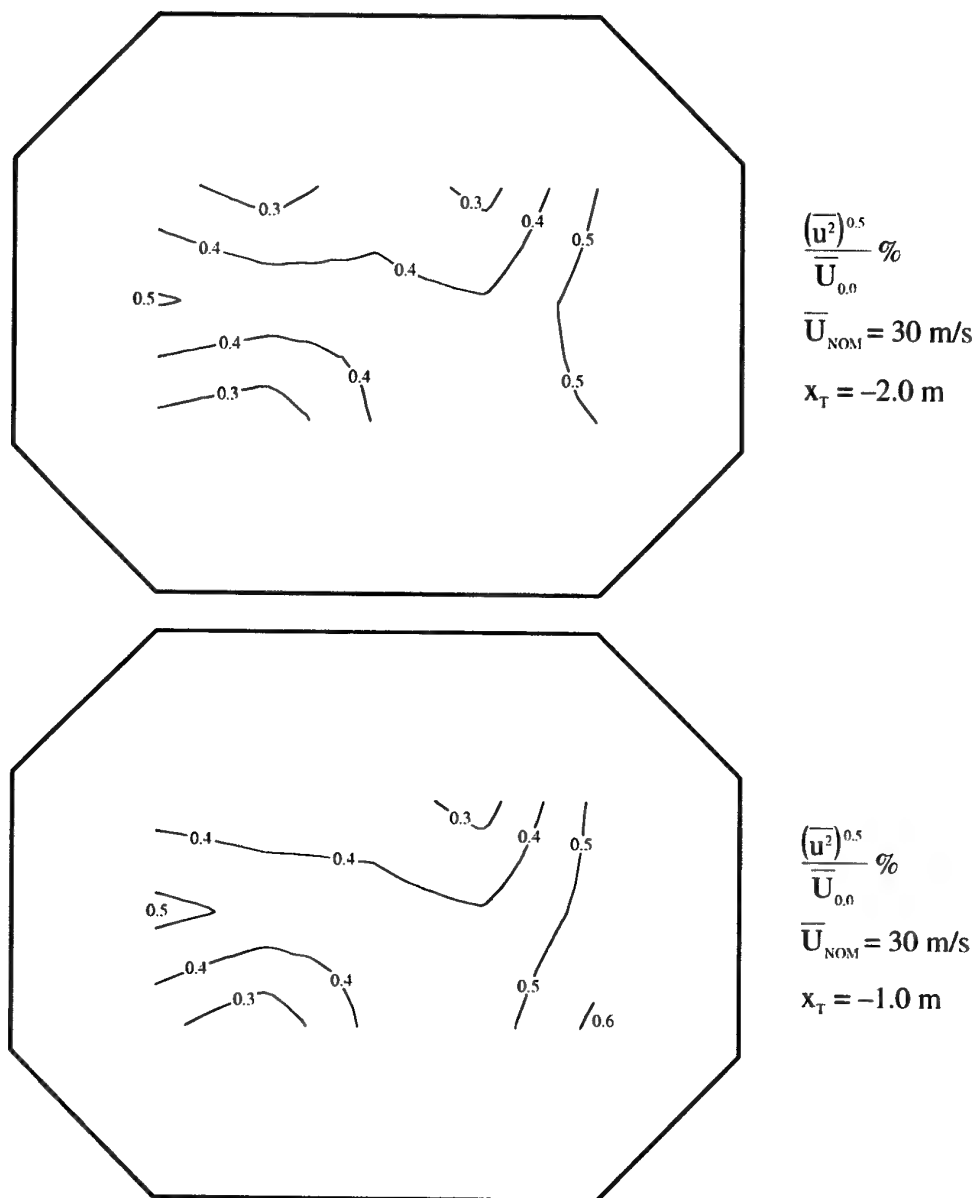


Figure 27. Contours of u-component intensity for  $\overline{U}_{\text{NOM}} = 30 \text{ m/s}$  for  $x_T = -2.0, -1.0, 0.0$  and  $1.0 \text{ m}$ .

(a)  $x_T = -2.0$  and  $-1.0 \text{ m}$ .

The flow is out of the page.

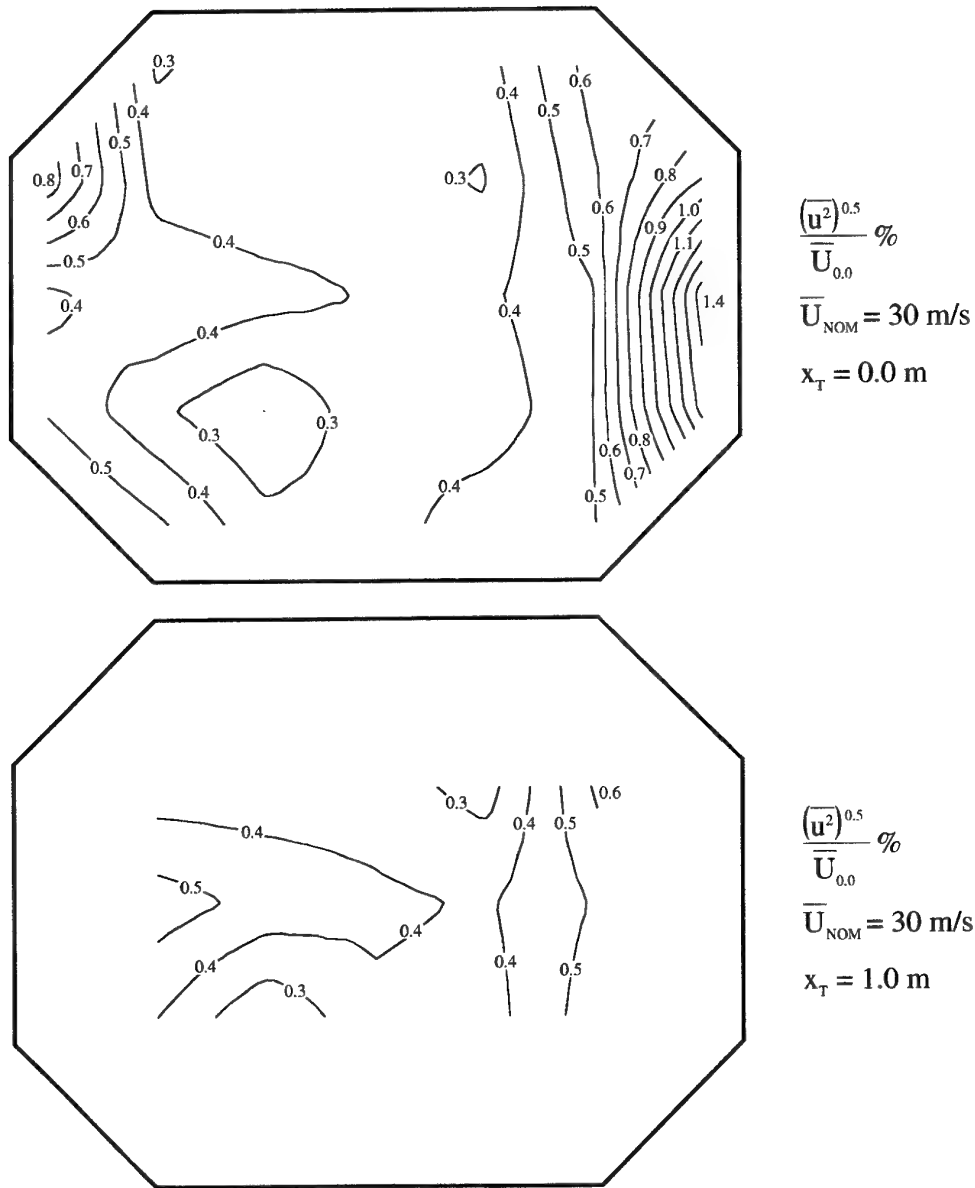


Figure 27 cont'd. Contours of u-component intensity for  $\overline{U}_{\text{NOM}} = 30 \text{ m/s}$  for  $x_T = -2.0, -1.0, 0.0$  and  $1.0 \text{ m}$ .

(b)  $x_T = 0.0$  and  $1.0 \text{ m}$ .

The flow is out of the page.

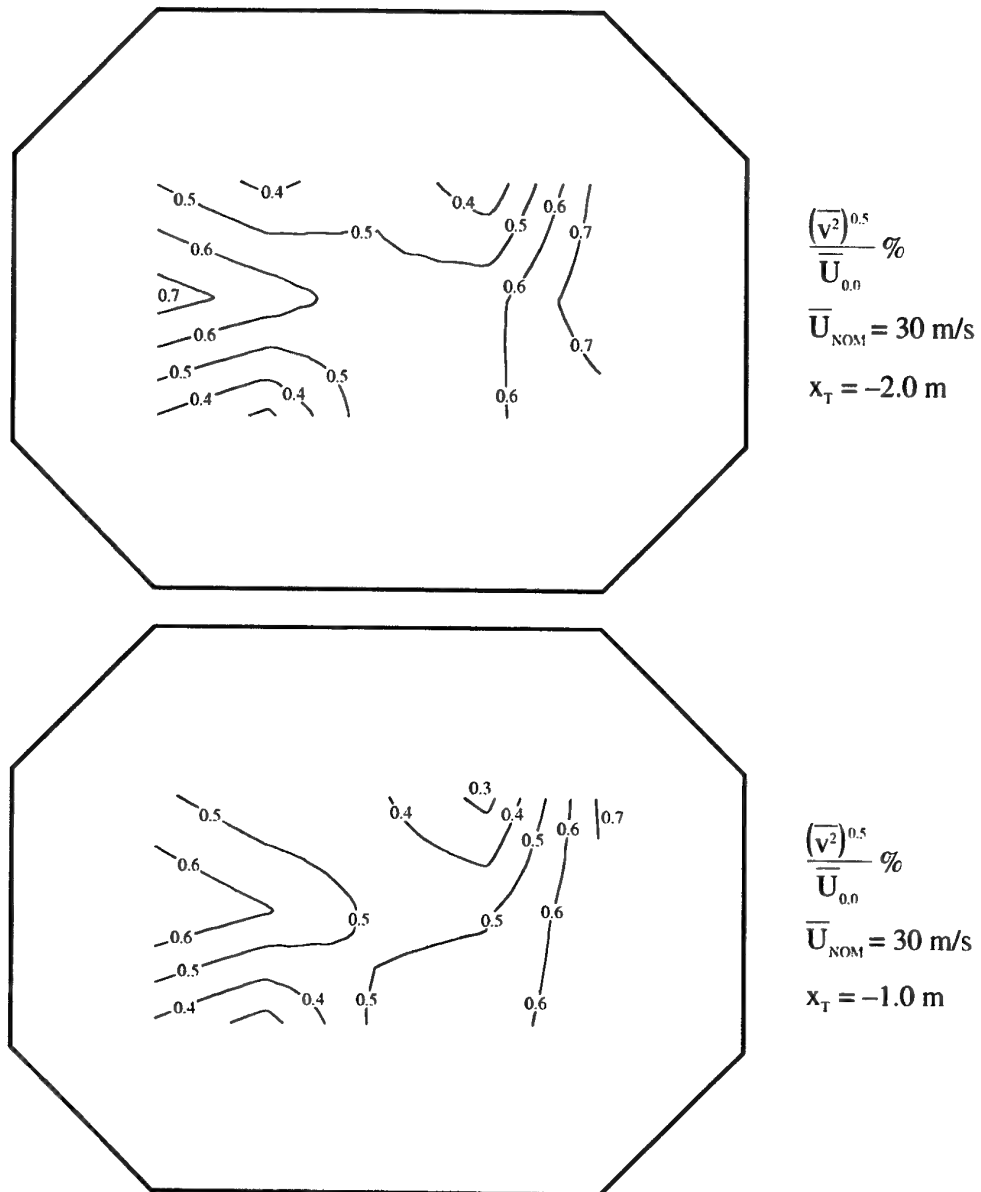


Figure 28. Contours of v-component intensity for  $\overline{U}_{NOM} = 30$  m/s for  $x_T = -2.0, -1.0, 0.0$  and  $1.0$  m.

(a)  $x_T = -2.0$  and  $-1.0$  m.

The flow is out of the page.

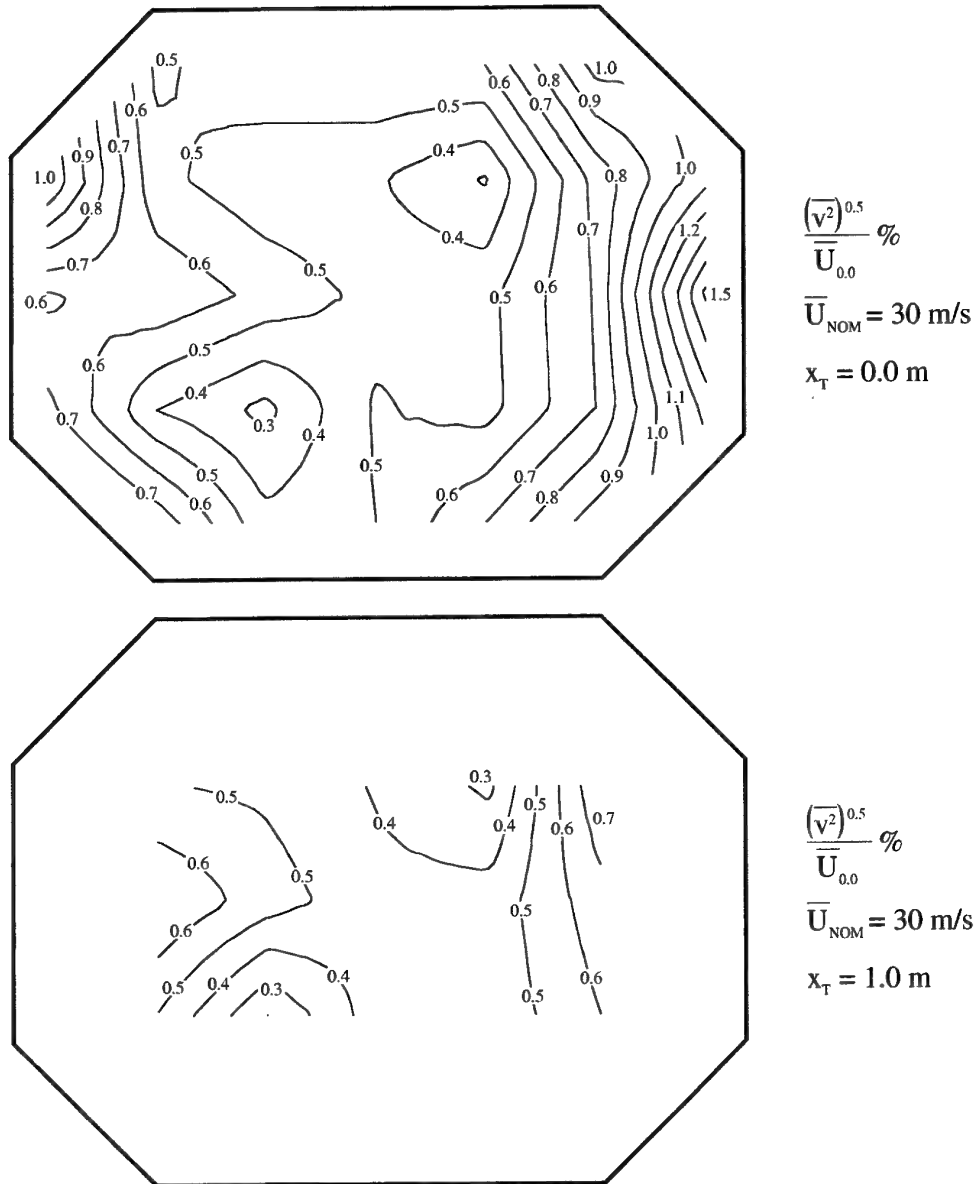


Figure 28 cont'd. Contours of  $v$  component intensity for  $\overline{U}_{\text{NOM}} = 30 \text{ m/s}$  for  $x_T = -2.0, -1.0, 0.0$  and  $1.0 \text{ m}$ .

(b)  $x_T = 0.0$  and  $1.0 \text{ m}$ .

The flow is out of the page.



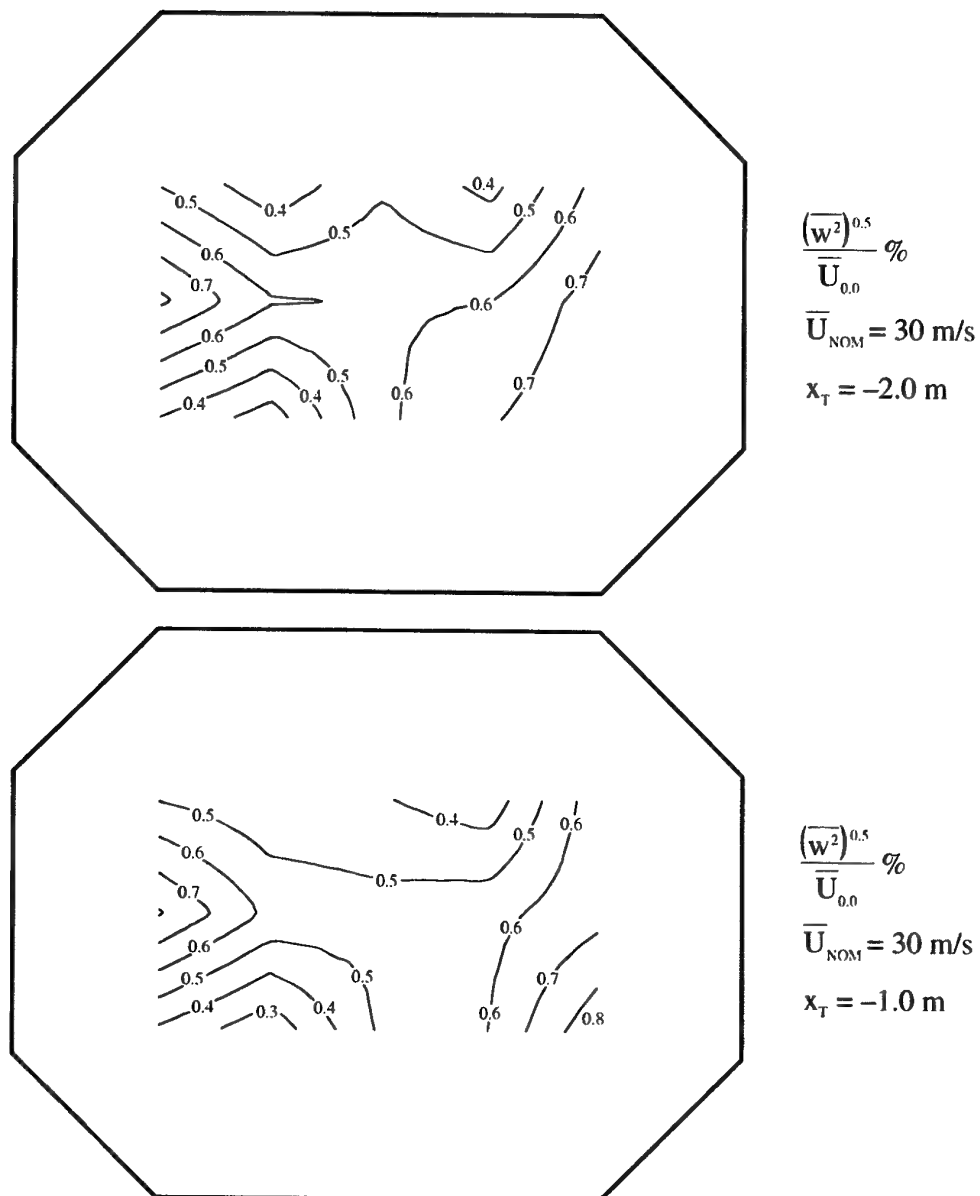


Figure 29. Contours of w component intensity for  $\overline{U}_{NOM} = 30 \text{ m/s}$  for  $x_T = -2.0, -1.0, 0.0$  and  $1.0 \text{ m}$ .

(a)  $x_T = -2.0$  and  $-1.0 \text{ m}$ .

The flow is out of the page.

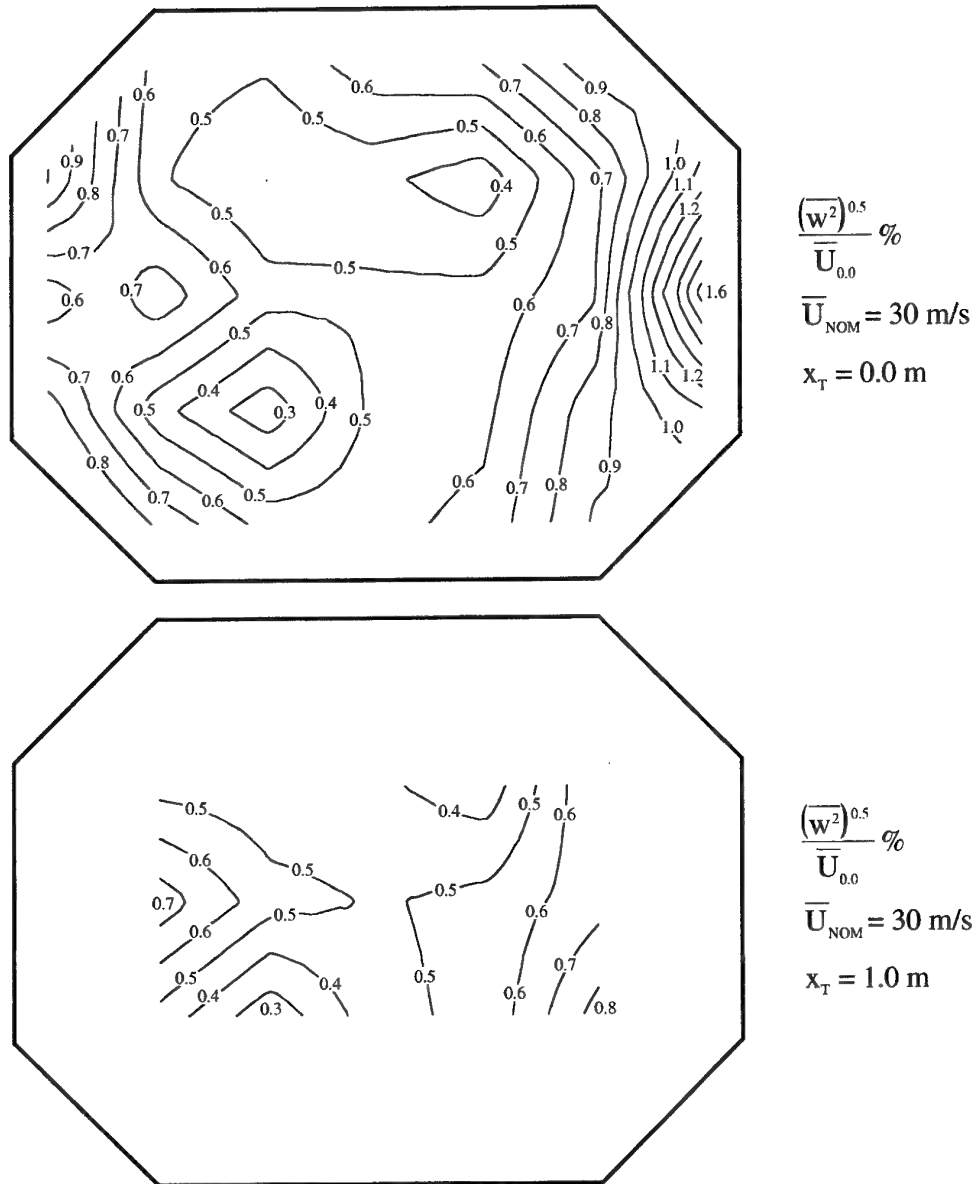


Figure 29 cont'd. Contours of w-component intensity for  $\overline{U}_{\text{NOM}} = 30 \text{ m/s}$  for  $x_T = -2.0, -1.0, 0.0$  and  $1.0 \text{ m}$ .

(b)  $x_T = 0.0$  and  $1.0 \text{ m}$ .

The flow is out of the page.

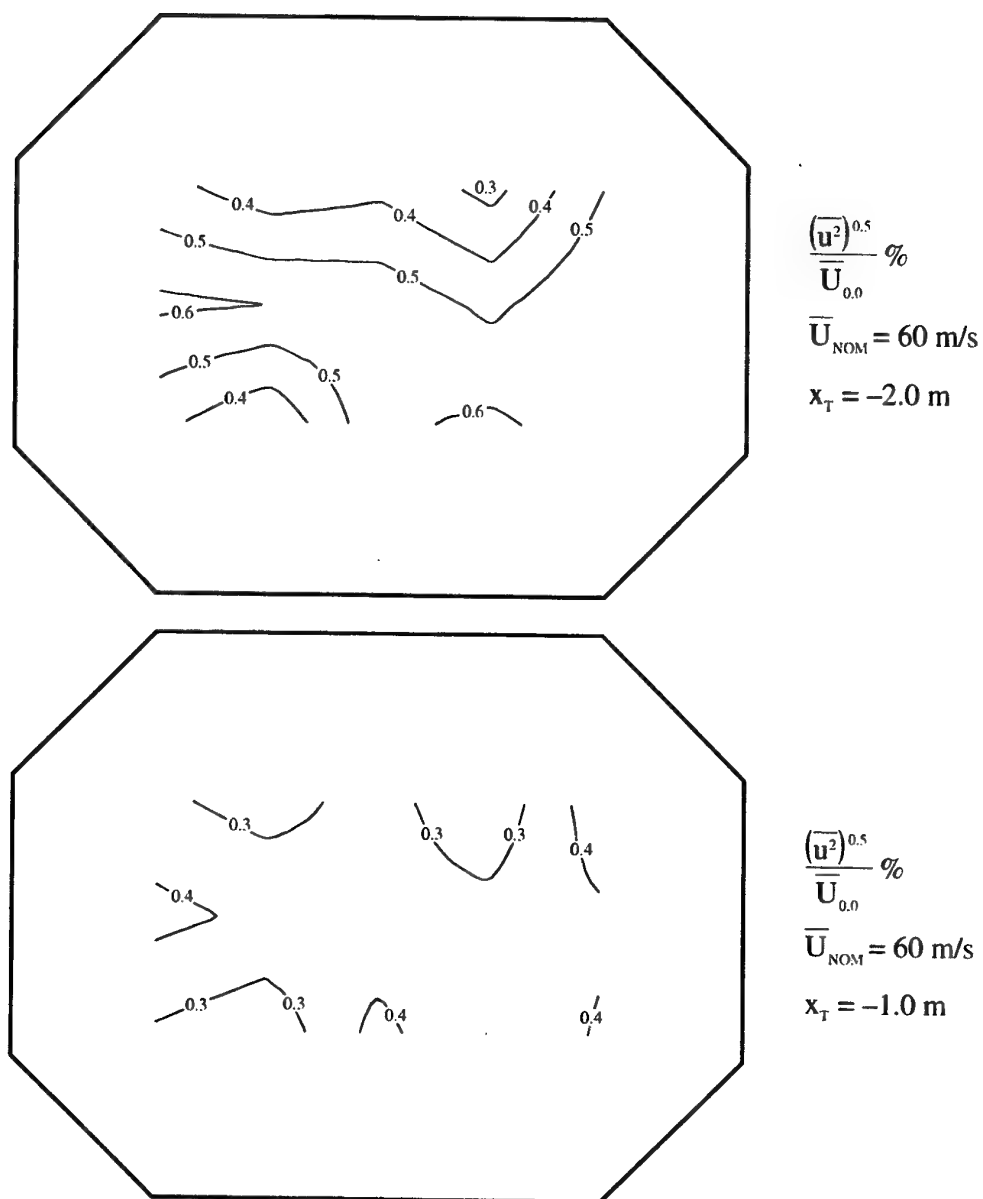


Figure 30. Contours of u-component intensity for  $\overline{U}_{NOM} = 60$  m/s for  $x_T = -2.0, -1.0, 0.0$  and  $1.0$  m.

(a)  $x_T = -2.0$  and  $-1.0$  m.

The flow is out of the page.

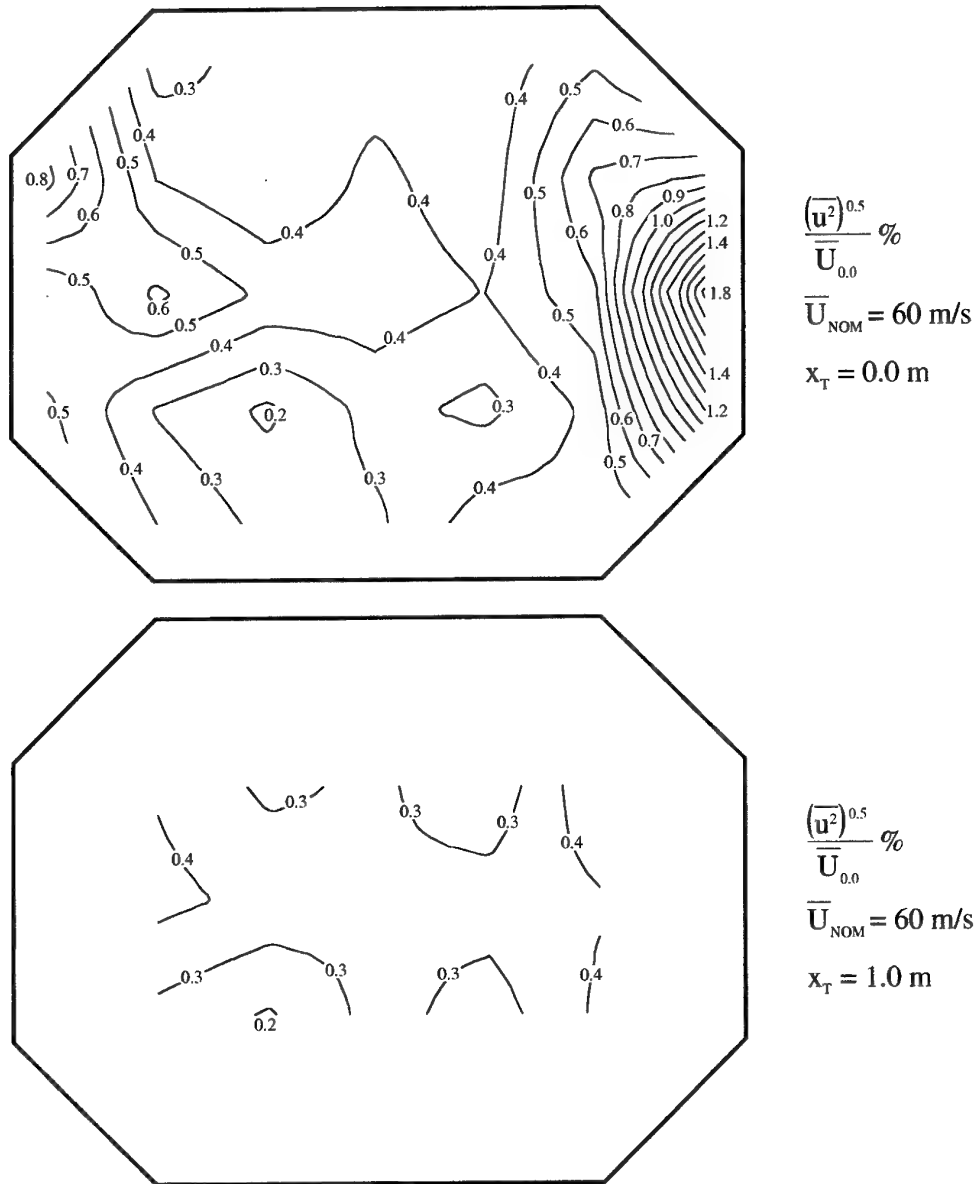


Figure 30 cont'd. Contours of u-component intensity for  $\overline{U}_{\text{NOM}} = 60$  m/s for  $x_T = -2.0, -1.0, 0.0$  and  $1.0$  m.

(b)  $x_T = 0.0$  and  $1.0$  m.

The flow is out of the page.

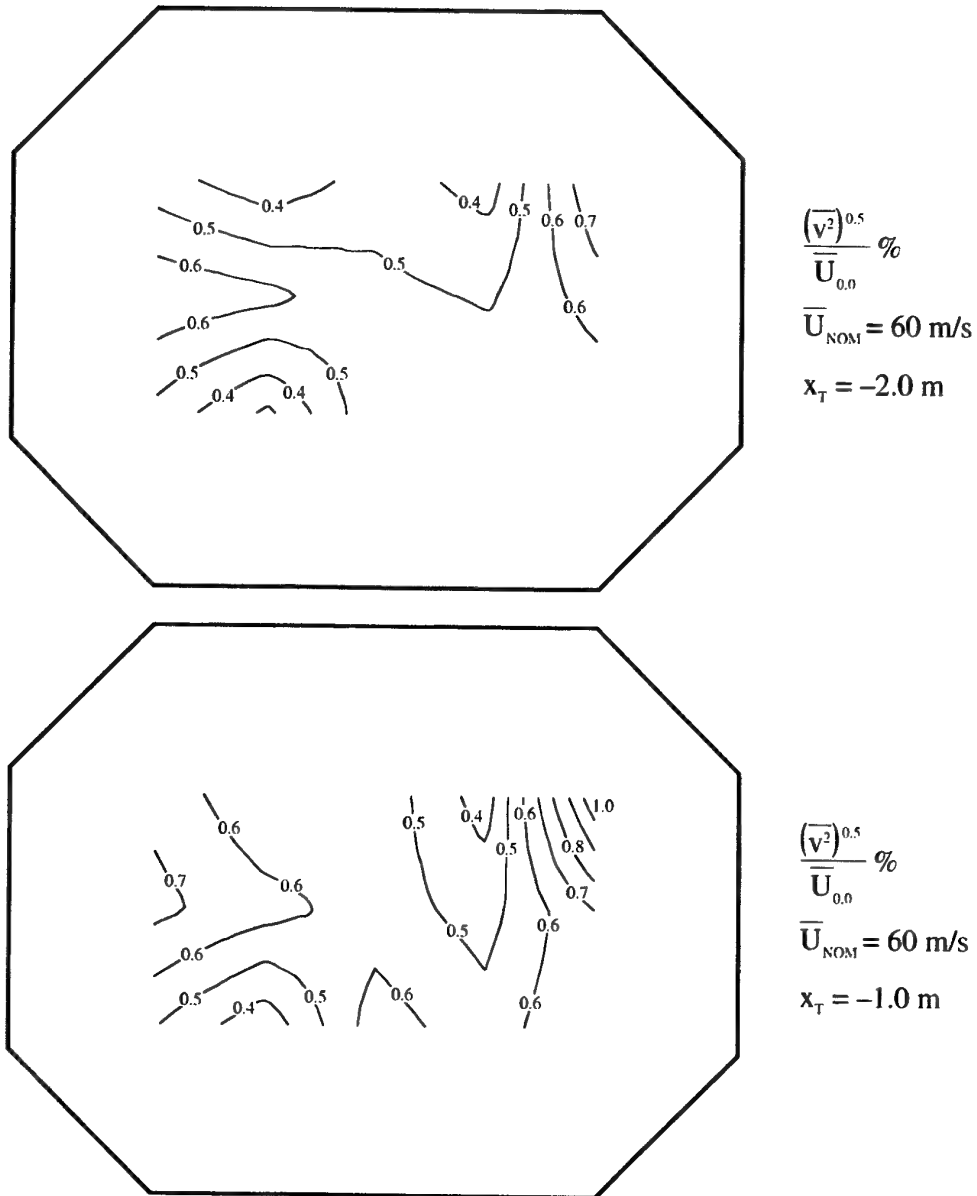


Figure 31. Contours of v-component intensity for  $\overline{U}_{NOM} = 60$  m/s for  $x_T = -2.0, -1.0, 0.0$  and  $1.0$  m.

(a)  $x_T = -2.0$  and  $-1.0$  m.

The flow is out of the page.

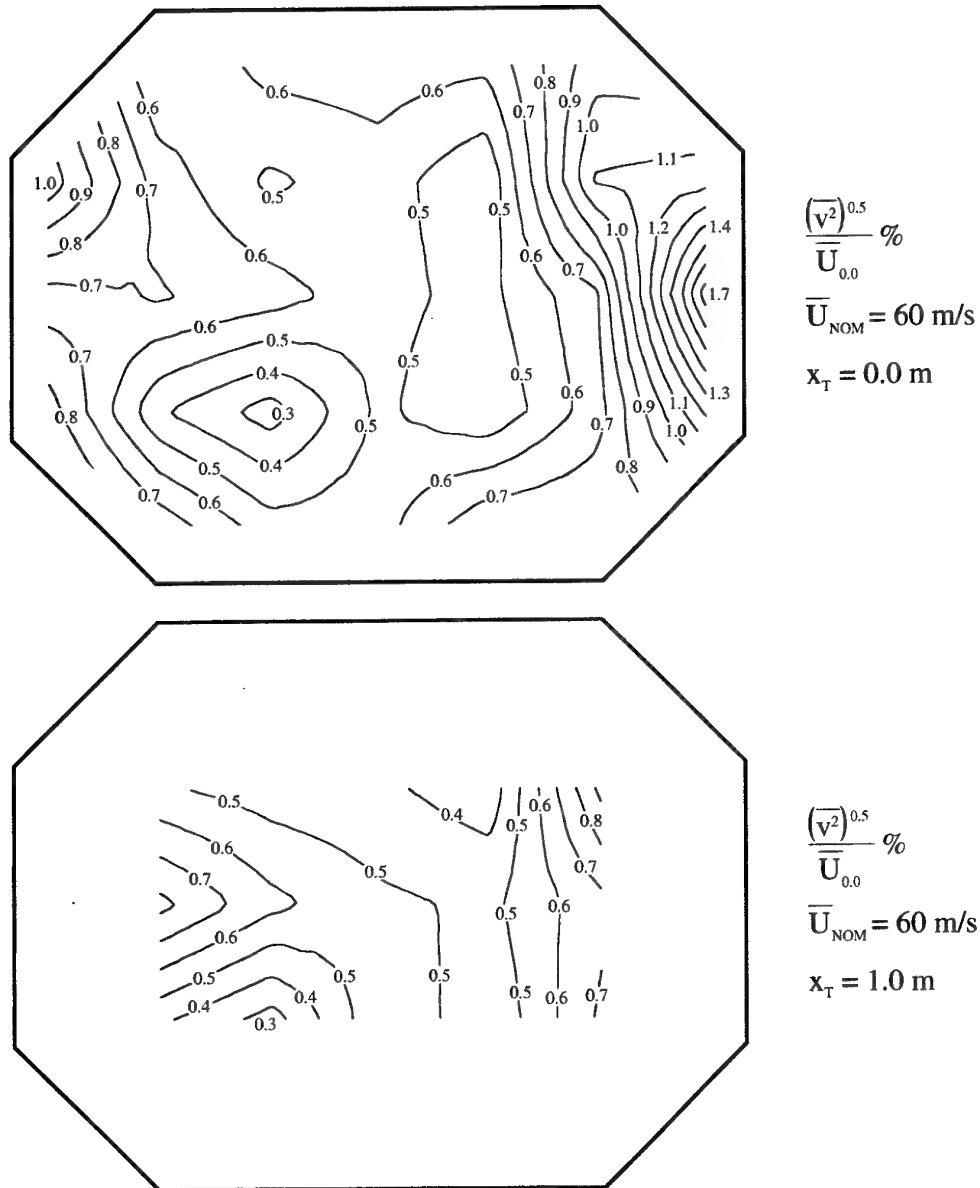


Figure 31 cont'd. Contours of v-component intensity for  $\overline{U}_{\text{NOM}} = 60 \text{ m/s}$  for  $x_T = -2.0, -1.0, 0.0$  and  $1.0 \text{ m}$ .

(b)  $x_T = 0.0$  and  $1.0 \text{ m}$ .

The flow is out of the page.

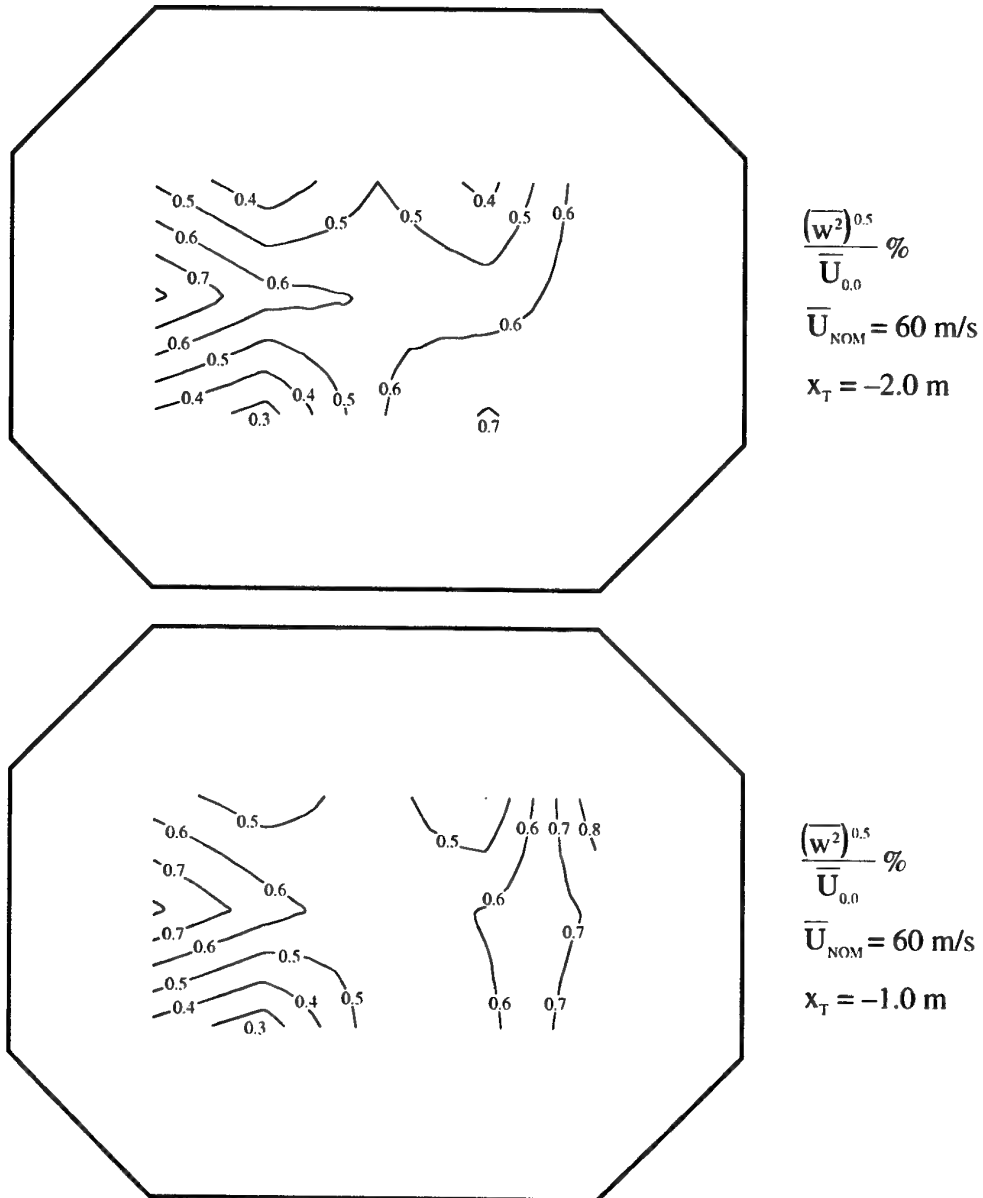


Figure 32. Contours of w-component intensity for  $\overline{U}_{NOM} = 60 \text{ m/s}$  for  $x_T = -2.0, -1.0, 0.0$  and  $1.0 \text{ m}$ .

(a)  $x_T = -2.0$  and  $-1.0 \text{ m}$ .

The flow is out of the page.

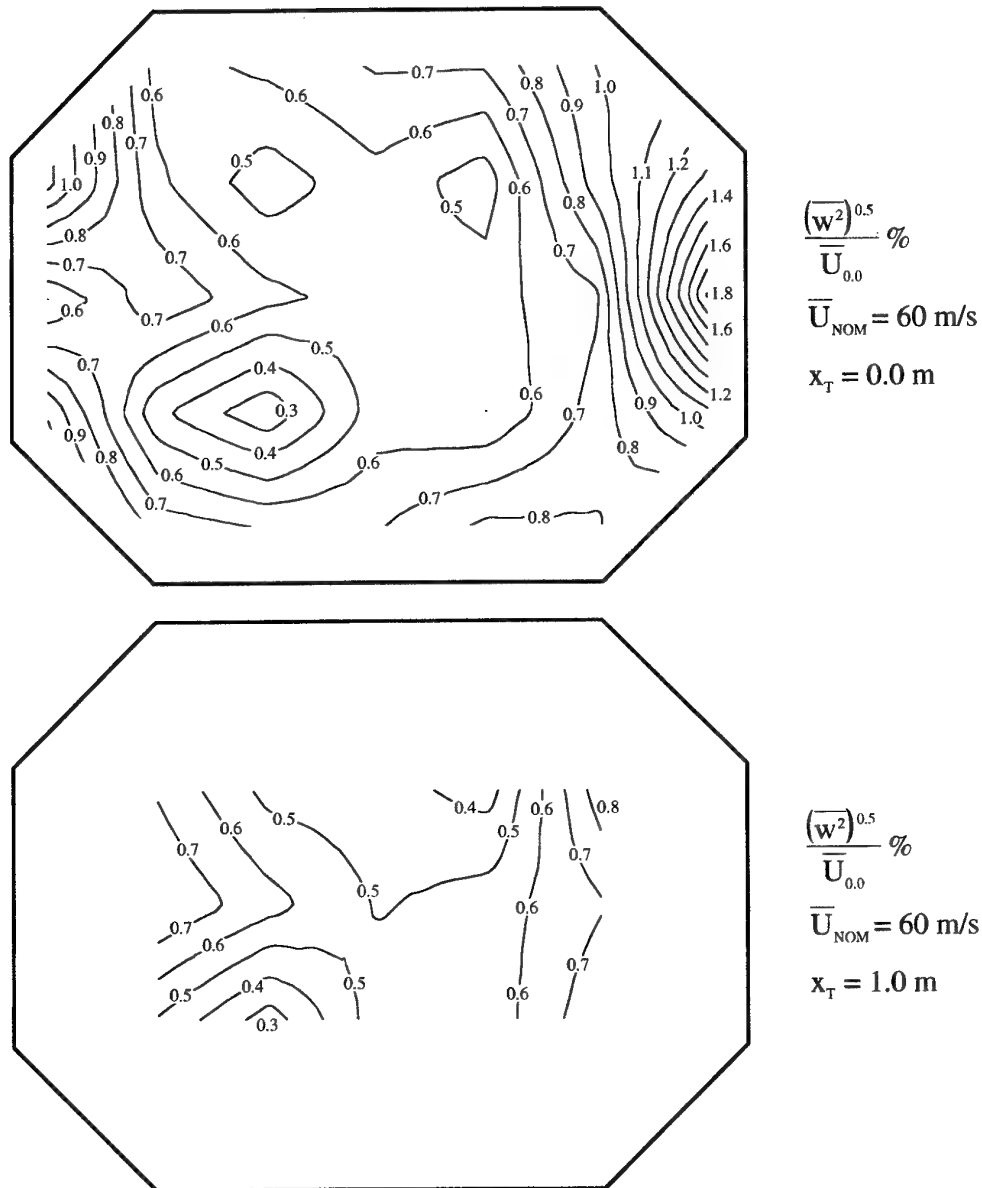


Figure 32 cont'd. Contours of w-component intensity for  $\overline{U}_{\text{NOM}} = 60 \text{ m/s}$  for  $x_T = -2.0, -1.0, 0.0$  and  $1.0 \text{ m}$ .

(b)  $x_T = 0.0$  and  $1.0 \text{ m}$ .

The flow is out of the page.



When measuring spectra, each hot-wire voltage was sampled 65536 times (i.e.  $2^{16}$  times –see below) at a sampling frequency of 20 kHz and the low-pass filters were set at 10 kHz. This filter setting was used since velocity fluctuations above 10 kHz in the free-stream have negligible energy (Reference 14) and the setting corresponds to the maximum frequency that can be resolved when sampling at 20 kHz, due to aliasing. Spectra were obtained by processing hot-wire voltages, rather than by processing velocities determined from voltages, as for the intensities, and it was not necessary to know hot-wire sensitivities. Power spectral densities,  $S_u$ ,  $S_v$  and  $S_w$ , were computed from the voltages using a Fast-Fourier-Transform (FFT) algorithm (where the number of data points required is a power of 2). For each spectrum, power spectral densities were computed using the 65536 ( $= 2^{16}$ ) consecutively sampled voltages, without any averaging. For a sampling frequency of 20 kHz, the frequencies at which power spectral densities were computed ranged from 0.3052 Hz to 10 kHz in increments of 0.3052 Hz, i.e.  $20000/65536$  Hz, corresponding to  $32768$  ( $= 2^{15}$ ) values of frequency.

Whenever a fluctuating velocity waveform is represented by a finite number of points, then the mean velocities near the start and finish of the finite sample can be significantly different. When computing spectra from these waveforms, this behaviour can be interpreted as a low-frequency phenomenon, coupled with high frequency effects due to the step change between the beginning and end of the sample, and it can cause an increase in spectral densities at low frequencies. One way of correcting for this behaviour is to apply a Blackman window to the data (Reference 15). A Blackman window adjusts velocities (or any given measurand) so that their values at the start and finish of the chosen range are gradually diminished, becoming zero at the extremes. The application of a Blackman window also smooths the spectra. This is done by first smoothing with a Hanning window and then further smoothing with weights of 0.16, 0.68 and 0.16 (Reference 15). All spectra given in this report have been smoothed with a Blackman window and the spectra have been normalized by dividing by the variance.

### 5.3 Analysis of Spectra

Spectra corresponding to conventional wind-tunnel-generated turbulence should be relatively smooth, but if the turbulent flow contains eddies of dominant frequencies, such as vortices shed by the fan, then these will produce harmonics or spikes on the spectra. If there is any significant “noise” on a fluctuating turbulent signal, caused by say electrical interference or probe vibration, then this will also cause spikes. As a result of this noise, calculated turbulence intensities will be higher than actual intensities existing in the tunnel. By noting the frequency at which the spikes occur, it is often possible to identify the source of the irregularities, e.g. the frequency of the spikes may correspond with the frequency of the electrical mains supply or the frequency of rotation of the fan. A knowledge of the causes of the irregularities is valuable when trying to eradicate them.

Power spectral densities,  $S_u$ , plotted against frequency,  $f$ , are shown in Figure 33 at the grid points shown in Figure 26 for  $\bar{U}_{\text{NOM}} = 30$  m/s for  $x_T = -2.0, -1.0, 0.0$ , and  $+1.0$  m. Corresponding spectra for  $S_v$  and  $S_w$  are shown in Figures 34 and 35 respectively. The spectra in each of Figures 33 to 35 are plotted together without being identified individually. Figures 36 to 38 show spectra for  $\bar{U}_{\text{NOM}} = 60$  m/s. The spectra cover the central region of the flow in the test section. The spectra show that there are no major irregularities in the turbulence signals over the frequency range 0.3 Hz to 10 kHz. For all of the u-component spectra, there are small but consistent spikes at about 150 Hz, and the reason for these is uncertain. The spikes are not associated with the frequency of the fan rotation since they are present at about 150 Hz for both  $\bar{U}_{\text{NOM}} = 30$  and 60 m/s and they do not appear to be caused by electrical interference from mains supply (50 Hz). Similar spikes were found on spectra measured in the LSWT prior to the tunnel being modified in 1996, as shown in Reference 3. However, it was shown that this type of irregularity did not significantly affect measured values of turbulence intensities. There are also some isolated spikes at the high-frequency ends of some spectra.

## 6. Comparison of Flow Quality in the Original and the Extended Test Sections of the LSWT

As indicated in Section 1, the LSWT was modified in 1996 by extending the length of the test section and installing a new contraction (see Appendix A for details of the modifications to the tunnel). This was done to enable longer models to be tested in the tunnel and hopefully to obtain some improvement in the quality of the flow in the test section. The flows in the original and the extended test sections are now compared to see how the modifications to the tunnel have affected the flow. Plots are given for mean velocities, flow angles, turbulence intensities and spectra for  $x_T = 0.0$  m in the original (see Reference 3) and the extended test sections. Reference is made to Table 1, which lists how mean velocities, flow angles and turbulence intensities vary in the central 50% of the cross-sectional area of the test section between  $x_T = -1.0$  and  $+1.0$  m for the original and the extended test sections. Further comparisons can be made as required by comparing other results in this report with corresponding results in Reference 3.

### 6.1 Mean Velocities

Contours of  $(\bar{U} - \bar{U}_{0.0})/\bar{U}_{0.0}$  for  $x_T = 0.0$  m for  $\bar{U}_{\text{NOM}} = 30$  and 45 m/s for the extended and the original test section are shown in Figure 39. Corresponding contours for  $\bar{U}_{\text{NOM}} = 60$  and 75 m/s are shown in Figure 40. The distributions of corresponding mean velocities in the extended and the original test sections are very similar. Table 1 shows that the range of variation of  $(\bar{U} - \bar{U}_{0.0})/\bar{U}_{0.0}$  between  $x_T = -1.0$  and  $+1.0$  m is generally slightly less in the extended test section over the velocity range. Overall, the modifications to the tunnel have only very slightly improved the mean velocities.

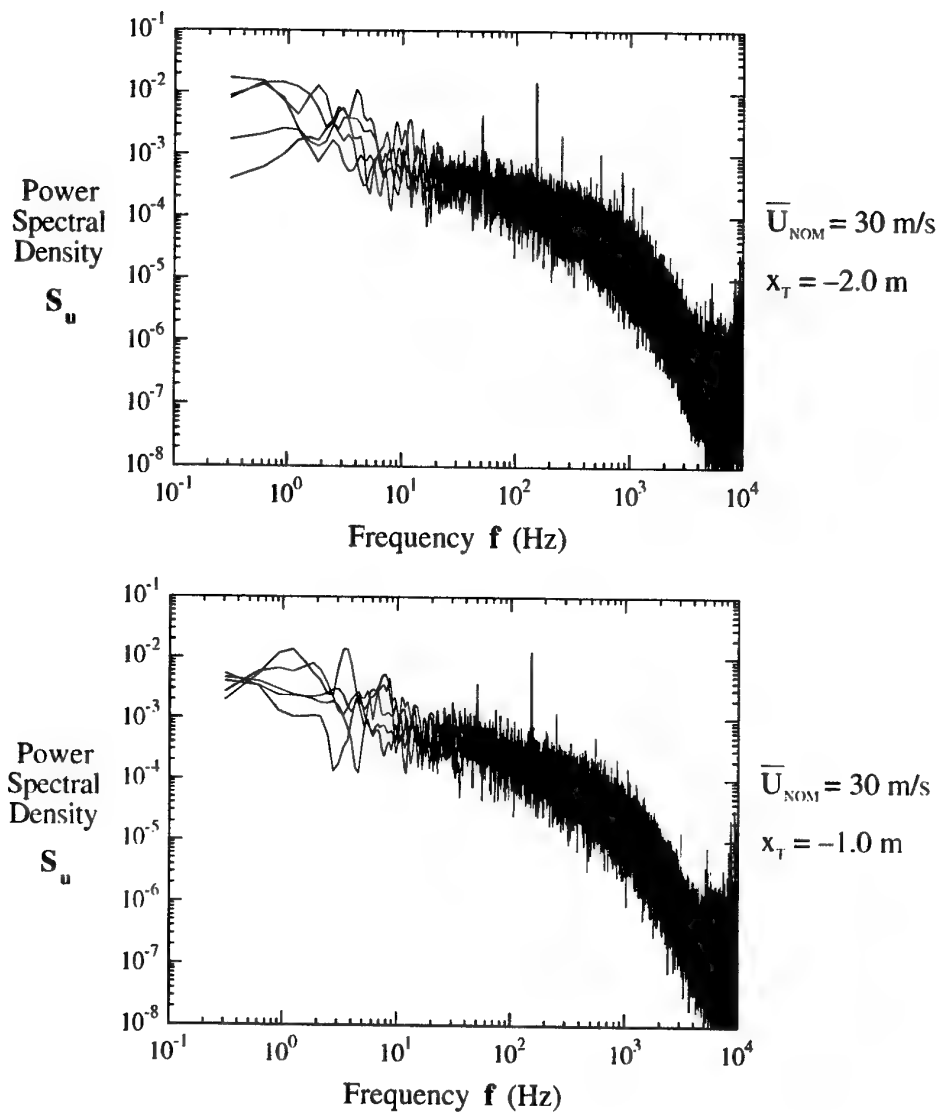


Figure 33. Spectra for the  $u$  component of the turbulence for  $\bar{U}_{NOM} = 30$  m/s for  $x_T = -2.0, -1.0, 0.0$  and  $1.0$  m for  $y_T$  and  $z_T$  locations denoted by filled circles in Figure 26.  
(a)  $x_T = -2.0$  and  $-1.0$  m.

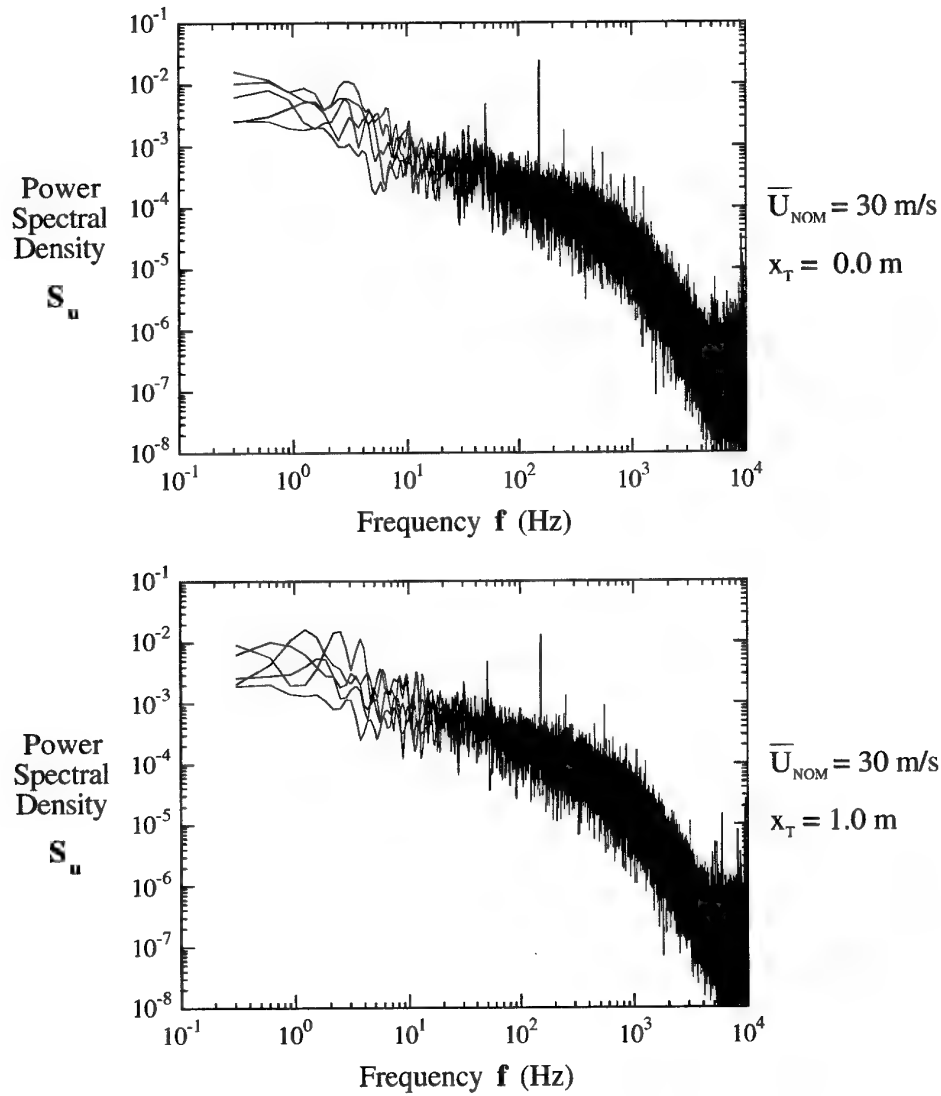


Figure 33 cont'd. Spectra for the  $u$  component of the turbulence for  $\overline{U}_{\text{NOM}} = 30 \text{ m/s}$  for  $x_T = -2.0, -1.0, 0.0$  and  $1.0 \text{ m}$  for  $y_T$  and  $z_T$  locations denoted by filled circles in Figure 26.

(b)  $x_T = 0.0$  and  $1.0 \text{ m}$ .

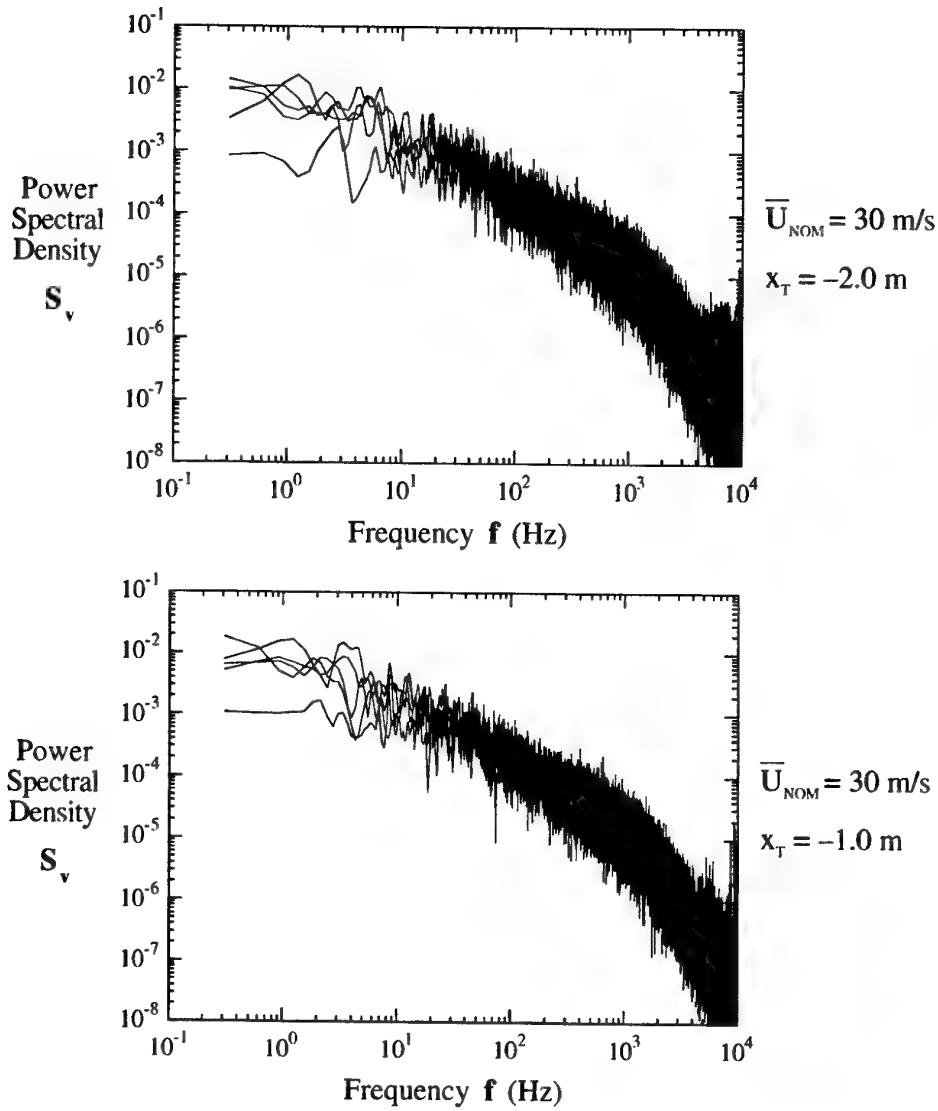


Figure 34. Spectra for the  $v$  component of the turbulence for  $\bar{U}_{NOM} = 30$  m/s for  $x_T = -2.0, -1.0, 0.0$  and  $1.0$  m for  $y_T$  and  $z_T$  locations denoted by filled circles in Figure 26.  
(a)  $x_T = -2.0$  and  $-1.0$  m.

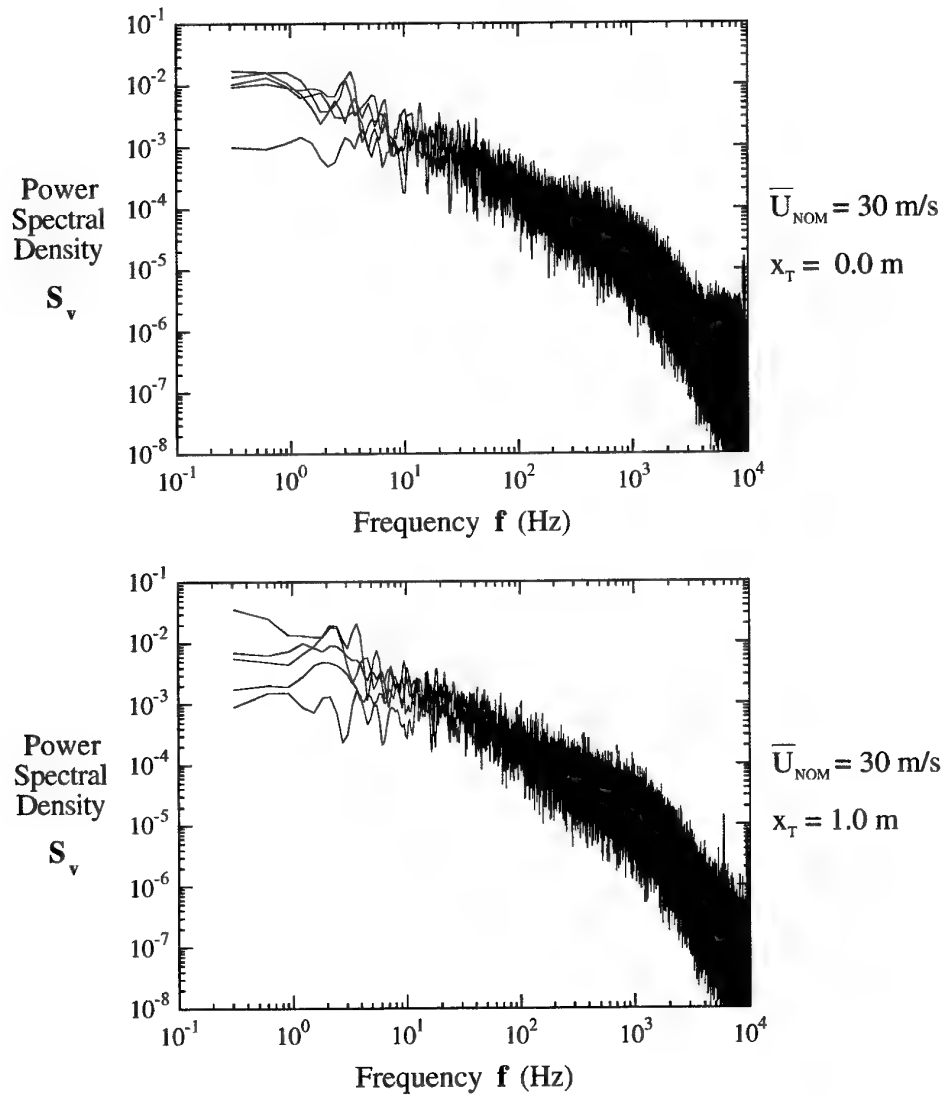


Figure 34 cont'd. Spectra for the  $v$  component of the turbulence for  $\overline{U}_{\text{NOM}} = 30 \text{ m/s}$  for  $x_T = -2.0, -1.0, 0.0$  and  $1.0 \text{ m}$  for  $y_T$  and  $z_T$  locations denoted by filled circles in Figure 26.

(b)  $x_T = 0.0$  and  $1.0 \text{ m}$ .

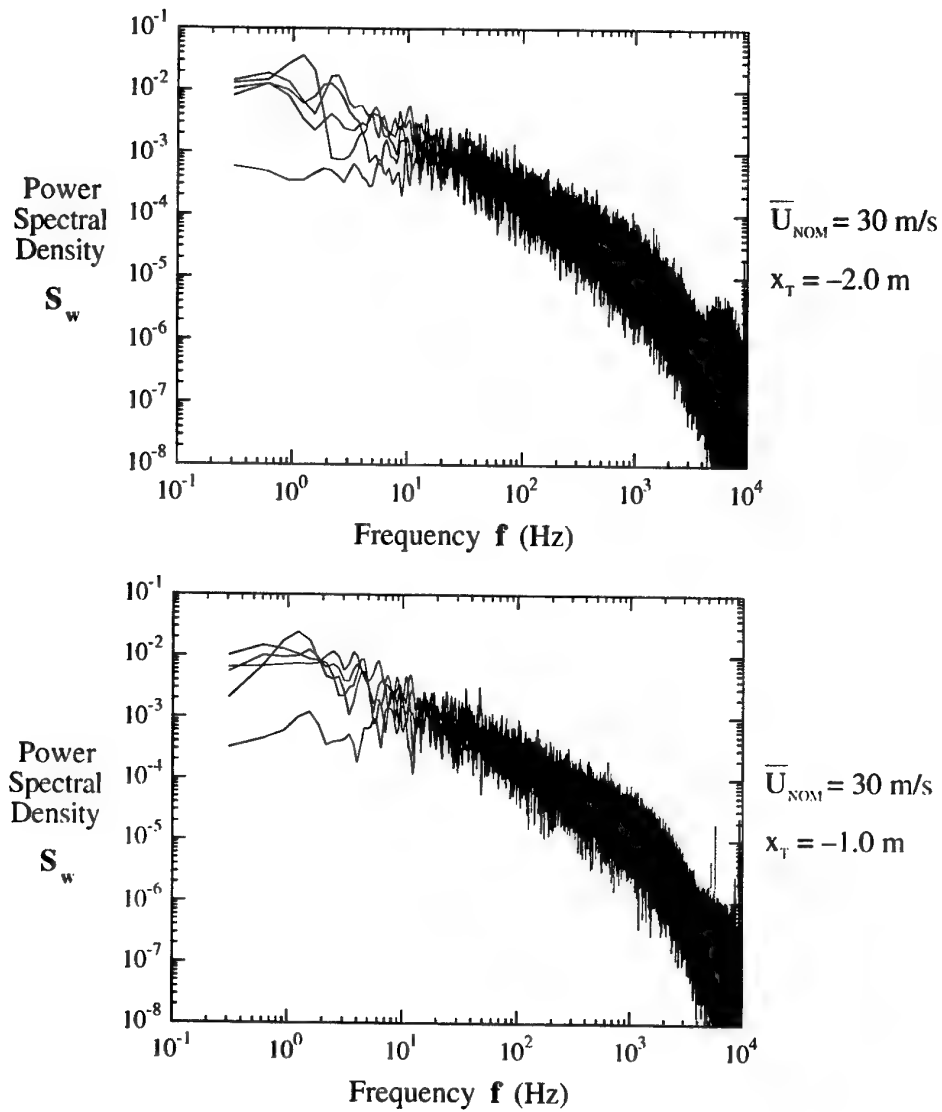


Figure 35. Spectra for the  $w$  component of the turbulence for  $\bar{U}_{\text{NOM}} = 30$  m/s for  $x_T = -2.0, -1.0, 0.0$  and  $1.0$  m for  $y_T$  and  $z_T$  locations denoted by filled circles in Figure 26.

(a)  $x_T = -2.0$  and  $-1.0$  m.

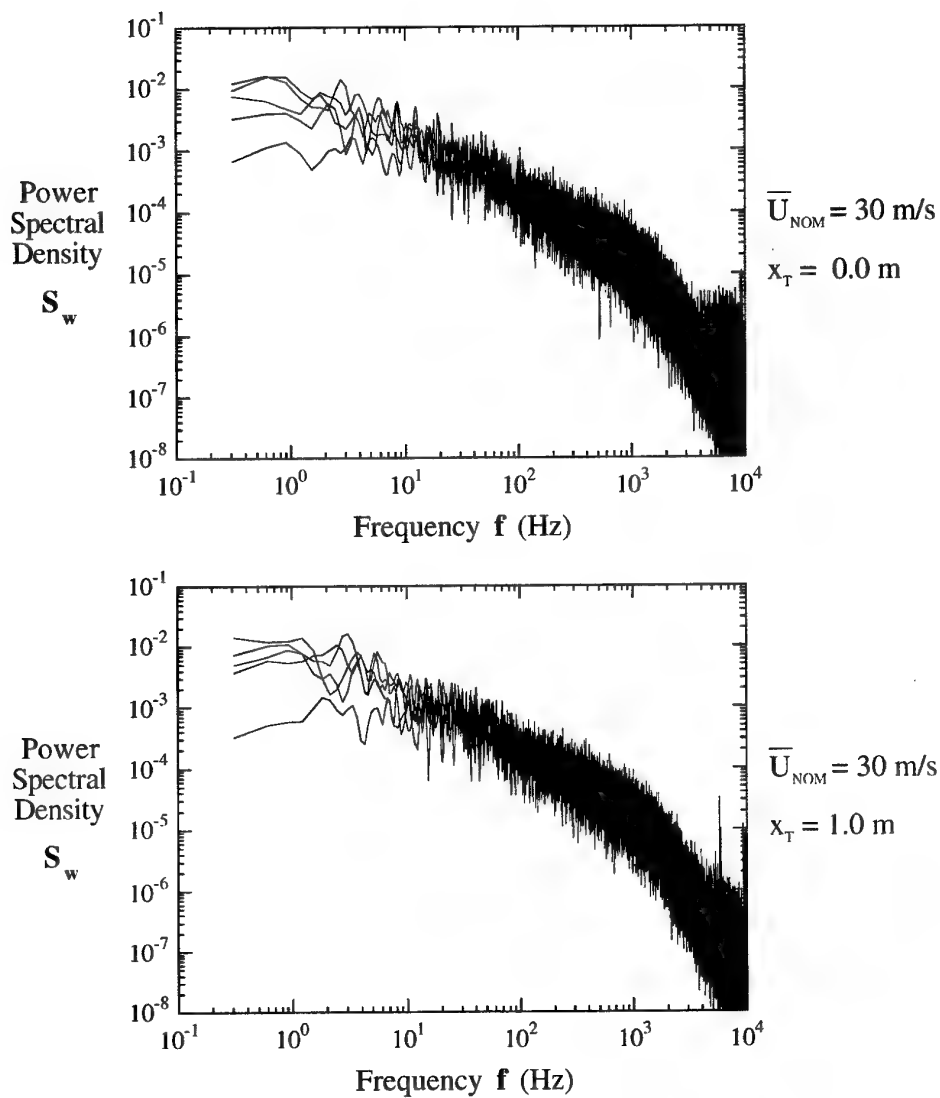


Figure 35 cont'd. Spectra for the  $w$  component of the turbulence for  $\bar{U}_{\text{NOM}} = 30 \text{ m/s}$  for  $x_T = -2.0, -1.0, 0.0$  and  $1.0 \text{ m}$  for  $y_T$  and  $z_T$  locations denoted by filled circles in Figure 26.

(b)  $x_T = 0.0$  and  $1.0 \text{ m}$ .



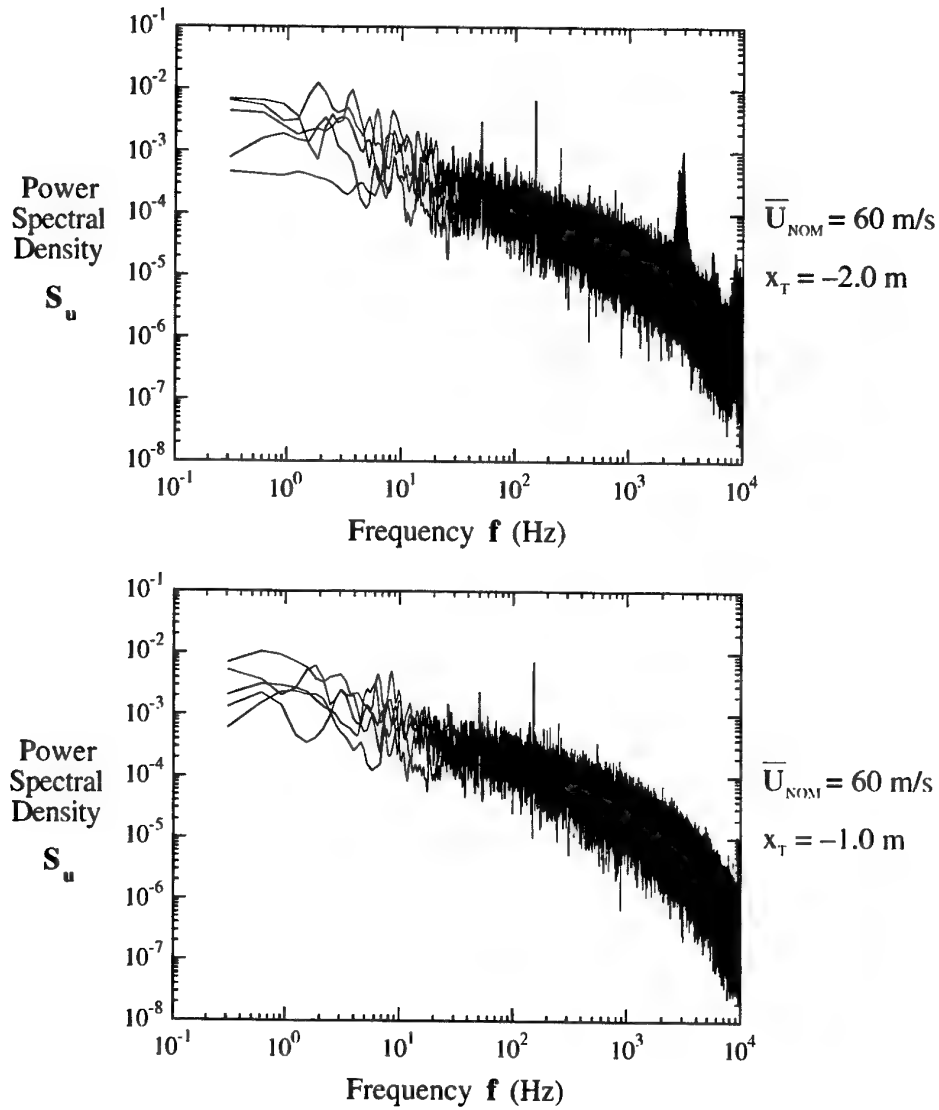


Figure 36. Spectra for the  $u$  component of the turbulence for  $\bar{U}_{NOM} = 60$  m/s for  $x_T = -2.0, -1.0, 0.0$  and  $1.0$  m for  $y_T$  and  $z_T$  locations denoted by filled circles in Figure 26.

(a)  $x_T = -2.0$  and  $-1.0$  m.

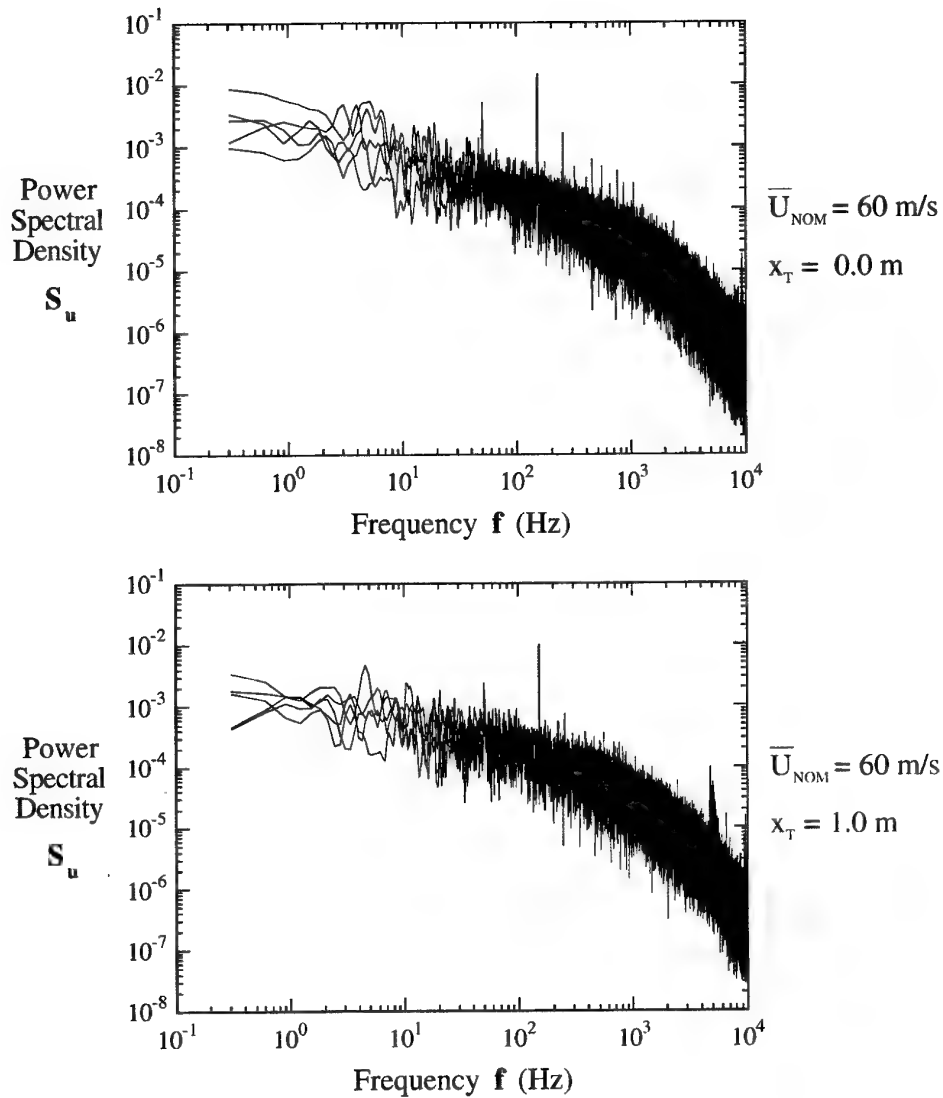


Figure 36 cont'd. Spectra for the u component of the turbulence for  $\bar{U}_{\text{NOM}} = 60 \text{ m/s}$  for  $x_T = -2.0, -1.0, 0.0$  and  $1.0 \text{ m}$  for  $y_T$  and  $z_T$  locations denoted by filled circles in Figure 26.

(b)  $x_T = 0.0$  and  $1.0 \text{ m}$ .

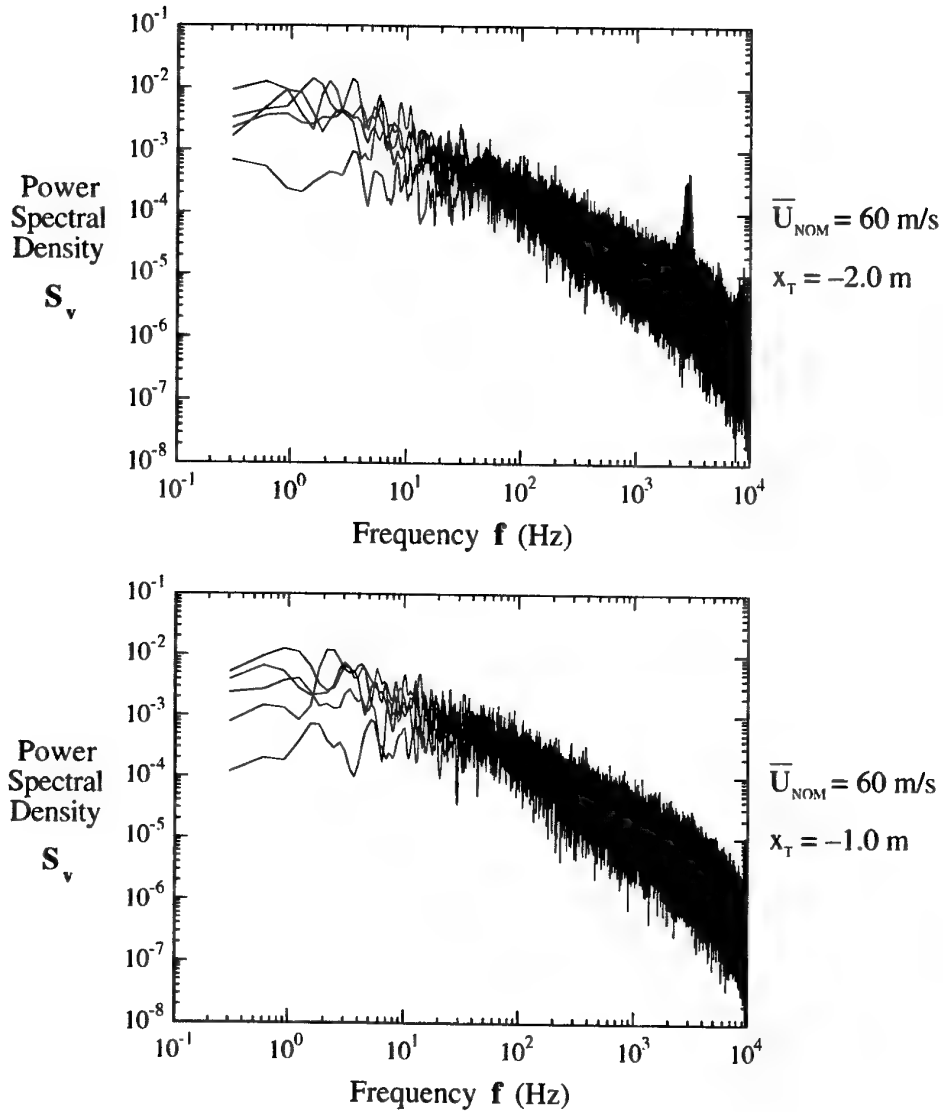


Figure 37. Spectra for the  $v$  component of the turbulence for  $\bar{U}_{\text{NOM}} = 60 \text{ m/s}$  for  $x_T = -2.0, -1.0, 0.0$  and  $1.0 \text{ m}$  for  $y_T$  and  $z_T$  locations denoted by filled circles in Figure 26.

(a)  $x_T = -2.0$  and  $-1.0 \text{ m}$ .

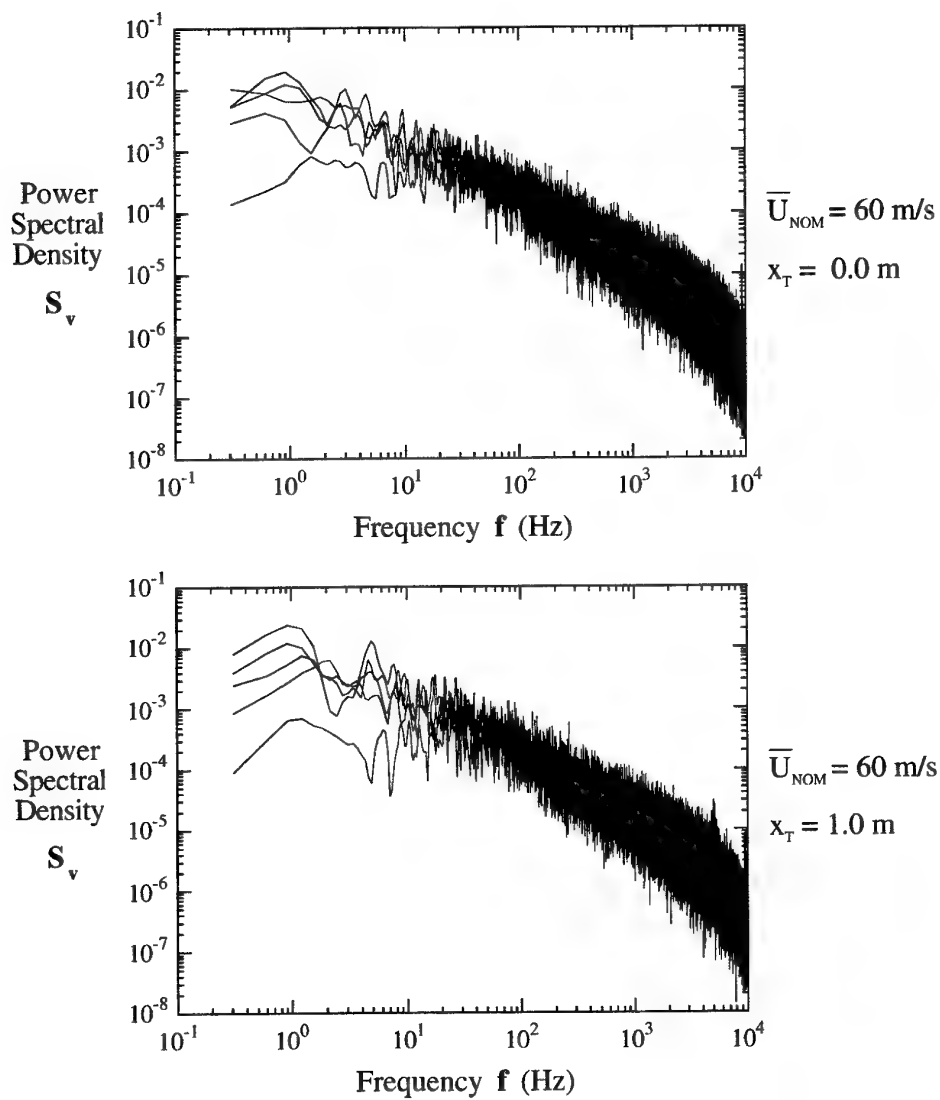


Figure 37 cont'd. Spectra for the  $v$  component of the turbulence for  $\bar{U}_{\text{NOM}} = 60 \text{ m/s}$  for  $x_T = -2.0, -1.0, 0.0$  and  $1.0 \text{ m}$  for  $y_T$  and  $z_T$  locations denoted by filled circles in Figure 26.

(b)  $x_T = 0.0$  and  $1.0 \text{ m}$ .

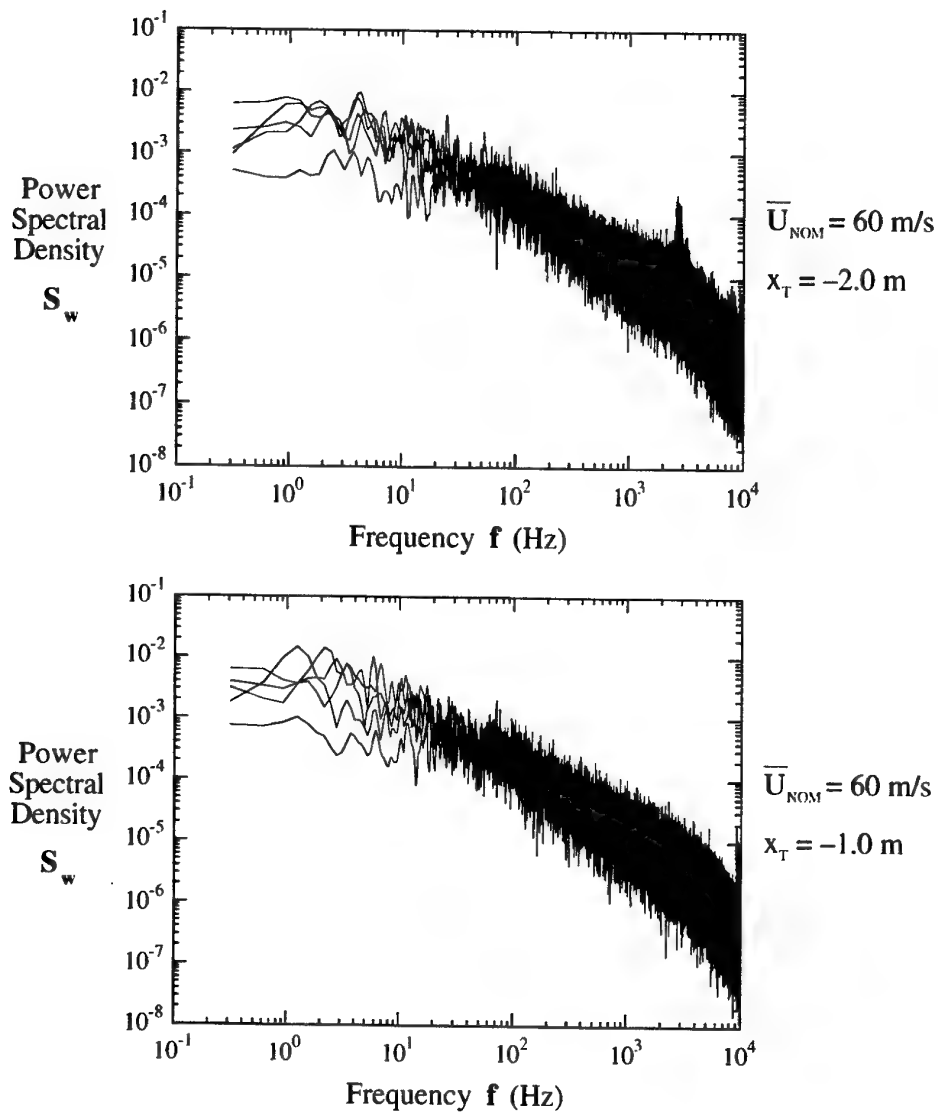


Figure 38. Spectra for the  $w$  component of the turbulence for  $\bar{U}_{NOM} = 60 \text{ m/s}$  for  $x_T = -2.0, -1.0, 0.0$  and  $1.0 \text{ m}$  for  $y_T$  and  $z_T$  locations denoted by filled circles in Figure 26.  
(a)  $x_T = -2.0$  and  $-1.0 \text{ m}$ .

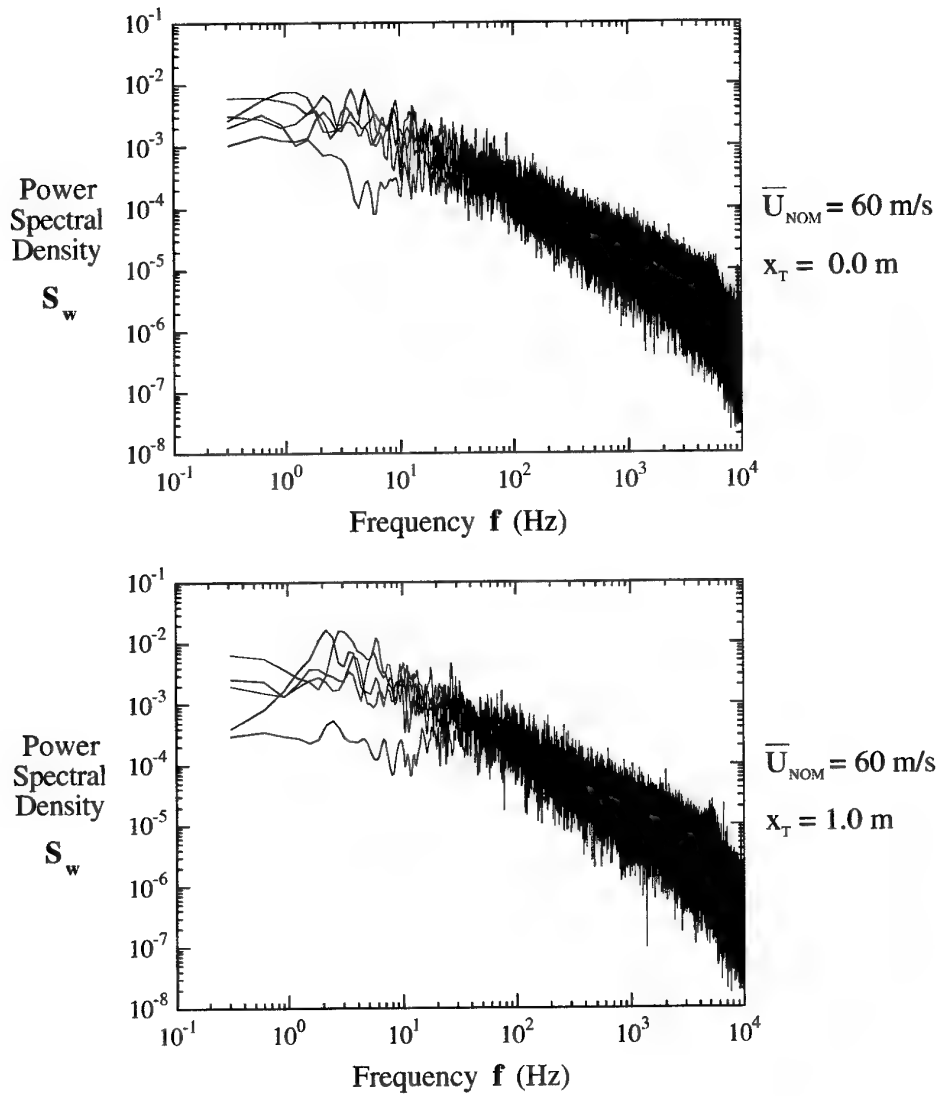


Figure 38 cont'd. Spectra for the  $w$  component of the turbulence for  $\bar{U}_{\text{NOM}} = 60 \text{ m/s}$  for  $x_T = -2.0, -1.0, 0.0$  and  $1.0 \text{ m}$  for  $y_T$  and  $z_T$  locations denoted by filled circles in Figure 26.

(b)  $x_T = 0.0$  and  $1.0 \text{ m}$ .

Table 1. Variation of flow parameters in the original and the extended test sections of the LSWT for  $-1.0 \text{ m} \leq x_r \leq +1.0 \text{ m}$ .

	Parameter	$\bar{U}_{\text{NOM}}$ m/s	LSWT with Original Test Section		LSWT with Extended Test Section	
			Limits of Variation	Range of Variation	Limits of Variation	Range of Variation
Mean Velocity Measurements	$(\bar{U} - \bar{U}_{0.0})/\bar{U}_{0.0}$	30	-0.6% to 2.0%	2.6%	-1.0% to 1.4%	2.4%
	$(\bar{U} - \bar{U}_{0.0})/\bar{U}_{0.0}$	45	-0.8% to 1.6%	2.4%	-0.6% to 1.6%	2.2%
	$(\bar{U} - \bar{U}_{0.0})/\bar{U}_{0.0}$	60	-0.6% to 1.8%	2.4%	-0.6% to 1.4%	2.0%
	$(\bar{U} - \bar{U}_{0.0})/\bar{U}_{0.0}$	75	-0.2% to 2.0%	2.2%	-0.8% to 1.4%	2.2%
Flow Angle Measurements	$\epsilon_H$	30	$-0.8^\circ$ to $0.6^\circ$	$1.4^\circ$	$-0.8^\circ$ to $0.4^\circ$	$1.2^\circ$
	$\epsilon_V$	30	$-0.8^\circ$ to $0.4^\circ$	$1.2^\circ$	$-0.8^\circ$ to $0.4^\circ$	$1.2^\circ$
	$\epsilon_H$	60	$-0.4^\circ$ to $0.8^\circ$	$1.2^\circ$	$-0.4^\circ$ to $0.8^\circ$	$1.2^\circ$
	$\epsilon_V$	60	$-1.0^\circ$ to $0.4^\circ$	$1.4^\circ$	$-1.0^\circ$ to $0.4^\circ$	$1.4^\circ$
Turbulence Intensity Measurements	$(\bar{u}^2)^{0.5}/\bar{U}_{0.0}$	30 & 60	up to 0.4%		up to 0.4%	
	$(\bar{v}^2)^{0.5}/\bar{U}_{0.0}$	30 & 60	up to 0.7%		up to 0.7%	
	$(\bar{w}^2)^{0.5}/\bar{U}_{0.0}$	30 & 60	up to 0.7%		up to 0.7%	

## 6.2 Flow Angles

Contours of  $\epsilon_H$  and  $\epsilon_V$  for  $x_T = 0.0$  m for  $\bar{U}_{NOM} = 30$  m/s for the extended and the original test sections are shown in Figure 41. Corresponding contours for  $\bar{U}_{NOM} = 60$  m/s are shown in Figure 42. The distributions of corresponding flow angles in the extended and the original test sections are similar. Table 1 shows that the range of variation of flow angles between  $x_T = -1.0$  and  $+1.0$  m are approximately the same in the original and the extended test sections for the two velocities used. Overall, the modifications to the tunnel have had virtually no effect on the flow angles.

## 6.3 Turbulence Intensities

Contours of  $(\bar{u}^2)^{0.5}/\bar{U}_{0.0}$ ,  $(\bar{v}^2)^{0.5}/\bar{U}_{0.0}$  and  $(\bar{w}^2)^{0.5}/\bar{U}_{0.0}$  for  $x_T = 0.0$  m for  $\bar{U}_{NOM} = 30$  m/s for the extended and original test sections are shown in Figure 43. Corresponding contours for  $\bar{U}_{NOM} = 60$  m/s are shown in Figure 44. Table 1 shows that the intensities between  $x_T = -1.0$  and  $+1.0$  m over the central regions of the cross sections are the same in the extended and the original test sections at the two velocities. While the distributions of corresponding intensities in the central regions of the extended and the original test sections are similar, the gradients of the intensities and absolute values of intensities near the walls of the test sections are often significantly lower for the extended test section. This could be due to the fact that the flow near the contraction walls has had to negotiate different curved paths in the two cases because the shapes of the two contractions are different. However, the reasons for the observed flow behaviour in the current investigation are probably quite complex, since the two contractions have different concave and also different convex radii of curvature, and it is not possible to give a precise explanation for the changes.

## 6.4 Spectra

Spectra for the u-, v- and w-components of the turbulence for  $x_T = 0.0$  m for  $\bar{U}_{NOM} = 30$  m/s for the extended and the original test sections are shown in Figure 45. Corresponding spectra for  $\bar{U}_{NOM} = 60$  m/s are shown in Figure 46. Corresponding spectra in the extended and the original test sections are virtually the same, indicating that the modifications to the tunnel have had little effect on the spectra.

## 6.5 Overall Effect of Modifying the Contraction and the Length of the Test Section of the LSWT in 1996

The installation of the extended test section and the new contraction has had only a minimal effect on improving the quality of the flow in the test section. However, since the contraction ratio for the new contraction was the same as that for the original contraction, i.e. 4:1, it was not expected that simply altering the shape of the contraction would result in a large improvement in the quality of the flow in the test section. The main reason for modifying the tunnel in 1996 was to extend the length of the test section to enable longer models to be tested.



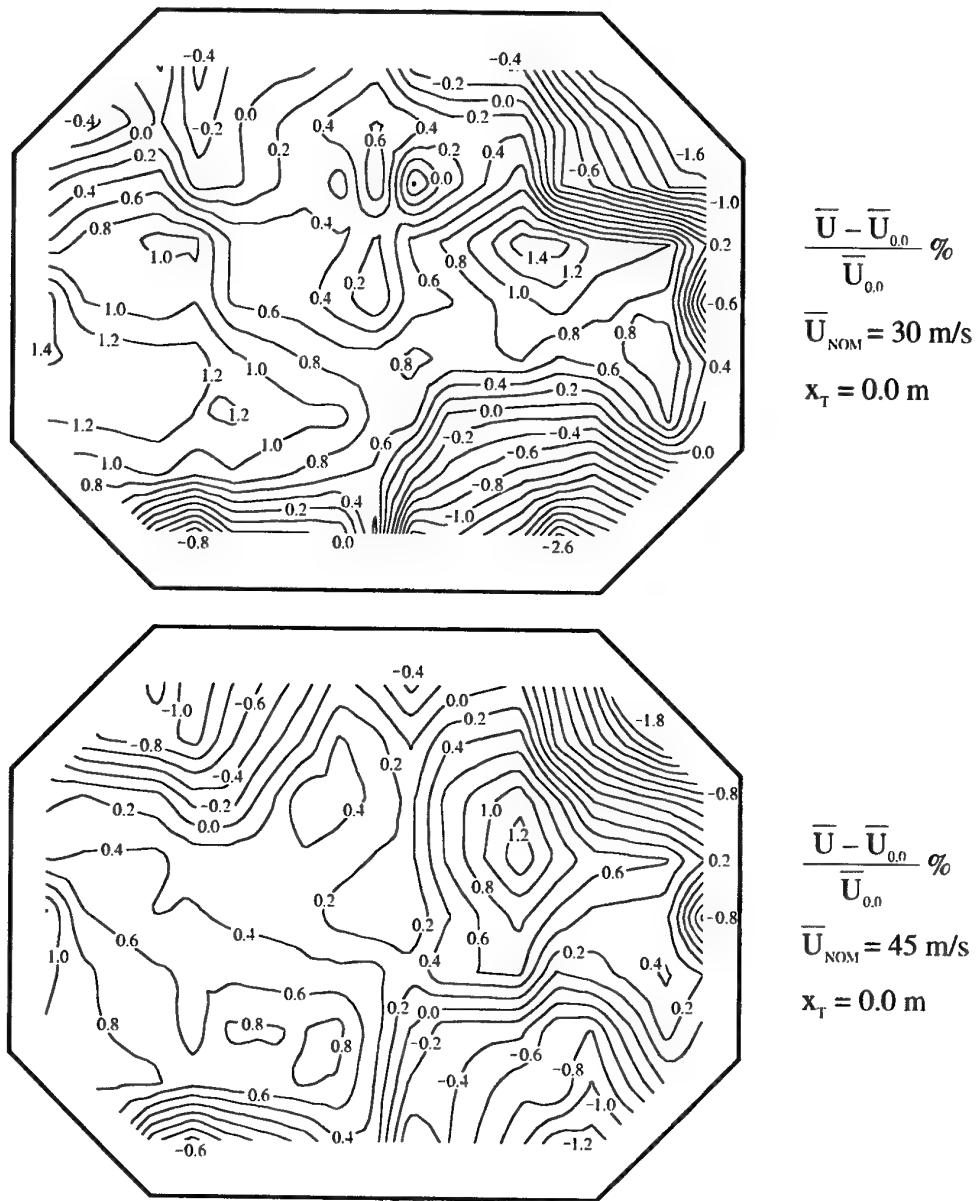


Figure 39. Contours of velocity deviation for  $\bar{U}_{\text{NOM}} = 30$  and  $45 \text{ m/s}$  for  $x_T = 0.0 \text{ m}$ .

(a) Data taken in the LSWT with the extended test section and new contraction.

The flow is out of the page.

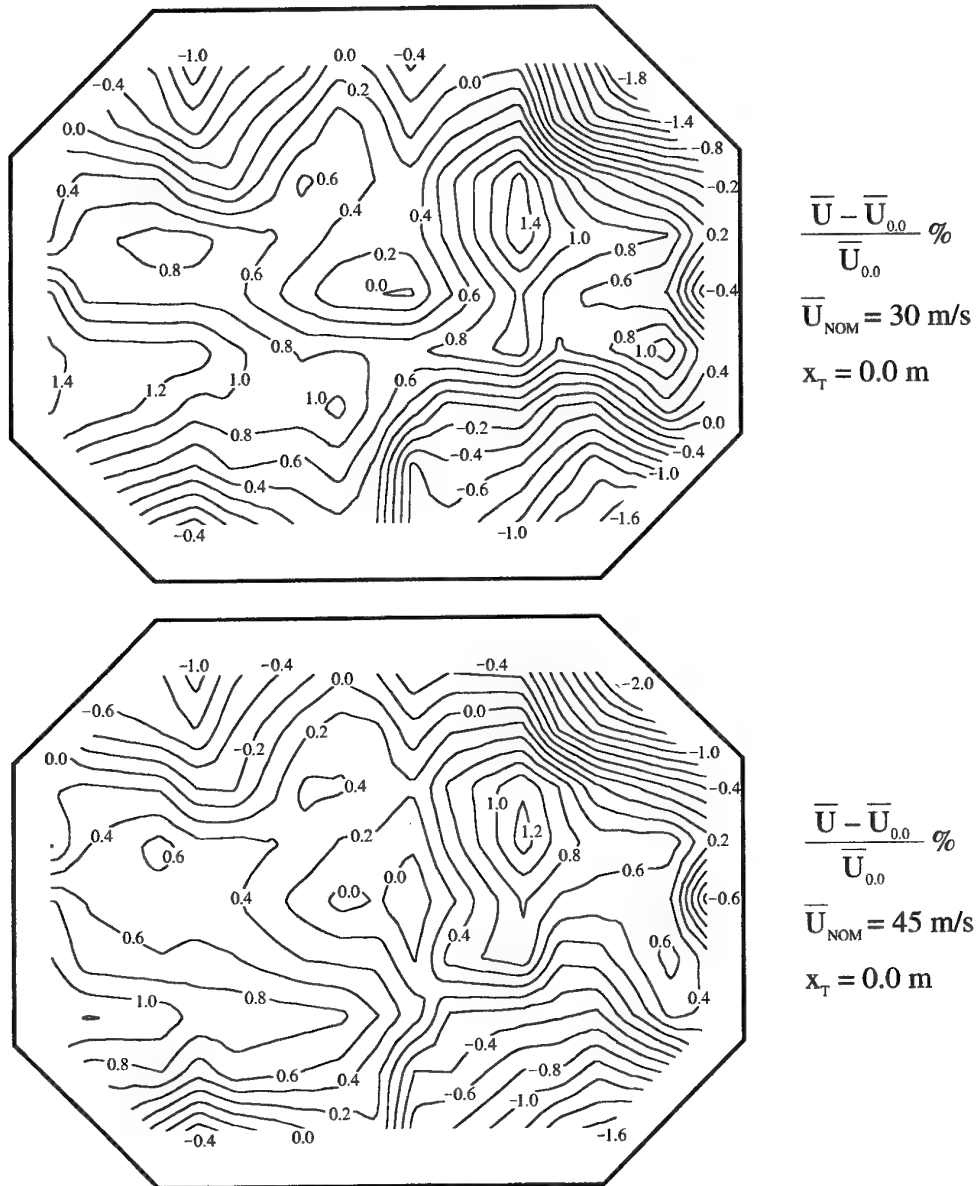


Figure 39 cont'd. Contours of velocity deviation for  $\bar{U}_{\text{NOM}} = 30$  and  $45 \text{ m/s}$  for  $x_T = 0.0 \text{ m}$ .

(b) Data taken in the LSWT prior to modifications to the tunnel in 1996.

The flow is out of the page.

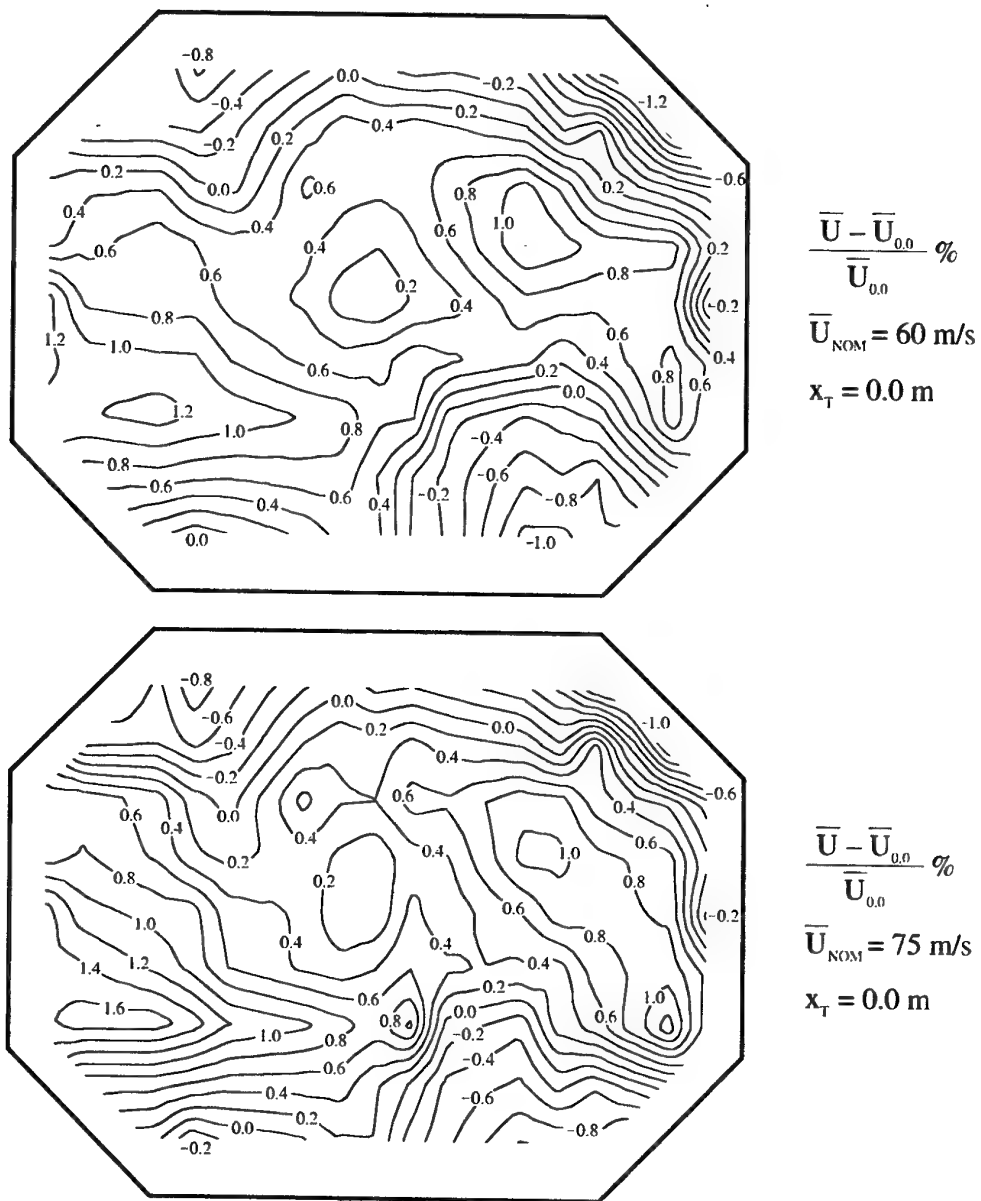


Figure 40. Contours of velocity deviation for  $\bar{U}_{\text{NOM}} = 60$  and  $75 \text{ m/s}$  for  $x_T = 0.0 \text{ m}$ .

(a) Data taken in the LSWT with the extended test section and new contraction.

The flow is out of the page.

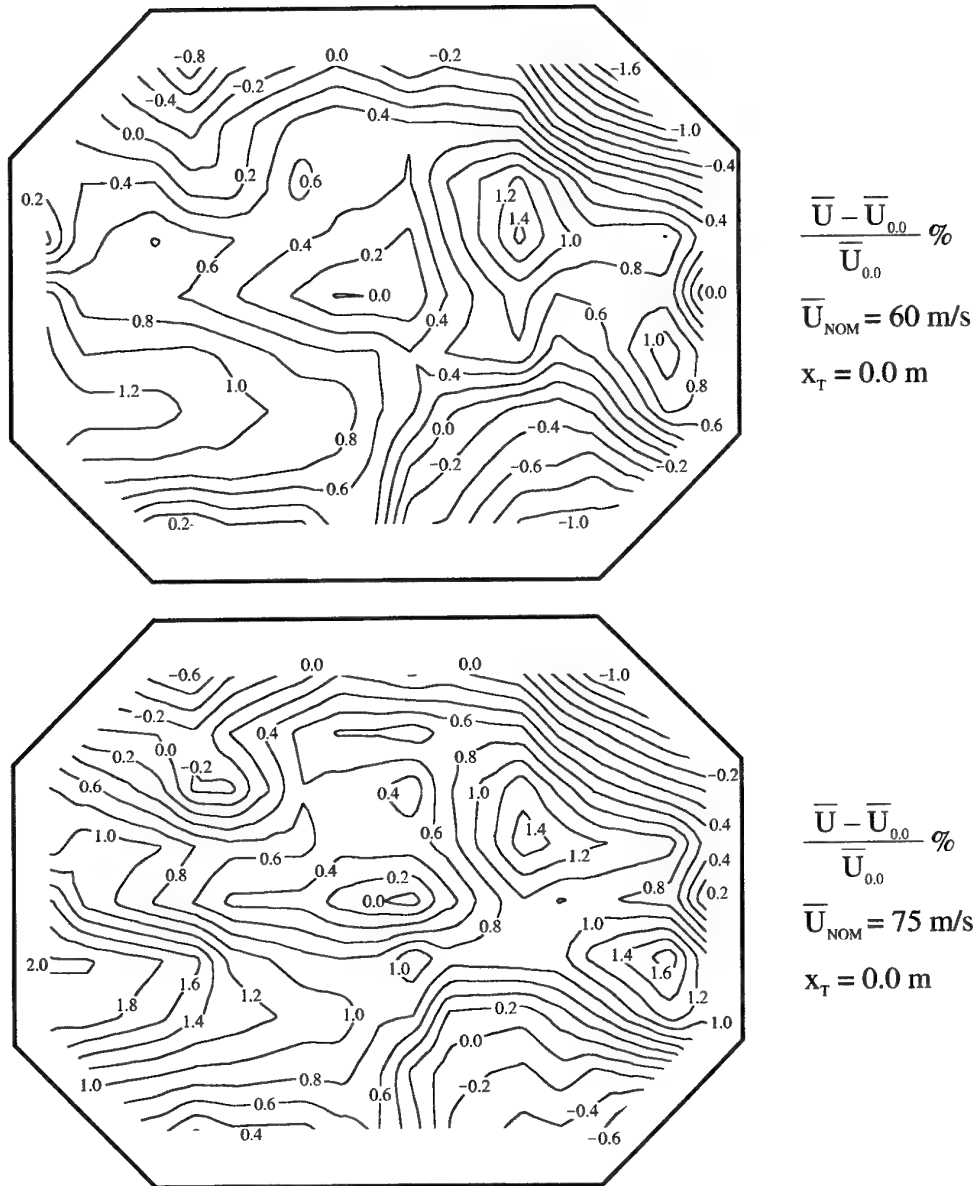


Figure 40 cont'd. Contours of velocity deviation for  $\bar{U}_{\text{NOM}} = 60$  and  $75$  m/s for  $x_T = 0.0$  m.

(b) Data taken in the LSWT prior to modifications to the tunnel in 1996.

The flow is out of the page.

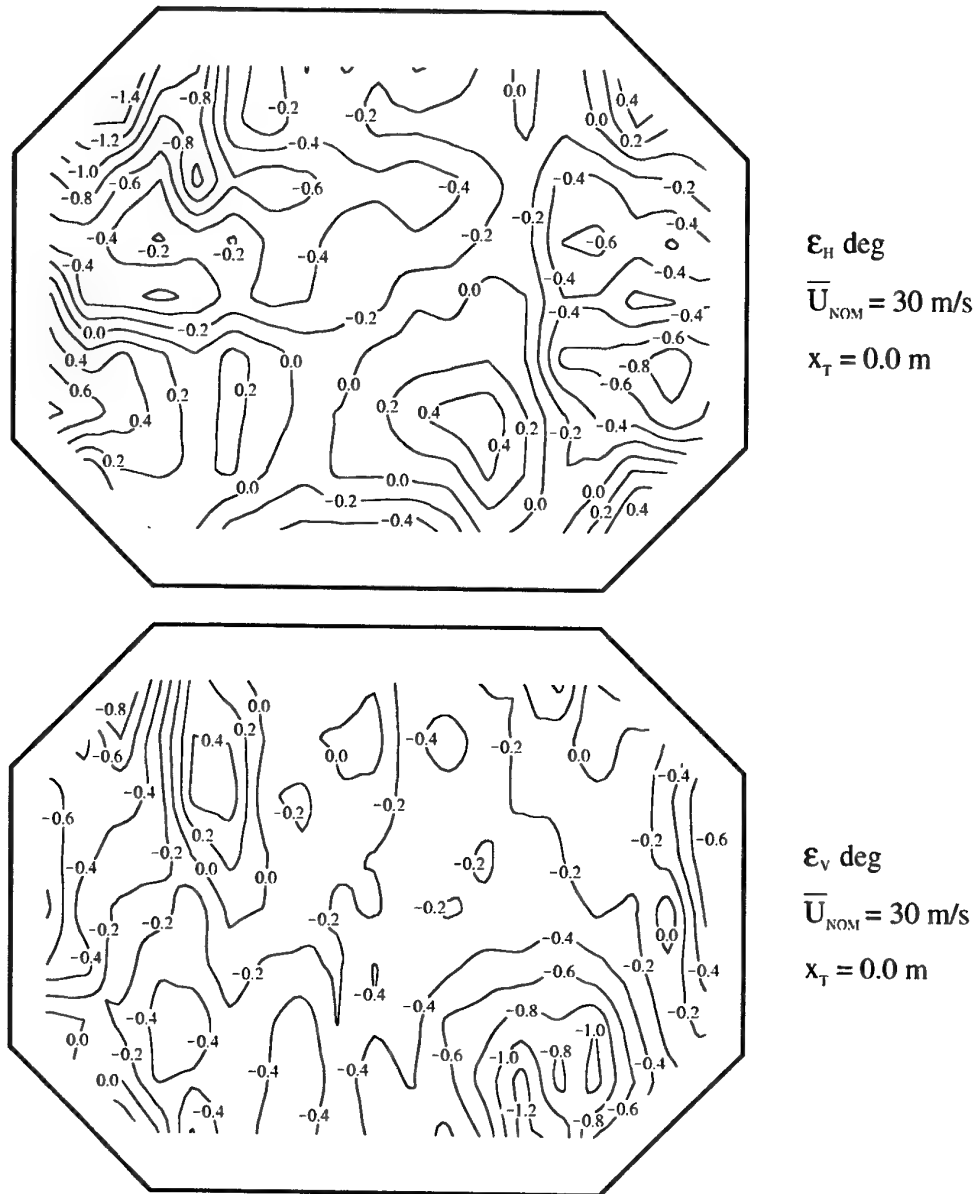


Figure 41. Contours of horizontal and vertical flow angle for  $\bar{U}_{NOM} = 30$  m/s for  $x_T = 0.0$  m.

(a) Data taken in the LSWT with the extended test section and new contraction.

The flow is out of the page.

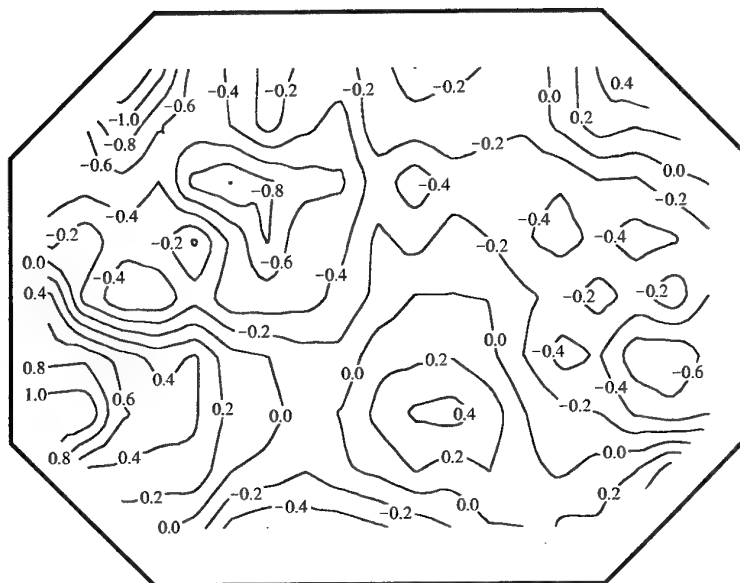
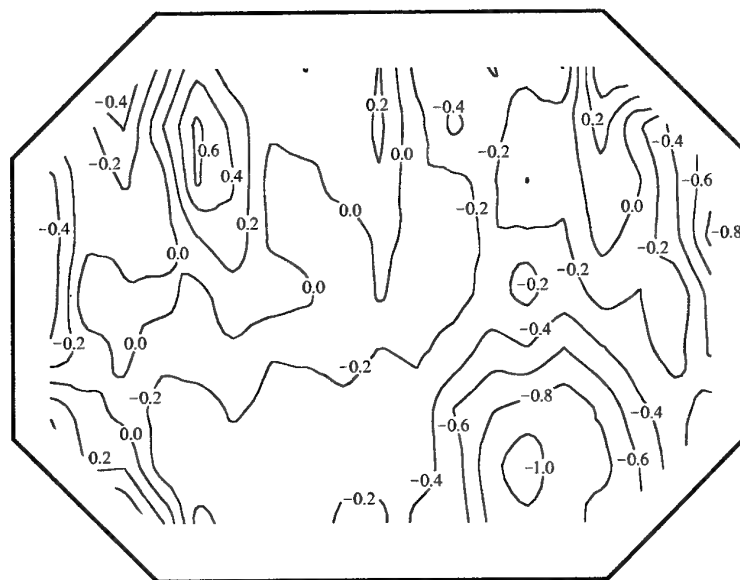
 $\epsilon_H$  deg $\bar{U}_{\text{NOM}} = 30 \text{ m/s}$  $x_T = 0.0 \text{ m}$  $\epsilon_V$  deg $\bar{U}_{\text{NOM}} = 30 \text{ m/s}$  $x_T = 0.0 \text{ m}$ 

Figure 41 cont'd. Contours of horizontal and vertical flow angle for  $\bar{U}_{\text{NOM}} = 30 \text{ m/s}$  for  $x_T = 0.0 \text{ m}$ .

(b) Data taken in the LSWT prior to modifications to the tunnel in 1996.

The flow is out of the page.

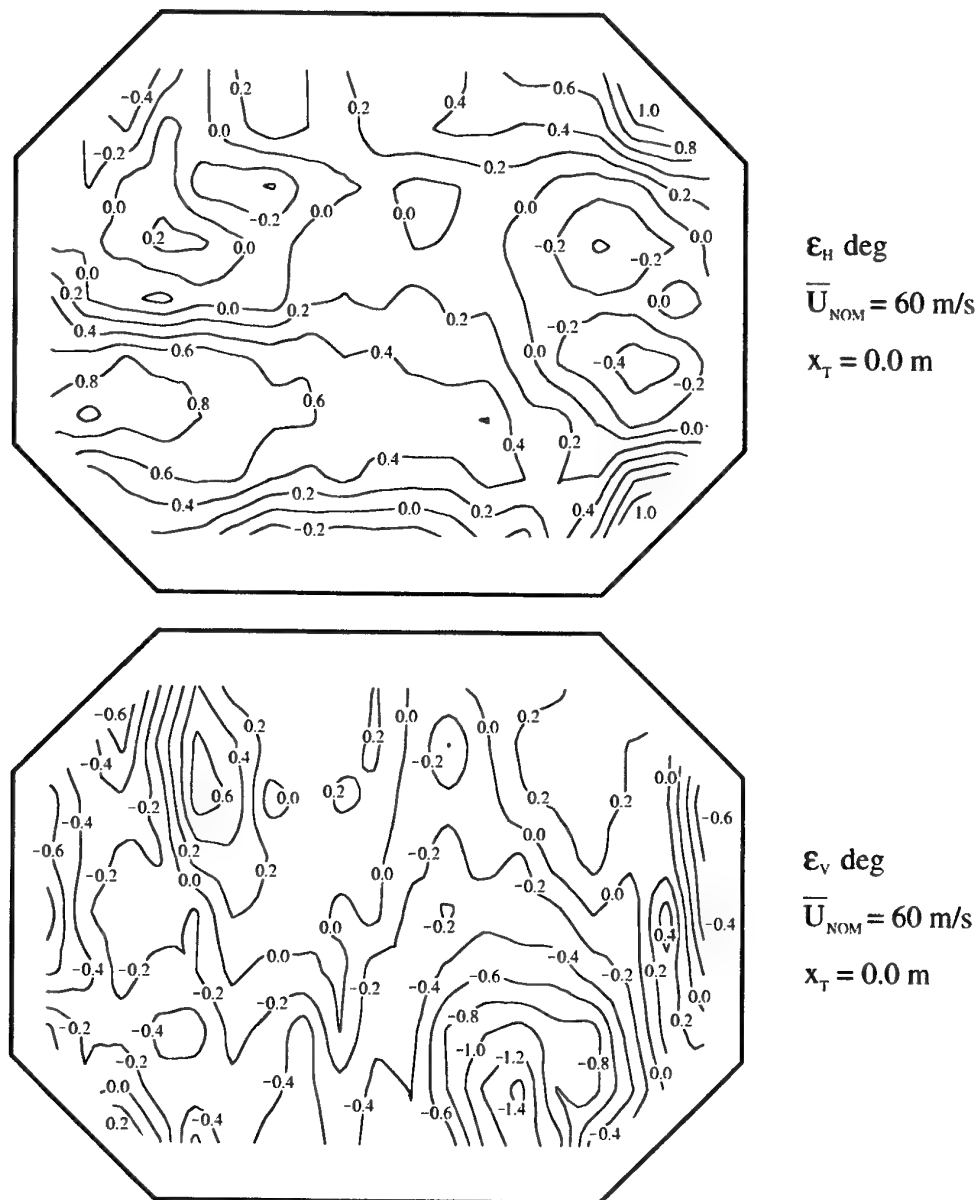


Figure 42. Contours of horizontal and vertical flow angle for  $\bar{U}_{NOM} = 60$  m/s for  $x_T = 0.0$  m.

(a) Data taken in the LSWT with the extended test section and new contraction.

The flow is out of the page.

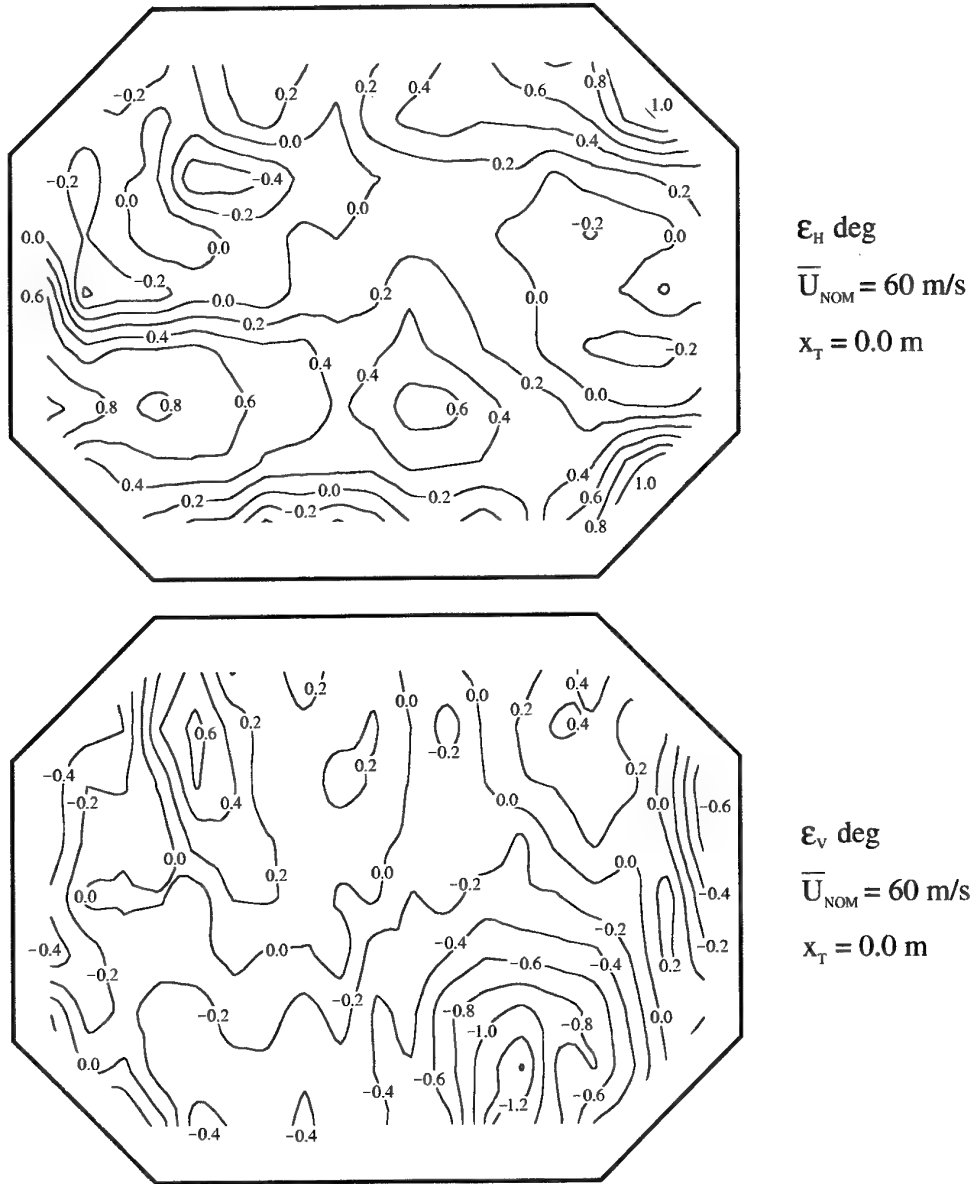


Figure 42 cont'd. Contours of horizontal and vertical flow angle for  $\bar{U}_{\text{NOM}} = 60 \text{ m/s}$  for  $x_T = 0.0 \text{ m}$ .

(b) Data taken in the LSWT prior to modifications to the tunnel in 1996.

The flow is out of the page.



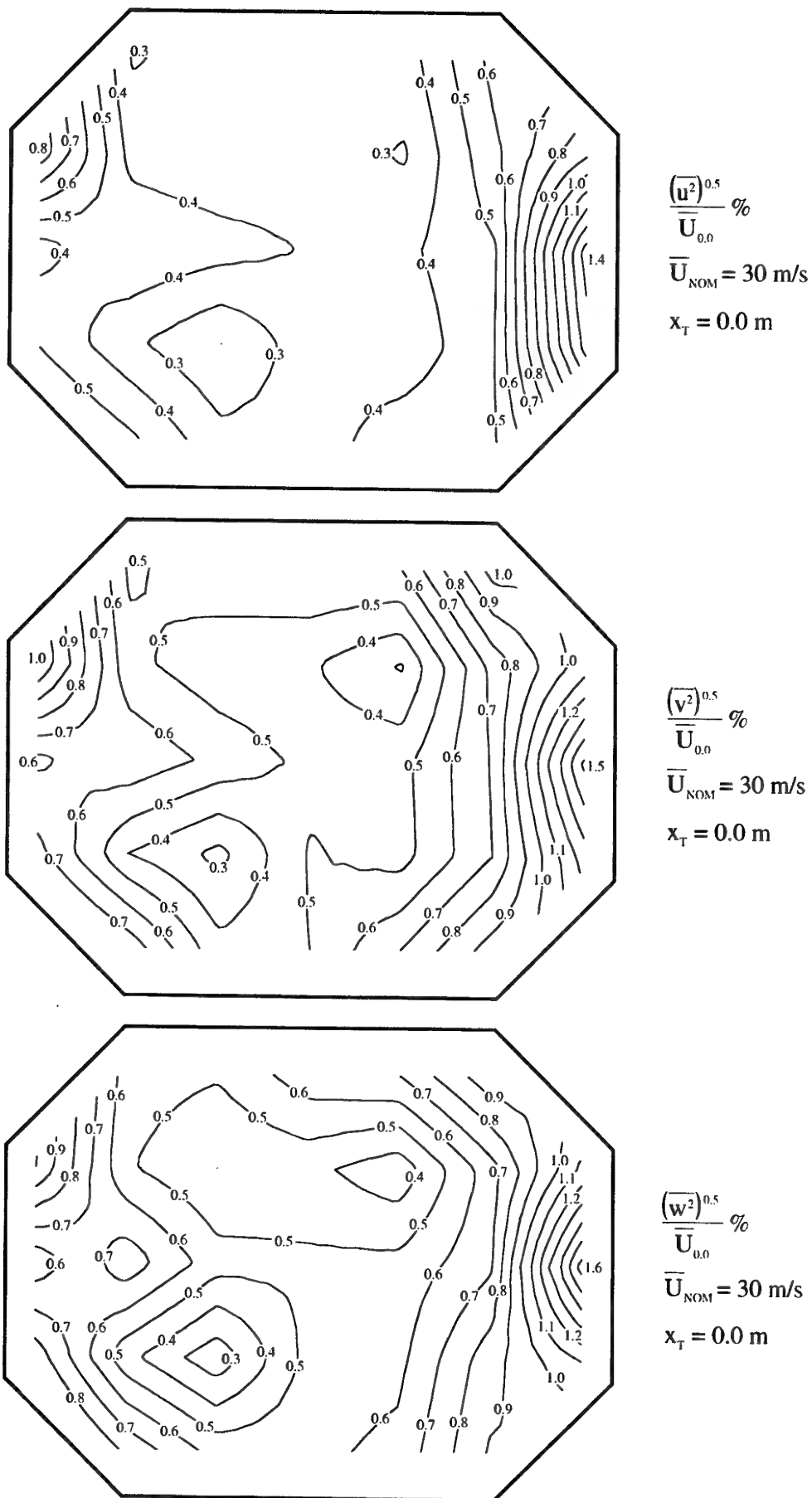
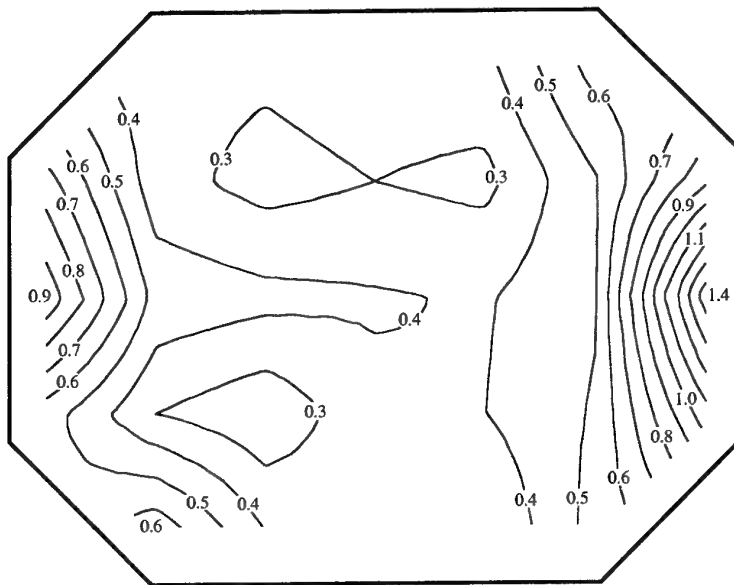


Figure 43. Contours of u- v- and w-component intensities for  $\overline{U}_{\text{NOM}} = 30 \text{ m/s}$  for  $x_T = 0.0 \text{ m}$ .

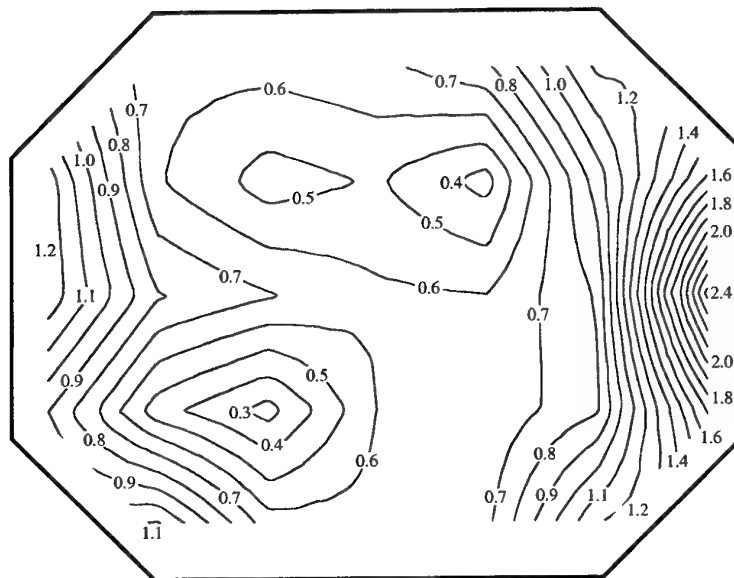
(a) Data taken in the LSWT with the extended test section and new contraction.



$$\frac{(\overline{u^2})^{0.5}}{\overline{U}_{0.0}} \%$$

$$\overline{U}_{\text{NOM}} = 30 \text{ m/s}$$

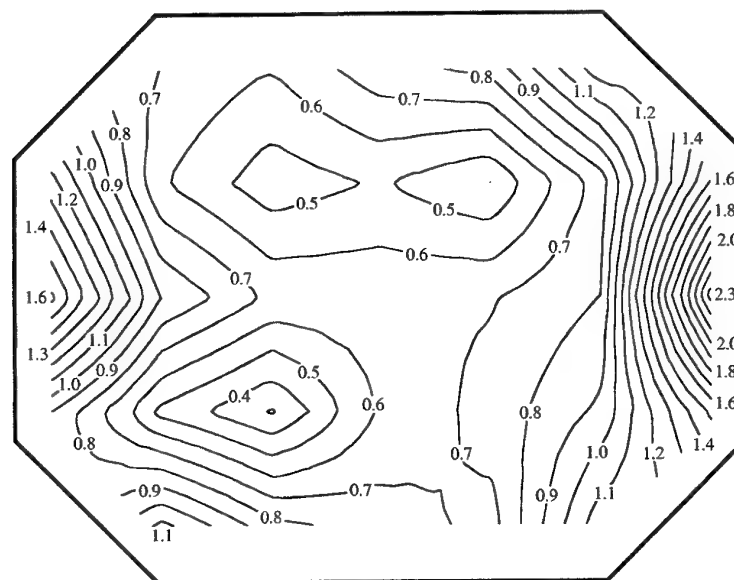
$$x_T = 0.0 \text{ m}$$



$$\frac{(\overline{v^2})^{0.5}}{\overline{U}_{0.0}} \%$$

$$\overline{U}_{\text{NOM}} = 30 \text{ m/s}$$

$$x_T = 0.0 \text{ m}$$



$$\frac{(\overline{w^2})^{0.5}}{\overline{U}_{0.0}} \%$$

$$\overline{U}_{\text{NOM}} = 30 \text{ m/s}$$

$$x_T = 0.0 \text{ m}$$

Figure 43 cont'd. Contours of u- v- and w-component intensities for  $\overline{U}_{\text{NOM}} = 30 \text{ m/s}$  for  $x_T = 0.0 \text{ m}$ .

(b) Data taken in the LSWT prior to modifications to the tunnel in 1996.

The flow is out of the page.

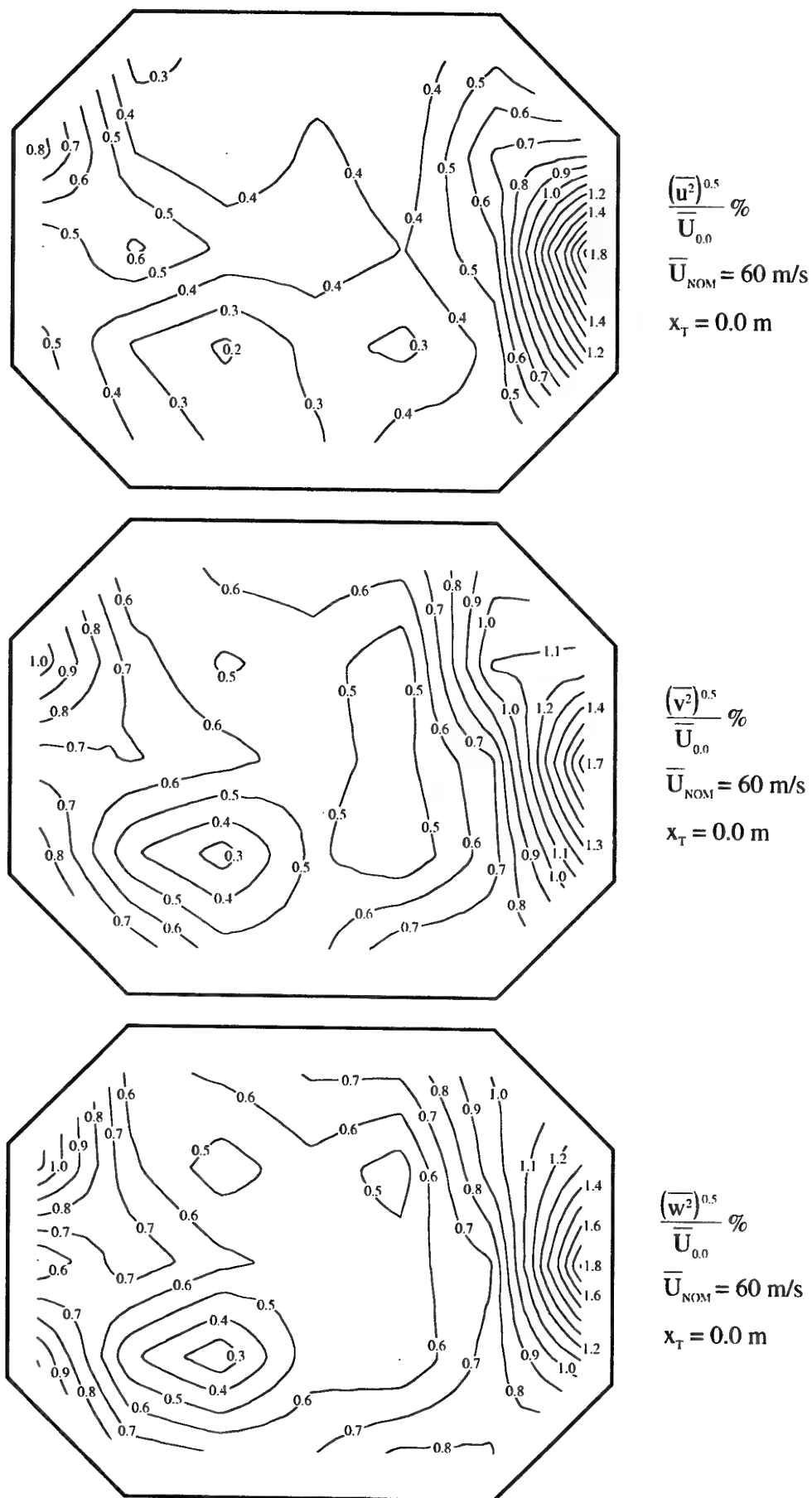
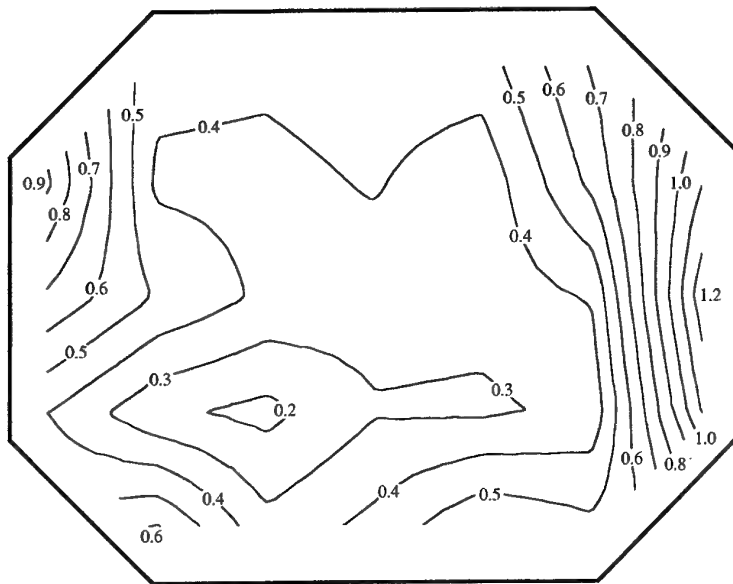


Figure 44. Contours of u- v- and w-component intensities for  $\bar{U}_{\text{NOM}} = 60 \text{ m/s}$  for  $x_T = 0.0 \text{ m}$ .

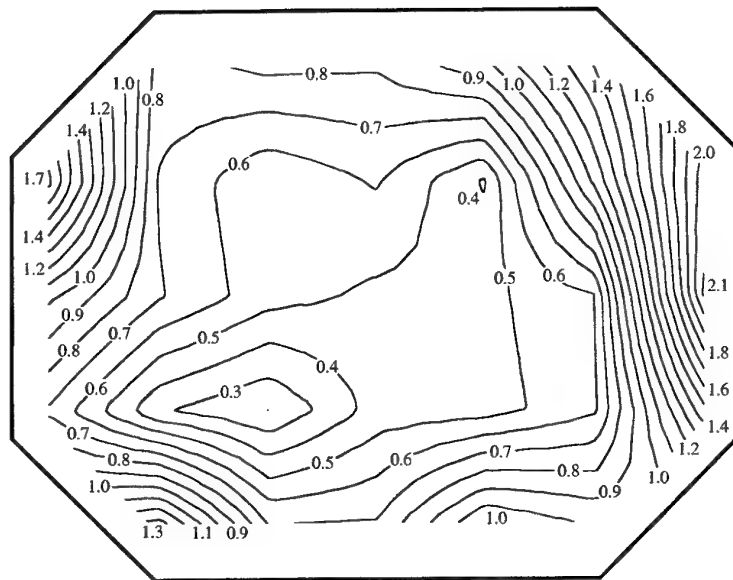
(a) Data taken in the LSWT with the extended test section and new contraction.



$$\frac{(\overline{u^2})^{0.5}}{\overline{U}_{0.0}} \%$$

$$\overline{U}_{\text{NOM}} = 60 \text{ m/s}$$

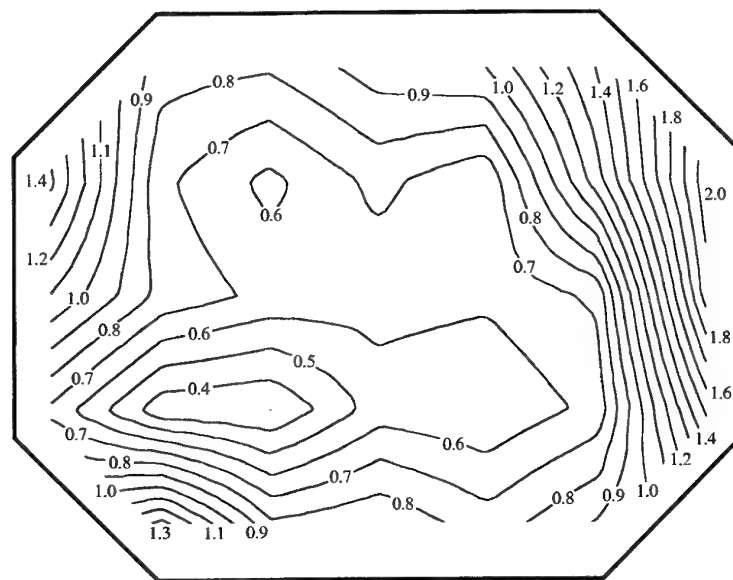
$$x_T = 0.0 \text{ m}$$



$$\frac{(\overline{v^2})^{0.5}}{\overline{U}_{0.0}} \%$$

$$\overline{U}_{\text{NOM}} = 60 \text{ m/s}$$

$$x_T = 0.0 \text{ m}$$



$$\frac{(\overline{w^2})^{0.5}}{\overline{U}_{0.0}} \%$$

$$\overline{U}_{\text{NOM}} = 60 \text{ m/s}$$

$$x_T = 0.0 \text{ m}$$

Figure 44 cont'd. Contours of u- v- and w-component intensities for  $\overline{U}_{\text{NOM}} = 60 \text{ m/s}$  for  $x_T = 0.0 \text{ m}$ .

(b) Data taken in the LSWT prior to modifications to the tunnel in 1996.

The flow is out of the page.

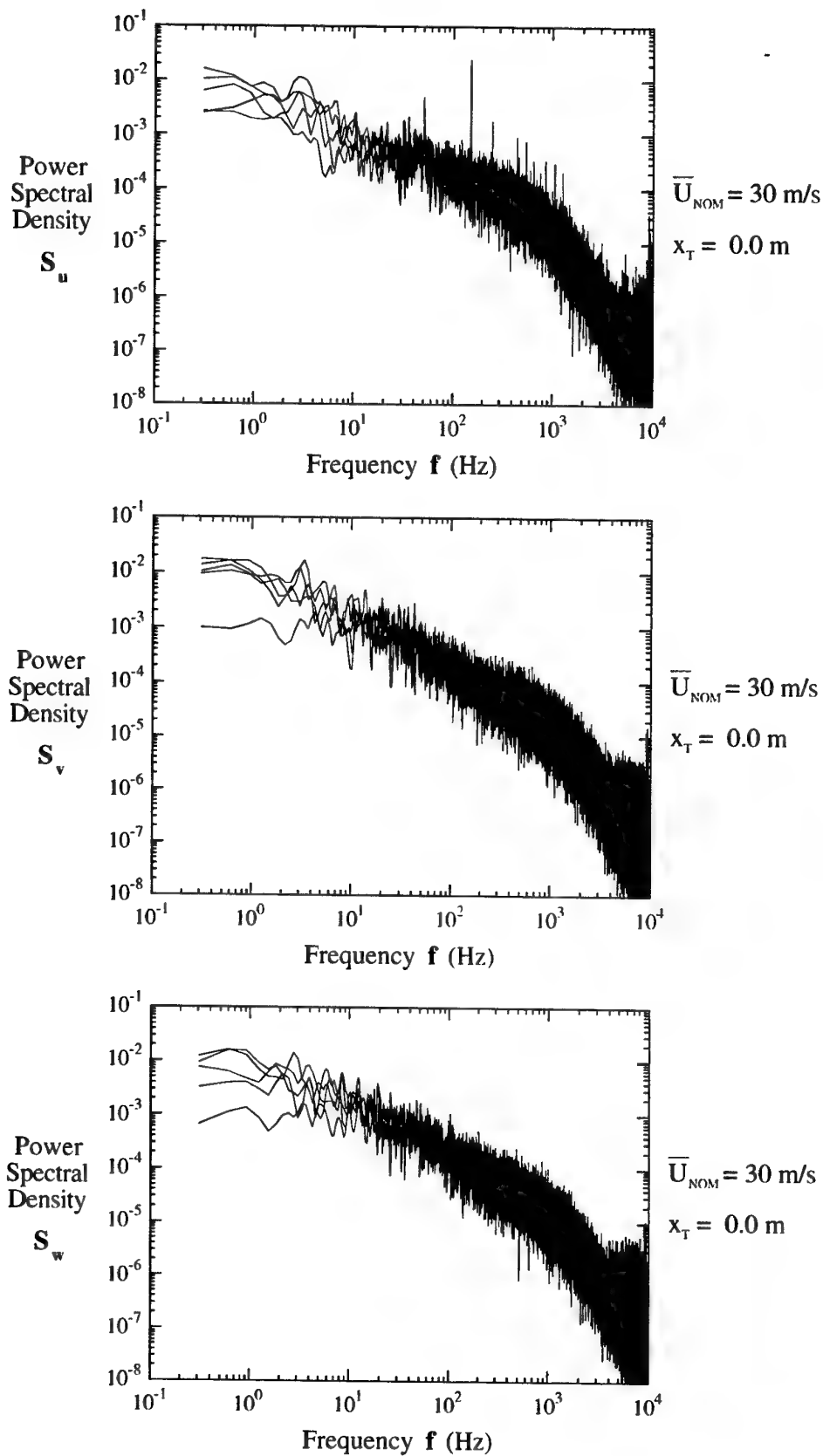


Figure 45. Spectra for the u, v and w components of the turbulence for  $\bar{U}_{\text{NOM}} = 30 \text{ m/s}$  for  $x_T = 0.0 \text{ m}$  for  $y_T$  and  $z_T$  locations denoted by filled circles in Figure 26.  
(a) Data taken in the LSWT with the extended test section and new contraction.

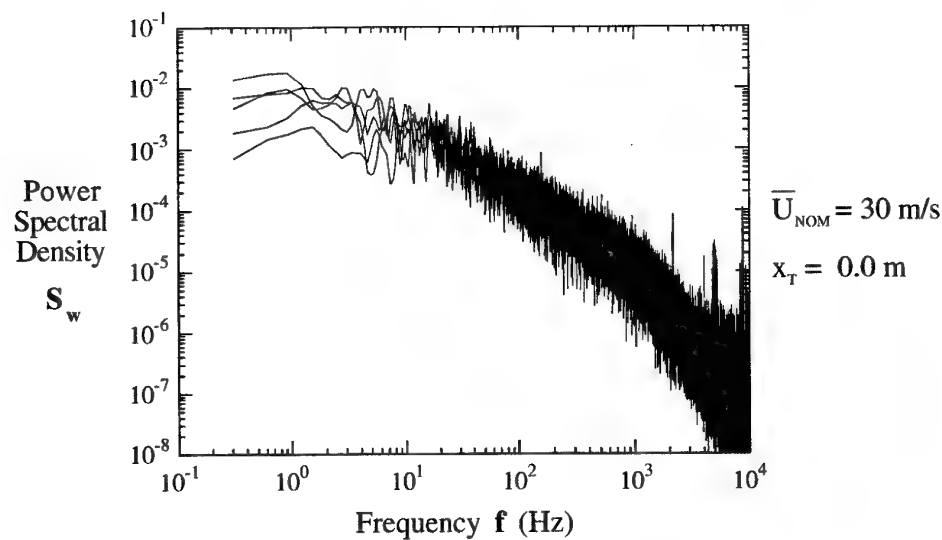
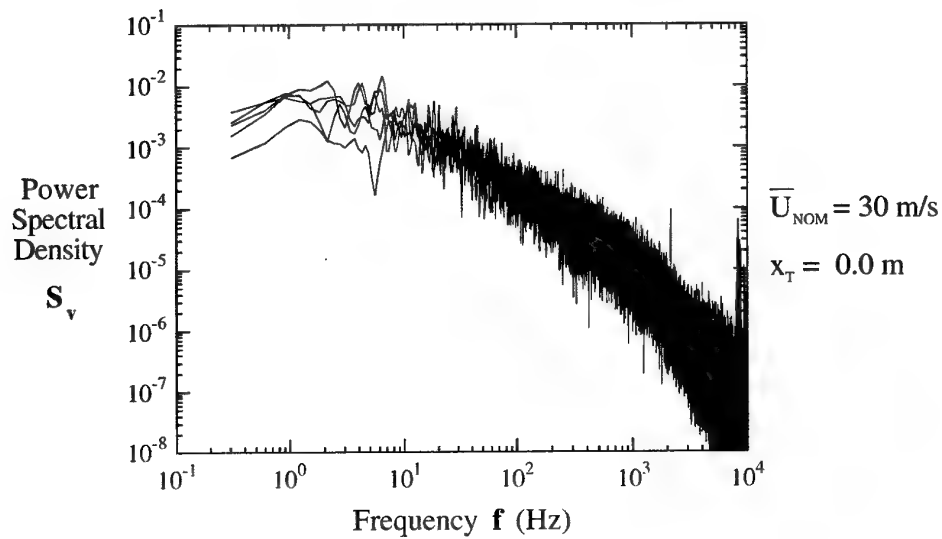
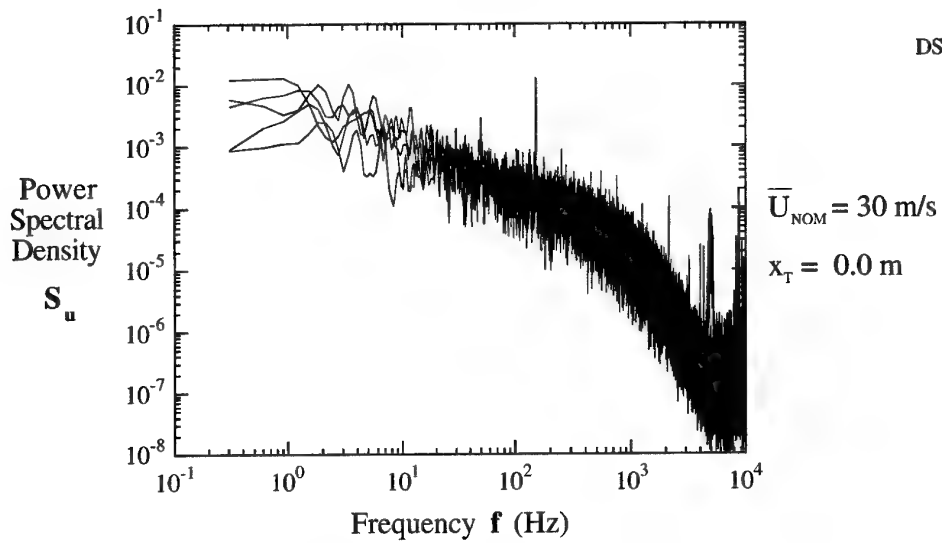


Figure 45 cont'd. Spectra for the u, v and w components of the turbulence for  $\bar{U}_{\text{NOM}} = 30 \text{ m/s}$  for  $x_T = 0.0 \text{ m}$  for  $y_T$  and  $z_T$  locations denoted by filled circles in Figure 26.  
 (b) Data taken in the LSWT prior to modifications to the tunnel in 1996.

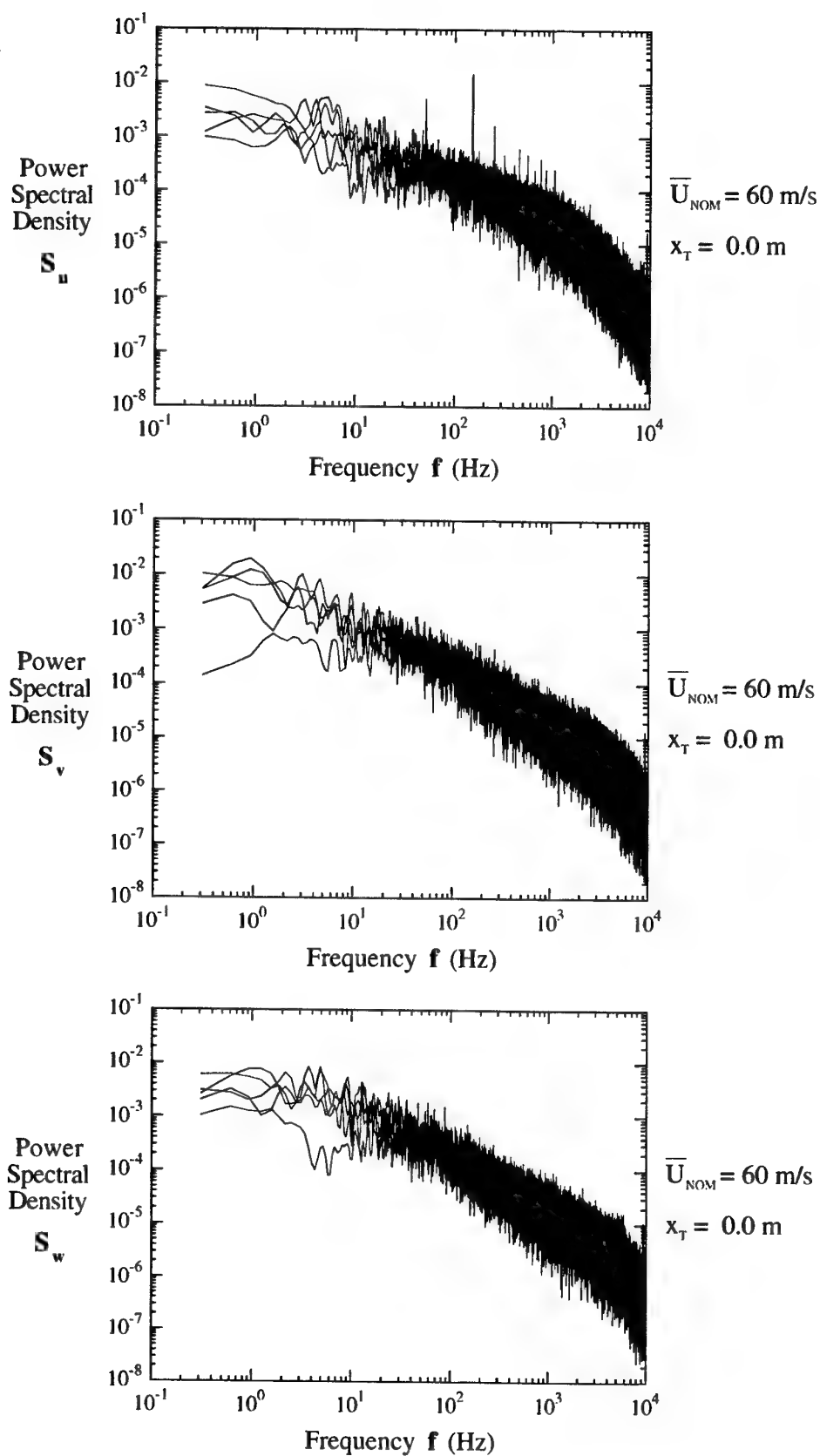


Figure 46. Spectra for the  $u$ ,  $v$  and  $w$  components of the turbulence for  $\bar{U}_{\text{NOM}} = 60 \text{ m/s}$  for  $x_T = 0.0 \text{ m}$  for  $y_T$  and  $z_T$  locations denoted by filled circles in Figure 26.  
(a) Data taken in the LSWT with the extended test section and new contraction.

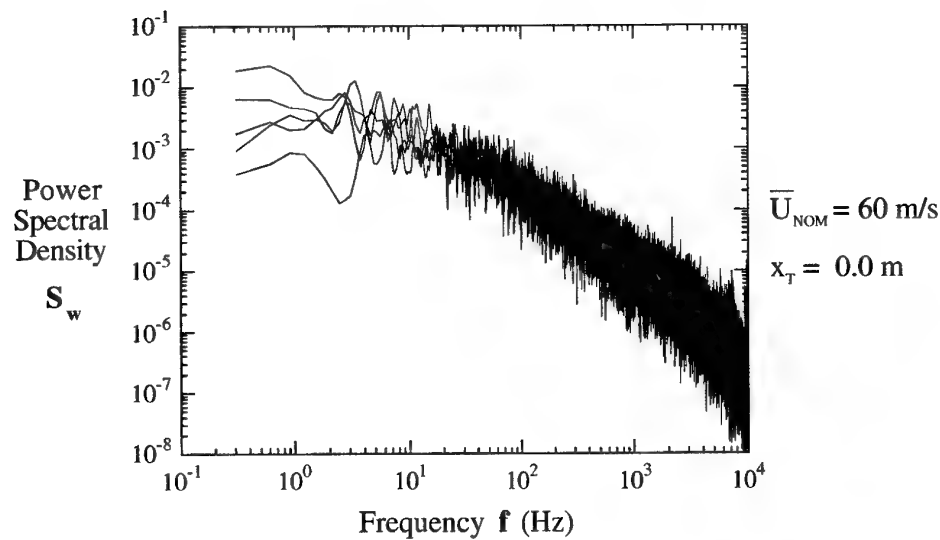
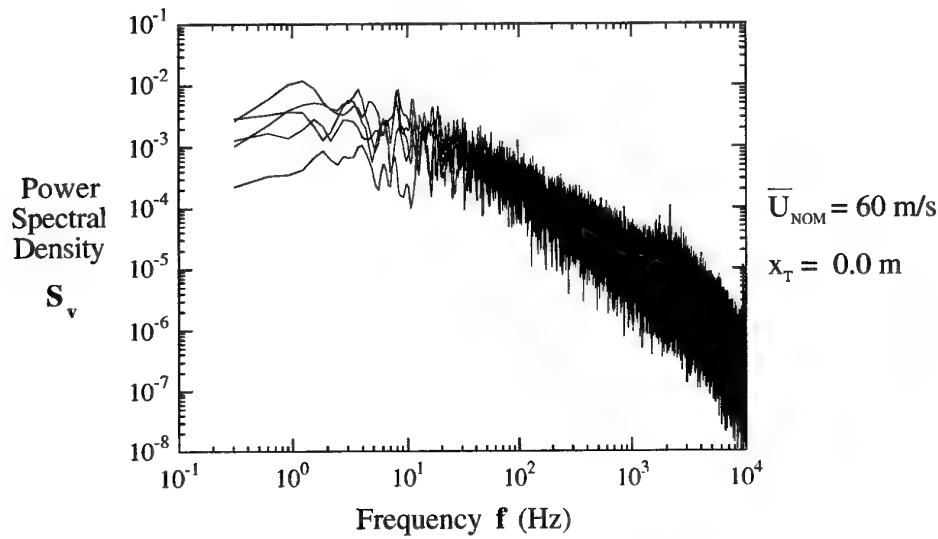
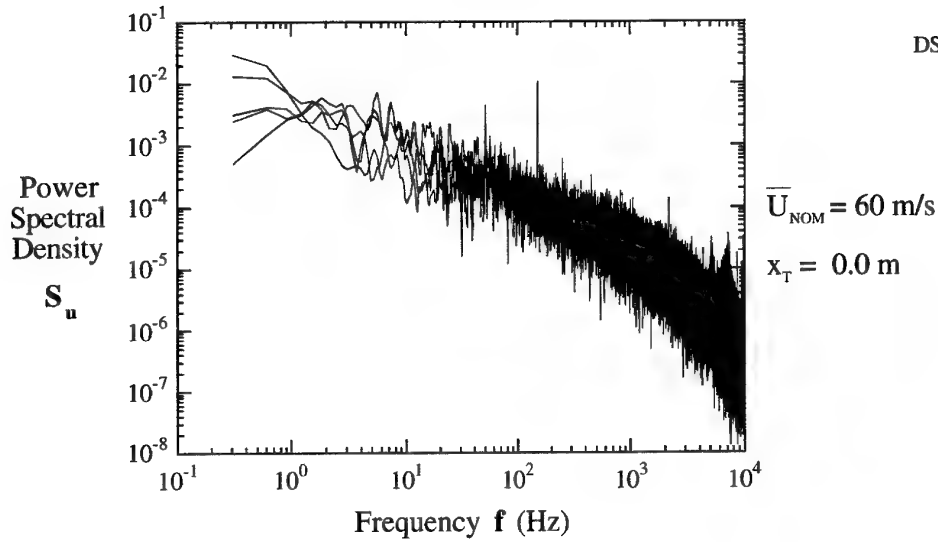


Figure 46 cont'd. Spectra for the u, v and w components of the turbulence for  $\bar{U}_{\text{NOM}} = 60 \text{ m/s}$  for  $x_T = 0.0 \text{ m}$  for  $y_T$  and  $z_T$  locations denoted by filled circles in Figure 26.  
 (b) Data taken in the LSWT prior to modifications to the tunnel in 1996.



## 7. Assessment of Flow Quality in the LSWT

It has been shown that, like nearly all fully-enclosed flows, the flow in the extended test section of the LSWT has some non-uniformity in terms of mean-velocity deviations, flow angularity and turbulence intensities. In the following, flow non-uniformities for the tunnel are quoted for approximately the central 50% of the cross-sectional area of the test section.

### 7.1 Mean Velocities

For  $\bar{U}_{\text{NOM}} = 30$  m/s, between  $x_T = -2.0$  and  $+1.0$  m, longitudinal mean velocities deviated between  $-1.0\%$  and  $+1.4\%$  from their values at the centre of the test section ( $x_T = 0.0$ ,  $y_T = 0.0$  and  $z_T = 0.0$  m) (Figure 8). Corresponding deviations for other values of  $\bar{U}_{\text{NOM}}$  were from  $-1.2\%$  to  $+1.6\%$  for  $\bar{U}_{\text{NOM}} = 45$  m/s (Figure 9), from  $-1.0\%$  to  $+1.4\%$  for  $\bar{U}_{\text{NOM}} = 60$  m/s (Figure 10) and from  $-1.2\%$  to  $+1.4\%$  for  $\bar{U}_{\text{NOM}} = 75$  m/s (Figure 11).

In Reference 10 it is indicated that acceptable longitudinal mean-velocity deviations across the test section are often quoted in the range  $\pm 0.20\%$  to  $\pm 0.30\%$  variation from the average value of the mean velocity (not stated where in the test section). Reference 16 indicates that acceptable mean-velocity variations across the test section of a high performance tunnel are less than  $\pm 0.2\%$ . In the  $8 \text{ m} \times 6 \text{ m}$  test section of the German-Dutch large low-speed wind tunnel, the total-pressure deviations (expressed as pressure coefficients) are less than  $0.3\%$  at  $90$  m/s, and the static-pressure deviations (expressed as pressure coefficients) are well within  $0.6\%$  at  $100$  m/s (Reference 14). The deviations in the total and static pressures are relative to the total and static pressures respectively at the centre of the tunnel test section. (Unfortunately, it has not been possible to determine variations in mean velocity from the published data since the given deviations in total pressure apply to a region and not specific locations, so that total pressures and static pressures cannot be matched). According to Reference 17, velocities should not deviate from the mean value by more than  $\pm 0.75\%$ . The five metre low-speed wind tunnel at the Defence Evaluation and Research Agency (formerly Royal Aircraft Establishment) has mean-velocity variations of about  $\pm 0.12\%$  although the design aim was only  $\pm 0.05\%$  (Reference 18).

### 7.2 Flow Angles

For  $\bar{U}_{\text{NOM}} = 30$  m/s, between  $x_T = -2.0$  and  $+1.0$  m, horizontal flow angles varied from  $-0.8^\circ$  to  $+0.4^\circ$  (Figure 21) and vertical flow angles varied from  $-1.0^\circ$  to  $+0.4^\circ$  (Figure 22). For  $\bar{U}_{\text{NOM}} = 60$  m/s, horizontal flow angles varied from  $-0.6^\circ$  to  $+0.8^\circ$  (Figure 23) and vertical flow angles varied from  $-1.2^\circ$  to  $+0.4^\circ$  (Figure 24).

According to Reference 10, it would be desirable to have horizontal and vertical flow angle variations of less than  $\pm 0.10^\circ$ , but if this cannot be achieved, then the variations

should be held to within  $\pm 0.20^\circ$ . In Reference 16 it is indicated that acceptable flow angle variations for a high performance tunnel are  $\pm 0.1^\circ$ . For the German-Dutch wind tunnel (Reference 14), the horizontal and vertical flow angles vary by less than  $0.2^\circ$  across the central region of the  $8 \text{ m} \times 6 \text{ m}$  test section for a reference free-stream velocity of  $90 \text{ m/s}$ . According to Reference 17, horizontal and vertical flow angles should not deviate from the axial direction by more than  $\pm 0.25^\circ$ .

### 7.3 Turbulence Intensities and Spectra

For  $\bar{U}_{\text{NOM}} = 30$  and  $60 \text{ m/s}$ , for  $x_T = -2.0, -1.0, 0.0$  and  $+1.0 \text{ m}$ , values of  $(\bar{u}^2)^{0.5}/\bar{U}_{0.0}$  were generally below about  $0.4\%$ , whereas corresponding values of  $(\bar{v}^2)^{0.5}/\bar{U}_{0.0}$  and  $(\bar{w}^2)^{0.5}/\bar{U}_{0.0}$  were generally below about  $0.7\%$  (Figures 27 to 32). Spectra for the  $u$ -  $v$ - and  $w$ -components of the turbulence were relatively smooth over the frequency range  $0.3 \text{ Hz}$  to  $10 \text{ kHz}$ , with no significant spikes associated with irregularities in the flow (Figures 33 to 38).

Reference 13 indicates that a root-mean-square  $u$ -component fluctuation of  $0.1\%$  of the mean velocity is often quoted as low enough for most experiments and that the best low-turbulence research tunnels have a turbulence intensity of the order of  $0.02\%$  at low speeds. In Reference 10 it is indicated that tunnels used for developmental testing can have longitudinal turbulence intensities as high as  $0.5\%$ , and that tunnels used for research in boundary layers and boundary layer transition should have lateral values of intensity below about  $0.05\%$ . In the German-Dutch wind tunnel (Reference 14), the longitudinal intensities are quoted to be less than about  $0.08\%$  and the lateral intensities less than about  $0.15\%$  in the central region of the  $8 \text{ m} \times 6 \text{ m}$  test section for a reference free-stream velocity of  $75 \text{ m/s}$ . However, for a velocity of about  $40 \text{ m/s}$ , the longitudinal intensities are  $0.02\%$ , which is comparable with the best low turbulence wind tunnels.

### 7.4 Adequacy of Flow Quality in the LSWT

The foregoing suggests that although the quality of the flow in the extended test section of the LSWT is acceptable, it could be improved. However, there is no point spending a large amount of money on the tunnel to improve the flow if it is adequate for the investigations likely to be undertaken. The question of whether the quality of the flow is adequate depends upon the types of tests likely to be undertaken in the tunnel.

For flow-visualization investigations, where qualitative rather than quantitative answers are often required, the quality of the flow is not all that important and the tunnel should be adequate for this type of work.

For experiments in which boundary-layer transition phenomena are important, the free-stream turbulence intensities should be low since high intensities can cause early transition and this can lead to difficulties in interpreting experimental results.

Longitudinal turbulence intensities of 0.1% to 0.5%, similar to those in the LSWT, are classed as moderate turbulence levels (Reference 19), so that some lack of similarity may result if the tunnel was used for these types of experiments.

Accurate force, moment and surface pressure measurements taken on a model of say an aircraft are needed in a number of areas, including to determine loading programs for fatigue tests on full-scale aircraft, to provide data for the development of flight-dynamic models of aircraft behaviour, and to provide data for the verification of computational-fluid-dynamic (CFD) codes. If there are imperfections in the flow, then this may lead to data being produced that does not represent the full-scale aircraft to the accuracy required. For example, if the angle of the flow incident on one of the wings of a model of a typical fighter aircraft is  $1^\circ$  different from that on the other wing, due to the flow asymmetry in the test section, then potentially this could produce an error of the order of 5 to 10% in the maximum measured rolling moment coefficient for the aircraft. However, to provide accurate data from wind-tunnel tests to enable the performance of a full-scale aircraft to be predicted, irregularities in the flow is only one of the factors that needs to be considered. Reynolds number effects and the size of the model with respect to the size of the test section are also important.

Overall, the quality of the flow in the LSWT is considered to be adequate to enable tests to be carried out with sufficient accuracy to meet the requirements of the majority of the test programs undertaken in the tunnel.

## **8. Possible Causes of Flow Non Uniformities and Possible Methods for Improving the Flow**

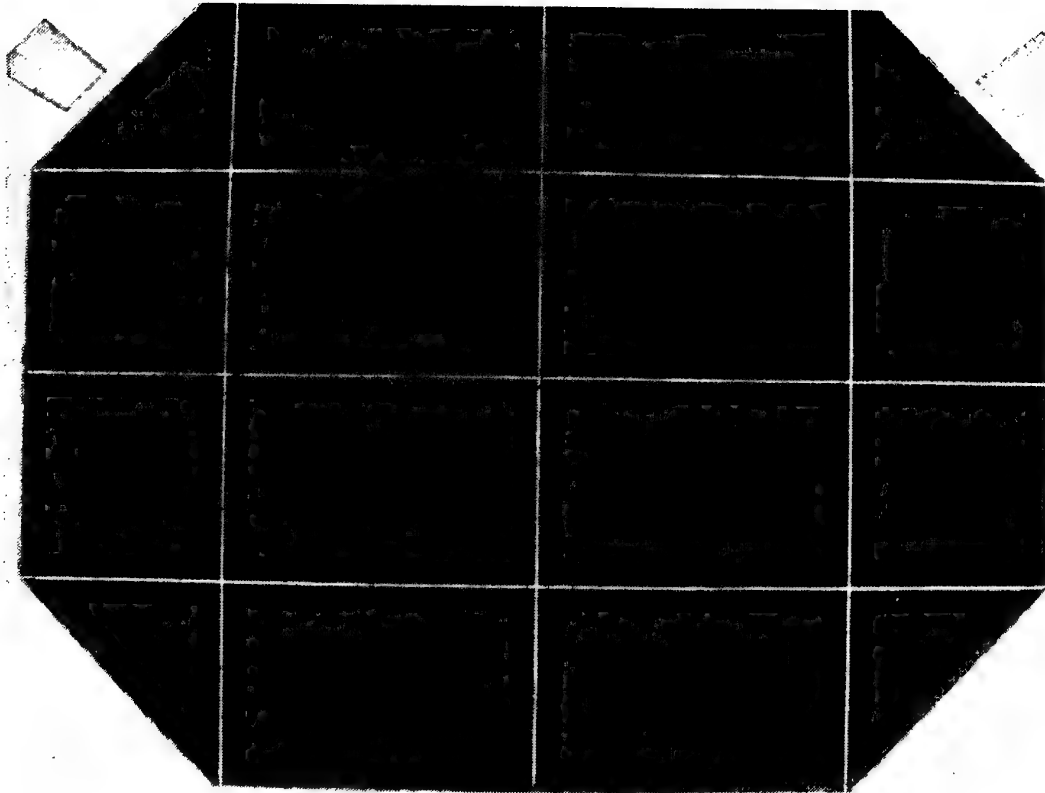
Flow irregularities in the test sections of wind tunnels may arise from a number of different flow mechanisms and generally it is not possible to identify with certainty the causes of these irregularities simply by analysing measured calibration data. Variations in mean velocity can be caused by flow separations in the tunnel return circuit, flow separations in the contraction, poor corner vane design or incorrectly set vanes (resulting in the vanes over or under turning the flow), and poor design of the fan or straightening vanes (resulting in a rotation of the whole flow downstream of the fan). Turbulence can be generated in the boundary layers on the tunnel walls and from the wakes of the fan blades, the turning vanes and the honeycombs. Angularity in the flow can persist into the test section if the honeycomb has cells of an inappropriate size and aspect ratio (see below). Despite the uncertainties involved in making a precise assessment of the causes of flow irregularities in a tunnel, it is possible to identify some of the likely causes for the irregularities in the extended test section of the LSWT at PSL.

If the contraction in a wind tunnel is not well designed then adverse pressure gradients can occur near the inlet and this can lead to either continuous flow separation, or

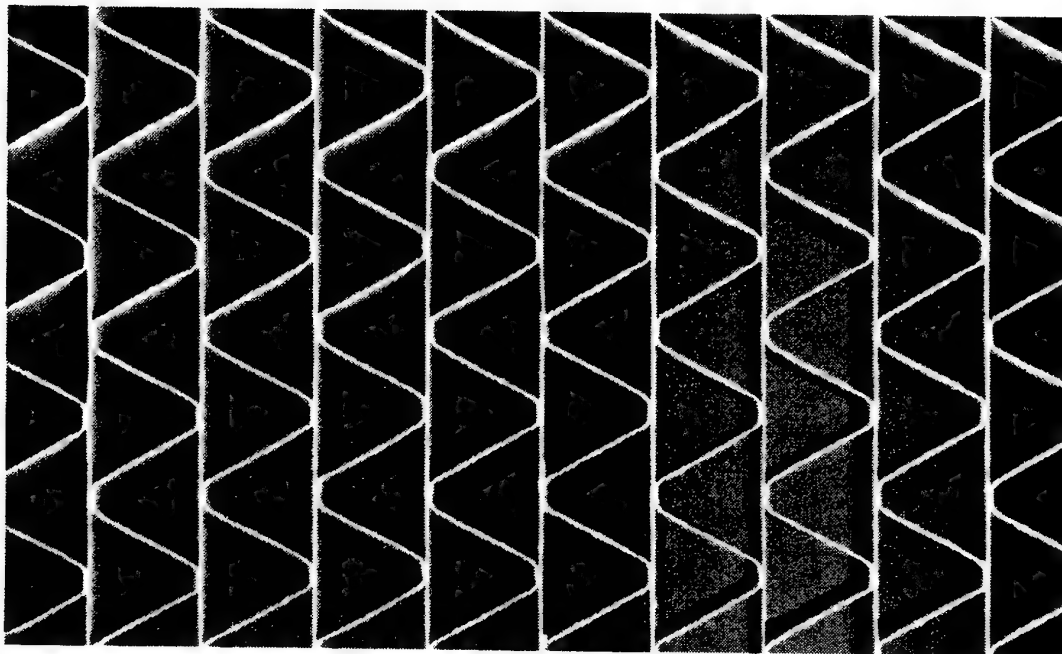
intermittent flow separation, depending on the magnitude of the adverse pressure gradient (Reference 10). This separation can have an adverse effect on the quality of the flow in the test section. Recent wool-tuft studies near the inlet of the new contraction did not show any evidence of flow separation. This suggests that the small flow irregularities that occur in the extended test section must come from other sources in the tunnel flow circuit.

Honeycombs and screens are known to improve the quality of the flow in the test section of a tunnel, both in terms of improved longitudinal and lateral mean-velocity distributions and reduced longitudinal and lateral turbulence intensities. Screens reduce longitudinal components of mean velocities and intensities more than lateral components, as for a contraction, whereas honeycombs reduce lateral components of mean velocities and intensities more than longitudinal components. The honeycomb in the LSWT has triangular cells whose frontal dimensions are 48, 41 and 41 mm and the depth of the cells is 127 mm (approximate dimensions), as shown in Figure 47. The diameter of a circle having the same cross-sectional area of a cell is about 32 mm so that the ratio of the depth of the cells to the effective diameter of the cells is about 4:1, which is somewhat lower than the recommended aspect ratio of about 6:1 to 8:1 (References 10 and 13). The sizes of the cells in the honeycomb are also larger than normal. In Reference 20, a study was made of honeycombs in wind tunnels and it was found that the honeycombs had cell sizes ranging from 1.6 mm (1/16 inch) to 9.5 mm (3/8 inch) and aspect ratios varying between 6:1 and 8:1. The existing honeycomb is not continuous as it has been installed in the tunnel in 16 sections. Between each section there is a solid edge about 15 mm thick and these edges may have a detrimental effect on the flow in the test section (Reference 10). If it is decided that a new honeycomb is needed (see below), then it should have cells with a smaller frontal area and a larger aspect ratio, and follow the design dimension guidelines given above. It would be preferable to use a honeycomb having hexagonal cells since the pressure loss for this type of honeycomb is less than for honeycombs having square or circular cross sections (Reference 10). It would probably be necessary to use some type of supporting structure to prevent the honeycomb deflecting, and it should be less intrusive than the rigid supporting structure presently in the tunnel. Currently the tunnel does not have any screens. If it is decided to install them, an open-to-total area ratio of the order of 57% is preferable (Reference 21).

Most likely there is not a single cause of the flow non uniformities and it may be necessary to change more than one component of the tunnel to obtain a large improvement in the quality of the flow in the test section. It is preferable that the modifications to the tunnel be carried out in stages. Extending the test section and installing a redesigned contraction has had only a minimal effect on improving the flow. It will be necessary to make additional modifications to the tunnel to improve the flow further. If it is decided to install a new honeycomb, then preformed aluminium hexagonal honeycomb or stacks of thin-walled hexagonal metal tubing could be inserted into the existing honeycomb structure to replace the current triangular cells and minimize cost. Modifying the honeycomb and/or installing screens would increase losses and reduce



(a) view of complete honeycomb, showing details of the 16 sections



(b) close-up view of the honeycomb, showing frontal details of the triangular cells

Figure 47. Honeycomb used in the low-speed wind tunnel.

the maximum velocity obtainable in the test section. Additional cleaning would also be necessary as both the modified honeycomb and screens could accumulate more dust which could change the quality of the flow with time (Reference 10). A new honeycomb may provide sufficient improvement in the flow without screens. Further studies would be needed to determine the best way to proceed.

## 9. Concluding Remarks

A detailed calibration of the flow in the extended test section of the low-speed wind tunnel is given in this report. An extensive range of longitudinal mean-flow velocities, flow angles, turbulence intensities and turbulence spectra were measured at up to 155 grid points across the flow for longitudinal positions,  $x_T$ , of  $-2.0$ ,  $-1.0$ ,  $0.0$  and  $+1.0$  m from the centre of the turntables in the test section and for nominal free-stream velocities,  $\bar{U}_{\text{NOM}}$ , ranging from 30 to 75 m/s.

Longitudinal mean-flow velocities were measured using pressure probes fitted to a rake which spanned the test section. Flow angles were measured using a six-hole probe mounted on a specially-designed traversing mechanism. Turbulence intensities and power spectral densities were obtained using constant-temperature hot-wire anemometers.

Considering approximately the central 50% of the cross-sectional area of the test section, between a length of  $x_T = -2.0$  and  $+1.0$  m, the following flow non-uniformities were observed.

### • Mean-Flow Velocities

For  $\bar{U}_{\text{NOM}} = 30$  m/s, longitudinal mean velocities deviated between  $-1.0\%$  and  $+1.4\%$  from the mean value at the centre of the test section ( $x_T = 0.0$ ,  $y_T = 0.0$  and  $z_T = 0.0$  m). Corresponding deviations for other values of  $\bar{U}_{\text{NOM}}$  were from  $-1.2\%$  to  $+1.6\%$  for  $\bar{U}_{\text{NOM}} = 45$  m/s, from  $-1.0\%$  to  $+1.4\%$  for  $\bar{U}_{\text{NOM}} = 60$  m/s, and from  $-1.2\%$  to  $+1.4\%$  for  $\bar{U}_{\text{NOM}} = 75$  m/s. No significant periodic variations in mean velocities were found.

### • Flow angles

For  $\bar{U}_{\text{NOM}} = 30$  m/s, horizontal flow angles varied from  $-0.8^\circ$  to  $+0.4^\circ$  and vertical flow angles varied from  $-1.0^\circ$  to  $+0.4^\circ$ . For  $\bar{U}_{\text{NOM}} = 60$  m/s, horizontal flow angles varied from  $-0.6^\circ$  to  $+0.8^\circ$  and vertical flow angles varied from  $-1.2^\circ$  to  $+0.4^\circ$ .

### • Turbulence Intensities and Spectra

For  $\bar{U}_{\text{NOM}} = 30$  and 60 m/s, at  $x_T = -2.0$ ,  $-1.0$ ,  $0.0$  and  $+1.0$  m, the root-mean-square u-component intensities were generally below about 0.4%, whereas corresponding v- and w-component intensities were generally below about 0.7%. Spectra for the u- v- and w-components of the turbulence were relatively smooth over the frequency range 0.3 Hz to 10 kHz, with no significant spikes associated with irregularities in the flow.

The installation of the extended test section and new contraction in 1996 has slightly improved the quality of the flow in the test section, but some variations in mean velocities, flow angles, turbulence intensities and spectra still remain. From the present calibration measurements it is not possible to identify with certainty the causes of these irregularities. Wool-tuft studies near the inlet to the new contraction did not show any evidence of flow separation, and it is unlikely that the flow irregularities result from any flow separation in this area. The honeycomb has larger cells with a lower aspect ratio (cell depth divided by effective cell diameter) than recommended for this type of tunnel, and this could contribute to the irregularities. If further improvement of flow quality is required, the honeycomb could be replaced with one having smaller cells that have a larger aspect ratio. The tunnel does not have any screens and it may be necessary to install them to reduce turbulence intensities. However, this will result in a reduction in the maximum velocity obtainable in the test section and increased maintenance, particularly cleaning.

## **10. Acknowledgements**

The author is grateful for help received from Dr N. Matheson, Head Flight Mechanics Technology, and from Messrs P. T. Malone, I. D. Amott, A. A. Gonzalez, J. C. Clayton, D. M. Carnell and G. D. Ainger, who assisted with the experimental program.

## 11. References

1. 'The 9 ft.  $\times$  7 ft. wind tunnel at C.S.I.R. Division of Aeronautics, Fishermen's Bend, Melbourne'. *Report No. A.6.*, Council for Scientific and Industrial Research, Division of Aeronautics, August 1943.
2. Watmuff, J. H. 'Design of a new contraction for the ARL low speed wind tunnel'. *Aerodynamics Report 171*, Aeronautical Research Laboratories, Melbourne, Australia, August 1986.
3. Erm, L. P. 'Calibration of the flow in the test section of the low-speed wind tunnel at AMRL'. *DSTO Technical Report 1073*, Aeronautical & Maritime Research Laboratory, Melbourne, Australia, November 2000.
4. 'U. S. Standard Atmosphere 1962'. Prepared under sponsorship of National Aeronautics and Space Administration, United States Air Force and United States Weather Bureau, Washington, D. C. For sale by the Superintendent of Documents, U. S. Government Printing Office, Washington 25, D. C., USA.
5. Pressures Systems Incorporated. 'System 8400 Users Manual, Version 3.0'. Published by Pressures Systems Incorporated, Hampton, Virginia, USA, May 1990.
6. Glaister, M. K. & Hill, S. D. 'Electronic pressure scanning experience and software development'. *Proceedings of the Commonwealth Advisory Aeronautical Research Council (CAARC) specialists meeting on experimental aerodynamics and test techniques*, Defence Research Agency, Farnborough, UK, September 1992.
7. Chue, S. H. 'Pressure probes for fluid measurement'. *Progress in Aerospace Sciences*, Vol. 16, No. 2, 1975.
8. Melbourne, W. H. & Griss, R. J. 'Digital computation of velocity vectors using a suitably calibrated hemispherical head yawmeter'. *Aerodynamics Technical Memorandum 245*, Aeronautical Research Laboratories, Melbourne, Australia, November 1968.
9. Fairlie, B. D. 'Algorithms for the reduction of wind-tunnel data derived from strain gauge force balances'. *Aerodynamics Report 164*, Aeronautical Research Laboratories, Melbourne, Australia, May 1984.
10. Rae, W. H. Jr. & Pope, A. 'Low-speed wind tunnel testing', John Wiley & Sons, New York, USA, 1984.



11. Erm, L. P. 'Modifications to a constant-temperature hot-wire anemometer system to measure higher-order turbulence terms using digital signal processing'. *DSTO Technical Report 0506*, Aeronautical and Maritime Research Laboratory, Melbourne, Australia, September 1997.
12. Watmuff, J. H. 'A hybrid hot-wire data acquisition system'. *Aerodynamics Report 172*, Aeronautical Research Laboratories, Melbourne, Australia, November 1986.
13. Bradshaw, P. '*Experimental fluid mechanics*'. Pergamon Press Ltd, London, UK, 1964.
14. 'Compilation of calibration data of the German-Dutch wind tunnel'. *Duits-Nederlandse Windtunnel, Deutsch-Niederlandischer Windkanal*, MP-82.01, March 1982.
15. Blackman, R. B. '*Linear data-smoothing and prediction in theory and practice*'. Addison-Wesley, Massachusetts, USA, 1965.
16. Bradshaw, P. & Pankhurst, R. C. 'The design of low speed wind tunnels'. *Progress in Aeronautical Sciences*, Vol. 5, Edited by D. Kucheman & L. H. G. Sterne, Pergamon Press, New York, USA, 1964.
17. Gorlin, S. M. & Slezinger, I. I. 'Wind tunnels and their instrumentation'. Translated from Russian, Israel Program for Scientific Translations, Jerusalem, 1966.
18. Spence, A. Woodward, D. S., Caiger, M. T., Sadler, A. J. & Jeffery, R. W. 'The RAE 5 metre pressurised low speed wind tunnel'. Proceedings of the Eleventh Congress of the International Council of the Aeronautical Sciences, Lisbon, Spain, September 1978.
19. Coles, D. E. 'The turbulent boundary layer in a compressible fluid'. *Rand Report R-403-PR*, Appendix A: A manual of experimental boundary layer practice for low-speed flow, September 1962.
20. Scheiman, J. & Brooks, J. D. 'Comparison of experimental and theoretical turbulence reduction from screens, honeycomb, and honeycomb-screen combinations'. *JAS*, Vol. 18, pp. 638-643, 1981.
21. Bradshaw, P. 'The effect of wind tunnel screens on nominally two-dimensional boundary layers'. *J. Fluid Mech.*, Vol. 22, pp. 679-689, 1965.

## Appendix A: Modifications to the LSWT in 1996

To enable longer models to be tested, an extended test section and a new contraction were installed in the LSWT in 1996. It was anticipated that these modifications would also produce a slight improvement in the quality of the flow in the test section. The tunnel was modified according to the design recommendations given in 1986 by Watmuff (see Reference 2).

### A.1 Details of the Extended Test Section

The length of the test section was increased from 4.12 m to 6.56 m by installing a liner in the tunnel upstream of the original test section. The cross-sectional dimensions of the extended test section were the same as those for the existing test section.

### A.2 Details of the New Contraction

The cross-sectional dimensions of the new contraction at its inlet and outlet were the same as those for the original contraction.

The procedure used by Watmuff to select a new contraction shape for the LSWT is described in detail in Reference 2, and summarized in the following.

Watmuff indicated that a variety of axi-symmetric contraction shapes can be specified by two simple polynomial arcs which are joined together at an inflection point (see Reference 2), as shown in Figure A1. Using the notation shown in this figure, the equations for the two arcs, AB and BC, are respectively

$$R = R_i - A_1 x^n \quad (A1)$$

and

$$R = R_o + A_2 (L_c - x)^n \quad (A2)$$

where  $R$  is the distance from the tunnel centreline to the surface of an axi-symmetric contraction and  $x$  is the distance from the contraction inlet in the longitudinal direction. Subscripts  $i$  and  $o$  refer to the inlet and the outlet of the contraction respectively.  $L_c$  denotes the contraction length and  $n$  is an exponent which controls the maximum steepness of the contraction shape. By matching the gradient of the arcs at the inflection point, the constants  $A_1$  and  $A_2$  are given by

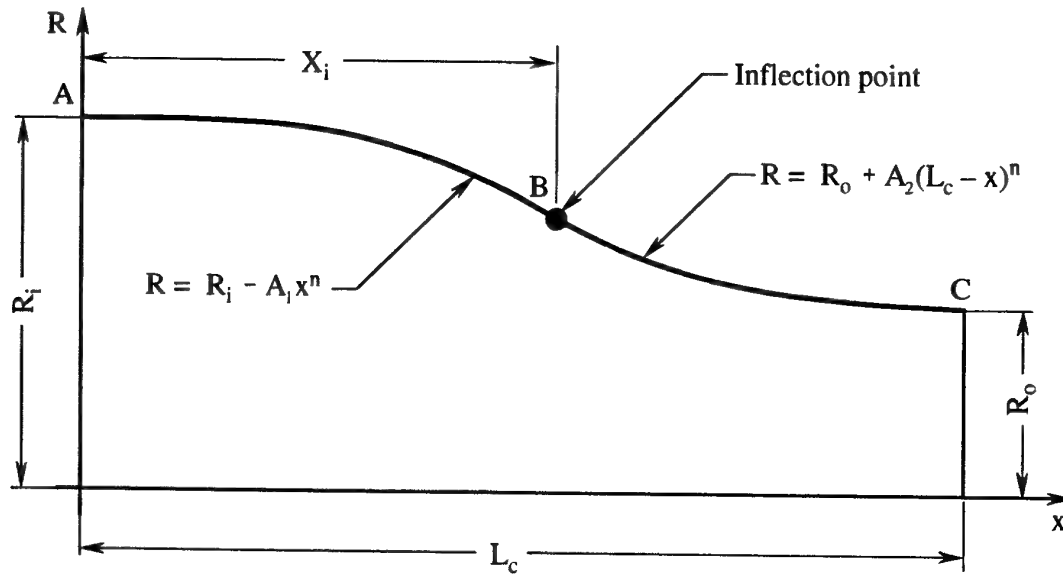


Figure A1. Notation for contraction wall contour constructed from two arcs (based on a figure given in Reference 2).

$$A_1 = \frac{R_i - R_o}{X_i^{(n-1)} L_c} \quad (A3)$$

and

$$A_2 = \frac{R_i - R_o}{(L_c - X_i)^{(n-1)} L_c} \quad (A4)$$

respectively.  $X_i$  is the longitudinal distance from the contraction inlet to the inflection point. Different contraction shapes are obtained using different values of  $L_c$ ,  $n$ ,  $R_i$ ,  $R_o$  and  $X_i$ .

A question that had to be answered by Watmuff was what values of these parameters were the "best" to use for the new contraction in the LSWT. He decided that the shape of the new contraction should be selected on the basis of the likely pressure distribution along its length. He indicated that a reasonable criterion for the selection of a new contraction shape is to minimize any adverse pressure gradient near the contraction inlet while not significantly increasing the adverse pressure gradient near the contraction outlet, compared with the then existing contraction. It is known that adverse pressure gradients at the inlet to a contraction should be as small as possible to reduce the likelihood of flow separation at the contraction inlet, which could adversely affect the flow quality in the test section (Reference 10). Watmuff developed a numerical method

for the solution of Stoke's stream function, enabling pressure distributions for idealized axi-symmetric flow to be predicted. He used the technique to predict idealized flow through the then existing LSWT contraction shape, using the approximation of axial symmetry for the octagonal cross section of the contraction, and also neglecting viscous forces. Calculated theoretical pressure distributions were compared with experimental measurements obtained in a pilot tunnel using a scale model of the contraction specially built to measure the pressure distributions. Reasonable agreement was obtained, which meant that the method could be used to determine a new contraction shape for the LSWT.

Watmuff calculated the likely pressure distributions along a range of axi-symmetric contractions having different values of  $n$ ,  $X_i/L_c$  and  $L_c/D_i$ , where  $D_i$  is the inlet diameter of an axi-symmetric contraction. He showed that for  $n = 3.0$ ,  $X_i/L_c = 0.5$  and  $L_c/D_i = 1.0$ , the calculated pressure gradients at the inlet and outlet of a contraction were about 20% and 90% respectively of those for the then existing contraction. Based on this finding, the dimensions of the eight surfaces of a new octagonal contraction for the LSWT were made to correspond to  $n = 3.0$ ,  $X_i/L_c = 0.5$  and  $L_c/D_i = 1.0$ , where  $D_i = 2R_i = 5187.7^3$  mm is the diameter of a circle having the same cross-sectional area as the inlet to the contraction in the LSWT. Similarly,  $D_o = 2R_o = 2593.9$  mm is the diameter of a circle having the same cross-sectional area as the outlet to the contraction in the LSWT.

A diagrammatic view of the new and original (prior to being modified in 1996) contractions is shown in Figure A2. The curved surfaces of the new contraction, labeled as curves 1, 2, 3 and 4 in Figure A2, are defined in terms of mathematical relationships. Curves 2 and 4 for the corner fillets are the same. It is convenient to use a different coordinate system for each type of curved surface when specifying dimensions. The coordinate system for curve 1 is shown by thick lines in Figure A2. The coordinate systems for curves 2, 3 and 4 have the same origin and the same x axis as the coordinate system for curve 1, but are rolled about the x axis by  $45^\circ$ ,  $90^\circ$  and  $135^\circ$  respectively, as shown in Figure A2 (z axes not shown to avoid confusion).

Parameters have the following values for the different curves:

- Curve 1 (upper and lower surfaces)

$$L_c = 5187.7 \text{ mm}$$

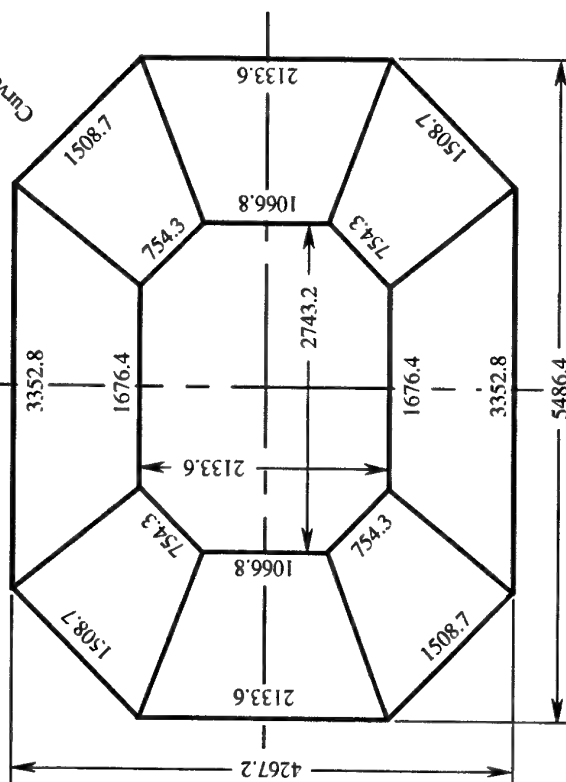
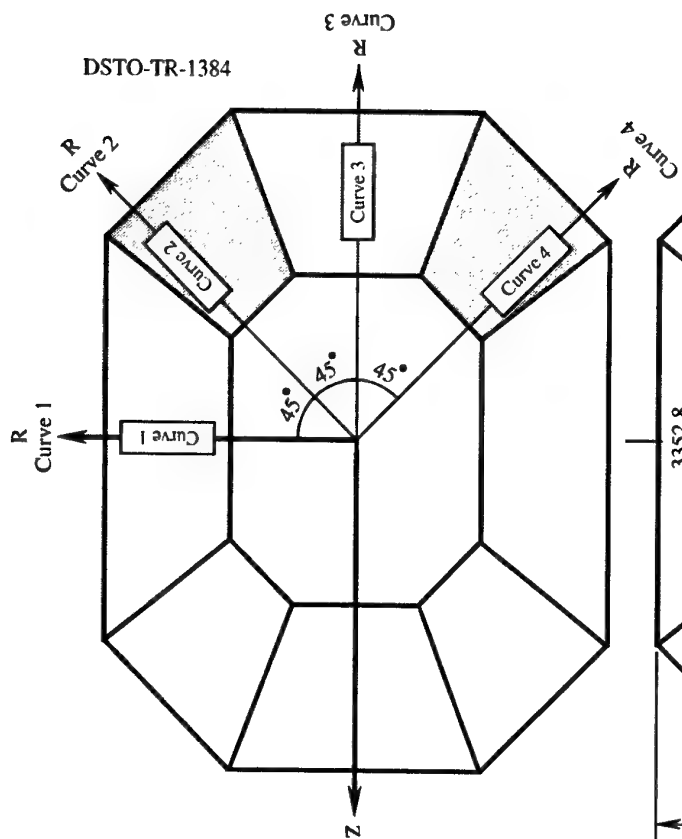
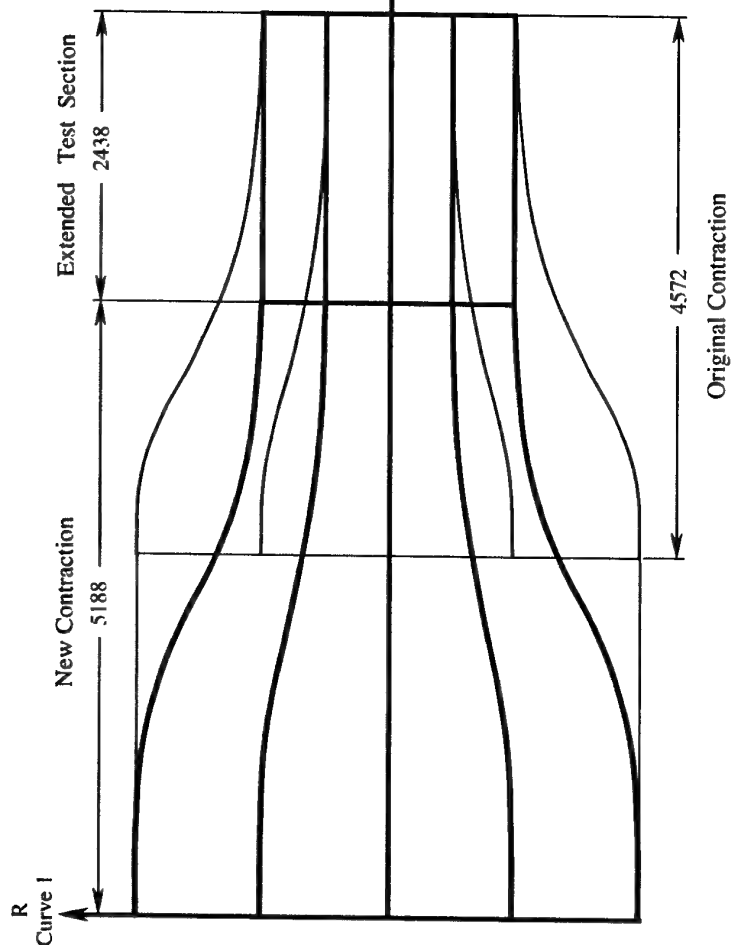
$$n = 3.0$$

$$R_i = 2133.6 \text{ mm}$$

$$R_o = 1066.8 \text{ mm}$$

$$X_i = 2593.9 \text{ mm}$$

<sup>3</sup> In this Appendix, dimensions are given to an accuracy of 0.1 mm since it may be necessary in the future to set up the idealized boundaries of the flow when predicting the flow through the tunnel using computational-fluid-dynamic (CFD) techniques.



All Dimensions in mm

Figure A2. Diagrammatic representation of the new and original contractions, showing the coordinate systems used to define the curved surfaces on the new contraction.

- Curves 2 and 4 (surfaces forming the corner fillets)

$$L_c = 5187.7 \text{ mm}$$

$$n = 3.0$$

$$R_i = 2694.1 \text{ mm}$$

$$R_o = 1347.0 \text{ mm}$$

$$X_i = 2593.9 \text{ mm}$$

- Curve 3 (side surfaces)

$$L_c = 5187.7 \text{ mm}$$

$$n = 3.0$$

$$R_i = 2743.2 \text{ mm}$$

$$R_o = 1371.6 \text{ mm}$$

$$X_i = 2593.9 \text{ mm}$$

Using these parameters,  $x$  and  $R$  coordinates corresponding to the four different curves were computed using equations A1 to A4 and the coordinates are given in Tables A1 to A4. Coordinates were computed for  $x$  increments of 50 mm. Positive and negative values of  $z$  defining points on a surface where it intersects with adjoining surfaces are also shown in Tables A1 to A4. All dimensions given in Tables A1 to A4 apply to the inner-flow surfaces of the contraction. The contraction was constructed to these coordinates.

Table A1. Dimensions of the Upper and Lower Surfaces of the Contraction (Curve 1).

x mm	R mm	z (+) mm	z (-) mm	x mm	R mm	z (+) mm	z (-) mm
0.0	2133.6	1676.4	-1676.4	2600.0	1596.4	1254.3	-1254.3
50.0	2133.6	1676.4	-1676.4	2650.0	1566.3	1230.7	-1230.7
100.0	2133.6	1676.4	-1676.4	2700.0	1537.4	1207.9	-1207.9
150.0	2133.5	1676.3	-1676.3	2750.0	1509.6	1186.1	-1186.1
200.0	2133.4	1676.2	-1676.2	2800.0	1482.9	1165.1	-1165.1
250.0	2133.1	1676.0	-1676.0	2850.0	1457.3	1145.0	-1145.0
300.0	2132.8	1675.8	-1675.8	2900.0	1432.8	1125.7	-1125.7
350.0	2132.3	1675.4	-1675.4	2950.0	1409.3	1107.3	-1107.3
400.0	2131.6	1674.9	-1674.9	3000.0	1386.8	1089.7	-1089.7
450.0	2130.8	1674.2	-1674.2	3050.0	1365.4	1072.8	-1072.8
500.0	2129.8	1673.4	-1673.4	3100.0	1344.9	1056.7	-1056.7
550.0	2128.5	1672.4	-1672.4	3150.0	1325.4	1041.4	-1041.4
600.0	2127.0	1671.2	-1671.2	3200.0	1306.8	1026.8	-1026.8
650.0	2125.2	1669.8	-1669.8	3250.0	1289.2	1012.9	-1012.9
700.0	2123.1	1668.2	-1668.2	3300.0	1272.4	999.7	-999.7
750.0	2120.7	1666.3	-1666.3	3350.0	1256.5	987.2	-987.2
800.0	2118.0	1664.1	-1664.1	3400.0	1241.4	975.4	-975.4
850.0	2114.8	1661.7	-1661.7	3450.0	1227.2	964.2	-964.2
900.0	2111.3	1658.9	-1658.9	3500.0	1213.7	953.6	-953.6
950.0	2107.4	1655.8	-1655.8	3550.0	1201.1	943.7	-943.7
1000.0	2103.0	1652.4	-1652.4	3600.0	1189.1	934.3	-934.3
1050.0	2098.2	1648.6	-1648.6	3650.0	1177.9	925.5	-925.5
1100.0	2092.9	1644.4	-1644.4	3700.0	1167.4	917.3	-917.3
1150.0	2087.1	1639.9	-1639.9	3750.0	1157.6	909.6	-909.6
1200.0	2080.8	1634.9	-1634.9	3800.0	1148.5	902.4	-902.4
1250.0	2073.9	1629.5	-1629.5	3850.0	1140.0	895.7	-895.7
1300.0	2066.5	1623.6	-1623.6	3900.0	1132.1	889.5	-889.5
1350.0	2058.4	1617.3	-1617.3	3950.0	1124.8	883.7	-883.7
1400.0	2049.7	1610.5	-1610.5	4000.0	1118.0	878.4	-878.4
1450.0	2040.4	1603.2	-1603.2	4050.0	1111.8	873.6	-873.6
1500.0	2030.4	1595.4	-1595.4	4100.0	1106.1	869.1	-869.1
1550.0	2019.8	1587.0	-1587.0	4150.0	1101.0	865.0	-865.0
1600.0	2008.4	1578.0	-1578.0	4200.0	1096.3	861.3	-861.3
1650.0	1996.3	1568.5	-1568.5	4250.0	1092.0	858.0	-858.0
1700.0	1983.4	1558.4	-1558.4	4300.0	1088.2	855.0	-855.0
1750.0	1969.8	1547.7	-1547.7	4350.0	1084.8	852.3	-852.3
1800.0	1955.4	1536.3	-1536.3	4400.0	1081.7	849.9	-849.9
1850.0	1940.1	1524.4	-1524.4	4450.0	1079.1	847.8	-847.8
1900.0	1924.0	1511.7	-1511.7	4500.0	1076.7	846.0	-846.0
1950.0	1907.0	1498.3	-1498.3	4550.0	1074.7	844.4	-844.4
2000.0	1889.1	1484.3	-1484.3	4600.0	1073.0	843.1	-843.1
2050.0	1870.3	1469.5	-1469.5	4650.0	1071.6	841.9	-841.9
2100.0	1850.6	1454.0	-1454.0	4700.0	1070.3	841.0	-841.0
2150.0	1829.8	1437.7	-1437.7	4750.0	1069.4	840.2	-840.2
2200.0	1808.2	1420.7	-1420.7	4800.0	1068.6	839.6	-839.6
2250.0	1785.5	1402.9	-1402.9	4850.0	1068.0	839.1	-839.1
2300.0	1761.7	1384.2	-1384.2	4900.0	1067.5	838.8	-838.8
2350.0	1737.0	1364.7	-1364.7	4950.0	1067.2	838.5	-838.5
2400.0	1711.1	1344.4	-1344.4	5000.0	1067.0	838.4	-838.4
2450.0	1684.1	1323.2	-1323.2	5050.0	1066.9	838.3	-838.3
2500.0	1656.0	1301.2	-1301.2	5100.0	1066.8	838.2	-838.2
2550.0	1626.8	1278.2	-1278.2	5150.0	1066.8	838.2	-838.2
2593.9	1600.2	1257.3	-1257.3	5187.7	1066.8	838.2	-838.2

Table A2. Dimensions of the Corner-Fillet Surfaces of the Contraction (Curve 2).

x mm	R mm	z (+) mm	z (-) mm	x mm	R mm	z (+) mm	z (-) mm
0.0	2694.1	323.6	-1185.0	2600.0	2015.8	242.1	-886.6
50.0	2694.1	323.6	-1185.0	2650.0	1977.8	237.6	-869.9
100.0	2694.1	323.6	-1185.0	2700.0	1941.2	233.2	-853.8
150.0	2694.0	323.6	-1184.9	2750.0	1906.1	229.0	-838.4
200.0	2693.8	323.6	-1184.8	2800.0	1872.4	224.9	-823.6
250.0	2693.5	323.5	-1184.7	2850.0	1840.1	221.0	-809.4
300.0	2693.1	323.5	-1184.5	2900.0	1809.1	217.3	-795.7
350.0	2692.4	323.4	-1184.3	2950.0	1779.5	213.8	-782.7
400.0	2691.6	323.3	-1183.9	3000.0	1751.1	210.4	-770.2
450.0	2690.6	323.2	-1183.4	3050.0	1724.0	207.1	-758.3
500.0	2689.3	323.0	-1182.9	3100.0	1698.2	204.0	-747.0
550.0	2687.7	322.8	-1182.2	3150.0	1673.6	201.0	-736.1
600.0	2685.8	322.6	-1181.3	3200.0	1650.1	198.2	-725.8
650.0	2683.5	322.3	-1180.3	3250.0	1627.8	195.5	-716.0
700.0	2680.9	322.0	-1179.2	3300.0	1606.6	193.0	-706.7
750.0	2677.8	321.7	-1177.8	3350.0	1586.5	190.6	-697.8
800.0	2674.3	321.2	-1176.3	3400.0	1567.5	188.3	-689.5
850.0	2670.4	320.8	-1174.6	3450.0	1549.5	186.1	-681.6
900.0	2666.0	320.2	-1172.6	3500.0	1532.5	184.1	-674.1
950.0	2661.0	319.6	-1170.4	3550.0	1516.5	182.2	-667.1
1000.0	2655.5	319.0	-1168.0	3600.0	1501.5	180.4	-660.4
1050.0	2649.4	318.3	-1165.3	3650.0	1487.3	178.7	-654.2
1100.0	2642.7	317.4	-1162.4	3700.0	1474.1	177.1	-648.4
1150.0	2635.4	316.6	-1159.2	3750.0	1461.7	175.6	-642.9
1200.0	2627.4	315.6	-1155.6	3800.0	1450.1	174.2	-637.9
1250.0	2618.7	314.6	-1151.8	3850.0	1439.4	172.9	-633.1
1300.0	2609.3	313.4	-1147.7	3900.0	1429.4	171.7	-628.7
1350.0	2599.1	312.2	-1143.2	3950.0	1420.2	170.6	-624.7
1400.0	2588.2	310.9	-1138.4	4000.0	1411.7	169.6	-620.9
1450.0	2576.4	309.5	-1133.2	4050.0	1403.8	168.6	-617.5
1500.0	2563.8	308.0	-1127.7	4100.0	1396.7	167.8	-614.3
1550.0	2550.4	306.4	-1121.8	4150.0	1390.1	167.0	-611.5
1600.0	2536.0	304.6	-1115.5	4200.0	1384.2	166.3	-608.8
1650.0	2520.7	302.8	-1108.7	4250.0	1378.8	165.6	-606.5
1700.0	2504.5	300.8	-1101.6	4300.0	1374.0	165.1	-604.4
1750.0	2487.3	298.8	-1094.0	4350.0	1369.7	164.5	-602.5
1800.0	2469.0	296.6	-1086.0	4400.0	1365.9	164.1	-600.8
1850.0	2449.7	294.3	-1077.5	4450.0	1362.5	163.7	-599.3
1900.0	2429.4	291.8	-1068.6	4500.0	1359.6	163.3	-598.0
1950.0	2407.9	289.2	-1059.1	4550.0	1357.0	163.0	-596.9
2000.0	2385.3	286.5	-1049.2	4600.0	1354.8	162.8	-595.9
2050.0	2361.6	283.7	-1038.7	4650.0	1353.0	162.5	-595.1
2100.0	2336.7	280.7	-1027.8	4700.0	1351.5	162.3	-594.5
2150.0	2310.5	277.5	-1016.3	4750.0	1350.2	162.2	-593.9
2200.0	2283.2	274.3	-1004.2	4800.0	1349.2	162.1	-593.5
2250.0	2254.5	270.8	-991.6	4850.0	1348.5	162.0	-593.1
2300.0	2224.5	267.2	-978.5	4900.0	1347.9	161.9	-592.9
2350.0	2193.2	263.5	-964.7	4950.0	1347.5	161.9	-592.7
2400.0	2160.6	259.5	-950.3	5000.0	1347.3	161.8	-592.6
2450.0	2126.5	255.4	-935.4	5050.0	1347.1	161.8	-592.5
2500.0	2091.1	251.2	-919.8	5100.0	1347.0	161.8	-592.5
2550.0	2054.2	246.8	-903.5	5150.0	1347.0	161.8	-592.5
2593.9	2020.5	242.7	-888.7	5187.7	1347.0	161.8	-592.5



Table A3. Dimensions of the Side Surfaces of the Contraction (Curve 3).

x mm	R mm	z (+) mm	z (-) mm	x mm	R mm	z (+) mm	z (-) mm
0.0	2743.2	1066.8	-1066.8	2600.0	2052.6	798.2	-798.2
50.0	2743.2	1066.8	-1066.8	2650.0	2013.8	783.2	-783.2
100.0	2743.2	1066.8	-1066.8	2700.0	1976.6	768.7	-768.7
150.0	2743.1	1066.7	-1066.7	2750.0	1940.9	754.8	-754.8
200.0	2742.9	1066.7	-1066.7	2800.0	1906.6	741.4	-741.4
250.0	2742.6	1066.6	-1066.6	2850.0	1873.6	728.6	-728.6
300.0	2742.1	1066.4	-1066.4	2900.0	1842.1	716.4	-716.4
350.0	2741.5	1066.1	-1066.1	2950.0	1811.9	704.6	-704.6
400.0	2740.7	1065.8	-1065.8	3000.0	1783.1	693.4	-693.4
450.0	2739.6	1065.4	-1065.4	3050.0	1755.5	682.7	-682.7
500.0	2738.3	1064.9	-1064.9	3100.0	1729.2	672.5	-672.5
550.0	2736.7	1064.3	-1064.3	3150.0	1704.1	662.7	-662.7
600.0	2734.7	1063.5	-1063.5	3200.0	1680.2	653.4	-653.4
650.0	2732.4	1062.6	-1062.6	3250.0	1657.5	644.6	-644.6
700.0	2729.7	1061.6	-1061.6	3300.0	1635.9	636.2	-636.2
750.0	2726.6	1060.4	-1060.4	3350.0	1615.5	628.2	-628.2
800.0	2723.1	1059.0	-1059.0	3400.0	1596.1	620.7	-620.7
850.0	2719.1	1057.4	-1057.4	3450.0	1577.8	613.6	-613.6
900.0	2714.6	1055.7	-1055.7	3500.0	1560.5	606.9	-606.9
950.0	2709.5	1053.7	-1053.7	3550.0	1544.2	600.5	-600.5
1000.0	2703.9	1051.5	-1051.5	3600.0	1528.9	594.6	-594.6
1050.0	2697.7	1049.1	-1049.1	3650.0	1514.5	589.0	-589.0
1100.0	2690.9	1046.5	-1046.5	3700.0	1501.0	583.7	-583.7
1150.0	2683.4	1043.6	-1043.6	3750.0	1488.4	578.8	-578.8
1200.0	2675.3	1040.4	-1040.4	3800.0	1476.6	574.2	-574.2
1250.0	2666.5	1037.0	-1037.0	3850.0	1465.7	570.0	-570.0
1300.0	2656.9	1033.2	-1033.2	3900.0	1455.5	566.0	-566.0
1350.0	2646.5	1029.2	-1029.2	3950.0	1446.1	562.4	-562.4
1400.0	2635.4	1024.9	-1024.9	4000.0	1437.4	559.0	-559.0
1450.0	2623.4	1020.2	-1020.2	4050.0	1429.5	555.9	-555.9
1500.0	2610.6	1015.2	-1015.2	4100.0	1422.2	553.1	-553.1
1550.0	2596.9	1009.9	-1009.9	4150.0	1415.5	550.5	-550.5
1600.0	2582.2	1004.2	-1004.2	4200.0	1409.5	548.1	-548.1
1650.0	2566.7	998.2	-998.2	4250.0	1404.0	546.0	-546.0
1700.0	2550.1	991.7	-991.7	4300.0	1399.1	544.1	-544.1
1750.0	2532.6	984.9	-984.9	4350.0	1394.7	542.4	-542.4
1800.0	2514.0	977.7	-977.7	4400.0	1390.8	540.9	-540.9
1850.0	2494.4	970.0	-970.0	4450.0	1387.4	539.5	-539.5
1900.0	2473.7	962.0	-962.0	4500.0	1384.4	538.4	-538.4
1950.0	2451.8	953.5	-953.5	4550.0	1381.8	537.4	-537.4
2000.0	2428.8	944.5	-944.5	4600.0	1379.6	536.5	-536.5
2050.0	2404.7	935.1	-935.1	4650.0	1377.7	535.8	-535.8
2100.0	2379.3	925.3	-925.3	4700.0	1376.2	535.2	-535.2
2150.0	2352.7	914.9	-914.9	4750.0	1374.9	534.7	-534.7
2200.0	2324.8	904.1	-904.1	4800.0	1373.9	534.3	-534.3
2250.0	2295.6	892.7	-892.7	4850.0	1373.1	534.0	-534.0
2300.0	2265.1	880.9	-880.9	4900.0	1372.5	533.8	-533.8
2350.0	2233.2	868.5	-868.5	4950.0	1372.1	533.6	-533.6
2400.0	2200.0	855.5	-855.5	5000.0	1371.9	533.5	-533.5
2450.0	2165.3	842.1	-842.1	5050.0	1371.7	533.4	-533.4
2500.0	2129.2	828.0	-828.0	5100.0	1371.6	533.4	-533.4
2550.0	2091.6	813.4	-813.4	5150.0	1371.6	533.4	-533.4
2593.9	2057.4	800.1	-800.1	5187.7	1371.6	533.4	-533.4

Table A4. Dimensions of the Corner-Fillet Surfaces of the Contraction (Curve 4).

x mm	R mm	z (+) mm	z (-) mm	x mm	R mm	z (+) mm	z (-) mm
0.0	2694.1	1185.0	-323.6	2600.0	2015.8	886.6	-242.1
50.0	2694.1	1185.0	-323.6	2650.0	1977.8	869.9	-237.6
100.0	2694.1	1185.0	-323.6	2700.0	1941.2	853.8	-233.2
150.0	2694.0	1184.9	-323.6	2750.0	1906.1	838.4	-229.0
200.0	2693.8	1184.8	-323.6	2800.0	1872.4	823.6	-224.9
250.0	2693.5	1184.7	-323.5	2850.0	1840.1	809.4	-221.0
300.0	2693.1	1184.5	-323.5	2900.0	1809.1	795.7	-217.3
350.0	2692.4	1184.3	-323.4	2950.0	1779.5	782.7	-213.8
400.0	2691.6	1183.9	-323.3	3000.0	1751.1	770.2	-210.4
450.0	2690.6	1183.4	-323.2	3050.0	1724.0	758.3	-207.1
500.0	2689.3	1182.9	-323.0	3100.0	1698.2	747.0	-204.0
550.0	2687.7	1182.2	-322.8	3150.0	1673.6	736.1	-201.0
600.0	2685.8	1181.3	-322.6	3200.0	1650.1	725.8	-198.2
650.0	2683.5	1180.3	-322.3	3250.0	1627.8	716.0	-195.5
700.0	2680.9	1179.2	-322.0	3300.0	1606.6	706.7	-193.0
750.0	2677.8	1177.8	-321.7	3350.0	1586.5	697.8	-190.6
800.0	2674.3	1176.3	-321.2	3400.0	1567.5	689.5	-188.3
850.0	2670.4	1174.6	-320.8	3450.0	1549.5	681.6	-186.1
900.0	2666.0	1172.6	-320.2	3500.0	1532.5	674.1	-184.1
950.0	2661.0	1170.4	-319.6	3550.0	1516.5	667.1	-182.2
1000.0	2655.5	1168.0	-319.0	3600.0	1501.5	660.4	-180.4
1050.0	2649.4	1165.3	-318.3	3650.0	1487.3	654.2	-178.7
1100.0	2642.7	1162.4	-317.4	3700.0	1474.1	648.4	-177.1
1150.0	2635.4	1159.2	-316.6	3750.0	1461.7	642.9	-175.6
1200.0	2627.4	1155.6	-315.6	3800.0	1450.1	637.9	-174.2
1250.0	2618.7	1151.8	-314.6	3850.0	1439.4	633.1	-172.9
1300.0	2609.3	1147.7	-313.4	3900.0	1429.4	628.7	-171.7
1350.0	2599.1	1143.2	-312.2	3950.0	1420.2	624.7	-170.6
1400.0	2588.2	1138.4	-310.9	4000.0	1411.7	620.9	-169.6
1450.0	2576.4	1133.2	-309.5	4050.0	1403.8	617.5	-168.6
1500.0	2563.8	1127.7	-308.0	4100.0	1396.7	614.3	-167.8
1550.0	2550.4	1121.8	-306.4	4150.0	1390.1	611.5	-167.0
1600.0	2536.0	1115.5	-304.6	4200.0	1384.2	608.8	-166.3
1650.0	2520.7	1108.7	-302.8	4250.0	1378.8	606.5	-165.6
1700.0	2504.5	1101.6	-300.8	4300.0	1374.0	604.4	-165.1
1750.0	2487.3	1094.0	-298.8	4350.0	1369.7	602.5	-164.5
1800.0	2469.0	1086.0	-296.6	4400.0	1365.9	600.8	-164.1
1850.0	2449.7	1077.5	-294.3	4450.0	1362.5	599.3	-163.7
1900.0	2429.4	1068.6	-291.8	4500.0	1359.6	598.0	-163.3
1950.0	2407.9	1059.1	-289.2	4550.0	1357.0	596.9	-163.0
2000.0	2385.3	1049.2	-286.5	4600.0	1354.8	595.9	-162.8
2050.0	2361.6	1038.7	-283.7	4650.0	1353.0	595.1	-162.5
2100.0	2336.7	1027.8	-280.7	4700.0	1351.5	594.5	-162.3
2150.0	2310.5	1016.3	-277.5	4750.0	1350.2	593.9	-162.2
2200.0	2283.2	1004.2	-274.3	4800.0	1349.2	593.5	-162.1
2250.0	2254.5	991.6	-270.8	4850.0	1348.5	593.1	-162.0
2300.0	2224.5	978.5	-267.2	4900.0	1347.9	592.9	-161.9
2350.0	2193.2	964.7	-263.5	4950.0	1347.5	592.7	-161.9
2400.0	2160.6	950.3	-259.5	5000.0	1347.3	592.6	-161.8
2450.0	2126.5	935.4	-255.4	5050.0	1347.1	592.5	-161.8
2500.0	2091.1	919.8	-251.2	5100.0	1347.0	592.5	-161.8
2550.0	2054.2	903.5	-246.8	5150.0	1347.0	592.5	-161.8
2593.9	2020.5	888.7	-242.7	5187.7	1347.0	592.5	-161.8

## **DISTRIBUTION LIST**

Calibration of the Flow in the Extended Test Section of the  
Low Speed Wind Tunnel at DSTO

Lincoln P. Erm

### **AUSTRALIA**

#### **DEFENCE ORGANISATION**

**Task Sponsor**  
DSTO

#### **S&T Program**

Chief Defence Scientist	}	shared copy
FAS Science Policy		
AS Science Corporate Management		
Director General Science Policy Development		
Counsellor Defence Science, London (Doc Data Sheet only)		
Counsellor Defence Science, Washington (Doc Data Sheet only)		
Scientific Adviser to MRDC Thailand (Doc Data Sheet only)		
Scientific Adviser Joint		
Navy Scientific Adviser (Doc Data Sheet and Distribution List only)		
Scientific Adviser - Army (Doc Data Sheet and Distribution List only)		
Air Force Scientific Adviser (Doc Data Sheet and Distribution List only)		
Scientific Adviser to the DMO (Doc Data Sheet and Distribution List only)		
Director of Trials		

#### **Platforms Sciences Laboratory**

Chief of Air Vehicles Division, C. R. Guy	
Research Leader Aircraft Systems, D. Graham	
Head Flight Mechanics Technology, N. Matheson	
Head Flight Dynamics Applications, J. S. Drobik	
Author, L. P. Erm (5 copies)	
V. Baskaran	A. H. Blandford
D. M. Carnell	J. C. Clayton
S. J. Coras	A. A. Gonzalez
K. A. Henderson	O. F. Holland
S. S. Lam	P. T. Malone
H. A. Quick	

#### **DSTO Library and Archives**

Library Fishermans Bend (Doc Data Sheet only)  
Australian Archives

**Capability Systems Division**

Director General Maritime Development (Doc Data Sheet only)  
Director General Aerospace Development (Doc Data Sheet only)  
Director General Information Capability Development (Doc Data Sheet only)

**Office of the Chief Information Officer**

Chief Information Officer (Doc Data Sheet only)  
Deputy CIO (Doc Data Sheet only)  
Director General Information Policy and Plans (Doc Data Sheet only)  
AS Information Structures and Futures (Doc Data Sheet only)  
AS Information Architecture and Management (Doc Data Sheet only)  
Director General Australian Defence Information Office (Doc Data Sheet only)  
Director General Australian Defence Simulation Office (Doc Data Sheet only)

**Strategy Group**

Director General Military Strategy (Doc Data Sheet only)  
Director General Preparedness (Doc Data Sheet only)

**HQAST**

SO (ASJIC) (Doc Data Sheet only)

**Navy**

Director General Navy Capability, Performance and Plans, Navy Headquarters (Doc Data Sheet only)  
Director General Navy Strategic Policy and Futures, Navy Headquarters (Doc Data Sheet only)

**Army**

SO (Science), Deployable Joint Force Headquarters (DJFHQ) (L), Enoggera QLD (Doc Data Sheet only)  
SO (Science) - Land Headquarters (LHQ), Victoria Barracks NSW (Doc Data Sheet and Executive Summary Only)

**Intelligence Program**

DGSTA Defence Intelligence Organisation  
Manager, Information Centre, Defence Intelligence Organisation  
Assistant Secretary Corporate, Defence Imagery and Geospatial Organisation (Doc Data Sheet only)

**Defence Materiel Organisation**

Head Airborne Surveillance and Control (Doc Data Sheet only)  
Head Aerospace Systems Division (Doc Data Sheet only)  
Head Electronic Systems Division (Doc Data Sheet only)  
Head Maritime Systems Division (Doc Data Sheet only)  
Head Land Systems Division (Doc Data Sheet only)

**Defence Libraries**

Library Manager, DLS-Canberra

Library Manager, DLS - Sydney West (Doc Data Sheet only)

**OUTSIDE AUSTRALIA****INTERNATIONAL DEFENCE INFORMATION CENTRES**

US Defense Technical Information Center, 2 copies

UK Defence Research Information Centre, 2 copies

Canada Defence Scientific Information Service, 1 copy

NZ Defence Information Centre, 1 copy

**ABSTRACTING AND INFORMATION ORGANISATIONS**

Library, Chemical Abstracts Reference Service

Engineering Societies Library, US

Materials Information, Cambridge Scientific Abstracts, US

Documents Librarian, The Center for Research Libraries, US

**INFORMATION EXCHANGE AGREEMENT PARTNERS**

Acquisitions Unit, Science Reference and Information Service, UK

SPARES (5 copies)

**Total number of copies:      43**

<b>DEFENCE SCIENCE AND TECHNOLOGY ORGANISATION</b> <b>DOCUMENT CONTROL DATA</b>				1. PRIVACY MARKING/CAVEAT (OF DOCUMENT)	
2. TITLE  Calibration of the Flow in the Extended Test Section of the Low-Speed Wind Tunnel at DSTO.			3. SECURITY CLASSIFICATION (FOR UNCLASSIFIED REPORTS THAT ARE LIMITED RELEASE USE (L) NEXT TO DOCUMENT CLASSIFICATION)  Document (U) Title (U) Abstract (U)		
4. AUTHOR(S)  Lincoln P. Erm			5. CORPORATE AUTHOR  Platforms Sciences Laboratory PO Box 4331 Melbourne Vic 3001		
6a. DSTO NUMBER DSTO-TR-1384		6b. AR NUMBER AR-012-551		6c. TYPE OF REPORT Technical Report	
7. DOCUMENT DATE January 2003		8. FILE NUMBER M1/9/971		9. TASK NUMBER RDI 01/255	
10. TASK SPONSOR RDI		11. NO. OF PAGES 121		12. NO. OF REFERENCES 21	
13. URL ON THE WORLD WIDE WEB  <a href="http://www.dsto.defence.gov.au/corporate/reports/DSTO-TR-1384.pdf">http://www.dsto.defence.gov.au/corporate/reports/DSTO-TR-1384.pdf</a>			14. RELEASE AUTHORITY  Chief, Air Vehicles Division		
15. SECONDARY RELEASE STATEMENT OF THIS DOCUMENT  <p style="text-align: center;"><i>Approved for public release</i></p> <p>OVERSEAS ENQUIRIES OUTSIDE STATED LIMITATIONS SHOULD BE REFERRED THROUGH DOCUMENT EXCHANGE. PO BOX 1500, SALISBURY. SA 5108.</p>					
16. DELIBERATE ANNOUNCEMENT  No limitations					
17. CASUAL ANNOUNCEMENT <span style="float: right;">Yes</span>					
18. DEFTTEST DESCRIPTORS  low speed wind tunnels, calibration, measurement, velocity, flow, turbulence, spectra					
19. ABSTRACT <p>In 1996, the circuit of the low-speed wind tunnel was modified by extending the length of the test section and installing a redesigned contraction. This was done to enable longer models to be tested in the tunnel and also to possibly obtain some improvement in the quality of the flow in the test section. In this report, the results are given of a detailed calibration of the flow in the extended test section of the tunnel. The calibration was performed to: (1) provide a data base of the flow quality, to be used when analysing tests carried out in the tunnel since 1996, and (2) provide a data base for assessing the changes in the flow quality resulting from installing the extended test section and new contraction in 1996. Longitudinal mean-flow velocities, flow angles, turbulence intensities and spectra, were measured at up to 155 grid points across the flow for longitudinal positions of <math>x_T = -2.0, -1.0, 0.0</math> and <math>+1.0</math> m from the centre of the turntables in the test section for nominal free-stream velocities of 30, 45, 60 and 75 m/s. The most important area of the test section, where models are usually located, is the region comprising approximately the central 50% of the cross sectional area of the test section. In this region, over the longitudinal measurement range (<math>x_T = -2.0</math> to <math>+1.0</math> m), the following flow non-uniformities were observed. For the four velocities, longitudinal mean-flow velocities deviated within the range <math>-1.2\%</math> to <math>+1.6\%</math> from their values at the centre of the tunnel test section (<math>x_T = 0.0</math> m). For velocities of 30 and 60 m/s, horizontal flow angles deviated within the range <math>-0.8^\circ</math> to <math>+0.8^\circ</math> and vertical flow angles deviated within the range <math>-1.2^\circ</math> to <math>+0.4^\circ</math>. For velocities of 30 and 60 m/s, the u-component turbulence intensities were generally below 0.4%, and the v- and w-component intensities were generally below 0.7%. Corresponding spectra for the u- v- and w-components of the turbulence were relatively smooth over the frequency range 0.3 Hz to 10 kHz, with no significant spikes associated with irregularities in the flow. There was a slight improvement in the quality of the flow in the test section resulting from the modifications to the tunnel in 1996.</p>					